



**HAL**  
open science

# Systemes à fermions lourds à base d'Ytterbium : une instrumentation novatrice avec un enjeux fondamental

Amalia Fernandez-Panyella Fernandez-Panyella

## ► To cite this version:

Amalia Fernandez-Panyella Fernandez-Panyella. Systemes à fermions lourds à base d'Ytterbium : une instrumentation novatrice avec un enjeux fondamental. Autre [cond-mat.other]. Université de Grenoble, 2012. Français. NNT : 2012GRENY050 . tel-00858322

**HAL Id: tel-00858322**

**<https://theses.hal.science/tel-00858322v1>**

Submitted on 5 Sep 2013

**HAL** is a multi-disciplinary open access archive for the deposit and dissemination of scientific research documents, whether they are published or not. The documents may come from teaching and research institutions in France or abroad, or from public or private research centers.

L'archive ouverte pluridisciplinaire **HAL**, est destinée au dépôt et à la diffusion de documents scientifiques de niveau recherche, publiés ou non, émanant des établissements d'enseignement et de recherche français ou étrangers, des laboratoires publics ou privés.

## THÈSE

Pour obtenir le grade de

### DOCTEUR DE L'UNIVERSITÉ DE GRENOBLE

Spécialité : **Physique de la matière condensée et du rayonnement**

Arrêté ministériel : 7 août 2006

Présentée par

**Amalia Fernandez Pañella**

Thèse dirigée par **Daniel Braithwaite**

préparée au sein du **Service de Physique Statistique, Magnétisme et Supraconductivité (SPSMS)**  
et de **dans l'École Doctorale de Physique, Grenoble**

# Ytterbium-based heavy fermion compounds under extreme conditions: a new instrumentation to tackle fundamental questions

Thèse soutenue publiquement le **6 décembre 2012**,  
devant le jury composé de :

**Dr. Claudine Lacroix**

CNRS Grenoble, Président

**Dr. Didier Jaccard**

Université de Genève, Rapporteur

**Dr. Sébastien Burdin**

Université de Bordeaux 1, Rapporteur

**Dr. Rikio Settai**

Université de Niigata, Examineur

**Dr. Daniel Braithwaite**

Commissariat de l'Énergie Atomique, Directeur de thèse





## Abstract

In this thesis, three Yb-based heavy fermion compounds,  $\text{YbCu}_2\text{Si}_2$ ,  $\text{YbCo}_2\text{Zn}_{20}$  and  $\text{YbRh}_2\text{Si}_2$  are studied under extreme conditions, i.e, high pressure, low temperatures and high magnetic fields. An important part of the work has been the setup of an *in-situ* tuning pressure device to measure diamond anvil cells at dilution fridge temperatures. This has enable most of the experimental results presented in this work.

In  $\text{YbCu}_2\text{Si}_2$ , the nature of the pressure-induced magnetic order that arises for  $P_c > 8$  GPa has been clarified to be ferromagnetic by ac-susceptibility and magnetization measurements under pressure. The interplay of magnetism and valence change has been investigated by measuring the valence of the title compound at high pressures and low temperatures using resonant inelastic x-ray scattering (RIXS). As expected, pressure favors the trivalent state but the Yb ion valence remains below 3 even at the highest pressure and at low temperatures very close to the onset of the magnetic order. We have also performed a detailed search for signatures of metamagnetism.

The second part of my thesis focuses on  $\text{YbCo}_2\text{Zn}_{20}$ . We have extended the  $(P - T)$  phase diagram up to 14 GPa by ac-calorimetry and ac-susceptibility measurements. Our results shed some light on the nature of the magnetic order that arises for  $P > 1$  GPa which is antiferromagnetic. The strong field effects observed in the physical properties in  $\text{YbCo}_2\text{Zn}_{20}$  are probably related to the interaction between the magnetic field and the spin of the  $4f$  electrons rather than to their charge as the valence of the Yb ion is insensitive to the application of a magnetic field of 10 T.

The final part of this thesis is devoted to the detailed study of the  $(H - T)$  phase diagram under pressure in  $\text{YbRh}_2\text{Si}_2$  to determine the evolution of the magnetic ordering temperatures  $T_N$  as a function of  $H$  and  $P$  to better understand the interplay of the two control parameters.

## Key words

Heavy fermion compounds

Intermediate-valence systems

high pressure quantum critical point

$\text{YbCu}_2\text{Si}_2$

$\text{YbCo}_2\text{Zn}_{20}$

$\text{YbRh}_2\text{Si}_2$



# Acknowledgements

Already...? The adventure that has represented the PhD has come to an end and now I would like to warmly thank all the people who has been involved in it in so many different ways and who has made it possible. Because one thing is sure... I have not done this long and intense way all alone...

First of all, I would like to thank Claudine Lacroix, Rikio Settai, Didier Jaccard and Sébastien Burdin for accepting to be in my jury and for their careful reading of the manuscript and their valuable comments.

Daniel, I feel very grateful for having you as my PhD advisor. From a scientific but also human point of view you have been a good and very valuable reference for me. Also I really appreciate that you let me follow my own initiatives and you supported and encouraged me to pursue them. It has been a pleasure to work with you and I will be always amazed how do you keep your calm whatever happens!

Bernard, je te suis très reconnaissante pour tout le savoir que tu m'as transmis sur la haute-pression et pour être toujours disponible!

Jean-Michel, sans aucun doute tu as mérité le titre de "génie de la cryogénie"! Merci pour tous les coups de mains (assez nombreux!) et ta bonne humeur: "On y croit, on y croit!".

A tout le groupe du laboratoire: un grand merci pour votre accueil, pour les bons moments partagés et pour votre aide: Georg, Alex, Dai, Jean-Pascal, Jacques, Gérard, Christophe, Carine, Marie-Jo (j'oublierais jamais la bonne texture de l'isolation: celle d'un "vieux chewing-gum!"), Michel, Frédéric, Stéphane, François, Marielle ...

Grâce aux collaborations et aux conférences j'ai eu aussi l'opportunité de faire de belles rencontres: Jean-Pascal, Victor et Luigi: c'était un plaisir travaillé et faire les manips au synchrotron avec vous! Sébastien, tu es un des (rares?) théoriciens qui sache divulguer très bien la physique des fermions lourds à des expérimentateurs. J'ai apprécié énormément les échanges et discussions qu'on a eu. William, Ilya et Albin, je suis très contente d'avoir fait votre connaissance et d'avoir collaboré avec vous. Patricia, working with you in Cambridge was a very enriching (and challenging!) experience and I praise the passion you have for what you do. Joe, it was a pleasure meeting you and also all the discussions we had. I really appreciated visiting LANL, thank you very much. Askhan, I'm so glad you invited me to the Gordon Seminar. I spent a great time in the High Pressure conference. It boosted me to keep on doing research and moreover, I had the opportunity to meet many interesting people, especially Gilbert Collins which I want to thank for giving me the opportunity to come to LLNL.

Qu'est-ce que c'est un labo sans les doctorants?! Qui si non reste jusqu'à 20h30 au CEA pour un transfert d'He? (ou même plus tard... Sshh!) Elena, Ludo, Valentin et Alejandra: merci pour la belle ambiance dans le bureau!, Tristan: un GRAND merci pour ton amitié et hospitalité, Mathieu: j'oublierai jamais la boîte avec les vis et le tournevis...!, Mounir: je doute fort qu'un autre thésard (ou personne en générale en fait) puisse faire des gâteaux mieux que les tiens, Audrey, Benoît, pas un mais deux!, Charlène, Paul... Je garderai dans mes souvenirs et avec beaucoup de joie les moments partagés ensemble.

"Les amis de mes amis... ce sont mes amis" n'est-ce pas Mèl, Julien, Antoine, Mag, Franck, Jérôme, Noël, Laure, Marjo, Isa, Adeline...? Merci pour m'avoir accueilli de façon aussi chaleureuse et naturelle depuis le début! Je porterai avec moi tellement de bons souvenirs! Seb, je suis très contente que nos chemins se soient croisés. Merci pour tous les moments vécus ensemble. MERCI,

tout simplement. Et aussi à ta famille: Gérard, Martine, Nadia, Yannick ("ça va pas du tout!"), Carole, Nanou, Henry et Serge. Je vous aime!

Il mio caro grupo d'italiani (e non solo): non importa si adesso siamo tutti in città diverse. Non dimenticherò tutti i momenti passati insieme qui a Grenoble: nella montagna, nel Hammam (eh Tita?), a Roma, a l'ESRF... Vi abbraccio forte, forte: Imma, Raffa e Francesco, Vale, Sheeba e Davide, Paul, Erminia, Bridgette e Fabio.

Quand je n'étais pas au labo j'étais probablement en train de... danser du Swing ou Blues! C'était une très belle découverte qui sans doute va m'accompagner pour un long but du temps et là aussi j'ai connu de gens formidables. Avec certains l'amitié a continué hors la piste de danse: Marie et Thibaut, Chrystelle, Arnaud et Fabien. Sans vous ça aurait été beaucoup plus dur mais surtout beaucoup moins drôle! Et en suite il y a une longue liste de gens de Grenoble Swing et ailleurs avec qui j'ai partagé de belles danses et pas seulement, aussi de très bons moments! Caro, Vale, Marie et Jeremy, Raphael, Laurent, Aurélien, Olivier, Maria, Muriel, Yann, Aurélie, Aude, ... et je tiens en spécial au groupe du Blues des mercredis! Ces moments partagés entre thés, rigolades et danses... je ne vais pas les oublier!

I ara arribem a les amistats de "largo recorrido". Irene, com molt bé ho vas resumir quan vas venir a veurem a Grenoble: sempre serem "TU i JO" (i efectivament, no és fàcil de trobar). Ari, ets part de la meva família! T'estimo. Gràcies a totes dues per la vostra presència encara que no ens veiem cada dia... un cop de telèfon i puf! És (gairebé) com teletransportar-se. Jaime, te quiero. El grup de "Casp": Anna-Iris, Dudu i Núria, Rai, Pere, Xavi, Mikel i Núria. M'encanta tenir la sensació com si fos "ahir" l'últim cop que ens vam veure. Va significar molt per mi que estiguéssiu presents el dia de la defensa de la tesi a Grenoble. Moltes Gràcies!

I finalment, la família! És a vosaltres a qui dedico aquesta tesi. Per tot el vostre amor i suport incondicional. No importa on vagi... sempre us portaré al meu cor. Papa, m'agrada molt compartir amb tu tantes aventures! I la tesi ens ha donat moltes oportunitats: a Grenoble, al CERN, a Cambridge... Mama, ets la persona més generosa que conec: gràcies! I vas tenir una gran vista al ensenyar-me idiomes des de ben petita! Blanca, com més creixem més ens estimem (no és bonic?), Mano, ets sense cap mena de dubte "La Super-Tieta". T'estimo! Com a l'Adri, l'Ignasi, el Jaime i la Ceni, la Helen, el Xavi, l'Alfred... Som una magnífica família. Per acabar, m'agradaria incloure als que ja no hi són: la tieta Mercé, el tio José, el Joan, la Tia Manolita i la Iaia.

# Contents

<b>1</b>	<b>Theoretical Background</b>	<b>3</b>
1.1	Heavy Fermions . . . . .	3
1.2	Kondo lattices . . . . .	8
1.2.1	Kondo lattice hamiltonian . . . . .	8
1.2.2	Intermediate-valence regime . . . . .	9
1.2.3	Competition between Kondo effect and RKKY interaction: Doniach phase diagram . . . . .	9
1.2.4	Crystal electric field . . . . .	10
1.2.5	Fermi-Liquid relations . . . . .	11
1.3	Quantum criticality . . . . .	14
1.3.1	Classical versus quantum phase transition . . . . .	14
1.3.2	Non-Fermi-Liquid behavior . . . . .	15
1.3.3	Theoretical approaches of quantum criticality . . . . .	15
1.4	Ce versus Yb systems . . . . .	18
1.4.1	Beyond the “hole” equivalent picture . . . . .	19
1.4.2	Doniach picture for Yb HF compounds . . . . .	20
1.4.3	Pressure dependence of $T_K$ in Ce and Yb systems . . . . .	21
1.4.4	First-order Valence instability . . . . .	23
1.4.5	Unconventional superconductivity . . . . .	28
<b>2</b>	<b>Experimental techniques</b>	<b>31</b>
2.1	Crystal growth . . . . .	31
2.2	Extreme conditions . . . . .	37
2.2.1	Low temperatures . . . . .	39
2.2.2	High pressure techniques . . . . .	39
2.2.3	High Magnetic fields . . . . .	50
2.3	High pressure measurements . . . . .	50
2.3.1	Electrical resistivity . . . . .	50
2.3.2	Specific heat . . . . .	51
2.3.3	Ac-susceptibility . . . . .	53
2.3.4	Magnetization . . . . .	55
2.4	X-ray spectroscopic measurements . . . . .	57
2.4.1	Valence measurement under extreme conditions . . . . .	57
2.4.2	Valence measurement under magnetic field . . . . .	59
<b>3</b>	<b>YbCu<sub>2</sub>Si<sub>2</sub></b>	<b>61</b>
3.1	Introduction . . . . .	61
3.2	$P - T$ Phase diagram - comparison with previously reported data . . . . .	64
3.3	Nature of the pressure-induced magnetic order . . . . .	69
3.3.1	Ac-susceptibility measurements under magnetic field . . . . .	71
3.3.2	P-T-H phase diagram . . . . .	71
3.3.3	Magnetization measurements under pressure . . . . .	73
3.4	Metamagnetism . . . . .	75

# CONTENTS

3.4.1	Magnetization at high magnetic fields . . . . .	75
3.4.2	Magnetoresistivity under pressure . . . . .	76
3.5	Fermi-Liquid studies throughout the P-T-H phase diagram . . . . .	80
3.6	Interplay of magnetism and valence change . . . . .	83
3.6.1	Valence measurements under extreme conditions . . . . .	83
3.6.2	Valence measurements under magnetic field . . . . .	88
3.7	Conclusions . . . . .	88
<b>4</b>	<b>YbCo<sub>2</sub>Zn<sub>20</sub></b>	<b>93</b>
4.1	The YbT <sub>2</sub> Zn <sub>20</sub> family . . . . .	93
4.2	Introduction of YbCo <sub>2</sub> Zn <sub>20</sub> . . . . .	96
4.2.1	Heavy fermion state . . . . .	96
4.2.2	Physical properties under magnetic field . . . . .	99
4.3	High pressure phase diagram . . . . .	105
4.3.1	Pressure-induced magnetic order . . . . .	105
4.3.2	$P - T$ phase diagram at low pressures . . . . .	107
4.3.3	$P - T$ phase diagram from ac-calorimetry studies under pressure . . . . .	108
4.3.4	Nature of the magnetic order . . . . .	110
4.4	Conclusions . . . . .	111
<b>5</b>	<b>YbRh<sub>2</sub>Si<sub>2</sub></b>	<b>115</b>
5.1	Introduction . . . . .	115
5.1.1	Crystal electric field . . . . .	116
5.1.2	Field-induced quantum critical point . . . . .	116
5.2	$P - T - H$ phase Diagram . . . . .	118
5.2.1	$P - T$ phase diagram . . . . .	120
5.2.2	Magnetic field effect under pressure . . . . .	121
5.2.3	H-T phase diagram under pressure . . . . .	123
5.3	Conclusions . . . . .	123
<b>6</b>	<b>Conclusions</b>	<b>127</b>
	<b>Bibliography</b>	<b>131</b>

# Introduction

Since the discovery of the Kondo effect more than forty years ago, heavy fermion compounds have become a relevant and very fruitful research field within strongly correlated electron systems. Their particular low-temperature physical properties such unconventional superconductivity in  $\text{CeCu}_2\text{Si}_2$  [Steglich 1979], the coexistence of magnetism and superconductivity which was firstly observed in  $\text{URu}_2\text{Si}_2$  [Maple 1986] or the observation of Non-Fermi-Liquid behavior in several heavy fermion compounds [Löhneysen 1994, Custers 2003], have attracted a lot of attention from an experimental and theoretical point of view.

The low energy scales of heavy fermions make them very suitable candidates for quantum criticality studies as they are often located close to a magnetic instability and by varying the strength of the electronic and magnetic exchange interactions via an external parameter like hydrostatic pressure, the system can be driven at a quantum critical point (QCP). In cerium systems quantum criticality has been studied extensively as pressure tends to destroy the magnetic order that is established at ambient pressure and a QCP is reached for rather low pressures. Therefore the physical properties near the QCP can be fully characterized. On the other hand, in Yb-based heavy fermion systems, the effect of pressure is usually opposite and a magnetic order is induced with pressure. The study of ytterbium systems presents challenges, as in general higher pressures are needed, and so they have been far less extensively studied to date. Especially in the field of high pressure advances in physics are strongly related to advances in instrumentation. A large part of this thesis has been devoted to setting up an *in-situ* pressure tuning device adapted for diamond anvil cells, to work in a dilution fridge and with magnetic field. This instrument makes possible a new generation of experiments.

In the first chapter I will give an overview of the important physical phenomena in heavy fermion compounds in general, before describing the relevant physical effects, interactions and theoretical models in more detail. I will finish with a detailed comparison of the differences between Ce and Yb-based heavy fermion compounds where I try to answer the question: “Why Ce-based heavy fermion compounds are so popular compared to Yb-based HF compounds?”.

In the second chapter, I will describe the characteristics and performance of the pressure-tuning device in detail and also all the experimental techniques used during this work.

The second part of my thesis has been focused in the study of three different Yb-heavy fermion compounds:  $\text{YbCu}_2\text{Si}_2$ ,  $\text{YbCo}_2\text{Zn}_{20}$  and  $\text{YbRh}_2\text{Si}_2$ .

In the third chapter I present the results we have obtained in  $\text{YbCu}_2\text{Si}_2$ . At the beginning of this work, the nature of the magnetic order that arises under pressure was still unknown but it has been determined via ac-susceptibility measurements under pressure during this work. We have also performed a detailed study of the Fermi liquid properties throughout the whole ( $P - H - T$ ) phase diagram, a careful research of metamagnetism and the valence measurements of the Yb ion under high pressure and low temperatures give more information of the interplay between magnetism and valence change in this intermediate-valence compound.

The fourth chapter is devoted to the study of the “super heavy-fermion”  $\text{YbCo}_2\text{Zn}_{20}$ . We present an extended ( $P - T$ ) phase diagram up to 13 GPa from ac-calorimetry measurements. From our results we can also shed some light about the nature of the pressure-induced magnetic order. The last chapter presents a detailed study of the ( $H - T$ ) phase diagram under pressure in  $\text{YbRh}_2\text{Si}_2$ .



# CHAPTER 1

## Theoretical Background

---

### 1.1 Heavy Fermions

Heavy fermions are intermetallic compounds containing a partly filled  $4f$  or  $5f$ -shell from a lanthanide (e.g., Ce, Yb, Sm) or actinide (e.g., U) element. Chemically, the special feature of the  $4f$  orbitals<sup>1</sup> in the rare earth (RE) ions is that they are well embedded within the atom, close to the atomic core and shielded by the  $5s$  and  $5p$  electrons as shown in figure 1.1. They keep the quasi-localized behavior even in solids. Nevertheless, the outer part of the  $4f$  wave function expands enough to overlap with the conduction electron bands [Fisk 1995, Jensen 1991]. All the remarkably properties of heavy fermions stem precisely from the interaction between the  $f$  “localized” electrons and the conduction electron band.

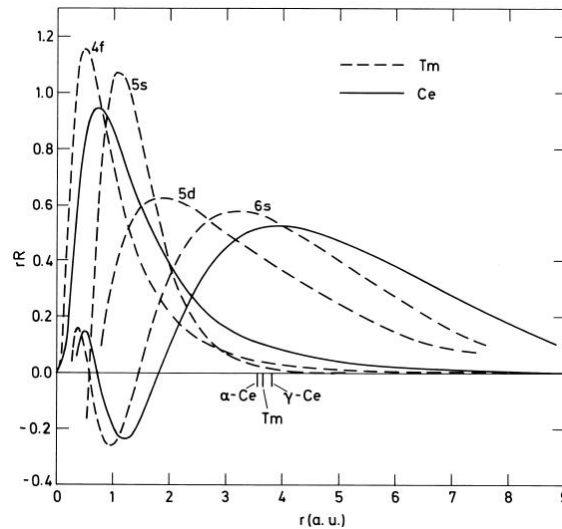


Figure 1.1: The radial components of atomic wave functions for Ce, with one  $4f$  electron and Tm with 13  $4f$  electrons are shown. The Tm wave functions are more contracted, i.e. more localized, than in Ce due to an incomplete shielding of the greater nuclear charge. This is known as the “lanthanide contraction” [Jensen 1991].

Heavy fermion (HF) compounds exhibit peculiar low-temperature physical properties that distinguish them from ordinary metals. Conventional metals are characterized by an increasing conductivity with decreasing temperature, a small paramagnetic Pauli susceptibility and a linear temperature dependence of the specific heat  $C(T)$  at low temperatures (i.e., for  $T \ll E_F, \Theta_D$ , where  $E_F$  is the Fermi energy and  $\Theta_D$  is the Debye temperature) [Fisk 1988].

---

<sup>1</sup>From now on I will only talk about rare earth systems ( $4f$ ).

## 1.1. Heavy Fermions

In a metal for  $T > 0$  the electrical resistivity  $\rho$  is due to several scattering mechanisms of the electrons which contribute additively in accordance with the Matthiessen's rule:

$$\rho = \rho_0 + \rho_{ele} + \rho_{ph} + \rho_{mag}, \quad (1.1)$$

where  $\rho_0$  is the residual resistivity due to elastic scattering of the electrons from impurities and lattice defects. The other terms reflect the scattering with the excitations of the system: electrons, phonons which is the dominant term at high temperatures, and for magnetically ordered materials, an another contribution  $\rho_{mag}$  should be taken in to account due to the scattering with collective magnetic excitations (magnons). At low temperatures, well below the Debye temperature, the phonon term which is proportional to  $T^5$ , is normally small.

At high temperatures,  $\rho(T)$  does not differ significantly in heavy fermion materials compared to conventional metals, except for a large magnetic term ( $\approx 100 \mu\Omega.cm$ ). As temperature decreases (and ignoring the phonon contribution)  $\rho(T)$  logarithmically increases,  $\rho(T) \propto -\ln T$ , as a signature of the Kondo effect, down to a characteristic temperature,  $T_{max}$ , where it shows a maximum. Below  $T_{max}$  there is a strong decrease of  $\rho(T)$  and at some point, at very low temperatures, it follows

$$\rho(T) = \rho_0 + AT^2, \quad (1.2)$$

such  $T^2$  dependence is usually identified with a Fermi-liquid (FL) behavior and the coefficient  $A$  is due to quasiparticle-quasiparticle scattering. In figure 1.2 a) the resistivity of  $Ce_xLa_{1-x}Cu_6$  for different Ce doping concentration,  $x$ , shows the onset of the Fermi-liquid behavior for  $x > 0.7$  at low temperatures.

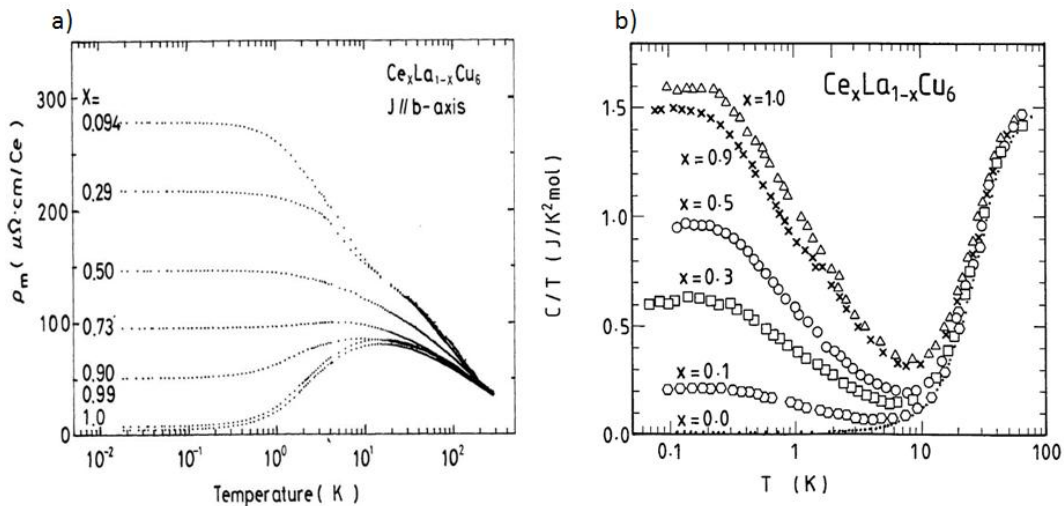


Figure 1.2: a) Resistivity of  $Ce_xLa_{1-x}Cu_6$  [Sumiyama 1986]. When the number of impurity becomes large ( $x > 0.7$ ), coherence effects appear and a Fermi-liquid regime is observed. b) Temperature dependence of  $C/T$  for  $Ce_xLa_{1-x}Cu_6$  [Sato 1989]. A large enhancement of  $C/T$  is observed at low temperatures for increasing Ce doping.

Other macroscopic properties like susceptibility and specific heat again show two distinct regimes depending on temperature. At high temperatures, the  $f$ -electrons behave as localized magnetic moments that weakly interact with the conduction electrons. This gives rise to a Curie-Weiss susceptibility,  $\chi \propto \frac{\mu_{eff}^2}{T - \Theta_{CW}}$ . The Curie-Weiss temperature  $\Theta_{CW}$  is often negative, indicating an

antiferromagnetic exchange, and the effective magnetic moment  $\mu_{eff}^2$  is close, but in general smaller because of the crystal-electric field (CEF) splitting, than the value obtained by Hund's rules for the free RE ion. At low temperatures,  $\chi(T)$  does not have a unique behavior but often it reaches a constant value near  $T_{Max}$  and on further cooling it behaves like

$$\chi(T) = \chi_0(1 + aT^2), \quad (1.3)$$

which is characteristic of Fermi liquids [Béal-Monod 1968]. Moreover, the value of  $\chi$  at low temperatures is two or more orders of magnitude higher than the Pauli susceptibility observed in ordinary non-magnetic metals.

The specific heat,  $C/T$  strongly increases below  $T_{max}$  and at sufficiently low temperatures it is almost constant.

$$C(T) = \gamma T, \quad (1.4)$$

where the Sommerfeld coefficient,  $\gamma$ , can attain values as high as  $1 \text{ J/molK}^2$ , significantly higher than the typical value of ordinary metals like Cu or Al with  $\gamma \sim 1 \text{ mJ/molK}^2$  [Ashcroft 1975]. Often, the  $\beta T^3$  term reflecting the phonon contribution is in comparison negligible at low temperatures.

It turns out that the low-temperature physical properties of heavy fermion materials are consistent with Landau's theory of Fermi liquids where the strongly interacting electrons are described as weakly interacting fermionic quasiparticles and it is possible to assume a one-to-one correspondence between the quasiparticle excitations of the complex system and those of a free electron gas by normalizing a few parameters like the effective mass  $m^*$ .

The Sommerfeld coefficient,  $\gamma$  in the framework of Fermi-liquid theory is expressed as

$$\gamma = \frac{\pi^2}{3} k_B^2 N_F = \frac{k_B^2}{3\hbar^2} k_F m^*, \quad (1.5)$$

where  $N_F$  is the total quasiparticle density of states (DOS) at the Fermi surface and  $k_F$  is the Fermi wave vector.

The enhanced  $\gamma$  observed in heavy fermions comes from the large effective mass <sup>2</sup> than can be as high as  $m^* = 1000m_0$ , being  $m_0$  the bare electron mass. It has been confirmed experimentally that the large  $m^*$  is directly related to the presence of the magnetic impurities by measuring the  $\gamma$  of isostructural RE compounds with no  $4f$  electrons (e.g. La, Lu) [Fisk 1995], as reflected in figure 1.2 b) for  $\text{Ce}_x\text{La}_{1-x}\text{Cu}_6$  where the temperature dependence of the specific heat for different Ce doping concentration is shown and for the case  $x = 0$ , i.e. without magnetic impurities,  $C/T$  is very small.

The origin behind these anomalous properties is the so-called Kondo effect. The Kondo effect was firstly observed in the 30' when a minimum in the resistivity of several metals (Cu, Au, Ag) was observed [de Haas 1934]. 30 years later, the resistance minimum was linked to the presence of magnetic impurities [Clogston 1962]. Kondo [Kondo 1964] solved in 1964 the "mystery" of this resistance minimum by a perturbative model where the presence of the magnetic impurities were considered to weakly modify the metal as the energy of the interaction was small. This perturbative approach turned out to be not appropriate as it gave a non physical divergence of the resistivity at low temperatures. Finally, the solution of the Kondo impurity problem was solved by renormalization group [Nozières 1980] and the Bethe Ansatz method [Andrei 1983].

---

<sup>2</sup>Since  $k_F$  is determined by the density of conduction electrons which is of the order of  $10^{22} \text{ cm}^{-3}$  independent of metals.

## 1.1. Heavy Fermions

Nevertheless, the work of Kondo successfully explained the process by which a free magnetic moment (at high temperatures) becomes screened by the spins of the conduction electrons at low temperatures. This screening process is continuous and takes place once the temperature drops below a characteristic energy scale,  $T_K$

$$k_B T_K \propto D \exp\left(\frac{-1}{N(E_F)J}\right) \quad (1.6)$$

where  $D$  is the bandwidth of the conduction electrons,  $N(E_F)$  is the density of states of the conduction band at the Fermi level and  $J$  is the coupling between the spins of the conduction electrons and the spin of the magnetic impurity.

The ground state of the system corresponds to a Kondo singlet where the spin of the  $4f$  and conduction electrons couple antiferromagnetically,  $J > 0$ . In dilute magnetic alloys, these Kondo singlets are randomly distributed and they act as elastic scattering potentials for the conduction electrons which explains the increasing resistivity observed at low temperatures (figure 1.4) and at the same time they give rise to a peak in the conduction density of states near the Fermi energy known as the Kondo or Abrikosov-Suhl resonance [Abrikosov 1965, Suhl 1965] as shown in figure 1.3 a).

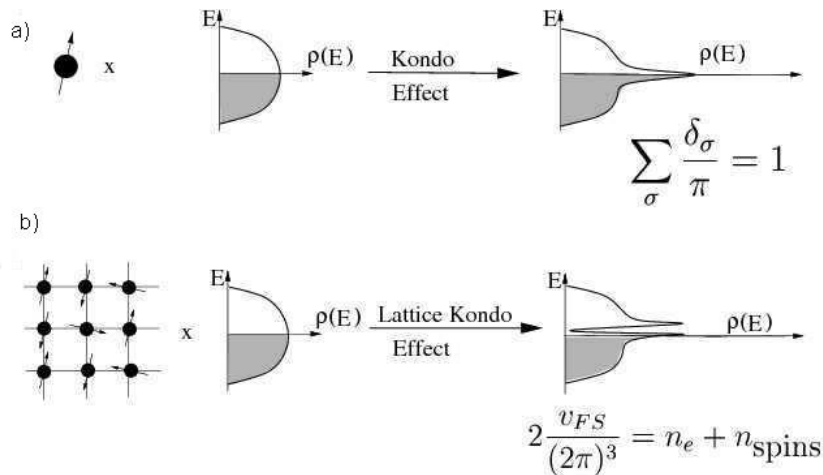


Figure 1.3: a) *Single impurity Kondo effect gives rise to a peak (Abrikosov-Suhl resonance) in the conduction density of states.* b) *In a Kondo lattice a narrow band of width  $k_B T_K$  of heavy quasiparticles is formed [Coleman 2007].*

Heavy fermions are often called Kondo lattices owing to the large concentration of localized magnetic moments and the fact that they are periodically arranged. In a Kondo lattice, below a certain temperature,  $T^*$ , coherent scattering among the quasiparticles develops and it is reflected in the resistivity with a strong drop (and the FL regime (figure 1.4) ) as previously mentioned. In 1985, Nozières posed the question known as “the exhaustion”: if there is only one energy scale,  $T_K$  (as in the single impurity case), only electrons within  $T_K$  of the Fermi level are eligible to participate in magnetic screening of impurities<sup>3</sup>. This implies that *few electrons must screen many impurities* [Nozières 2005]. As a consequence, Nozières suggested that the coherent FL regime would appear for a  $T^* \ll T_K$ . A few years ago, Burdin demonstrated that this exhaustion problem does not take place because in a Kondo lattice there are in fact two energy scales: one is related to the onset of local Kondo screening ( $T_K$ ) and the second,  $T^*$  is associated with the onset of the

<sup>3</sup>The other ones are blurred by thermal fluctuations and they can not achieve coherent singlets.

Fermi-liquid coherence regime. He also showed that in the exhaustion limit,  $n_c \ll 1$  ( $n_c$  is the number of conduction electrons), as Nozières pointed out,  $T^* \ll T_K$  [Burdin 2000, Nozières 2005]. Experimentally, it is very difficult to distinguish both temperatures. For the sake of simplicity, we often consider that  $T^* \propto T_K \propto T_{max}$  and typical values are comprised between 1 K and 50 K.

In contrast to the impurity case, in a lattice, the density of states develops a real narrow band of heavy quasiparticles near  $E_F$  with an hybridization gap of width  $\approx k_B T_K$ , as depicted in figure 1.3 b). This implies that the previously localized  $f$ -electrons now are delocalized and participate in the Fermi surface. This strong renormalization at the Fermi surface leads to the enhanced effective masses in these systems.

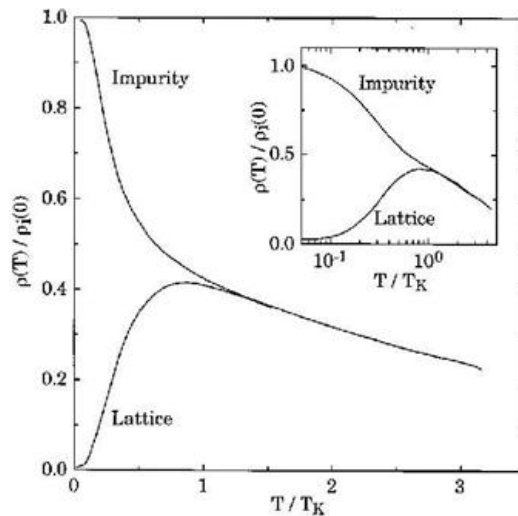


Figure 1.4:  $\rho(T)$  in the sixfold degenerated Anderson lattice (bottom curve) and for the single impurity (upper curve).  $\rho_i(0)$  is the resistivity at  $T=0$  K per ion in the dilute limit. The inset shows both the impurity and lattice curves in a logarithmic scale to bring out the  $\ln(T/T_K)$  dependence for the single impurity case [Degiorgi 1999].

The Kondo effect causes a screening of the magnetic moments. Nevertheless, many heavy fermion systems order magnetically at low temperatures. In metals containing a dilute magnetic elements there is an additional interaction known as the Ruderman-Kittel-Kasuya-Yosida (RKKY) exchange interaction. The magnetic impurities do not interact directly own to its localized character but they couple to each other indirectly by polarizing the conduction electrons. A characteristic energy scale is associated and defined as

$$k_B T_{RKKY} \propto J^2 N(E_F) \frac{\cos(2k_F r)}{k_F r} \quad (1.7)$$

where  $k_F$  is the Fermi vector and  $r$  the distance between the magnetic impurities. This interaction extends over a long range and it is damped with a sinusoidal oscillation of wave vector  $k_F$  (Friedel oscillations) [Ruderman 1954, Reinhold 1996]. Depending on  $r$ , the magnetic moments  $\vec{S}_i$  and  $\vec{S}_j$  (figure 1.5) can couple either ferro- or antiferromagnetically.

The competition between the RKKY interaction (inter-site), which favors long range magnetic order and the Kondo effect (on-site), which tends to screen the magnetic moments, leads to different ground states in heavy fermion systems which give rise to rich and complex phases diagrams. The details of this competition are described in the section 1.2.

## 1.2. Kondo lattices

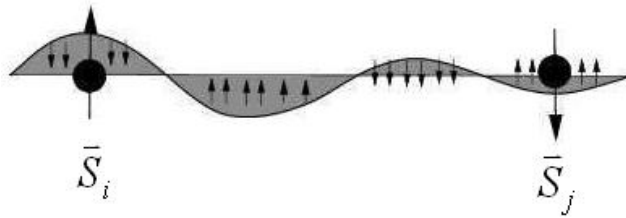


Figure 1.5: *Spin polarization around magnetic impurities contain Friedel oscillations and induces a RKKY interaction between the spins  $\vec{S}_i$  and  $\vec{S}_j$  [Coleman 2007].*

## 1.2 Kondo lattices

The Periodic Anderson Hamiltonian (PAM) is considered as the basic microscopic model for investigating the rich physics of heavy fermions [Anderson 1961, Hewson 1993]. It simulates the hybridization between an atomic-like level (the  $4f$  electrons) with strong on-site Coulomb repulsion interaction with a conduction band. Often, the PAM is written as follows

$$\mathcal{H} = \sum_{k,\sigma} \varepsilon(k) s_{k\sigma}^\dagger s_{k\sigma} + \sum_{i\sigma} \varepsilon_f f_{i\sigma}^\dagger f_{i\sigma} + V \sum_{i,\sigma} (f_{i\sigma}^\dagger s_{i\sigma} + s_{i\sigma}^\dagger f_{i\sigma}) + \frac{1}{2} U \sum_{i\sigma} n_{i\sigma} n_{i-\sigma}, \quad (1.8)$$

where  $s_{k\sigma}$  ( $f_{i\sigma}$ ) and  $s_{k\sigma}^{dag}$  ( $f_{i\sigma}^\dagger$ ) are the annihilation and creation operators for an electron in a conduction-band state (localized  $f$  state), and  $n_{i\sigma} = f_{i\sigma}^\dagger f_{i\sigma}$  is the occupation number operator for the  $f$  states.  $\varepsilon(k)$  is the dispersion relation for the conduction electrons and  $\varepsilon_f$  is the position of the  $f$  level.  $\sigma$  corresponds to the spin index  $\sigma = \uparrow, \downarrow$  whereas  $k$  characterizes the wave vector of the conduction band.

The first two terms in (1.8) represent the kinetic energy of the conduction band and the energy  $\varepsilon_f$  of the  $f$  electron respectively. The hybridization between the  $f$  and conduction electrons is given by the matrix element  $V$  in the third term. Finally, the last term corresponds to the Coulomb repulsion,  $U$ , between two  $f$  electrons on the same lattice site.

Different *regimes* can be considered within this model. Here we will focus on two of them: the *Kondo* and the *intermediate-valence regime* which are closely related with heavy fermions.

### 1.2.1 Kondo lattice hamiltonian

In the Kondo regime, each  $f$  orbital is occupied by a single electron, and PAM can be reduced to the single-impurity Anderson model [Anderson 1961]. The Coulomb repulsion is the decisive term of the model as it allows the local-moment formation if the impurity level ( $\varepsilon_f$ ) lies below the Fermi energy, i.e.,  $\varepsilon_f < 0$ , while  $2\varepsilon_f + \frac{U}{2} > 0$ , and the bare hybridization width  $\Gamma = \pi N_0 V^2$  is small, i.e.,  $\Gamma \ll \varepsilon_f, \varepsilon + U$ . In this situation, the impurity level is mainly occupied by a single electron, i.e.,  $n \approx 1$ , rather than being empty or doubly occupied and thus represents a local moment of spin  $1/2$  [Löhneysen 1994]. This is illustrated in figure 1.6 a) which is known as the Kondo limit ( $n \approx 1$ ).

In this regime, the low-energy physics can be described by an effective model where the  $f$ -electron degrees of freedom are represented by localized spins, known as the Kondo lattice hamiltonian<sup>4</sup>:

<sup>4</sup>Thus, The Kondo lattice hamiltonian is a particular case of the PAM that is obtained via the Schrieffer-Wolff transformation (i.e.,  $U \rightarrow \infty$  to obtain  $n \approx 1$ ) [Schrieffer 1966].

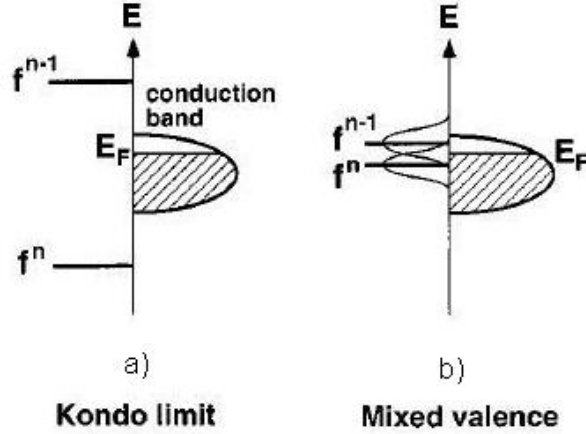


Figure 1.6: Schematic level scheme of a localized orbital and a conduction band for different regimes: a) Kondo limit where  $n \approx 1$ ,  $\epsilon_f < 0$  and  $\Gamma \ll \epsilon_f$ . b) the intermediate-valence (mixed valence in the scheme) regime where  $|\epsilon_f - E_F| \approx \Gamma$  (see details in text) [Tsunetsugu 1997].

$$\mathcal{H} = \sum_{k,\sigma} (\epsilon(k) - \mu) s_{k\sigma}^\dagger s_{k\sigma} + J \sum_i s_i S_i, \quad (1.9)$$

where  $\mu$  is the chemical potential and  $J$  is the coupling exchange between the conduction and the  $f$  electrons.

### 1.2.2 Intermediate-valence regime

A different scenario takes place when  $\epsilon_f$  is located close to the Fermi energy as shown in figure 1.6 b). Now,  $|\epsilon_f - E_F| \approx \Gamma$  and both configurations,  $4f^n$  and  $4f^{n-1}$  can be quasi-degenerated. This corresponds to the intermediate-valence regime. Here, we refer to (“homogeneously”) intermediate-valence systems<sup>5</sup>: globally the valence is not an integer number but all the sites are equivalent. We talk about valence fluctuations on each site of the lattice between the two quasi-degenerate configurations. The order of magnitude of the fluctuating frequency is about  $10^{13}$  Hz [Kasuya 1996, Sampathkumaran 1986, Varma 1976].

Many Yb-based intermetallic compounds are intermediate-valence compounds. In general, they have smaller values of  $\gamma$ , about  $10^2$  mJ/(K<sup>2</sup>mol) and the average valency is between 2+ and 3+. Often at low temperatures these systems also show unusual temperature dependences in their transport properties like heavy fermions [Kuramoto 1999]. As it will be discussed throughout this work, the boundary between the heavy fermion regime ( $n_f \approx 1$ ) and the intermediate-valence regime ( $n_f < 1$ ) often is not sharp but rather fuzzy.

### 1.2.3 Competition between Kondo effect and RKKY interaction: Doniach phase diagram

Doniach [Doniach 1977] was the first to point out the important consequences of the competition between the main two energy scales of a Kondo lattice, i.e. Kondo temperature and RKKY interaction. Both depend on the same exchange coupling  $J$  but differently. For small  $J$  values,  $T_{RKKY}$

<sup>5</sup>In contrast to “inhomogeneously” mixed-valent compounds where different sites of the lattice have different configurations like in some ferrites, e.g., Fe<sub>3</sub>O<sub>4</sub> [Varma 1976].

## 1.2. Kondo lattices

is larger than  $T_K$  and the system orders magnetically. Otherwise, for large  $J$  values, the formation of Kondo singlets will lead to a larger energy gain and the ground state will be non-magnetic. This competition is illustrated in the so-called Doniach phase diagram for a one-dimensional system as shown in figure 1.7.

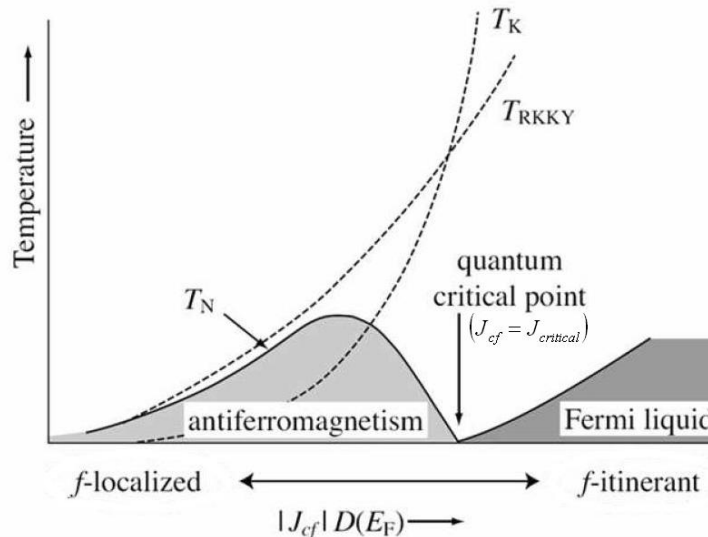


Figure 1.7: *The Doniach phase diagram shows the competition between the energies associated to the Kondo effect ( $T_K$ ) and the RKKY interaction ( $T_{RKKY}$ ) as a function of  $J D(E_F)$  (in text corresponds to  $J N(E_F)$ ) for a one-dimensional system.  $T_N$  corresponds to the Néel temperature [Brandt 1984].*

One of the major motivations on the study of heavy fermions is that in general, they are located in the Doniach phase diagram for intermediate  $J$  values where  $T_K$  and  $T_{RKKY}$  have similar values. Thus, by varying  $J$ , these systems can be tuned from a magnetic to a non-magnetic ground state by passing through a quantum critical point<sup>6</sup> (QCP) for a critical  $J = J_c$  where  $T_K \approx T_{RKKY}$  value. A QCP is reached when the magnetic order temperature is driven towards zero by varying an external parameter other than temperature (e.g., doping, magnetic field or high pressure). In the Doniach picture, the antiferromagnetic ordering temperature is driven continuously to zero through a second order transition to the QCP.

Even though the original Doniach phase diagram was proposed for a one-dimensional system and it does not take into account the effects of a non-integer valence, the above results can be taken as a good suggestion to what might happen in real three-dimensional systems [Doniach 1977].

### 1.2.4 Crystal electric field

In rare earth (RE) ions, due to the localized nature of the  $f$ -orbitals, the spin-orbit (SO) interactions are stronger than the crystalline electric field (CEF) (see table 1.1). The SO coupling combines the spin ( $S$ ) and angular momentum ( $L$ ) into a well define state  $J$ .

Let us consider a RE ion with a stable  $4f^n$  configuration with a ground state multiplet  $|n, L, S\rangle$ . This level is split by SO coupling into multiplets,  $|n, L, S, j\rangle$  and  $|n, L, S, j'\rangle$  with energies  $E_j, E_{j'} = E_j + \Delta E_{jj'}$ , with  $\Delta E_{jj'} > 0$  (Figure 1.8 a). The degeneracy factor is  $N = 2j + 1$ . For example, for the Ce ion,  $j = 5/2$ ,  $j' = 7/2$  and  $\Delta_{jj'} = 3150$  K and for the Yb ion,  $j = 7/2$ ,  $j' = 9/2$  and  $\Delta_{jj'} = 14800$  K [Jensen 1991].

<sup>6</sup>Technically, a quantum critical point is a second-order phase transition that takes place at absolute zero.

	<i>d</i> band in transition metal compounds	<i>f</i> band in rare-earth compounds
Bandwidth	~5 eV	<10 <sup>-1</sup> eV
Spin-orbit splitting	~10 <sup>-1</sup> eV	~10 <sup>-1</sup> eV
Crystal field splitting	~2 eV	~10 <sup>-3</sup> eV
Hund's rule energy	~1 eV	~1 eV
Electron-electron repulsion (Hubbard's <i>U</i> )	~5 eV	~5 eV

Table 1.1: *Characteristic energy parameters for rare earth compounds compared to transition metal compounds [Varma 1976].*

In the presence of a CEF, the lowest multiplet  $|n, L, S, j\rangle$  is split into multiplets, depending on the point symmetry. An example assuming that the lowest multiple is split into two multiples,  $|n, L, S, j, \gamma\rangle$  and  $|n, L, S, j, \gamma'\rangle$ , is given in figure 1.8 b); with degeneracies  $N_\gamma$  and  $N_{\gamma'}$ , and energies  $E_\gamma, E_{\gamma'} = E_j + \Delta E_{\gamma\gamma'}$  where  $\Delta E_{\gamma\gamma'} > 0$  and  $N_\gamma + N_{\gamma'} + N_j$ .

Since the CEF is responsible for lifting the degeneracy of the Hund's rule ground state multiplet at low temperatures, it is also an important energy scale in heavy fermion compounds as it can affect the magnetic properties of RE ions in Kondo lattices. If  $\Delta E_{\gamma\gamma'} \ll T_K$ , the low temperature thermodynamics is governed by the energy scale  $k_B T_K$ , the Kondo temperature associated with the unsplit multiplet (with  $N_j$ ). On the contrary, if  $\Delta E_{\gamma\gamma'} \gg T_K$ , then  $T_K$  will be appropriate for the lower CEF multiplet with a degeneracy factor  $N_\gamma$ . In a real system, the low temperature properties can be in general explained by the  $N = 2, (S = 1/2)$  Kondo model since most of the degeneracy is lost due to the large CEF splitting.

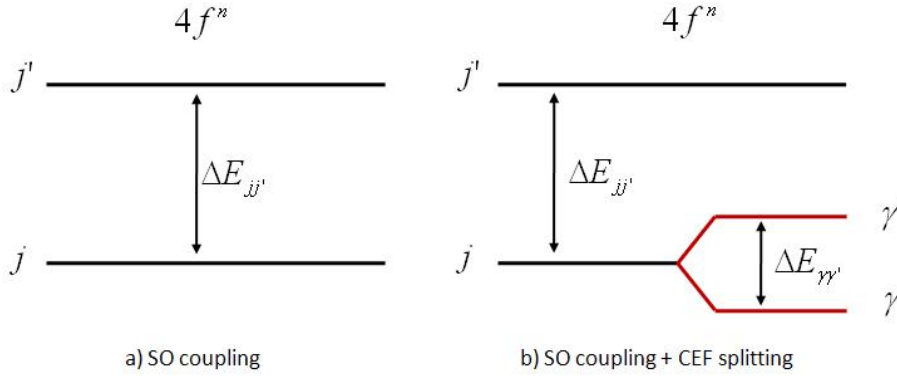


Figure 1.8: *Scheme of the lower multiplets for a rare earth ion in a configuration  $4f^n$  a) due to spin-orbit splitting  $\Delta E_{jj'}$  and b) with the lowest multiplet split by a crystalline electric field with an energy  $\Delta E_{\gamma\gamma'}$ .*

### 1.2.5 Fermi-Liquid relations

In section 1.1, we have already mentioned that the Landau Fermi-liquid theory, firstly developed to understand the electronic state of normal metals, successfully describes the physical properties observed in HF systems at low temperatures which show strong correlations. Two of such constants are the Kadowaki-Woods ratio and the Wilson ratio.

## 1.2. Kondo lattices

### 1.2.5.1 Kadowaki-Woods ratio

The Kadowaki-Woods (KW) ratio is a relation between the electrical resistivity and the specific heat. It has been noticed that several  $f$ -electron systems show a universal value  $A/\gamma^2 = 1.0 \times 10^{-5} \mu\Omega\text{cm}(\text{Kmol}/\text{mJ})^2$  [Kadowaki 1986]. However, recently it was pointed out that there are systematic deviations of the KW ratio in many HF compounds, especially in Yb-based systems (e.g. YbCu<sub>5</sub>, YbAgCu<sub>4</sub>, YbCuAl, YbNi<sub>2</sub>Ge<sub>2</sub>, YbInCu<sub>4</sub>, YbAl<sub>3</sub> and the family YbT<sub>2</sub>Zn<sub>20</sub>) and for Ce-based compounds such CeNi<sub>9</sub>Si<sub>4</sub> which show  $A/\gamma^2 \approx 0.4 \times 10^{-6} \mu\Omega\text{cm}(\text{Kmol}/\text{mJ})^2$ . These deviations can not be explained by specific characters of materials, such as carrier density, band structure or anisotropy [Tsujii 2005]. Recently, it was suggested that the values of  $A/\gamma^2$  depend on the degeneracy of the quasiparticles  $N$ , and so, a generalized KW ratio has been derived for systems with general  $f$ -orbital degeneracy [Kontani 2004]. As discussed above, in a solid,  $N$  can vary due to the competition between the CEF splitting and the Kondo temperature.

By considering the material dependence of  $N$ , the variation in KW ratio was estimated as [Kontani 2004, Tsujii 2005]

$$\frac{A}{\gamma^2} = \frac{1 \times 10^{-5}}{\frac{1}{2}N(N-1)} \mu\Omega\text{cm}(\text{Kmol}/\text{mJ})^2 \quad (1.10)$$

If the value of  $N$  is determined experimentally, it is possible to define a normalized  $\tilde{A}$  and  $\tilde{\gamma}$  coefficients as

$$\begin{aligned} \tilde{A} &= \frac{A}{\frac{1}{2}N(N-1)} \\ \tilde{\gamma} &= \frac{\gamma}{\frac{1}{2}N(N-1)} \end{aligned} \quad (1.11)$$

Then we obtain again for  $\tilde{A}/\tilde{\gamma}^2 \approx 1.0 \times 10^{-5} \mu\Omega\text{cm}(\text{Kmol}/\text{mJ})^2$  known as the grand-KW relation. In figure 1.9 a) the  $A$  coefficient is plotted versus  $\gamma$  for several HF compounds and also the KW ratio for different degeneracies  $N$  (colored lines) calculated from eq. 1.10 are shown [Tsujii 2005]. In figure 1.9 b) the coefficient  $\tilde{A}$  and  $\tilde{\gamma}$  are now plotted and we clearly observe how the experimental data follows in good agreement the grand-KW relation (the dotted line), one of the most fundamental relations in Fermi-liquid systems [Tsujii 2005].

### 1.2.5.2 Wilson ratio

Another relation in Fermi liquids is the so-called Wilson ratio ( $R_W$ ) that relates the susceptibility and the specific heat at low temperatures [Rasul 1984]:

$$R_W = \frac{\chi}{\gamma} \frac{4\pi^2}{g^2\mu(N^2-1)} = \frac{N}{(N-1)}, \quad (1.12)$$

where  $N$  is the degeneracy of the RE ion.

It was firstly deduced for the general Coqblin-Schrieffer model [Coqblin 1969]. For non-interacting electrons  $R_W = 1$ , ( $N \rightarrow \infty$ ) whereas it is enhanced in heavy fermions, e.g.  $R_W = 2$  for a doublet ground state with  $N = 2$ , ( $S = 1/2$ ). A plot of  $\gamma$  and  $\chi(0)$  ( $T \rightarrow 0$ ) for a number of HF compounds is given in figure 1.10 [Hewson 1993]. The straight line corresponds to  $R_W = 1$ . This plot shows that both quantities are enhanced in a similar way in HF systems, probably caused by the spin fluctuations.

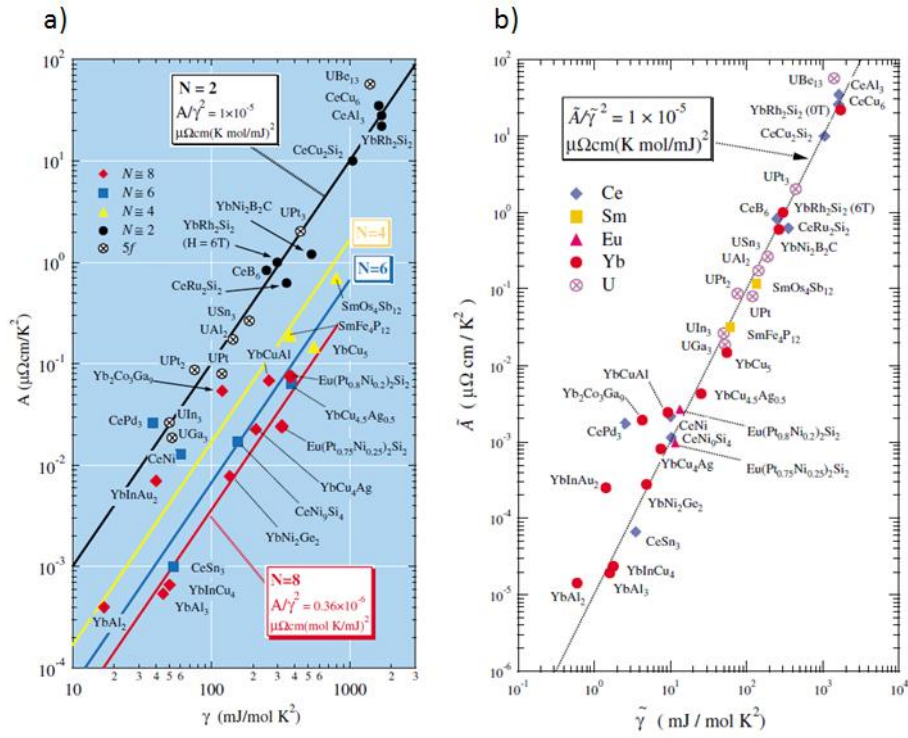


Figure 1.9: a)  $T^2$  coefficient of electrical resistivity  $A$  vs  $T$ -linear coefficient  $\gamma$  of specific heat for several heavy-fermion systems with different degeneracy. Colored lines correspond to the  $KW$  ratio for several  $N$  from eq. 1.10. b) Plot of  $\tilde{A}$  vs  $\tilde{\gamma}$  for several heavy-fermion compounds. The dotted line represents the grand- $KW$  ratio given in text:  $\tilde{A}/\tilde{\gamma}^2 = 1.0 \times 10^{-5} \mu\Omega\text{cm}(\text{K mol}/\text{mJ})^2$  [Tsuji 2005].

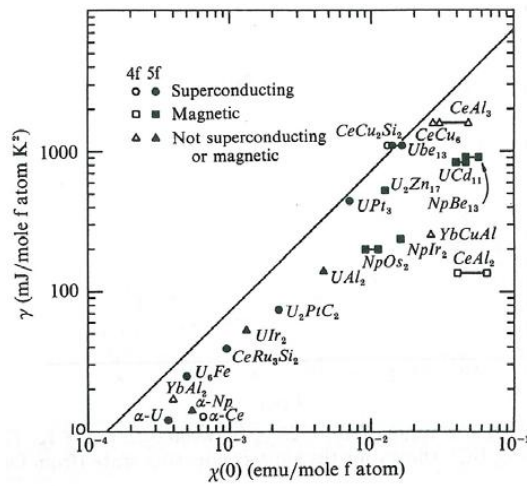


Figure 1.10: a) Plot of  $\gamma$  and  $\chi(0)$  for a number of HF compounds. The straight line corresponds to the Wilson ratio for non-interacting electrons,  $R_W = 1$  [Hewson 1993].

### 1.3. Quantum criticality

## 1.3 Quantum criticality

In this section we will first deal with the concept of a quantum phase transition. Next we will introduce the basis of the main theoretical models that try to explain the unusual behavior, known as non-Fermi-Liquid (NFL) behavior, often observed in heavy fermion compounds near a quantum critical point, QCP.

### 1.3.1 Classical versus quantum phase transition

“Classical” or “thermal” phase transitions are characterized by an increase of the entropy of the system with rising temperatures. If we take for example the molecule  $H_2O$ , we are all familiar with the phase transition between liquid water and ice. Another famous example is the ferromagnetic transition of iron at  $770^\circ\text{C}$ , above which the magnetic moments vanish.

Phase transitions are commonly classified into first order (discontinuous) and second order (continuous). The example of the phase transition between liquid water and ice is a first order transition, where an amount of latent heat ( $l$ ) is released at the transition temperature as the two coexisting phases have different entropies (e.g.:  $S_{ice} < S_{water}, l = T(S_{water} - S_{ice}) \neq 0$ ). In contrast, in a second order phase transition, such as the ferromagnetic transition of iron, both phases do not coexist and there is no latent heat associated. The transition point in this case is also called the critical point. Both types of phase transitions can be characterized by an order parameter which corresponds to a thermodynamic property. In a first-order transition, the order parameter shows a jump, i.e., is discontinuous, at the transition temperature whereas the order parameter in a second-order phase transition varies continuously and vanishes at the disordered phase. Sometimes it is easy to define the order parameter like in the previous examples, e.g. the density in the liquid-solid transition and the total magnetization for the ferromagnetic transition, but sometimes the choice is not trivial.

For classical phase transitions, a system in thermal equilibrium will acquire the state that minimizes its free energy:

$$F(p, T, H) = E(p, H) - TS(p, H). \quad (1.13)$$

where  $p$ ,  $T$ , and  $H$  are control parameters: pressure, temperature and magnetic field respectively. For the molecule  $H_2O$ , the internal energy  $E(p, H)$  is determined by the interactions between the molecules and it is minimized in the crystalline ice structure. The entropy,  $S(p, H)$ , as explained by Boltzmann, is a measure of the degree of randomness in a phase. Clearly, the entropy is larger in the liquid phase. It is now easy to see that at low temperatures,  $F(p, T, H)$  will be smaller in the ice phase, while at higher temperatures the contributions of the entropy,  $S(p, H)$ , to the free energy,  $F(p, T, H)$ , become more important, and the free energy of the liquid water phase is lower. The free energies of ice and liquid water cross each other at  $0^\circ\text{C}$ , accounting for the phase transition at this temperature.

Strictly speaking, a quantum phase transition takes place at absolute zero temperature where the system is driven between two different ground states by only varying  $E(p, H)$  with an external parameter (e.g.: pressure, doping or magnetic field). Phase transitions at  $T = 0$  are dominated by quantum effects, in contrast to classical phase transitions at  $T > 0$ . Luckily, because all experiments are necessarily at some nonzero temperature, quantum phase transitions leave characteristic fingerprints in the physical properties of materials at  $T > 0$  that the theory of quantum phase transitions has tried to describe [Sachdev 2011].

### 1.3.2 Non-Fermi-Liquid behavior

At the vicinity of a QCP the macroscopic physical properties of heavy fermions often exhibit strong deviations from Fermi-liquid theory, e.g., near the field-induced QCP in  $\text{YbRh}_2\text{Si}_2$  [Custers 2003] and  $\text{CeCu}_{6-x}\text{Au}_x$  for  $x \approx 0.1$  [Löhneysen 1994] to cite but a few examples. For a thorough experimental review see [Stewart 2001].

Even though the anomalous properties in the Non-Fermi-liquid (NFL) region are not equal for all systems they share some similarities:

- $C/T$  increases at low temperatures and theoretically diverges. Often it shows a singular logarithmic temperature dependence  $C/T \approx -\log T/T_0$ , or close to  $1/T^{1/2}$  to lowest temperatures.
- The resistivity does not exhibit the standard  $T^2$  dependence. Usually it can be expressed as  $\rho(T) = \rho_0 + AT^n$  where  $n < 2$ .
- An increase or even a divergence of the susceptibility when  $T \rightarrow 0$  like  $\chi(T) \approx 1/T^n$ .

Figure 1.11 a) shows the specific heat data for different concentrations in the vicinity of the critical Au concentration  $x_c = 0.1$  in  $\text{CeCu}_{6-x}\text{Au}_x$  where NFL is observed between 0.06 K and 2.5 K (over almost two decades in T). The bump in the specific heat curves corresponds to the antiferromagnetic transition. In panel b), the temperature dependence of the electrical resistivity for two different doping  $x = x_c = 0.1$  and  $x = 0$  are shown. Clearly, at  $x = 0.1$  the linear  $\rho(T)$  dependence signals NFL behavior whereas for  $x = 0$  the system follows the characteristic FL behavior of HF compounds [Löhneysen 1996].

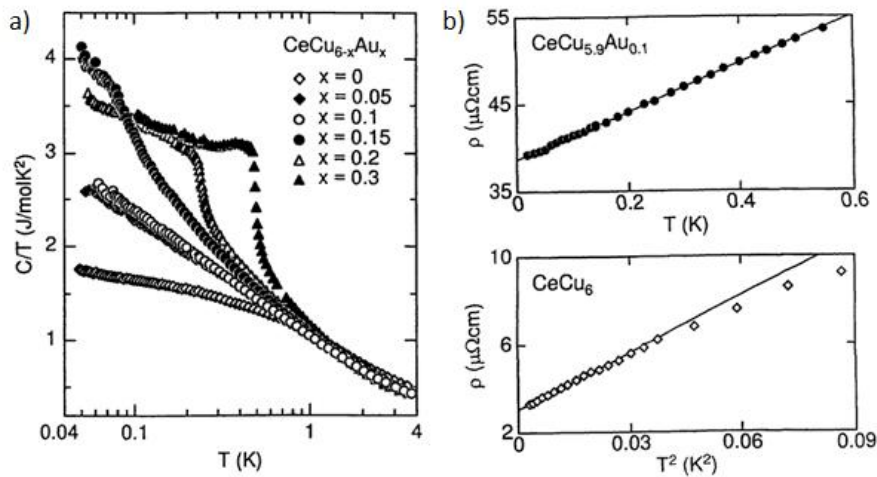


Figure 1.11: a) Specific-heat data for several concentrations in the vicinity of the critical Au doping  $x_c = 0.1$ . b) The temperature dependence of the  $\rho$  is shown for two different concentrations  $x = 0.1$  and  $x = 0$ . NFL behavior is observed for  $x = 0.1$  [Löhneysen 1996].

### 1.3.3 Theoretical approaches of quantum criticality

Mainly two different theoretical approaches are currently used to explain the NFL behavior that arises near a QCP: the spin density wave (SDW) instability or global criticality, and the Kondo breakdown scenario or local criticality.

### 1.3. Quantum criticality

#### 1.3.3.1 Spin density wave scenario

Several theoretical models [Hertz 1976, Millis 1993, Moriya 1995] take into consideration the magnetic fluctuations to describe the phase diagram near the critical region. In the paramagnetic phase, spin fluctuations become stronger as the system is driven close to the QCP and the associated energy,  $T_{sf}$ , becomes larger. The magnetic correlations are characterized by a correlation length,  $\xi_s$ , and by a relaxation time,  $\tau$ , which are related as follows

$$\tau \approx \xi_s^z \quad (1.14)$$

where  $z$  is the so-called critical exponent and depends on the nature of the fluctuations;  $z = 2$  for antiferromagnetic fluctuations and  $z = 3$  for ferromagnetic ones. Both,  $\xi_s$  and  $\tau$ , diverge at the QCP but  $\tau$  does it faster. In this region NFL behavior is found.

The self-consistent renormalization (SCR) theory proposed by Moriya *et al.* is based in weakly interacting spin fluctuations above a  $T = 0$  phase transition. The dynamical susceptibility,  $\chi(q, \omega)$ , takes into account the coupling among different modes of spin fluctuations in a self-consistent manner. The equation of  $\chi(q, \omega)$  for a three-dimensional antiferromagnetic metal contains two characteristic energy parameters  $T_A$  and  $T_0$ , which are related to the spin fluctuation energies in  $\omega$  and  $q$  space [Stewart 2001]. In this model,  $\chi(q, \omega)$  is enhanced and increases with decreasing temperature at the well-defined wave vector  $Q$  of the magnetic structure.

Table 1.2 shows the temperature dependence of resistivity, specific heat and susceptibility obtained from the SCR model for two and three dimensions in a ferro- (FM) or antiferromagnetic (AFM) system.

		C/T	$\rho \approx T^n$	$\chi Q$
FM	3D	$-\ln T$	$T^{5/3}$	$T^{-4/3}$
	2D	$T^{-1/3}$	$T^{4/3}$	$-T^{-1}/\ln T$
AFM	3D	$T^{1/2}$	$T^{3/2}$	$T^{-3/2}$
	2D	$-\ln T$	$T$	$-\ln T/T$

Table 1.2: *Temperature dependence of the macroscopic properties (specific heat, resistivity and dynamic susceptibility) within the SCR model at the quantum critical point.*

A crucial aspect of the spin density wave (SDW) scenario is that as the FL undergoes a transition to a SDW metal at the QCP, the local moments remain screened across the phase transition, i.e., the heavy quasiparticles survive on both sides of the transition and the lattice Kondo temperature stays finite at the QCP. Therefore, the Fermi surface volume remains constant at the transition with a folding of the Brillouin zone due to the appearance of the magnetic order. This folding modifies the shape of the Fermi surface with some singularities at the “hot” lines regions. The schematic phase diagram for the SDW scenario is illustrated in figure 1.12.

For a long time the SDW theory has been applied to explain the experimental results and some systems can be understood very satisfactorily within this model (e.g., CeRu<sub>2</sub>Si<sub>2</sub> and itinerant d-electron systems). Many systems, especially Ce-base compounds, qualitatively follow the theoretical predictions with some discrepancies. It should be noted that this theory is however rather crude in several aspects, for example, the real Fermi surface shape or disorder effects are not taken into account. Rosch [Rosch 2000] has shown that microscopic disorder can have strong effects on the critical exponents of the SCR theory.

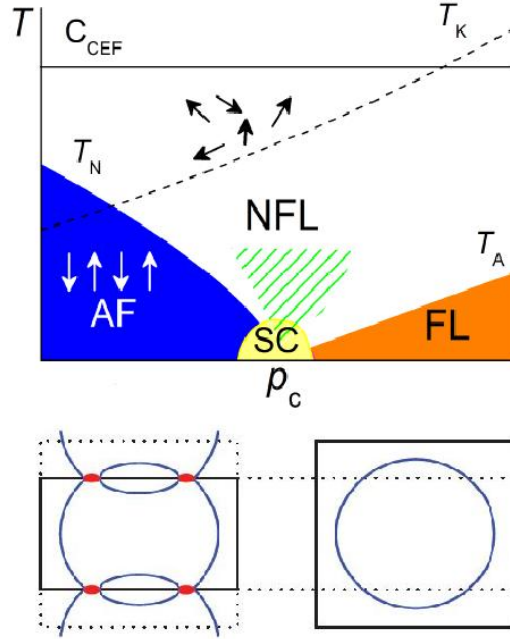


Figure 1.12: Schematic phase diagram of the SDW scenario of quantum criticality. The Kondo temperature is not affected when crossing through the QCP (top panel) whereas  $T_A$  the characteristic spin fluctuation temperature collapses at  $P_c$ , the critical pressure. The volume of the Fermi surface is unchanged, but due to the folding of the Brillouin zone (dotted lines on the bottom panel) hot spots can appear (red regions).

### 1.3.3.2 Local quantum criticality

There are some systems that show larger discrepancies and can not be explained within the SCR model. For example, the anomalous behavior close to an AFM QCP in some heavy fermion systems like  $\text{CeCu}_{6-x}\text{Au}_x$  and  $\text{YbRh}_2\text{Si}_2$  is inconsistent with the Moriya-Hertz SDW scenario. For  $\text{CeCu}_{6-x}\text{Au}_x$  series, inelastic neutron scattering measurements have shown that the magnetic instability near  $P_c$  appears to involve all the wavevector response instead of a well defined  $Q$  wave vector. That has led to derive the so-called local criticality model. The main feature in this model is a Fermi surface instability at  $P_c$  that corresponds to the so-called “Kondo breakdown” picture. The heavy-quasiparticles in the paramagnetic state do not survive through the QCP due to competing magnetic fluctuations. Therefore, an abrupt change in the Fermi surface, passing from a large to small one, is expected.

The schematic phase diagram proposed within this model is shown in figure 1.13. From an experimental point of view, the collapse of the Fermi surface might be detected via photoemission and de Haas-van Alphen measurements. Transport properties like the Hall conductivity will show a jump upon crossing the transition at low  $T$ <sup>7</sup>.  $\text{CeRh}_2\text{Si}_2$  and  $\text{CeRhIn}_5$  are two compounds where dHvA experiments show clearly a FS change at  $P_c$  and an excellent agreement between dHvA frequencies with band structure calculations are found (assuming that below  $P_c$  the  $4f$  electrons are localized and above  $P_c$  they are itinerant).

<sup>7</sup>In the SDW approach the Fermi surface evolves continuously, and the Hall coefficient displays a kink, but not a jump.

## 1.4. Ce versus Yb systems

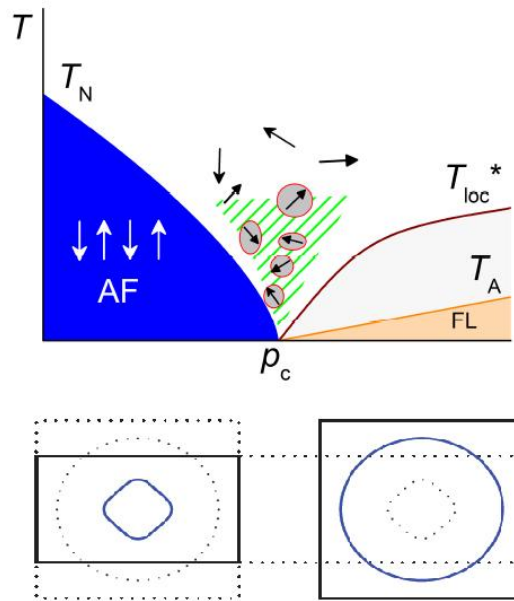


Figure 1.13: *Schematic phase diagram of the local quantum criticality. In this model it is stressed the reconstruction of the Fermi surface (FS) with the image of a small FS in the AF phase and a large FS in the PM phase. The modification of the FS may be achieved through a crossover regime at  $T_{Loc}^*$ .*

## 1.4 Ce versus Yb systems

Up to now we have talk about the physical properties of the  $4f$  systems in general. In this section we will focus on a sub-group of particular interest, classified with the rare earth ions Ce and Yb.

In 1975, Andres *et al.* discovered the first heavy fermion compound,  $CeAl_3$  [Andres 1975]. Since then, several Ce-based HF compounds have been discovered and extensively studied like  $CeCu_6$ ,  $CeRu_2Si_2$ ,  $CePd_3$ ,  $CeIn_3$  and the 115 family  $CeMIn_5$  ( $M=Co,Rh,Ir$ ), to cite but a few examples.

The first Yb-based HF compound,  $YbCuAl$ , was found in 1980 by Mattens *et al.* [Mattens 1980]. Even though there are also several Yb-based HF compounds like  $YbAl_3$ , the  $YbM_2Si_2$  family ( $M=Cu, Rh, Pd$ ) and the recent  $YbT_2Zn_{20}$  family ( $T=Ir, Co, Rh, Ru$ ), one question arises almost inevitably: “Why Ce-based HF compounds are so popular compared to Yb-based HF compounds?”.

Several arguments may help to answer this question. First, due to the “lanthanide contraction” (see figure 1.1), Yb ions in intermetallic compounds show more localized character than Ce (the radial extension of the  $4f$  orbital is  $0.37 \text{ \AA}$  and  $0.25 \text{ \AA}$  for Ce and Yb respectively [Waber 1965]). Also, Yb tends to form the divalent state which is the same as the non-magnetic Lu, so relatively few compounds with trivalent Yb have been found [Thompson 1994]. Additionally, difficulties in single crystal growth due to the rather low vapor pressure of Yb has limited the rapid synthesis and discovery of new materials. Finally, higher pressures are often needed to study the ( $P - T$ ) phase diagram region near the QCP, and their magnetic ordering temperatures are in general lower compared to their Ce counterparts. So roughly speaking, the study of Yb-based intermetallic compounds requires more experimental efforts.

Interestingly, both Ce and Yb ions can fluctuate between a magnetic trivalent state ( $Ce^{3+} (4f^1)$ ;  $Yb^{3+}, (4f^{13})$ ), and a non-magnetic state corresponding to the tetravalent state for Ce with an

empty  $4f$  shell, and a divalent state for Yb with a full  $4f$  level according to the following scheme:

$$\begin{aligned} Ce^{3+} &\rightleftharpoons Ce^{4+} + 5d; \quad v = 4 - n_f \\ Yb^{2+} &\rightleftharpoons Yb^{3+} + 5d; \quad v = 2 + n_h \end{aligned} \quad (1.15)$$

As we will see in detail in the next section, the asymmetry in the liberation or absorption of a  $5d$  electron for a deviation of  $n_f$  from unity between Ce and Yb has important consequences in their pressure behavior [Flouquet 2009]. Pressure tends to increase the delocalization of the  $4f$  electrons in both cases: the non-magnetic ( $4f^0$ ) state is favored for Ce at high pressure whereas in Yb it is favored the magnetic ( $4f^{13}$ ) state which has a smaller ionic radius than the divalent state. Hence, the magnetic Yb state with 13 electrons (one hole) in the  $4f$  shell is often considered as the “hole” equivalent of trivalent Ce. This analogy is also used to calculate the valence (eq. 1.15) of the RE ion as a function of the number of  $f$  electrons ( $n_f$  for Ce) or number of holes ( $n_h$  for Yb).

### 1.4.1 Beyond the “hole” equivalent picture

From a theoretical point of view, a unified description of both Ce and Yb compounds is possible through the electron-hole symmetry in the Anderson Hamiltonian. In both cases, the hybridization between localized  $4f$  and conduction electrons couples an empty  $4f$  (full  $4f^{14}$  for Yb) state with a degenerate  $f^1$  ( $f^{13}$ ) state [Malterre 1996].

There are however, important differences between Yb and Ce. One of them has already been mentioned: the deeper localization of the  $4f$  electrons in Yb leads to a much narrower width,  $\Delta$ , of the  $4f$  level and the hybridization,  $V$ , is weaker than in the Ce case. Both quantities are related as follows:

$$\Delta = V^2 N(E_F) \quad (1.16)$$

Another factor that reinforces the local atomic character of the Yb case is the stronger spin orbit (SO) coupling  $\lambda_{ls}$  which splits the  $j = l - s$  and  $j = l + s$   $4f$  levels ( $j = 5/2$  for  $Ce^{3+}$  and  $j = 7/2$  for  $Yb^{3+}$ ). The SO coupling is almost five times higher for Yb than Ce [Brooks 1996].

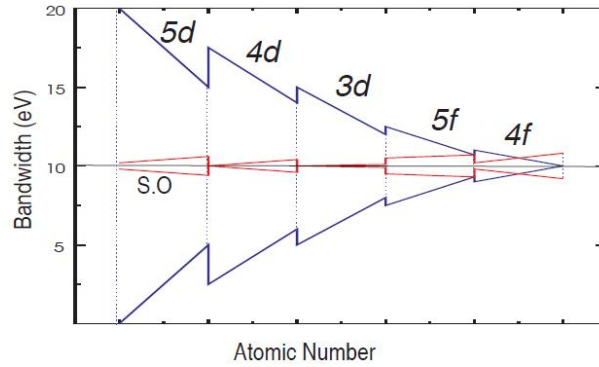


Figure 1.14: Widths of the  $d$  and  $f$  bands compared with SO splitting for the transition metals, rare earths and actinides [Brooks 1996].

As a result, there is a difference in the hierarchy of the relevant energy scales between Ce and Yb, i.e., CEF ( $\Delta_{CEF}$ ), SO coupling ( $\lambda$ ) and  $4f$  level width  $\Delta$ . From figure 1.14 we can infer the hierarchy between  $\lambda$  and  $\Delta$  for Ce and Yb and we know that in general the CEF splitting in rare earths is less strong than the SO coupling (see section 1.2.4). So the hierarchy for Ce is  $\Delta > \lambda > \Delta_{CEF}$  whereas for Yb is  $\lambda > \Delta > \Delta_{CEF}$ .

## 1.4. Ce versus Yb systems

The relevant result, as discussed in more detail in [Flouquet 2005, Flouquet 2009] is that in Yb systems the formation of the heavy fermion state may take place for a much wider range of the valence than in Ce.

Photoemission measurements support this argument by reflecting that the differences between Ce and Yb are based on a smaller interconfiguration energy in the Yb case. The  $4f^0$  and the  $4f^1$  configurations for Ce are separated by about 2 eV whereas the energy separation between the divalent and trivalent configuration in Yb can be less than 100 meV favoring a strong configuration mixing [Malterre 1996].

### 1.4.2 Doniach picture for Yb HF compounds

Pressure is one of the cleanest ways to tune the competition of  $T_K$  and  $T_{RKKY}$  and drive a system through its magnetic instability at the QCP. The lattice parameters change by applying pressure and thus the coupling between the conduction and the  $f$ -electron wave functions. In the case of strong Coulomb repulsion within the  $f$ -orbital ( $U \rightarrow \infty$ ) the exchange coupling  $J$ , the hybridization matrix element  $V$ , the width  $\Delta$  and the energy  $\varepsilon_{4f}$  of the  $4f$  level fulfill the following relation

$$JN(E_F) \approx \frac{\Delta}{|\varepsilon_f - E_F|} \Rightarrow J = \frac{V^2}{|\varepsilon_f - E_F|} \quad (1.17)$$

where  $\Delta = V^2 N(E_F)$ .

For Ce systems, the  $f$ -level becomes wider under pressure and the energy of the  $4f$  level also increases moving towards  $E_F$ . Thus, both effects combine to drive the system towards increasing  $J$  in the Doniach phase diagram, which leads to the suppression of the magnetic order as reflected in figure 1.7 even if the valence may still be close to the magnetic  $\text{Ce}^{3+}$  configuration.

For Yb the situation is less straightforward as the dominant effect will be the relative change of  $\varepsilon_f$  to  $E_F$ . Notice that now  $\varepsilon_f$  is the energy of the  $4f$  hole and it lies above  $E_F$  as indicated in figure 1.15.

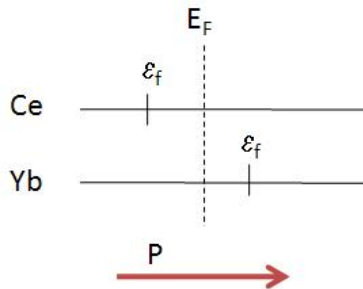


Figure 1.15: The position of  $\varepsilon_f$  relative to  $E_F$  is indicated for Yb and Ce systems. The arrow indicates where  $\varepsilon_f$  moves with pressure.

Therefore,  $|\varepsilon_f - E_F|$  will increase with pressure, driving the system towards decreasing  $J$ , i. e., decreasing  $T_K$  and increasing  $T_{RKKY}$ , in the Doniach diagram and so inducing magnetic order. So Yb systems should behave as the mirror image of the Ce Doniach phase diagram. However, for Yb,  $\Delta$  also increases under pressure. This implies, that the terms in  $J$  may be in competition, leading to a less effective pressure effect in ytterbium systems compared to cerium. As  $\varepsilon_f$  is strongly linked to the valence, if the valence change of Yb with pressure is weak,  $J$  may vary very little with pressure or it could even increase.

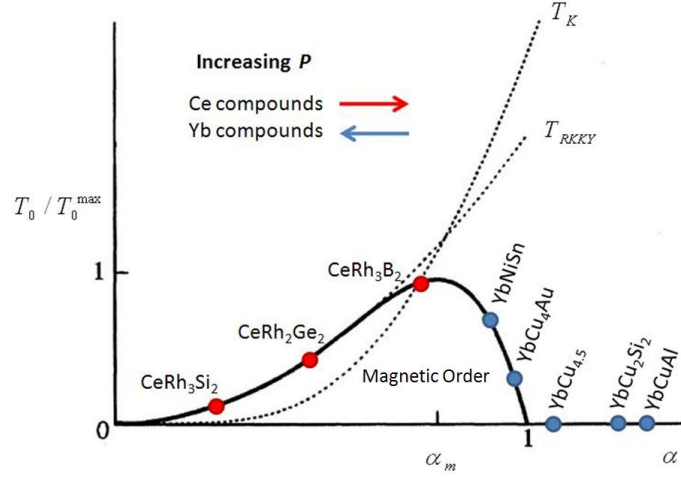


Figure 1.16: *Schematic representation of Doniach phase diagram where the estimated locations of various Ce and Yb compounds are indicated qualitatively.  $T_0$  is the magnetic ordering temperature, and  $\alpha \equiv |J_f N(E_F)|$ . The position of a given Ce (Yb) system in this diagram moves to the right (left) as pressure is applied (see more details in [Cornelius 1995]). The position of YbCu<sub>2</sub>Si<sub>2</sub> has been added ( $P_c \approx 8$  GPa). Its position has been chosen from a qualitative comparison with the position of YbCuAl ( $P_c \approx 10$  GPa).*

To illustrate this “mirror image” between Ce and Yb systems, in figure 1.16 adapted from [Cornelius 1995] the estimated locations for several Ce and Yb compounds are indicated in the Doniach phase diagram. The position of YbCu<sub>2</sub>Si<sub>2</sub> ( $P_c \approx 8$  GPa [Colombier 2009]) has been added. Its position has been chosen from a qualitative comparison with the critical pressure of YbCuAl,  $P_c \approx 10$  GPa. The magnetic ordering temperature  $T_0/T_0^{max}$  ( $T_0$  corresponds to the value at ambient pressure whereas  $T_0^{max}$  is its maximum value in their respective  $P - T$  phase diagrams) is plotted as a function of  $\alpha \equiv |J_f N(E_F)|$ , and  $\alpha_m$  corresponds to the value where  $T_0 = T_0^{max}$ . The position of a given Ce (Yb) system moves to the right (left) as pressure is applied as indicated by the red (blue) arrow.

Nevertheless, this simple “electron-hole” Doniach picture is far from being universal and not all the Yb-based HF compounds follow it as we will see throughout this work.

### 1.4.3 Pressure dependence of $T_K$ in Ce and Yb systems

In Ce heavy fermions  $T_K$  increases continuously with increasing pressure whereas in Yb systems it decreases. To characterize the dependence of  $T_K$  on pressure or sample volume,  $V$ , for a given system the Grüneisen parameter is a convenient parameter:  $\Omega = -\frac{\partial \ln T_K}{\partial \ln V}$ . It is positive for Ce systems and negative for Yb compounds as reflected in table 1.3, where the value of  $\Omega$  are summarized for several compounds.

In a recent work, Goltsev *et al.* have given an explanation for the pressure dependence of  $T_K$  for Ce and Yb systems and the negative Grüneisen parameter in Yb by introducing an additional mechanism of interaction between the localized  $f$  electrons and the lattice. In brief, *this interaction takes into account lattice deformations produced by fluctuations of the ionic radius of RE ions which accompany valence fluctuations of the ions* [Goltsev 2005]. As this approach differs from the previous Doniach picture (where no charge fluctuations are taken into account) we consider it was worthy to mention the main results of this study.

Goltsev *et al.* have added an electron-lattice coupling term in the Anderson Hamiltonian that takes into consideration the local lattice strain caused by a change of the valency of the  $f$  ions by

#### 1.4. Ce versus Yb systems

Ce compounds	$\Omega$	Yb compounds	$\Omega$
CeRu <sub>2</sub> Si <sub>2</sub>	80	YbCu <sub>2</sub> Si <sub>2</sub>	-48
CeCu <sub>6</sub>	115	YbCu <sub>4.5</sub>	-23
CePt <sub>2</sub> Si <sub>2</sub>	26	YbCuAl	-50
CeInCu <sub>2</sub>	83	YbCu <sub>4</sub> Ag	-28

Table 1.3: *Some values of  $\Omega$  for several Ce and Yb systems (from [Cornelius 1995]). Ce systems have in general higher values of  $\Omega$  and opposite sign of Yb systems reflecting the different pressure dependence of  $T_K$ .*

a value of  $\Delta\nu$  <sup>8</sup>.

The energy of this interaction can be written as follows:

$$E_{fl} = N_f D_{ij} e_{ji} \Delta\nu \quad (1.18)$$

where  $e_{ji}$  is a strain tensor,  $i, j = x, y, z$ .  $N_f$  is the total number of  $f$  electrons in the lattice <sup>9</sup>. The conventional hybridization between  $f$  and conduction electrons is expressed here as

$$V = V_0 \exp(-re_B) \quad (1.19)$$

where  $r > 0$ .

For the sake of simplicity we skip here some of the steps and we go directly to the main results.

The Grüneisen parameter in this model is expressed as follows:

$$\Omega \equiv -\frac{d \ln T_K}{d \ln v} = -\left. \frac{d \ln T_K}{de_B} \right|_{e_B=0} = \frac{2r}{N} + \frac{\pi}{N\Gamma_0} (\eta d_f + 2r(\mu - E_{0f})) \quad (1.20)$$

where  $\Gamma_0 \equiv \Gamma(e_B = 0)$  <sup>10</sup> and  $E_{0f}$  is the bare energy of the  $f$ -level without taking account this lattice strain contribution.

The experimental Grüneisen parameters for Ce and Yb systems can be understood in terms of the two interactions (1.18) and (1.19). For Ce ( $\eta = 1$ ) both give a positive contribution to  $\Omega$  whereas in Yb ( $\eta = -1$ ) the electron-lattice interaction gives rise a negative contribution and  $\Omega$  is negative for  $d_f > 2r(\Gamma_0)/(\pi + \mu - E_{0f})$ .

In figure 1.17 there is a schematic behavior of the pressure dependence of  $T_K$ , the exchange coupling,  $J$  and the ratio  $R \equiv \frac{T_{RKKY}}{T_K}$ . For Ce compounds both, the Kondo temperature and the antiferromagnetic exchange  $J$  increase monotonously with pressure whereas in Yb compounds both decrease at low pressures and show a wide broad minimum at higher pressures. This result agrees with the pressure dependence of the resistivity found in several Yb-based compounds like Yb<sub>2</sub>Ni<sub>2</sub>Al [Winkelmann 1998], YbCu<sub>2</sub>Si<sub>2</sub> [Winkelmann 1999] and YbRh<sub>2</sub>Si<sub>2</sub> [Plessel 2003]. Additionally, the  $T_K(P)$  dependence obtain in this model has been compared with experimental data for YbCu<sub>2</sub>Si<sub>2</sub> and qualitative and quantitative agreement is found.

<sup>8</sup>The authors expressed the valency  $\nu$  of Yb and Ce as  $\nu = 3 + \Delta\nu$  where  $\nu$  is positive for Ce and negative for Yb ions. The microscopic origin of this lattice strain is related with the Coulomb repulsion between  $f$  electrons and electron shells from nearest neighboring atoms caused by a change in the ionic radius of the RE ion when the valence fluctuates between two configurations  $f^n$  and  $f^{n-1}$ .

<sup>9</sup>For a cubic lattice the energy tensor is  $D_{ij} = \delta_{ij} d_f$  and  $E_{fl}$  takes the form  $E_{fl} = d_f e_B \Delta\nu$  where  $e_B = e_{xx} + e_{yy} + e_{zz}$  is the bulk strain related to a change of volume  $v$ , as  $e_B = \Delta v/v$ . The coupling constant  $D$  is assumed to be positive.

<sup>10</sup> $\Gamma \equiv \pi |V|^2 \delta_F$  characterizes the broadening of the  $f$  level. Further details in [Goltsev 2005].

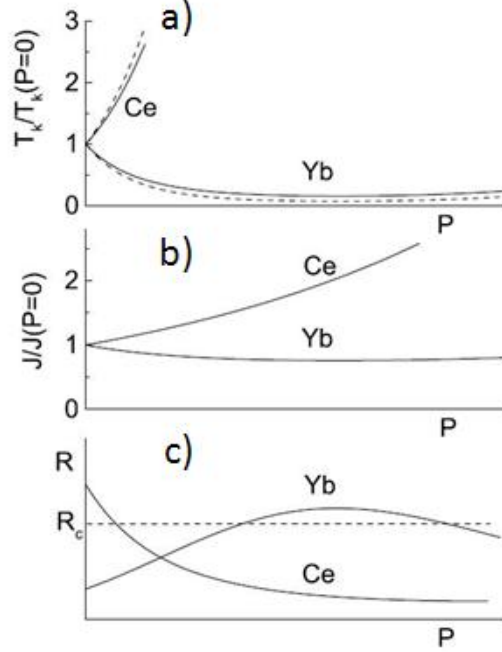


Figure 1.17: Schematic pressure dependence of the normalized  $T_K$ , the normalized exchange coupling  $J$  and the ratio  $R \equiv \frac{T_{RKKY}}{T_K}$ . The dashed curves in panel a) demonstrate the influence of the CEF splitting on  $T_K(P)$  for the case  $\Delta_{CEF} = T_K(\Delta_{CEF} = 0)/3$ , for an independent pressure CEF. The dotted curve in panel c) shows a critical value  $R_c$  at the QCP [Goltsev 2005].

The competition between the Kondo effect and magnetic ordering is expressed by the ratio  $R$ . In accordance with the Doniach approach, it is argued that a critical value  $R_c$  of the ratio  $R$  exists when a QCP occurs. For a Ce system  $R$  decreases monotonously and crosses the QCP  $R(P_c) = R_c$  at a critical pressure  $P_c$ . For Yb compounds,  $R(P)$  has a different behavior and shows a very broad maximum over a large pressure range.

At low  $P$  pressure moves Yb from the Kondo regime towards a regime with stable magnetic moments as  $R(P)$  increases. As a function of the initial  $R(P = 0)$  value, the system may reach a QCP (if  $R(P = 0) < R_c$  and  $\max(R(P)) > R_c$ ) or not (if  $\max(R(P)) < R_c$ ). Unfortunately, for a fully determination of the phase diagram, other mechanisms as the CEF have to be also taken into account. Nevertheless, the results obtained by Goltsev *et al.* may be useful to understand the effect of pressure in the phase diagram of HF compounds, especially for certain Yb systems that do not follow the Doniach picture (e.g: YbRh<sub>2</sub>Si<sub>2</sub>).

#### 1.4.4 First-order Valence instability

An intriguing aspect in intermediate valence systems is the nature of the valence change. Very often, it corresponds to a smooth and continuous valence-crossover in  $P$  and  $T$  between the two  $4f^n$  and  $4f^{n-1}$  configurations. Only few examples in literature show a sharp valence change corresponding to a first-order valence transition<sup>11</sup> (FOVT).

An archetypal example of a FOVT is the  $\gamma - \alpha$  transition in metallic Ce [Koshimaki 1978]. As a function of temperature or pressure it undergoes a first-order isostructural ( $fcc \rightarrow fcc$ ) phase

<sup>11</sup>A FOVT is an isostructural phase transition showing a valence jump of Ce or Yb ion when  $T$  and/or  $P$  are varied.

#### 1.4. Ce versus Yb systems

transition from the  $\gamma$ -phase, stable at ambient conditions, to a low-temperature (or high-pressure)  $\alpha$ -phase, with a loss of magnetic moments and a huge (15%) volume reduction [Dallera 2004]. The FOVT line reaches a critical end point at  $(P, T) = (2 \text{ GPa}, 600 \text{ K})$  as shown in figure 1.18 a). Above the CEP the valence change is not sharp anymore but a crossover, signaled by a valence-crossover line,  $T_v^*$ . The  $4f$  occupation varies between  $n_f \approx 0.95$  in  $\gamma$ -Ce and  $n_f \approx 0.85$  in  $\alpha$ -Ce [Dallera 2004].

In contrast to the FOVT in Ce, metallic Yb is divalent in the fcc phase (0-4 GPa) and trivalent in the hcp phase (above 30 GPa). A continuous valence transition towards the trivalent configuration is observed in the bcc phase (4-30 GPa) [Syassen 1982].

However, there is also a relevant example of a FOVT in Yb systems,  $\text{YbInCu}_4$  [Felner 1986, Kojima 1989]. At temperatures above  $T_v > 42 \text{ K}$ ,  $\text{YbInCu}_4$  is characterized by a Curie-Weiss temperature dependence in magnetic susceptibility and a semimetallic behavior in transport measurements due to its localized  $4f$  electrons. At  $T_v$ , there is a FOVT accompanied by a volume increase of +0.5%. The volume expansion induces strong charge hybridization and a change in the Yb valence from 3+ at  $T > T_v$  to an intermediate-valence value of 2.9+ below  $T_v$ , and an enhanced Pauli-like susceptibility corresponding to a modestly large  $\gamma = 50 \text{ mJ/molK}^2$ . Applied pressure stabilizes the high-temperature  $4f13$  configuration to progressively lower temperatures and eventually drives  $T_v$  to  $T = 0$  near 2.5 GPa as illustrated in figure 1.18 b).

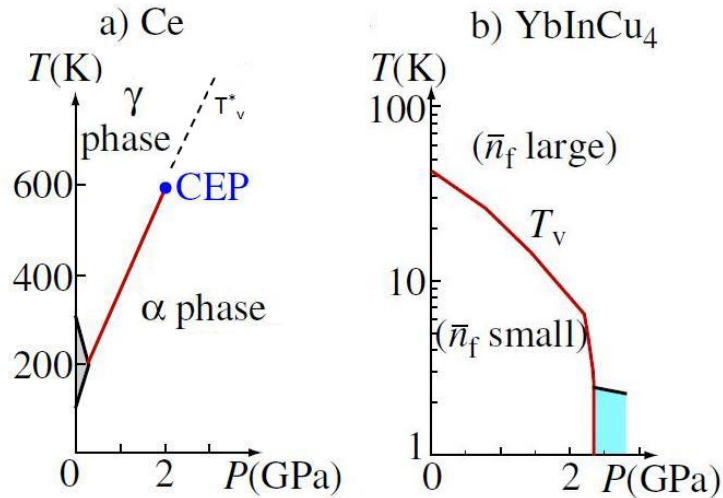


Figure 1.18:  $(P - T)$  phase diagram of a) metallic Ce and b)  $\text{YbInCu}_4$ . a) The FOVT between the  $\gamma - \alpha$  transition terminates at the critical end point (CEP). Above CEP,  $T_v^*$  marks the valence-crossover line. b) The FOVT is suppressed under pressure. The shaded area represents the magnetically ordered phase.  $\bar{n}_f$  denotes the number of holes per Yb [Watanabe 2009].

Recently, critical phenomena associated with charge degrees of freedom, in particular valence instability and its critical fluctuation, have attracted much attention. Valence fluctuations diverge at the CEP of the FOVT (like density fluctuations diverge in the liquid-gas transition). When the temperature of the CEP is driven to zero by an external control parameter a quantum critical end point emerges (QCEP) or also known as valence quantum critical point (V-QCP). At the QCEP, diverging valence fluctuations are considered to be coupled to the Fermi-surface instability and this mechanism may be a key origin to understand the anomalies observed in many Ce- and Yb-based heavy-fermion compounds [Watanabe 2011].

For example, it has been recently discussed that the pressure-induced enhancement of the superconducting transition temperature  $T_c$  and associated anomalies observed in  $\text{CeCu}_2(\text{Ge,Si})_2$  may be understood as due to the critical valence transition of the Ce ion under pressure [Miyake 2007, Rueff 2011]. Other compounds that do not follow the conventional spin-fluctuation theory or the Kondo breakdown scenario (see details in section 1.3), e.g.,  $\text{YbRh}_2\text{Si}_2$ <sup>12</sup>,  $\beta\text{-YbAlB}_4$  and  $\text{YbAuCu}_4$  suggest that quantum criticality of valence transitions may be an important mechanism to understand unconventional critical phenomena [Watanabe 2010b].

The minimal model that describes the physics in Ce- and Yb-based HF compounds exhibiting valence transition is based on the extended periodic Anderson hamiltonian [Watanabe 2008, Watanabe 2010b, Watanabe 2011]

$$\mathcal{H} = H_c + H_f + H_{hyb} + H_{U_{fc}} = H_{PAM} + H_{U_{fc}} \quad (1.21)$$

$$H_{U_{fc}} = U_{fc} \sum_{i=1}^N n_i^f n_i^c \quad (1.22)$$

where  $H_c$ ,  $H_f$  and  $H_{hyb}$  correspond to the PAM hamiltonian (1.8) and  $H_{U_{fc}}$  is an extra term that accounts the repulsion between  $f$  and conduction electrons ( $U_{fc}$ ). The occupation number  $n^a \equiv \sum_{\sigma} \sum_{i=1}^N \langle a_{i\sigma}^{\dagger} a_{i\sigma} \rangle / N$  where  $a = f$  or  $c$  and  $N$  is the number of sites in the lattice.  $H_{U_{fc}}$  is the key ingredient for explaining the valence transition as well as the anomalies caused by enhanced Ce- or Yb-valence fluctuations: a T-linear resistivity, an enhancement of the residual resistivity, the Sommerfeld constant and  $T_c$  [Watanabe 2011]. Within this model the filling  $n \equiv (n_f + n_c)/2$  is set slightly smaller than 1 (half filling) as is often the case in Ce- and Yb- HF systems.

For the sake of simplicity we will focus only in the main results of the model. In figure 1.19 the ground state phase diagram in the  $(U_{fc}-\varepsilon_f)$  plane is shown. When  $\varepsilon_f$  is deep enough, the Kondo regime with  $n_f \approx 1$  is realized. As  $\varepsilon_f$  approaches the Fermi level, the  $f$  electrons are moved into the conduction band via hybridization, giving rise to the intermediate-valence (mixed-valence) regime with  $n_f < 1$ . Notice that the valence transition is a different process than the localized-to-itinerant transition of  $f$  electrons. The FOVT between both regimes is caused by large  $U_{fc}$ , since electrons are forced to pour from the  $f$  level to the conduction band and then the level crossing between the Kondo and the intermediate-valence regime shows a discontinuous jump in  $n_f = \partial \langle \mathcal{H} \rangle / \partial \varepsilon_f$ . The FOVT line in figure 1.19 a) finishes at the QCEP, at which the jump in  $n_f$  disappears but the valence susceptibility (i.e., valence fluctuation)  $\chi_v \equiv \partial^2 \langle \mathcal{H} \rangle / \partial \varepsilon_f^2 = -\partial n_f / \partial \varepsilon_f$  diverges. The dashed line represents the crossover line where  $\chi_v$  has a maximum as a function of  $\varepsilon_f$  and  $U_{fc}$ , implying that valence fluctuations are also developed. The Fermi surface is supposed to be always large as the hybridization between  $f$  and conduction electrons is finite in all the  $U_{fc}-\varepsilon_f$  plane [Watanabe 2011, Watanabe 2010a]<sup>13</sup>. Up to now we have discussed the ground state ( $T = 0$  K) of the  $(U_{fc}-\varepsilon_f)$  plane. When we add a temperature axis we obtained the  $(T - U_{fc} - \varepsilon_f)$  phase diagram as shown in figure 1.19 b). The previous FOVT line at  $T = 0$  K now is the line at the bottom FOVT surface (red surface). The critical-end line exhibiting diverging valence fluctuations ( $\chi_v \rightarrow \infty$ ) separates the FOVT surface and the valence-crossover surface (yellow surface).

Most of Ce- and Yb-based compounds have moderate  $U_{fc}$  due to its inter-site origin: the conduction electrons are often supplied by other elements than Ce or Yb (e.g., the  $4f$  electrons on

<sup>12</sup>The discussion of the nature of the quantum criticality in this compound has risen a big controversy and it will be discussed in chapter 5.

<sup>13</sup>The Fermi-surface volume will not change as long as the system remains in a paramagnetic state in both sides of the FOVT or valence-crossover.

## 1.4. Ce versus Yb systems

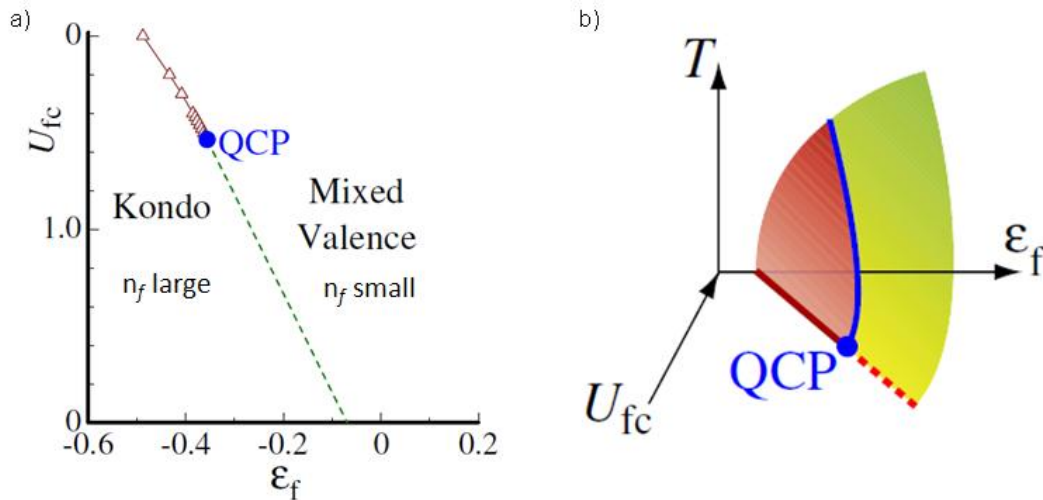


Figure 1.19: Schematic phase diagrams of a)  $U_{fc} - \epsilon_f$  plane at  $T = 0$  K and b)  $T - U_{fc} - \epsilon_f$ . a) The FOVT line (red) terminates at the QCEP (filled point signaled as QCP) and sharp valence crossover occurs above the QCEP (dashed line). b) the FOVT surface (red) and the valence-crossover surface (yellowish) are separated by the critical-end line (blue thick line) [Watanabe 2009].

the Ce site and the  $3p(4p)$  orbitals of Si are responsible for the bands in  $\text{CeCu}_2\text{Si}_2$ ). Hence they are located in the intermediate valence crossover regime. This is consistent with the experimental fact that most of those compounds do not show a FOVT, but a valence crossover. In contrast, Ce metal, which shows a FOVT, has a large  $U_{fc}$  due to its on-site origin:  $f$  and conduction electrons comes from the same Ce ion [Watanabe 2010a]. The magnitude of the valence jump in the FOVT is not very large about 0.1 (e.g., in the  $\gamma - \alpha$  transition in metallic Ce and in  $\text{YbInCu}_4$ ). Therefore, the magnitude of the valence change at the valence crossover for moderate  $U_{fc}$  compounds is smaller than that at the FOVT, about only 0.01 as observed in  $\text{YbAgCu}_4$  at the valence-crossover temperature,  $T_v^* = 40$  K [Watanabe 2010a]. Nevertheless, Ce- and Yb-based HF compounds can be affected by the proximity to the QCEP by applying an external control parameter as pressure or magnetic field.

### Field-induced valence crossover

Watanabe *et al.* have proposed that the magnetic field is an efficient parameter to change the critical end point of the FOVT to a QCEP [Watanabe 2008] as shown in figure 1.21.

They applied the Clausius-Clapeyron relation for the FOVT temperature  $T_v$ :

$$\frac{dT_v}{dh} = -\frac{m_K - m_{IV}}{S_K - S_{IV}} \quad (1.23)$$

where  $m$ ,  $S$  and  $h$  denote the magnetization and entropy in the Kondo (K) and the intermediate-valence (IV) regime and the magnetic field respectively. It turns out that in the Kondo regime the magnetization and the entropy are larger than in the IV regime [Watanabe 2008], and  $T_v$  is then suppressed by applying  $h$  and eventually a QCEP is reached [Watanabe 2009]. At the same time,  $T_{CEP}$  (blue curve) is also suppressed. To understand how the QCP of the FOVT is controlled by  $h$  at  $T = 0$  is not trivial.

The ground-state phase diagram of the  $(U_{fc}-\epsilon_f)$  plane under magnetic field is shown in figure 1.21. It has been obtained by introducing the Zeeman term in (eq. 1.21)

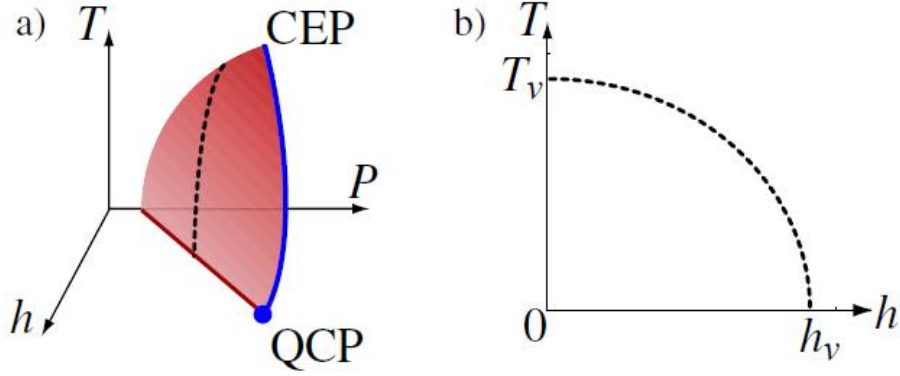


Figure 1.20: a) Schematic  $(T-P-h)$  phase diagram showing the FOVT surface.  $P$  is a control parameter (pressure, doping). The critical end points form a continuous transition line that reaches  $T = 0$  at a QCP (QCEP). b) FOVT line in the  $(T-h)$  phase diagram for a constant  $P$  [Watanabe 2009].

$$H_Z = -h \sum_i (S_i^{fz} + S_i^{cz}) \quad (1.24)$$

where  $h \equiv g\mu_B H$  and  $g$  is the Landé factor. Under field, the system is forced to be closer to the Kondo regime. Additionally, the QCEP can change significantly under  $h$  showing a non-monotonic dependence. The origin of the upturn is related to the relative strength between  $h$  and  $T_K$  (see [Watanabe 2008] for further details). If Ce- and Yb-based compounds are located just on the locus of QCEP's for  $h > 0$  (the grey line), metamagnetism will be observed at  $h = h_m$  at the QCEP. Therefore, not only the valence susceptibility  $\chi_v$  diverges at the QCEP but also the magnetic susceptibility,  $\chi_S \equiv -\partial m / \partial h$  [Watanabe 2008, Watanabe 2009].

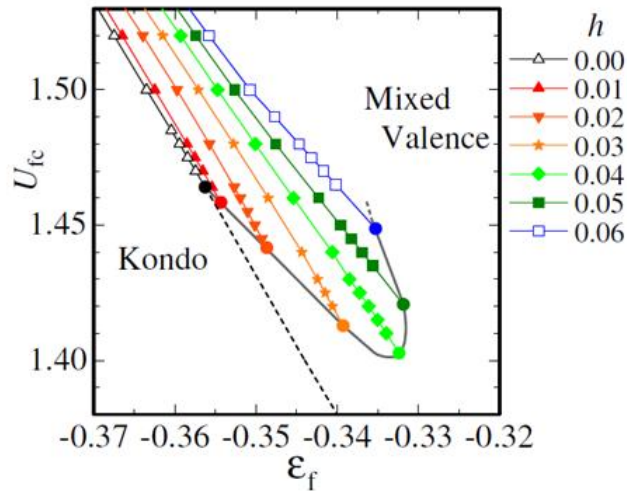


Figure 1.21: Field dependence of the ground state phase diagram in the  $(U_{fc}-\epsilon_f)$  plane. The grey line connects the QCEP under  $h$ , which is a guide for the eyes [Watanabe 2009].

In literature, measurements of the valence under magnetic field are still very scarce but highly desirable to contrast them within the theoretical predictions. In this work we will present some experimental data on the valence measurement under magnetic fields up to 10 T for several heavy

## 1.4. Ce versus Yb systems

fermion compounds (Ce, Yb and Sm-based HFC).

### 1.4.5 Unconventional superconductivity

Just a few years after the first HF compound was reported, CeAl<sub>3</sub>, Steglich *et al.* discovered the first HF superconductor, CeCu<sub>2</sub>Si<sub>2</sub> [Steglich 1979]. This finding definitively boosted the interest in heavy fermions.

The discovery of superconductivity in HF compounds revealed new surprising features: the anomalous large jump in the specific heat  $\Delta \approx \gamma T_{sc}$ <sup>14</sup> proved that superconductivity was indeed coming from the heavy quasiparticles which form Cooper pairs instead of the light conduction electrons. This discovery was initially surprising since the addition of magnetic impurities is usually pair breaking in classical BCS superconductors with s-wave pairing type [Tinkham 2004].

### Magnetic fluctuations as a pair mechanism

In HF compounds, superconductivity often occurs in presence of magnetic ordering and at the proximity of a QCP where strong spin fluctuations arise. This suggest the possibility of unconventional pairing with a complicated order parameter.

There are several theoretical models that consider magnetic fluctuations as the mechanism to form Cooper pairs instead of the classical electron-phonon interaction, especially after the discovery of the high temperature superconductors. Among the theories concerning heavy fermion compounds [Pines 1990, Moriya 2000, Monthoux 2001] we will briefly mention the main conclusions from the work of Monthoux *et al.* based on mean-field theory for nearly antiferromagnetic and ferromagnetic metals in two and three dimensions:

- ferromagnetic fluctuations favor a p-wave (spin triplet) pairing whereas antiferromagnetic fluctuations favor a d-wave (spin singlet) pairing. Magnetic pairing is more robust in quasi-2D than in 3D systems.
- Antiferromagnetic fluctuations are more favorable for magnetic pairing with a critical temperature almost 10 times larger than for ferromagnetic fluctuations.

For both conventional and unconventional superconductivity the order parameter can vanish on lines or points on the Fermi surface but for unconventional superconductivity there is a change in the sign of the order parameter at these points which implies that there is no gap in these special directions. Consequently, there are no exponential temperature dependence of physical properties below the critical temperature but simple power laws.

### Valence fluctuations as a pair mechanism

As previously mentioned, the magnetic fluctuations that arise around a QCP are held responsible for electron pairing. However, in some HF materials, like CeCu<sub>2</sub>Si<sub>2</sub> the superconducting phase extends beyond the QCP [Bellarbi 1984, Holmes 2004], sufficiently far from magnetic ordering to consider other pairing mechanisms. CeCu<sub>2</sub>Si<sub>2</sub> exhibits a two-dome superconducting region under pressure, where  $T_c$  peaks at  $P_c = 4$  kbars and at  $P_v = 45$  kbars. Whereas around  $P_c$ , CeCu<sub>2</sub>Si<sub>2</sub> is located close to a QCP, increasing pressure however suppresses magnetism while superconductivity is enhanced. This suggests a different pairing mechanism around  $P_v$ . Transport measurements

---

<sup>14</sup> $T_{sc}$  is the superconducting transition temperature.

[Bellarbi 1984] and more recently, valence measurements under pressure [Rueff 2011] show hints of intermediate valence behavior under pressure and the hypothesis that critical valence fluctuations (CVF) may mediate electron pairing in this compound as it has been recently put on in a quantitative basis [Holmes 2007, Rueff 2011]. Therefore, CVF may also drive a superconducting state, providing that the Coulomb interaction  $U_{fc}$  between the f and conduction states is sufficiently strong as proposed in the theoretical model of Watanabe *et al.* discussed in section 1.4.4.

To conclude this section, I would like to point out that whereas superconductivity seems to be a general trend in Ce-based compounds, it is very rare in Yb-based HF systems. The first (and up to now unique) Yb-based heavy fermion superconductor,  $\beta$ -YbAlB<sub>4</sub>, has been found in 2008 by Macaluso *et al.* [Nakatsuji 2008]. An important target (and challenge) is to find new Yb heavy-fermion superconductors. It has been one of the aims of this thesis, but unfortunately not reached. However, the development of the *in-situ* pressure tuning device at dilution fridge temperatures is an essential tool for this search.



# CHAPTER 2

## Experimental techniques

---

### Contents

---

<b>2.1</b>	<b>Crystal growth</b>	<b>31</b>
<b>2.2</b>	<b>Extreme conditions</b>	<b>37</b>
<b>2.3</b>	<b>High pressure measurements</b>	<b>50</b>
<b>2.4</b>	<b>X-ray spectroscopic measurements</b>	<b>57</b>

---

In this chapter I will present in detail the experimental setups and methods used during this thesis. First, I will describe the crystal growth technique of the samples studied in this work and especially I will present in detail the growth of  $\text{YbAlB}_4$  in which I was actively involved. Secondly, the experimental setups in Diamond Anvil Cells (DACs) will be presented. Afterwards, the most relevant contribution of my experimental work will be introduced: the setting up of the *in-situ* pressure tuning device in a dilution fridge and adapted for DACs. Finally, the different measurements performed with DACs will be also described.

### 2.1 Crystal growth

The availability of high quality single crystals is a crucial step to study the physical properties of strongly correlated electron systems as they are, in general, very sensitive to the quality of the samples, i.e., the presence of impurities and/or defects like dislocations (e.g.:  $\text{YbAlB}_4$ ) [Nakatsuji 2008] and also to slight deviations in the chemical composition (e.g.  $\text{CeCu}_2\text{Si}_2$ ) [Steglich 1996].

Crystal growth and the research of novel materials have been an important and fruitful activity [Aoki 2001] inside the SPSMS laboratory which is mainly carried out by D. Aoki and G. Lapertot. The present equipment allows the growth of single crystals of either 4f (Ce, Yb or Sm-based HFC) and 5f systems (U-based HFC).

The samples used in this work were grown mostly by G. Lapertot at the SPSMS/CEA Grenoble:  $\text{YbCu}_2\text{Si}_2$  [Colombier 2008, Colombier 2009],  $\text{YbRh}_2\text{Si}_2$  [Knebel 2006a] and  $\text{YbNi}_3\text{Al}_9$ , whereas  $\text{YbCo}_2\text{Zn}_{20}$  was grown by the group of R. Settai in Osaka [Saiga 2008] following the procedure as described in detailed in [Torikachvili 2007].

At the beginning of this work we were very interested in  $\beta\text{-YbAlB}_4$  and I carried out the growth of  $\text{YbAlB}_4$  via a flux method technique which will be described in the next section.

#### Flux technique

All the crystals in this work were grown from a flux which consist of a solution of a metallic element with a low melting temperature  $T_m$  which is in excess, in general more than 95 % of the total molar concentration and the basic materials which are present only in a few %. This is one of the advantages of this technique: small amounts of the materials, which some of them can be very costly,

## 2.1. Crystal growth

are needed. Also it is convenient for the growth of Ytterbium based-compounds because diluted Yb has a much lower vapour pressure. The flux permits to lower the temperature at which the synthesis takes place (less than 1000 °C) compared to other techniques, like melting, where generally higher temperatures are needed (e.g.  $T_m$  of Boron is 2500 °C). As there is no thermal gradient in the solution, internal strain or defects during the crystallization are minimized. However, when working with metallic fluxes some caution must be taken to contain the liquid metal and prevent its reaction with the container to avoid the presence of impurities in the crystals [Kanatzidis 2005]. Chemical gradients are also minimized as crystals grow freely in the liquid metal media. They develop crystallographic forces which will be useful for optical measurements or visual orientation.

### YbAlB<sub>4</sub>

$\beta$ -YbAlB<sub>4</sub> is the first Ytterbium-based heavy fermion ( $\gamma \approx 300mJ/mol.K^2$ ) [Macaluso 2007] superconductor found to date [Nakatsuji 2008]. It has arisen a lot of interest and at the beginning of this work, we considered it an ideal candidate for pressure studies. That was the main motivation that lead us to grow our own  $\beta$ -YbAlB<sub>4</sub> samples. Unfortunately, it turned out to be much harder than expected and after many trials we finally discarded it.

There are actually two polymorphs of YbAlB<sub>4</sub>. According to Macaluso *et al.* the plate-shaped crystals correspond to  $\beta$ -YbAlB<sub>4</sub> which crystallizes with the orthorhombic ThMoB<sub>4</sub> structure type whereas the needle-shaped crystals correspond to the  $\alpha$ -YbAlB<sub>4</sub> which crystallizes in the orthorhombic YCrB<sub>4</sub> structure. In both polymorphs the Yb and Al atoms reside in the same *ab*-plane and are sandwiched between two B layers. The main difference between them is the packing arrangement of the B layers as shown in figure 2.1 [Macaluso 2007].

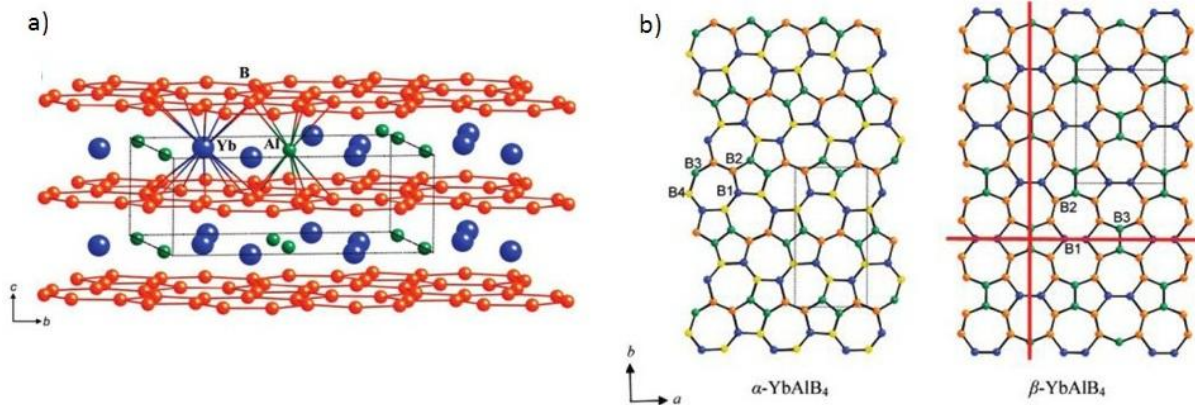


Figure 2.1: a) Crystal structure of  $\beta$ -YbAlB<sub>4</sub>. Boron (orange spheres) forms 2D sheets along the *ab*-plane. Yb atoms are depicted in blue and Al in green. Dashed lines show the orthorhombic unit cell. b) Boron layers along [020] for  $\alpha$ -YbAlB<sub>4</sub> and  $\beta$ -YbAlB<sub>4</sub>. The unit cell is outlined with gray lines. For  $\alpha$ -YbAlB<sub>4</sub>, the B1, B2, B3, and B4 atoms are shown as blue, orange, green and yellow spheres respectively. For  $\beta$ -YbAlB<sub>4</sub>, the B1, B2, and B3 atoms are shown as blue, orange and green spheres respectively. Mirror planes are depicted as solid red lines [Macaluso 2007].

As it was pointed out earlier, the sample quality in strongly correlated materials often plays a critical role and it can have dramatic effects in their physical properties as shown in figure 2.2. A usual test of sample quality is the RRR coefficient which is defined as  $RRR = \frac{\rho(300K)}{\rho_0}$  where  $\rho(300K)$  is the resistivity at room temperature, which is mainly dominated by the scattering of

the electrons with phonons, and  $\rho_0$  is the residual resistivity measured at very low temperatures, theoretically at absolute 0, which is due to the impurities of the crystal. At high temperatures all samples will have a similar value of the resistivity but  $\rho_0$  will be smaller for better samples and thus they will have a higher  $RRR$ . Curiously, superconductivity has been detected so far only in  $\beta$ -YbAlB<sub>4</sub> but for very high quality single crystals with a  $RRR \geq 300$  (Fig. 2.2) [Nakatsuji 2008].

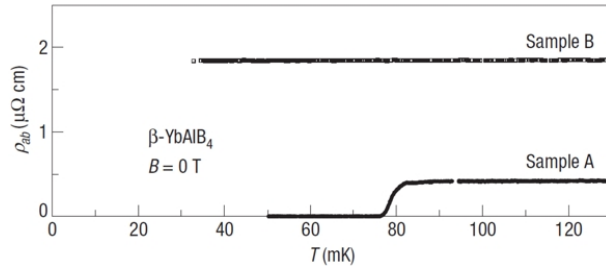


Figure 2.2: *Low temperature dependence of the in-plane resistivity  $\rho_{ab}(T)$  for two samples: sample A with a  $RRR \approx 300$  and for a lower-quality sample B with  $RRR \approx 70$ . See details in text [Nakatsuji 2008].*

### Growth of single crystals: YbAlB<sub>4</sub>

In order to grow high quality single crystals the first point is to use basic materials as pure as possible. In our case, they had a very high purity: Yb 99.99 %, Al 99.98% and B 99.99%. All the batches were grown from Al flux. The procedure we followed was similar as the one described in more detail in Macaluso *et al.* : First we put the basic materials Yb, B and Al in a Al<sub>2</sub>O<sub>3</sub> (alumina) crucible in the chosen stoichiometric proportions (see table 2.1). Then an upper crucible is filled with quartz wool and introduce in a quartz ampoule. This second crucible is placed on top of the first one to filter the liquid phase when the ampoule will be centrifuged. The ampoule is sealed with 0.3 At. of Argon before putting it in the furnace. Four different heat treatments were used as summarized in figure 2.3.

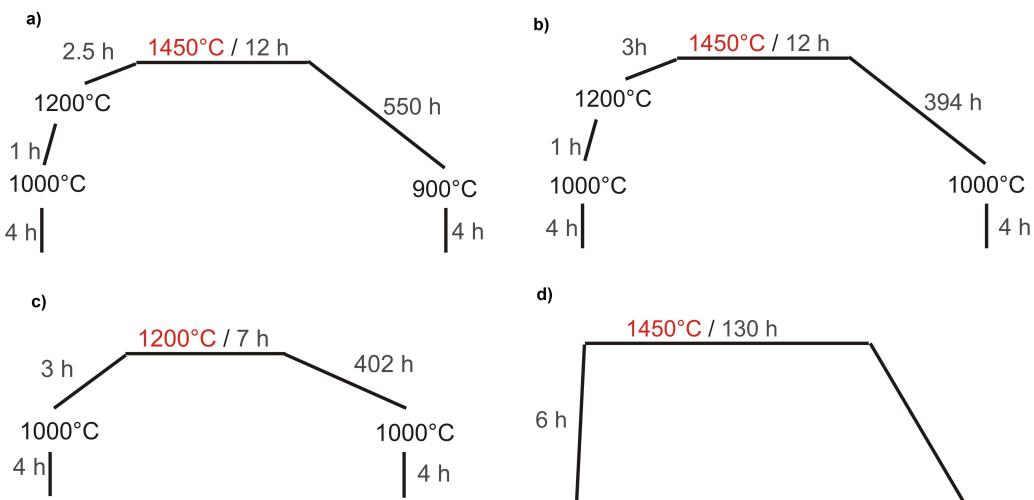


Figure 2.3: *Summary of the heat treatments that were used to grow the samples reported in table 2.1.*

## 2.1. Crystal growth

We wanted to see if the crystallization of the  $\beta$ -phase could be favored somehow by changing the following parameters: heating ramp, maximum temperature, waiting time at that temperature and the cooling ramp. In [Macaluso 2007] it is suggested that the  $\alpha$ -form might be the high-temperature phase as they found more alpha phase crystals in the heat treatment at 1873 K than at 1673 K. We worked at slightly lower maximum temperatures than in their study: 1723 K (1450 °C) for heat treatments (A),(B) and (D), and 1473 K (1200 °C) in (C).

Once the crucibles were removed from the furnace, we applied two different methods to etch the excess of Al flux: a chemical attack (ch. at.) using a NaOH solution and spinning, which requires to heat again the crucible in order to remove the Al. We obtained a mixture of both needle and plate-like crystals as in [Macaluso 2007]. Three selected samples are shown in figure 2.4: a) Plate-like sample B3 from Lap 508 III ( $548 \times 341 \times 30 \mu\text{m}^3$ ) b) needle-like sample B6 from Lap 508— ( $652 \times 185 \times 100 \mu\text{m}^3$ ) with the 4 contacts to measure resistivity and c) a needle-like sample from Lap 684 ( $364 \times 100 \times 115 \mu\text{m}^3$ ).



Figure 2.4: *Three selected samples from different growth: a) sample B3 from Lap 508 III b) sample B6 from Lap 508— and c) a sample from Lap 684. See details in text.*

In table 2.1 are shown the main crystal growth parameters of our samples: the stoichiometry, the heat treatment and the etching method. The last column summarizes the measurements carried out on the selected samples to characterize them: resistivity, heat capacity and X-ray diffraction measurements.

### Physical Property Measurements

The temperature dependence of the resistivity and specific heat capacity were measured using a commercial Quantum Design cryostat PPMS (Physical Property Measurement System). We measured the resistivity via a standard 4 point technique and we used the ACT transport option of the PPMS which is more convenient for small samples. The specific heat is measured with a relaxation technique (PPMS): the sample is glued with some grease to the puck of the PPMS which sends a known amount of heat and it measures the relaxation of the temperature via a thermometer located on the puck. The heat capacity of the puck and the grease are subtracted to obtained the specific heat of the sample. It is possible to use a  $\text{He}^3$  cryostat adapted for the PPMS and then the temperature range can be sweep from 300 K down to 0.3 K instead of 1.8 K.

Figure 2.5 shows the resistivity curves of 10 samples from 300 K to 1 K (color curves). The resistivity of  $\beta\text{-YbAlB}_4$  from [Nakatsuji 2008] in the same temperature range is also shown (open circles)<sup>1</sup>.

<sup>1</sup>The resistivity dependence of the alpha polymorph is not shown because no published data has been found at

Batch	Compound	Stoichiometry	Temperature cycle	Etching method	Measurement
Lap 478 I	YbAlB <sub>4</sub>	(Yb:B <sub>4</sub> ) <sub>2%</sub> , Al <sub>98%</sub>	a	Ch. at.	3 samples: $\rho(1-300\text{ K})$ , XR diffraction
Lap 508 --	YbAlB <sub>4</sub>	(Yb:B <sub>4</sub> ) <sub>2%</sub> , Al <sub>98%</sub>	a	Ch. at.	$\rho(1-300\text{ K})$
Lap 508	YbAlB <sub>4</sub>	(Yb:B <sub>4</sub> ) <sub>2%</sub> , Al <sub>98%</sub>	a	Ch. at.	$\rho(1-300\text{ K})$
Lap 508	YbAlB <sub>4</sub>	(Yb:B <sub>4</sub> ) <sub>2%</sub> , Al <sub>98%</sub>	a	Ch. at.	3 samples $\rho(1-300\text{ K})$ , XR diffraction
Lap 683	YbAlB <sub>4</sub>	(Yb:B <sub>4</sub> ) <sub>2%</sub> , Al <sub>98%</sub>	b	Spinning	C(0.5-20 K)
Lap 684	YbAlB <sub>4</sub>	(Yb <sub>1.3</sub> :B <sub>4</sub> ) <sub>2%</sub> , Al <sub>98%</sub>	b	Ch. at.	C(0.5-20 K), 1 sample $\rho(0.7-300\text{ K})$
Lap 686	YbAlB <sub>4</sub>	(Yb:B <sub>4</sub> ) <sub>1%</sub> , Al <sub>99%</sub>	d	Ch. at.	$\rho(0.7-300\text{ K})$
Lap 691	YbAlB <sub>4.4</sub>	(Yb:B <sub>4</sub> ) <sub>2%</sub> , Al <sub>98%</sub>	c	Ch. at.	C(0.5-20 K)

Table 2.1: Details of the growth parameters: stoichiometry, heat treatment and etching technique are shown. In the last column the number of samples on each batch and the measurements (resistivity,  $\rho(T)$ , heat capacity,  $C(T)$ , and X-ray diffraction, (XR) ) that were performed are also indicated.

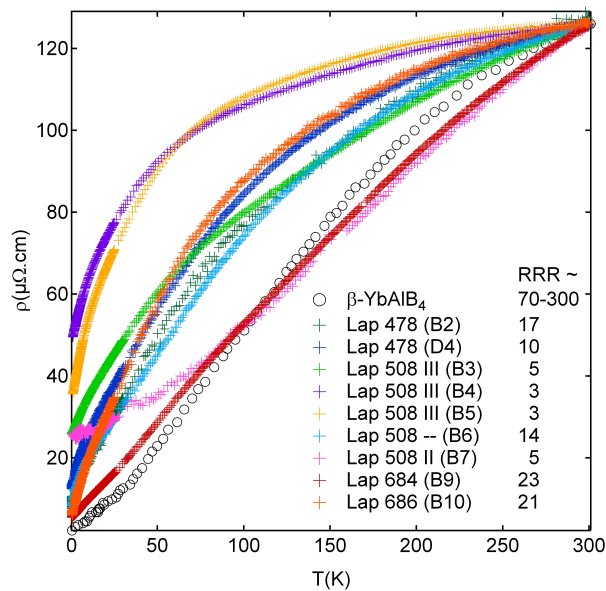


Figure 2.5: Temperature dependence of the resistivity,  $\rho(T)$ , from 300 K to 1 K and the RRR coefficient from selected samples of different batches (color curves) are shown. The resistivity curve of  $\beta$ -YbAlB<sub>4</sub> is plotted in open circles [Nakatsuji 2008].

## 2.1. Crystal growth

Actually, the quantity we measure at the PPMS is the resistance of the sample not the resistivity. Both quantities are related as follows:  $R = \rho * F$ , where  $F = L/S$  is the geometrical factor and  $L$  and  $S$  are the length and the section of the sample respectively. An estimation of  $F$  can be done by normalizing the room temperature resistance we measure to the resistivity value obtained in literature at 300 K. Here, we have normalized the experimental resistance curves using the resistivity value of  $\beta$ -YbAlB<sub>4</sub> at 300 K to estimate  $F$ . The error of the resistivity is mainly due to a wrong normalization but it will not have a deep impact on the interpretation of the results.

Even though several nice plate-shaped samples were measured, which in principle corresponds to the  $\beta$  polymorph, we can conclude from figure 2.5 that only the experimental curve of sample B9 (Lap 684) is similar to the actual curve of  $\beta$ -YbAlB<sub>4</sub>. This sample, B9, has also the highest quality obtained in this work, with a  $RRR \approx 20$ . Certainly, this value is significantly lower compare to the high quality samples from Nakatsuji *et al.* with  $RRR = 70 - 300$  [Nakatsuji 2008].

Figure 2.6 shows the specific heat capacity curves divided by temperature,  $C/T$ , of 4 samples and the curves of the two polymorphs [Macaluso 2007]. None of these samples belongs to the  $\beta$  form but to the  $\alpha$ . The "offset" between the experimental and the  $\alpha$  specific heat curves can be ascribed to the small masses of the measured samples and probably a contribution of the grease is still present, specially above 5 K. Actually, to measure properly the specific heat of a material with the PPMS a minimum mass of  $\approx 0.1$  mg is necessary. Three of them, A116, A119 and A120 are very close to this limit and they show bigger deviations than sample A115 ( $m = 0.29$  mg) which follows the  $\alpha$  curve below  $T < 5$  K.

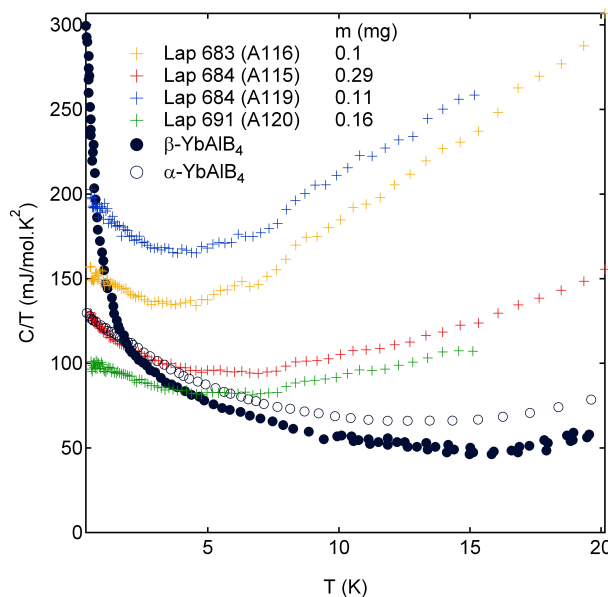


Figure 2.6: Temperature dependence of the specific heat divided by temperature,  $C/T$ , for 4 samples (color curves) with their corresponding masses are shown. The specific heat curves from  $\beta$ -YbAlB<sub>4</sub> (black filled circles) and  $\alpha$ -YbAlB<sub>4</sub> (open circles) [Macaluso 2007] are also plotted.

The last test we performed was a powder x-ray diffraction spectrum on two different batches to clearly identify the crystal structure of our samples. In figure 2.7 the powder diagram simulation using the Poudrix program and the crystal structure parameters from [Macaluso 2007] for  $\alpha$ -YbAlB<sub>4</sub>

---

the time of writing this work.

(left) and  $\beta$ -YbAlB<sub>4</sub> (right) are shown. The x-ray diffraction spectrum of a powder from several samples, nearly 20, from Lap 508 III is shown in figure 2.8 <sup>2</sup>. The experimental pattern and the corresponding peaks from the  $\alpha$  (squares) and  $\beta$  (triangles) polymorphs are visible. Each polymorph has a few peaks which characterized them and permit to identify the experimental crystal structure. We can observe that the spectrum from the samples of Lap 508 III perfectly matches with the simulated diagram of  $\alpha$ -YbAlB<sub>4</sub>, the pink squares.

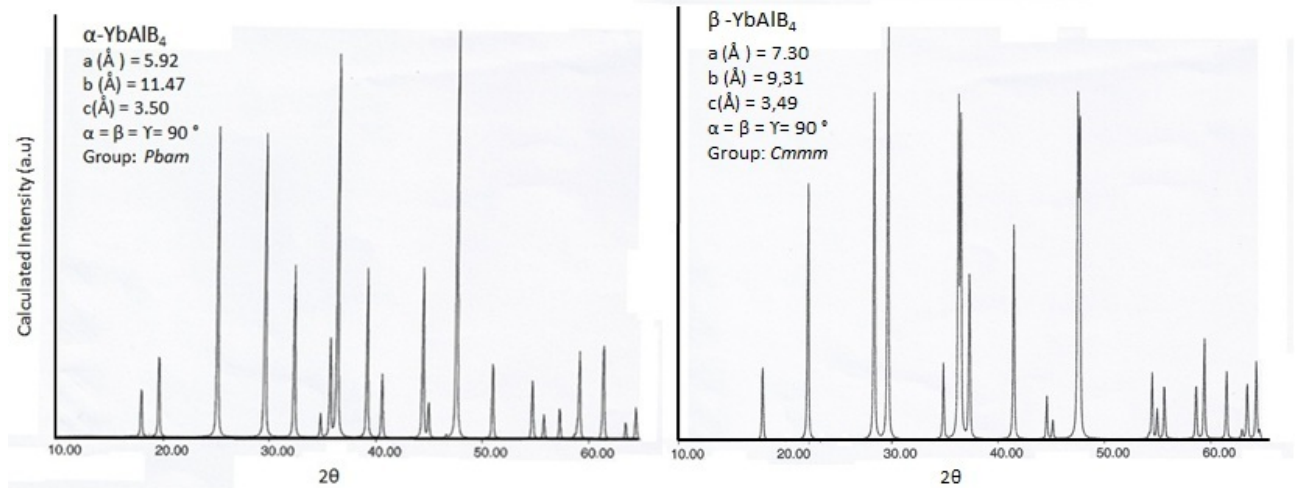


Figure 2.7: *Simulated powder diagram of  $\alpha$ -YbAlB<sub>4</sub> (left) and  $\beta$ -YbAlB<sub>4</sub> (right) using Poudrix.*

In conclusion, we have grown several batches of YbAlB<sub>4</sub> by Al flux and 16 samples, from several batches, have been characterized. Only one of them, the sample B9 (Lap 684), may be the sought  $\beta$ -YbAlB<sub>4</sub> but the quality it is not high enough to detect superconductivity as the  $RRR \approx 20$ . The other samples are likely to be  $\alpha$ -YbAlB<sub>4</sub>. Up to now, all the changes in the crystal parameters either in the heat treatment, the stoichiometry or in the etching method do not seem to improve the quality of the crystals nor to favor the growth of the  $\beta$  polymorph. Even though I stopped the growth of YbAlB<sub>4</sub> after all these trials, G. Lapertot is still working on it and hopefully he will succeed (very) soon.

## 2.2 Extreme conditions

From an experimental point of view, heavy fermions are very challenging as in general extreme conditions, i.e, low temperatures, high pressures and/or high magnetic fields are required to study their physical properties.

Hydrostatic pressure is known to be one of the cleanest ways to tune a system to its quantum critical point (QCP). The different physical phenomena that arise near a QCP like suppression/appearance of magnetic order, non Fermi liquid (NFL) behavior and/or superconductivity, generally exhibit a strong pressure dependence and thus it is highly convenient to have an accurate control of this parameter.

One of the strong motivations of this thesis was to develop an adequate setup to enable *in-situ* pressure tuning device at dilution fridge temperatures with the following performances:

<sup>2</sup>The x-ray diffraction spectrum of the Lap 478 I is not shown here as similar results were obtained.

## 2.2. Extreme conditions

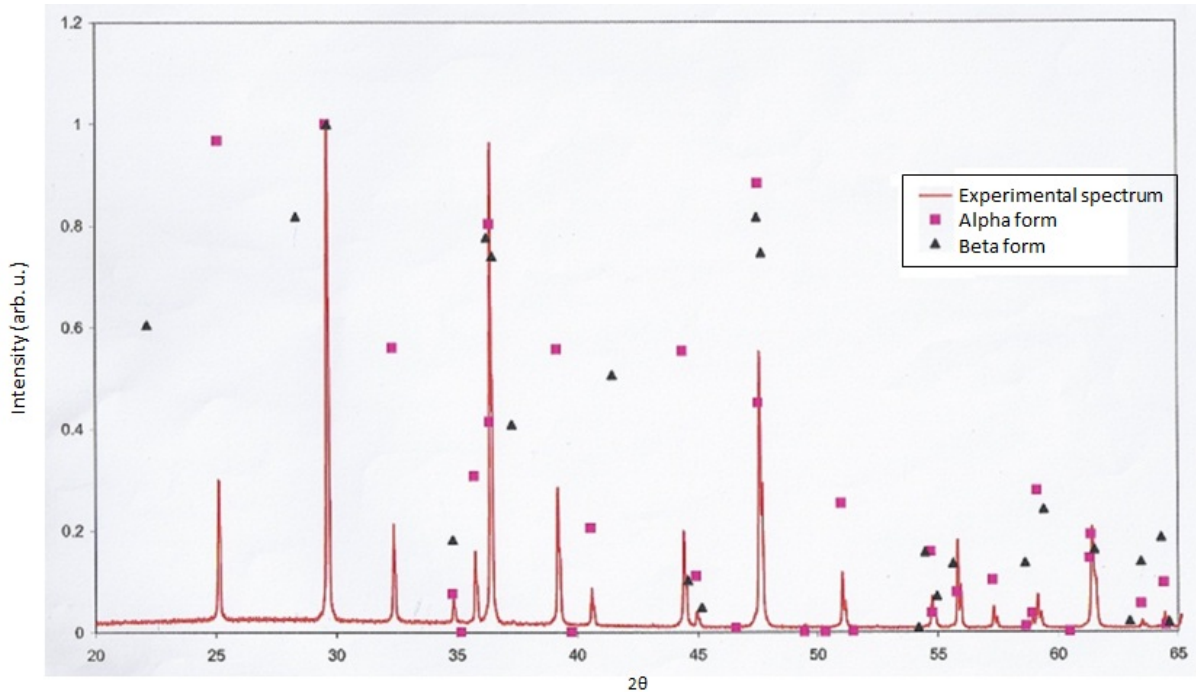


Figure 2.8: Powder diffraction spectrum of samples from Lap 508 III. Pink squares correspond to peaks of  $\alpha$ - $\text{YbAlB}_4$  and black triangles to  $\beta$ - $\text{YbAlB}_4$  peaks.

- low temperatures: a home-made dilution fridge with base temperature  $\leq 50$  mK.
- high pressures: to achieve above 10 GPa by modulating the pressure *in-situ* in a DAC.
- and magnetic fields: a superconducting coil up to 7 T.

Changing the pressure at low temperatures offer several advantages that largely compensates all the effort that has demanded:

- An important amount of time is spare. There is no need to warm the dilution fridge at each pressure. We can keep the dilution continuously running as long as we need (e.g: more than 10 weeks) in order to perform all the measurements with only one thermal cycle.
- The risk of breaking the contacts is therefore highly reduced.
- We have a greater control of the tuning of the pressure (e.g. the precision is about 1 kbar). This can be relevant when exploring the phase diagram of certain compounds that show abrupt changes in the pressure dependence of the critical temperatures.
- If needed, we can also decrease the pressure inside the DAC about 1-4 GPa without risks for the contacts. This can be very useful in order to confirm a particular region of the phase diagram.

The technical design work of the pressure tuning device was done by B. Salce before I joined the laboratory. In Fig. 2.13 it can be seen the bottom part of the mixing chamber level of the dilution fridge at the beginning of this work (left side) and after I installed the pressure *in-situ*

device (right side). Nowadays the setup works great after overcoming several long lasting problems mostly related to He leaks in the thin capillary and worst in the bellows. Several measurements have been performed proving its efficiency and potential (see Chapter 3, 4 and 5).

### 2.2.1 Low temperatures

In order to fully explore the ( $P - T$ ) phase diagram of the sought heavy fermion compounds in this work very low temperatures were required, i.e., below the Kelvin range. For that a home-built dilution fridge refrigerator (from an initial insert Kelvin-ox from Oxford,  $T_{Min} = 1.2$  K) was used in several experiments throughout this work. The base temperature of the dilution is 40 mK and 50 mK without and with magnetic field respectively. The principles of dilution cryostats as they are exhaustively described in the literature [White 1979, Lounasmaa 1979, Enns 2005] will not be mentioned here.

### 2.2.2 High pressure techniques

All measurements throughout this thesis were performed using diamond anvil cells (DACs). Therefore, in the next paragraphs I will present the main characteristics of a DAC: their elements, the preparation of the gasket, the loading process, the pressure transmitting media and the pressure measurement. Secondly, I will present the characteristics and performance of the *in-situ* pressure tuning device.

#### 2.2.2.1 Diamond anvil cell

The choice of the pressure cell depends on the pressure range which is sought and to technical limitations. Up to 4 GPa, other pressure cells as piston cylinder or indenter are in general more suitable than DAC as they have bigger working volumes and so the sample preparation and the manipulation of the cell is often easier.

In this work, however, we need to reach pressures as high as 10 GPa in order to study the physics near the QCP of our systems, especially in  $\text{YbCu}_2\text{Si}_2$ , where the QCP is located close to 8 GPa. This high pressure range is only possible with DACs which depending on the size of the anvils can attain pressures as high as 300 GPa. On the other hand, as we plan to change the pressure *in-situ*, we need to measure the pressure at low temperatures. As diamonds are transparent, optical measurements are possible. Thus, we can use the standard ruby fluorescence technique in order to measure the pressure inside the sample chamber.

Versatile and small DACs working at any temperature and under magnetic field have been widely used in a routinely way for many years [Jayaraman 1983, Dunstan 1989, Spain 1989]. However, experiments requiring electrical feedthroughs into the sample chamber for a long time was a challenge [Thomasson 1997, Gonzalez 1986]. A rather simple technique to perform transport measurements in DAC was developed by Thomasson *et al.* at the SPSMS [Thomasson 1997]. Throughout the years and the accumulated experience it has been consolidated and nowadays the success rate of loading a DAC is reasonably high.

Figure 2.9 shows the main elements, general scheme and typical dimensions of a diamond anvil cell currently used at the laboratory. For resistivity and ac-calorimetry measurements we work with diamonds with 1 mm culet whereas for ac-calorimetry measurements we use diamonds with 0.7 mm culet<sup>3</sup>. These dimensions are a good compromise between the minimum working space

<sup>3</sup>In the ac-calorimetry setup there are less wires inside the sample chamber so we can work with a smaller diamonds and thus higher pressures are easily achieved.

## 2.2. Extreme conditions

which is required to introduce the wires, the price of the diamonds and also the maximum pressure that is reached, about 20 GPa, which in general is enough to explore the phase diagrams of heavy fermions and other strongly correlated systems.

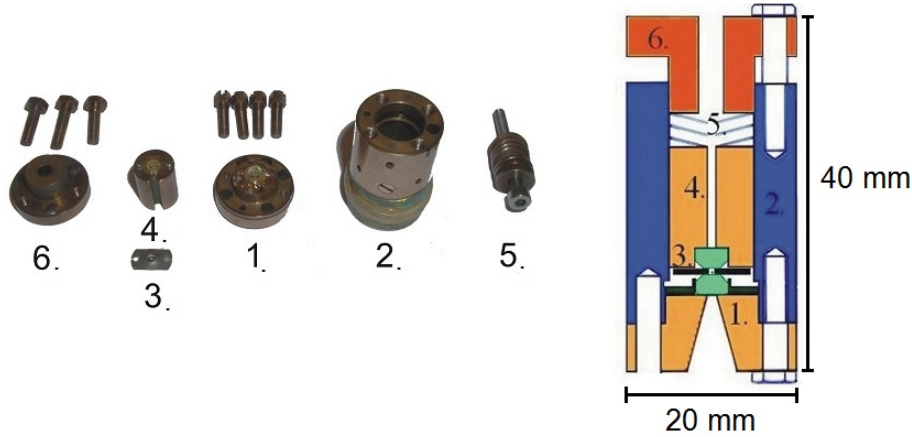


Figure 2.9: *The elements of our diamond anvil cell (left): 1. bottom fixed diamond, 2. body of the cell, 3. the gasket, 4. the mobile diamond fixed in the piston, 5. Belleville spring washers, 6. top closing element. On the right there is a scheme with all the elements pieced together and the standard dimensions are also indicated.*

The design of a DAC is rather simple: one anvil is fixed at the bottom of the cell (1.)<sup>4</sup> while the other is glued to the mobile piston (4.). The preformed gasket with a hand-drilled hole in its center (the sample chamber) is placed between them (3.). The sample and the pressure transmitting medium are placed inside the hole. The piston is well guided through the body of the cell (3.) and several Belleville spring washers (5.) minimize pressure changes due to thermal cycling. Finally, when the cell is closed, the locking nuts are screwed and a force is applied on the surface of the top element (6.) which is transmitted to the diamonds. The volume of the sample chamber will decrease and its internal pressure increase. The pressure at the sample is applied indirectly via the transmitting medium in hydrostatic conditions.

Even though the design is simple, loading a DAC for transport measurements turns out to be complicated by the necessity to introduce wires in the sample chamber and at each stage there is a possibility of failure: there is a risk of leakage and that the diamond breaks the wires at the border of the hand-drilled hole. The metallic gasket has to be insulated to avoid short circuits and this is a crucial stage<sup>5</sup>. Failures during the loading stage of the pressure transmitting medium may also happen. Finally, if pressure is changed at room temperature, the successive cooling-heating cycles can damage the wires.

The main stages of a DAC setup are:

### Gasket

Initially the gasket is a stainless sheet of 500  $\mu\text{m}$ . It is preformed by applying a force of 7000 N (5000 N)<sup>6</sup> to reduce its width to 100-120  $\mu\text{m}$ . Then a hole of 500  $\mu\text{m}$  (350  $\mu\text{m}$ ) is drilled by hand

<sup>4</sup>The numbers in brackets correspond to the elements shown in figure 2.9.

<sup>5</sup>Of course, a nonmetallic gasket it would be great help but unfortunately we do not know any other material with the required compromise of malleability, shear strength, and low compressibility under pressure.

<sup>6</sup>The values without or in brackets correspond for DACs with diamonds of 1 mm and 0.7 mm respectively.

at the center of the gasket and it is chamfered at both sides to avoid breaking the wires. The gasket is insulated to prevent short circuits. The insulating layer consists of a mixture between an epoxy (white Stycast 12%) saturated with alumina powder to improve its mechanical strength (the grains are about  $1\ \mu\text{m}$ ). The mixture covers all the surface of the gasket where the wires will pass through. Then it is polymerized during 7 min at  $70\ ^\circ\text{C}$  in the furnace. The hole is drilled again and its contour is insulated only with the epoxy (see Fig. 2.10). Next, the gasket is placed between the anvils. It is pressed with a force of 2000 N (1000 N) to get a flat and thin surface and hardened again at the furnace during 1 h. The ideal thickness of the insulating layer is about half of the height of the gasket, thus around  $50\ \mu\text{m}$ . If it is too thin or not saturated enough with alumina powder, there are big chances of short circuits whereas if it is too thick, when pressure is applied, the gasket deforms and the insulating layer may slide inside the sample chamber and it can break or damage the wires.

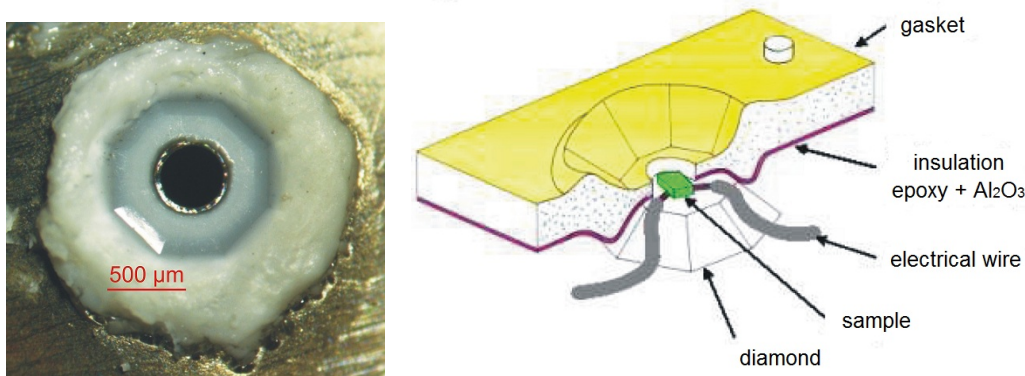


Figure 2.10: (Left) Gasket with the insulating layer. (Right) Scheme of the setup of a DAC cell (gasket, wires, sample, anvils) see details in section 2.3.

## Sample

As the sample chamber is not very big, the size of the samples is rather small, typically between  $150\text{-}300\ \mu\text{m}$  of length and up to  $50\ \mu\text{m}$  of height. Therefore, their manipulation is very delicate. As each measurement (resistivity, ac-calorimetry and ac-susceptibility) implies several specificities in the setup, the details will be given separately in section 2.3.

## Pressure transmitting media and loading

Argon has been used as pressure transmitting medium due to its high hydrostaticity up to 10 GPa [De Muer 2000]. Even though Helium has a higher hydrostaticity than Argon <sup>7</sup>, its strong compressibility at low temperatures <sup>8</sup> and its loading makes it less comfortable to work with. Argon is liquified with nitrogen and then the DAC (which is slightly closed) is simply submerged in it during 30 minutes. Finally, we pressurize with a force of 5000 N (3000 N). Typical sealing pressures at room temperature are about 10-15 kbars <sup>9</sup>. Argon is not liquid anymore at the pressure and temperature

<sup>7</sup>The pressure gradient of He inside the pressure chamber is about 0.1% whereas that for Argon is 0.6% at 10 GPa [De Muer 2000].

<sup>8</sup>It implies a large change of the volume in the sample chamber and thus, higher risks of breaking the wires.

<sup>9</sup>The international unit for pressure is Pa (1 GPa = 10 kbars) which I will use for all the graphics of this work. But for convenience, sometimes I will also use bars, kbars or GPa in the text.

## 2.2. Extreme conditions

range where we perform our measurements but as a noble gas, even when its compressed and becomes solid, its interatomic forces are weak and thus its quite malleable and isotropic.

### Pressure measurement

The ruby fluorescence is a well-known technique to measure the pressure in DACs [Forman 1972]. Some ruby chips are placed inside the sample chamber and they serve as pressure sensors. The wavelength of the ruby R-line fluorescence is pressure and temperature dependent but below 35 K the lines only depend on pressure. The rubies are excited by an Argon laser via an optical fiber that passes through all the cryostat. A second fiber directs the out coming light to the monochromator (HR 100) and the spectrometer (Andor Technology CCD). It is calibrated with a spectra at room temperature and ambient pressure where two lines are observed,  $\lambda_{R1} = 694.239$  nm and  $\lambda_{R2} = 694.82$  nm, and with the help of a reference Ne lamp. The lines shift 0.365 nm/GPa independently of the temperature (within 3%) [Noack 1979]. At low temperatures, the excited state which leads to the R<sub>2</sub> line is not populated anymore and thus it is not detectable. When there is a loss in the hydrostaticity because of strain in the pressure transmitting medium the different rubies will have slightly different emission lines which will lead to a broadening of the detected line. Hence its width indicates the homogeneity of pressure.

In figure 2.11 the ruby spectra at 4 K for selected pressures are plotted. In this example, pressure was changed using the pressure *in-situ* device.

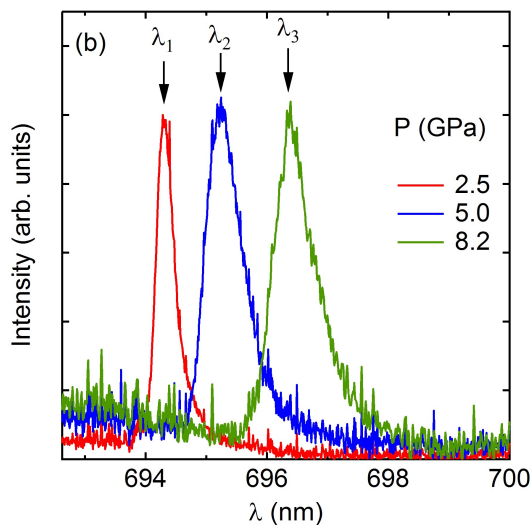


Figure 2.11: *Ruby spectra at selected pressures measured at 4 K. In this setup pressure was changed at low temperatures using the pressure in-situ device.*

The experimental spectra can be fitted with Gaussian functions to estimate the line width,  $\Delta$ , and the position of the maximum of the peak,  $\lambda_0$ , to precisely estimate the pressure. An example is shown in figure 2.12. Here, the peak is centered at  $\lambda_0 = 694.3$  nm which corresponds to 2.5 GPa and its width is  $\Delta = 0.235$  nm.

Technically, the measured  $\Delta$  does not only correspond to the intrinsic width of the ruby fluorescence. It can be decomposed in three different terms:

$$\Delta = \Delta_0 + \Delta_{spec} + \Delta_{inhom}, \quad (2.1)$$

where  $\Delta_0$  corresponds to the intrinsic width of the ruby signal (which in general is larger at 300 K than at 4 K),  $\Delta_{spec}$  is the limiting sensitivity of the transfer function of the spectrometer ( $\Delta_{spec}$ ) and finally  $\Delta_{inhom}$  corresponds to the broadening due to pressure inhomogeneity in the sample chamber, not only in the sample.

In Figure 2.12 a) we compare the  $\Delta$  of the ruby line when the pressure is changed at room temperature (black diamonds) and at low temperature (red diamonds). At room temperature, up to 2 GPa, the line width corresponds to the first two terms of eq. 2.1,  $\Delta = \Delta_0 + \Delta_{spec} \approx 0.18$  nm, i.e., there is no broadening effects due to inhomogeneity in the sample chamber. For higher pressures, a slight pressure inhomogeneity appears and at 5 GPa,  $\Delta_{inhom} \approx 0.06$  nm.

We find that up to 4 GPa the line width is roughly proportional to pressure when changing pressure at low temperatures (red solid line). Clearly, the homogeneity is higher when the pressure is changed at room temperature. At  $P \approx 2$  GPa, the measured  $\Delta$  when pressure is changed at 4 K is as large as the value at 5 GPa when pressure is changed at 300 K. In the ideal case, pressure is applied on a liquid but even at room temperature, Argon solidifies within the pressure range attained in our measurements (at 300 K the solid-liquid transition takes place at  $P \approx 12$  kbars), but it stays more malleable at high temperatures, i.e., with better hydrostatic conditions and thus with narrower line widths. Despite this broadening effect, we still have a good precision of the pressure and we can distinguish two spectra with a difference of  $\pm 0.5$  kbars.

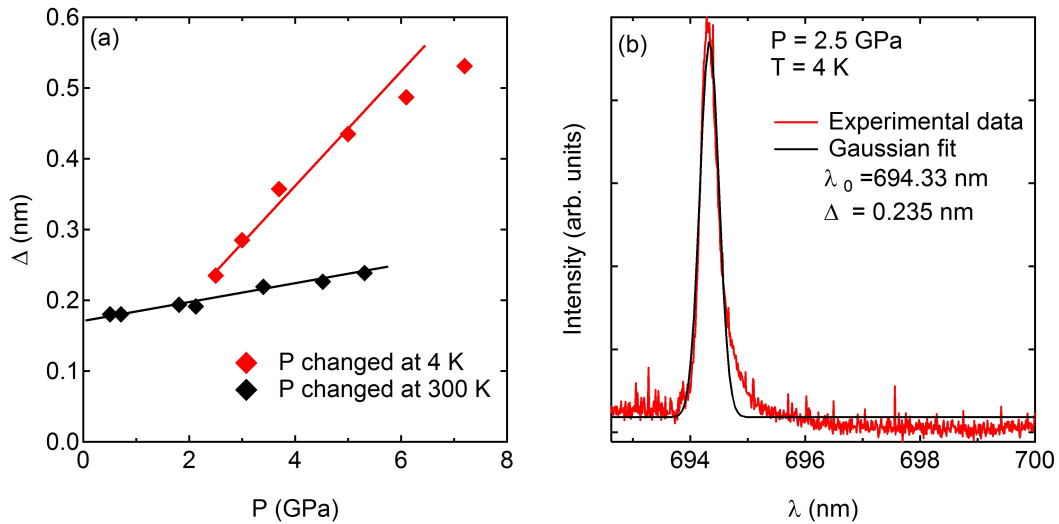


Figure 2.12: a) Line widths for two different setups: when pressure is changed at low temperatures (red diamonds) and at room temperature (black diamonds). b) Gaussian fit (in black) to a ruby line to obtain the line width,  $\Delta$ , and the position of the maximum of the peak,  $\lambda$ .

### 2.2.2.2 Force generating devices

Devices that generate forces at low temperatures exist since many years [Silvera 1985]. In Salce *et al.* detailed information can be found of an *in-situ* pressure device adapted to an  $^4\text{He}$  fridge which can generate forces up to 25 kN at 1.4 K and thus it permits to sweep a pressure range from 0 to  $\approx 20$  GPa in a DAC with a diamond table of 0.7 mm. This device was developed at the SPSMS laboratory more than ten years ago and it was used during this work for several measurements (see Chapter 3 and 4) [Salce 2000].

## 2.2. Extreme conditions

Even though there are fewer examples of force generating apparatus working at very low temperatures [Webb 1976], the operation principle is basically the same: pressurized bellows with He coupled to a mechanical amplifier force system. The main difficulty to overcome is the thermalization of the device which is placed at the bottom part of the calorimeter, after the mixing chamber level of the refrigerator. A preliminary development was carried out with success in a dilution fridge in the laboratory [De Muer 2000] and it proved its feasibility. However, further efforts to improve the design of the device (to lighten its mass and reduce its dimensions as much as possible) had to be done to minimize the thermal leakage and to adapt the device to the new dilution fridge with a magnetic superconducting coil with a standard 52 mm hole.

### 2.2.2.3 *In-situ* pressure tuning device at dilution fridge temperatures

#### Description

The main parts of the device are shown on the right side of figure 2.13:

- the bellows: they are made of stainless steel. Their external diameter is 56 mm and the internal about 39 mm. Their original height before being expand is about 35 mm. They are designed to stand pressures up to  $P \approx 19$  bars but we actually use them up to 24 bars<sup>10</sup> and they expand more than 13 mm.
- the capillary: it is made of Ni-Cu alloy which is convenient because of its weak thermal conductivity. Its internal diameter at the bottom part is about  $\Phi_{int} \approx 0.1$  mm to minimize the thermal leaks.
- the mechanical amplifier system: it consists of two levers made of Cu-Be (2% of Be) alloy.
- the cage of the mechanical amplifier system: also made of Cu-Be alloy.
- the optical fibers: two plastic fibers of diameter  $\Phi = 0.5$  mm placed at the top of the DAC.
- force sensor: a piezoelectric sensor is placed above the DAC in order to monitor the applied force.
- DAC
- thermometer: a RuO<sub>2</sub> thermometer is located at the external surface of the DAC to measure the temperature as close as possible to the sample.

#### Performance

The pressure circuit remains under vacuum until the dilution fridge is cold. The pressure in the bellows is controlled via a regulator fixed to a gaseous helium bottle at 200 bars and it is measured by an absolute pressure sensor in the pressurization circuit at 300 K. The helium passes through a nitrogen trap to avoid any blockage in the capillary at low temperatures. The capillary is thermalized at each stage of the cryostat: 1.2 K pot, the still and the mixing chamber.

The force is generated when the bellows are pressurized and it can be measured at any time by the piezoelectric sensor placed just above the DAC. The bellows can generate a force  $F = 3$  kN for an Helium pressure of  $P_{He} = 21$  bars and its effective surface is  $S_{eff} = F/P_{He} = 15.3$  cm<sup>2</sup>. The

---

<sup>10</sup>We could apply up to 25 bars which corresponds to the Helium liquid-solid phase transition at low temperatures.

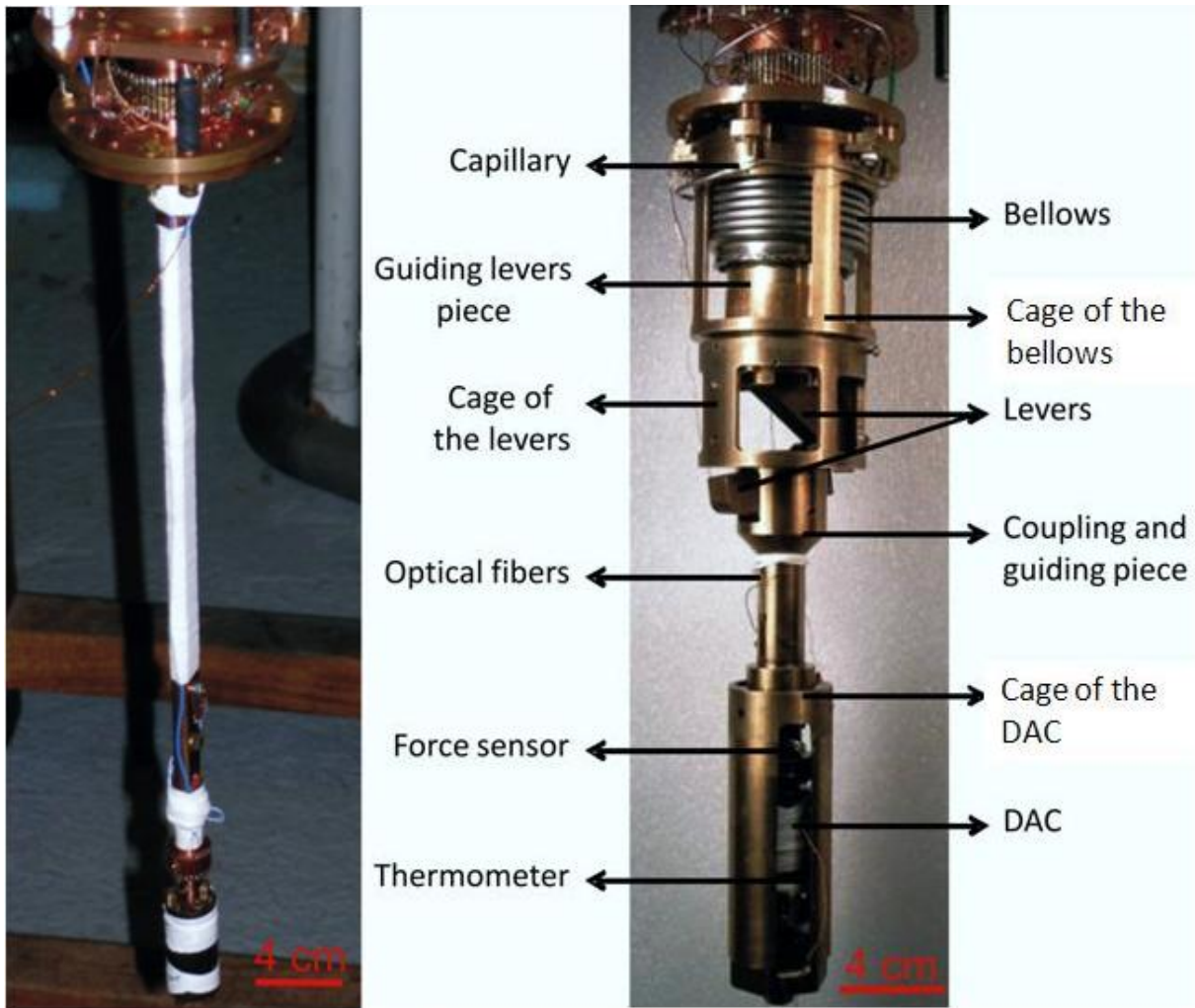


Figure 2.13: *Before (left) and after (right) the pressure device was set in placed.*

## 2.2. Extreme conditions

temperature has no effects on the performance of the bellows as shown in figure 2.14. However, the response of the mechanical amplifier system was found to be temperature dependent: at 300 K the amplifying factor is about 4.5 whereas at low temperature this ratio decreases to  $\approx 3.5$ . This force loss has not been observed in the other pressure *in-situ* devices [Salce 2000, De Muer 2000].

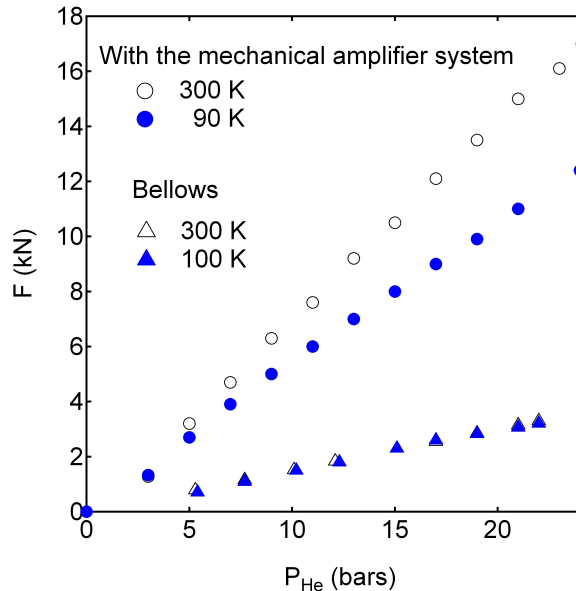


Figure 2.14: Performance of the bellows at room temperature and at 100 K (open and full triangles respectively). Circles (open and full) correspond to the force generated with the amplifier system at 300 K and 90 K respectively.

All the elements (the levers, their cage, the cage of the bellows and the one of the DAC cell) are made of the same non-magnetic Cu-Be alloy which is a good compromise between mechanical endurance and thermal conductivity. So thermal contractions are not responsible of the force loss. We tested the piezoelectric sensor which measures the force applied at the DAC and its response is not temperature dependent. We have not fully clarified the origin of the force loss but it has to be mechanical. In fact, there is a difference in the design of the cage of the levers between the  $^4He$  and the dilution fridge mainly because the dimensions and the mass had to be reduced in the later and they are less well guided. If during the cooling process they move (although we apply by hand about 1 kN of force to block the levers in the good position before we run an experiment) that could explain this loss of force. Nevertheless, we have achieved the pressure range we sought: for a DAC of 0.7 mm pressures up to 14 GPa (for a  $P_{He} = 13$  bars) (see Chapter 4) have been achieved and for a DAC of 1 mm culet about 10 GPa (with  $P_{He} = 19$  bars). Another design of the cage would probably clarify the origin of this loss. The pressurizing process is reflected in Fig 2.15 where it can be seen how the bellows expand for different  $P_{He}$  up to 15 bars (corresponding to about 10 GPa in the DAC).

In order to measure the pressure via the ruby fluorescence two optical fibers are passed through all the dilution fridge down to the DAC. Due to room limitations we could not measure in transmission mode as in the  $^4He$  fridge where one fiber is placed at the top of the DAC, and the other one at the bottom. In this case, we had to place both fibers on the top of the DAC, hence the change to 0.5 mm fibers, and measured the ruby fluorescence in reflection mode. Even in this configuration, which is less favorable, the signal was enough intense to be detected.

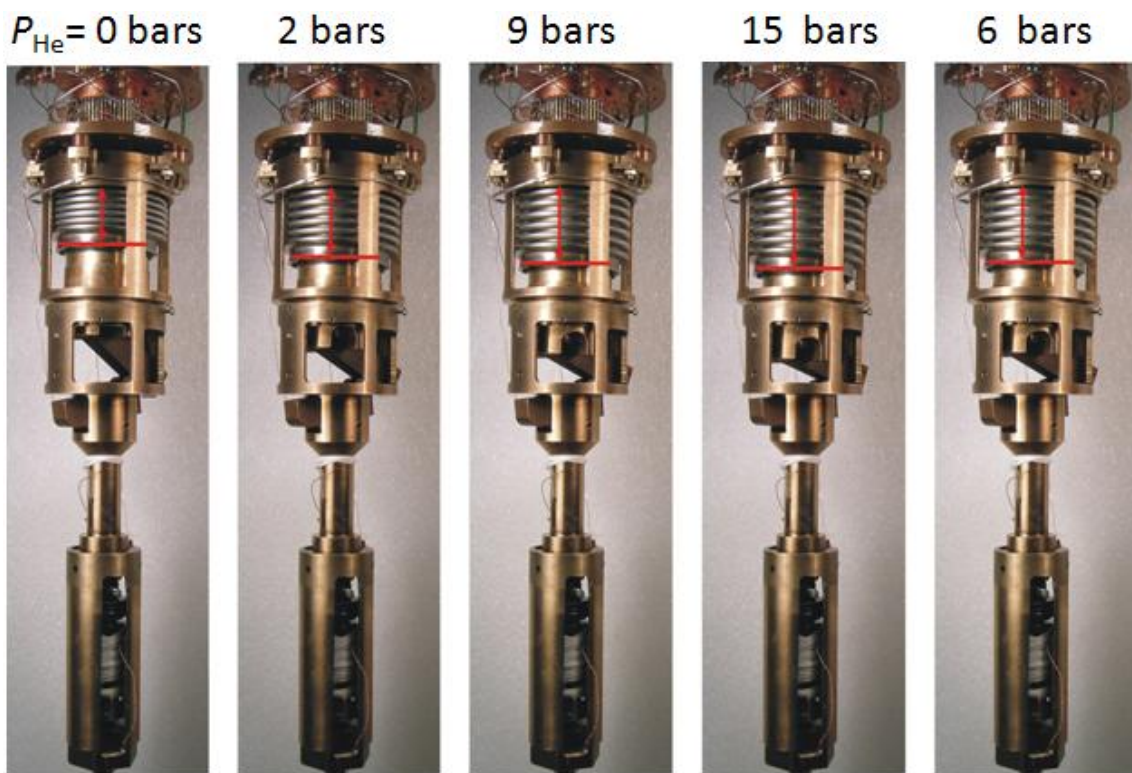


Figure 2.15: *From left to right: different moments of the pressurizing process of the bellows.  $P_{\text{He}}$  is indicated and also the expansion of the bellows. The red line are a guide to the eyes.*

## 2.2. Extreme conditions

### In-situ pressure modulation at low temperatures

Changing the pressure in a DAC at room temperature has several disadvantages like a noticeable reduction of the pressure when cooling from 300 K to low temperatures ( $\approx 8$ -10 kbars) which is not completely reproducible. Also several thermal cycles can weaken the contacts and the probability to have problems increases (e.g: breaking of the wires and short circuits). Moreover, the contacts rarely stand pressures above 6 GPa and several Yb-based heavy fermion compounds have higher critical pressures  $P_c \approx 8$  GPa. This technical difficulty is one of the reasons why Yb systems have been far less studied compared to their Ce counterparts. Another specificity of Yb compounds is their rather low energy scales which often implies transition temperatures below the Kelvin (e.g: YbRh<sub>2</sub>Si<sub>2</sub> and YbCo<sub>2</sub>Zn<sub>2</sub>O) so the use of a standard <sup>4</sup>He fridge is not enough. These disadvantages are avoided by modulating the pressure at dilution fridge temperatures where only one thermal cycle is needed and pressures above 10 GPa are attainable.

When we pressurize the bellows we can monitor the process by acquiring simultaneously the Helium pressure ( $P_{He}$ ), the generated force (F) and the temperature at the outside part of the DAC (T). Figure 2.16 shows two different situations: a) filling the bellows at the beginning of an experiment and b) changing the pressure in the DAC during an experiment between 18 to 20 kbars.

As we have previously mentioned, when we cool down for the first time the bellows are under vacuum. The filling process is quite long, a few hours, as we try to keep the temperature at the mixing chamber below 1 K to avoid the evaporation of all the mixture, even though a partial evaporation is very difficult to avoid. That is why we keep a low Helium pressure,  $P_{He} \approx 1$  bar, during the He condensation process (see Fig. 2.16a). For  $t > 330$  min the force starts to increase, indicating that the bellows are filled. Another way to check when the bellows are filled is by closing the valve from the He bottle and see if the  $P_{He}$  decreases or remains almost constant. The temperature will rise for quick ramps in  $P_{He}$  but as soon as the pressure is stable, the force will be constant and the temperature will decrease again. The strong increase of T up to 3 K are due to laser heating when we measure the ruby fluorescence to check if the pressure in the DAC has changed.

But it is in Fig. 2.16 b) where the advantages of changing the pressure at low temperatures can be plainly observed: even though the temperature will tend to increase a little bit, it remains below 1 K and thus the dilution keeps on running. Secondly, once the bellows are filled, changing the pressure is quite fast: in this example it has taken only 15 min to change from 18 to 20 kbars. A lot of time is spared compared to changing the pressure at room temperature. But not only time, also all the risks associated to the heating-cooling cycles in DAC are greatly reduced.

The mechanical amplifier system has a non reversible behavior under pressure. For  $t > 12$  min when the pressure circuit is pumped, the  $P_{He}$  decreases but the force remains constant. This behavior is interesting for temperature sweeps above 4 K. If we kept the same liquid He volume in the bellows the pressure would increase as He would become gaseous and consequently, the pressure in the DAC would also increase. With this “hysteretic” behavior this problem is avoided. Usually we pump until the force starts to decrease. This step is important when working with the <sup>4</sup>He fridge as often we measure up to 20 K but it is less critical with the dilution fridge because we rarely measure above 2 K where He is still liquid and no noticeable changes in pressure have been detected.

Despite all the advantages there is one weak point: changing the pressure at low temperatures is less hydrostatic than changing it at room temperature as it was already discussed in section 2.2.2.1.

In summary, we have been able to perform experiments for more than 10 weeks, if necessary, without warming up the cryostat.

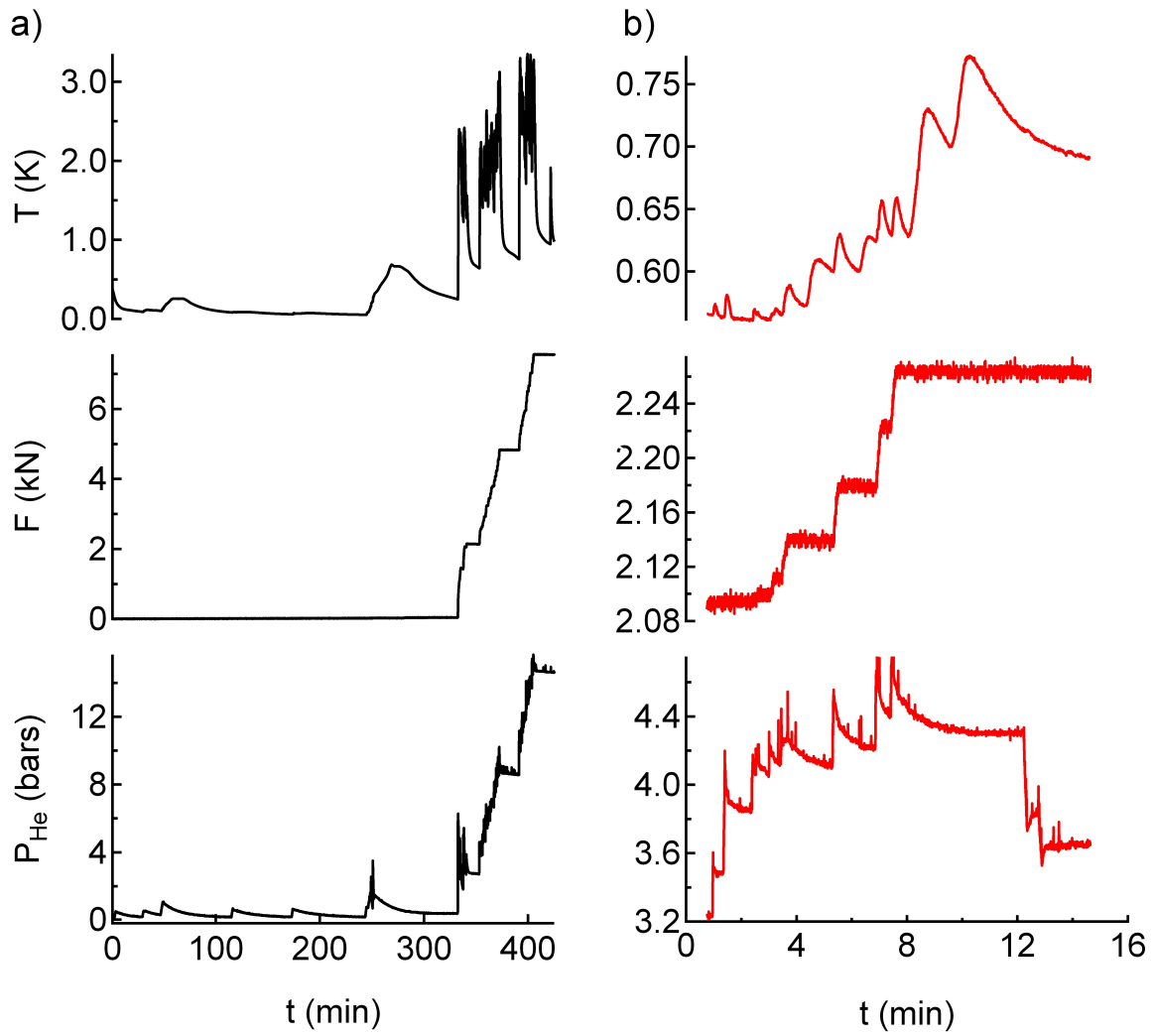


Figure 2.16: Changing the pressure at low temperatures: a) filling the bellows for the first time during an experiment and b) changing the pressure between 18 to 20 kbars (see details in text).

## 2.3. High pressure measurements

### 2.2.3 High Magnetic fields

Two different high-magnetic field experiments were carried out: resistivity measurements under pressure up to 35 T at the LNCMI (Grenoble, France) facility, and magnetization and resistivity measurements at ambient pressure at the high-pulsed magnetic field facility, LNCMI (Toulouse, France), up to 53 T.

### Magnetoresistivity measurements in high magnetic fields

The setup used for the resistivity measurements at the LNCMI-Grenoble was similar at the one we used in our laboratory which is based in the synchronous detection at low frequencies and it is described in the next section.

### Measurements in high-pulsed magnetic fields

There are several constraints when working with high pulsed magnetic fields. One of them is that the pulse duration (typically some hundreds of milliseconds) is too short to perform an average measure of the acquired data. Then numerical filters are needed. Transport measurements are performed also by a synchronous detection technique but the working frequency of the Lock-in amplifier,  $F$ , is much higher than the one used in constant magnetic fields (e.g., between 20 kHz and 60 kHz instead of 17 Hz). The necessity of such high frequencies is due to the duration of the pulsed but also to avoid different sources of noises like vibrations from the magnetic coil when working at low frequencies at the shot pulsed. The signal is acquired through different acquisition carts and it is treated by a digital Lock-in which performs the synchronous detection as a Lock-in amplifier but in this case at the end of the measurement. There is an optical fiber between the acquisition cart (PXI) inside the box (where the measurements are performed) and the computer outside the box to treat and recover the data [Levallois 2008].

## 2.3 High pressure measurements

### 2.3.1 Electrical resistivity

The electrical resistivity  $\rho$  is an intrinsic property of a given material while its resistance  $R$  depends on its dimension. For certain geometries, there is a simple relation between resistivity and resistance:

$$R = \frac{V}{I} = \frac{\rho * l}{S},$$

where  $F = \frac{l}{S}$  is the so-called geometrical factor.

Resistivity is a true quantitative measurement under high pressure except for geometry limitations which induces an uncertainty to the geometrical factor  $F$ . This is a systematic error, mainly because of a wrong normalization. Absolute values of the resistivity are obtained by normalizing the measured room temperature resistance to the resistivity value obtained in literature at 300 K so we can deduce the geometrical factor which we suppose to be pressure independent at low pressures.

### Resistivity measurement

Resistivity is measured via the standard four-point contact ac-technique with a lock-in detection (Stanford SR830). Four gold wires (12  $\mu\text{m}$ ) are spot welded on the sample. Typical welded

parameters for the samples of this work were  $U=5$  V and  $\tau =10$   $\mu$ s. Then, four flattened 25  $\mu$ m golden wires are glued with silver paint in four sides of the diamond anvil where they contact the wires that are fixed at the bottom of the DAC (see Fig. 2.10). The edge of the flattened wires on the diamond plate are cut so they do not enter inside the pressure chamber as shown in Fig. 2.17.

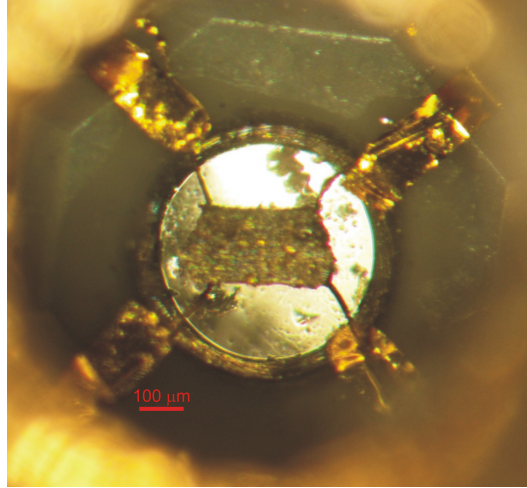


Figure 2.17: Resistivity setup for a DAC. The insulation layer of the gasket, the sample with the golden wires (12  $\mu$ m), the flattened golden wires (25 $\mu$ m) and several ruby chips are shown.

In order to maximize the signal-to-noise ratio we wanted to use the largest excitation current without heating the sample. A value of  $I = 100$   $\mu$ A was found to be a good compromise, i.e. no significant changes in the signal were detected by decreasing the current. We measured at a frequency of 17 Hz. The signal was amplified at room temperature by a transformer and then by a pre-amplifier before the Lock-in with a total gain of  $10^5$ .

### 2.3.2 Specific heat

The specific heat  $C$  is the amount of heat per unit mass required to raise the temperature by one degree Celsius. In this study, the measurement of the specific heat was helpful to determine the transition temperatures as a function of pressure because at a bulk transition it generally shows an anomaly. As it will be detailed in the next section, we did not work with absolute values of the measured signal so we could not determine thermodynamic properties like entropy,  $S$ , as can be usually done when working at ambient pressure.

#### Ac-calorimetry measurement

The main difficulty when working under pressure is the thermal coupling between the sample and its environment (the thermocouple, the Argon, the gasket and the body of the cell itself). As this coupling is temperature and pressure dependent, it is not easy to determine. The ac-calorimetry technique which is described in detailed in [De Muer 2000], is well adapted for small samples where the time constant needed to achieve the thermal equilibrium is rather small. In a simple model proposed by Sullivan *et al.*, the sample is coupled to the bath (the environment) by a thermal conductance,  $\kappa$ , as shown in Fig. 2.18 [Sullivan 1968]. The sample is heated with an alternative power  $P = P_0(1 + \cos wt)$ , where  $P_0$  is the mean value and  $w$  is the oscillating frequency. The induced temperature oscillations,  $T_{ac}$ , are related to the specific heat of the sample as follows

### 2.3. High pressure measurements

$$C_{ac} = \frac{P_0}{wT_{ac}} \propto \frac{1}{T_{ac}}.$$

The frequency  $w$  has to be chosen high enough to decouple the sample from its environment but small enough to achieve the thermal equilibrium in the sample.

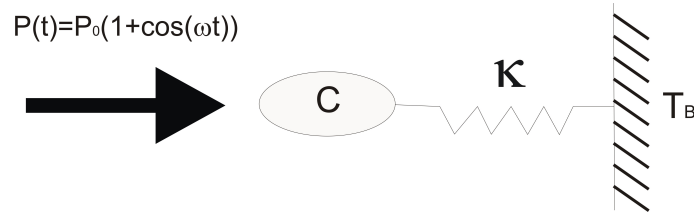


Figure 2.18: Principle of the ac-calorimetry technique proposed by Sullivan et al. An alternating power  $P$  is applied to the sample with a specific heat  $C$ . The sample is coupled via a thermal conductance  $\kappa$  to the bath  $T_B$ .

In practice, to measure the specific heat we use a thermocouple made of Au:Au(0.07%Fe). The Au wire is about  $12 \mu\text{m}$  whereas the AuFe which originally is about  $25 \mu\text{m}$  is flattened to reduced the risks of short circuits. The setup of the DAC is a little bit less complex than for resistivity and it is shown in figure 2.19. There are only two wires to weld on the sample. In these measurements we use diamond anvils with  $0.7 \text{ mm}$ .

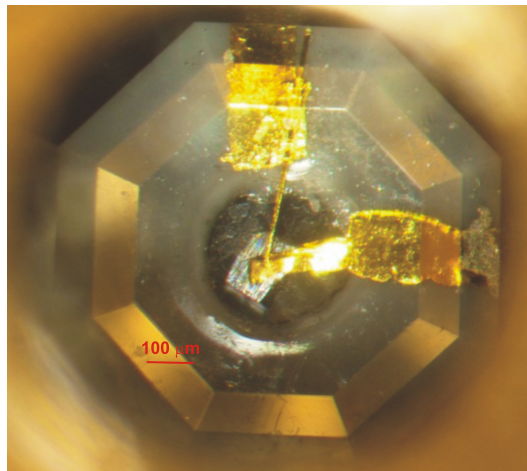


Figure 2.19: Setup for ac-calorimetry measurements in a DAC. A thermocouple Au:Au(0.07%Fe) is welded on the sample.

The temperature dependence of the sensitivity of the thermocouple was determined by Chaussy et. al and it is about  $S_{th}(1K) \approx 7\mu\text{V}/K$  [Chaussy 1982]. At our pressure range it is assumed to be pressure independent [Itskevich 1978]. A Lock-in amplifier measures the oscillating voltage of the thermocouple  $V_{ac}$  at the same frequency  $\omega$  which is proportional to  $T_{ac}$ ,  $V_{ac} = S_{th}T_{ac}$  and also the phase shift to the heating. The signal is amplified by a factor of  $10^5$  like in the resistivity measurement.

The power heating is generated via an argon laser ( $\lambda = 476.5 \text{ nm}$ ) with a maximum power of  $50 \text{ mW}$  coupled to a chopper with a modulable frequency when we measure with the  ${}^4\text{He}$  pressure *in-situ* device. In the dilution fridge, in order to achieve the lowest temperature possible, which

was about 200 mK, we have used a red laser diode with a maximum power of 20 mW coupled to a filter to reduce its intensity. We detected  $T_{ac} \approx 1.7$  mK at 200 mK.

There are several advantages when working with the laser diode:

- the power is electronically regulated and thus more stable than the power of the argon laser. This is reflected in the measured signal which is more stable in time when using the diode laser [Measson 2005].
- the range of frequencies is wider in the diode laser than using a chopper.
- the phase shift can be better known as the heating power in the diode is sinusoidal.

Nevertheless there are also some disadvantages: it will be more difficult to measure a big specific heat ( $T_{ac} \propto \frac{P_0}{C_{ac}}$ ) due to the limiting maximum power of the diode laser and secondly, we need to use a second laser to measure the ruby fluorescence.

This method is semi-quantitative (i.e., absolute values of  $C$  are not obtained) because the average heating  $P_0$  on the sample is not known as there is an unknown fraction of heat that goes to the sample environment. Another source of error is that even though we work at a frequency that in principle decouples the sample and the bath, in practice it is not a perfect decoupling so there is still a contribution of the environment in the measured signal. This gives rise to a background signal which is pressure and temperature dependent. Nevertheless, this technique allows us to determine the temperature transitions where  $C$  shows an anomaly and we can therefore plot the phase diagram of the sample.

## Frequency test

In order to choose the working frequency at the beginning of each experiment we have measured the frequency dependence of the signal at a constant temperature. Then we plot in a log-log plot the measured signal multiplied by the frequency as a function of the frequency. The frequency test for the ac-calorimetry measurements on  $\text{YbCu}_2\text{Si}_2$  is given as an example in figure 2.20. At low frequencies, a linear dependence is observed which indicates that the sample is not thermally uncoupled from the bath because in one period the heat can propagate not only inside the sample but also in its environment. An almost flattened (frequency-independent) region is visible in the appropriate frequency range, where quasi-adiabatic conditions can be assumed, i.e., the heat propagates throughout the sample but not in the bath. Finally, at higher frequencies, we observe again a frequency dependence of the signal. The increase of  $V_{ac} \times f$  at high frequencies is surprising: normally a decrease is expected when the sample starts to be decoupled from the thermometer. Probably the excitation is heating directly the thermocouple as discussed in more detailed in [Measson 2005].

The working frequency used in this work was between 77 and 733 Hz. And all pressures are compared at the same frequency.

### 2.3.3 Ac-susceptibility

Magnetic susceptibility is the response of a material with a magnetization  $M$  when a dc-magnetic field  $H$  is applied. In this study the magnitude we measured is the alternating current (ac) susceptibility which is defined as  $\chi_{ac} = \frac{dM}{dH_{ac}}$  where  $H_{ac}$  is an oscillating magnetic field. In the dc measurement, the magnetic moment of the sample will not change with time whereas in an ac measurement the magnetic moment of the sample is changing in response to  $H_{ac}$ . Thus the dynamics of the magnetic system, in principle, can be studied.

### 2.3. High pressure measurements

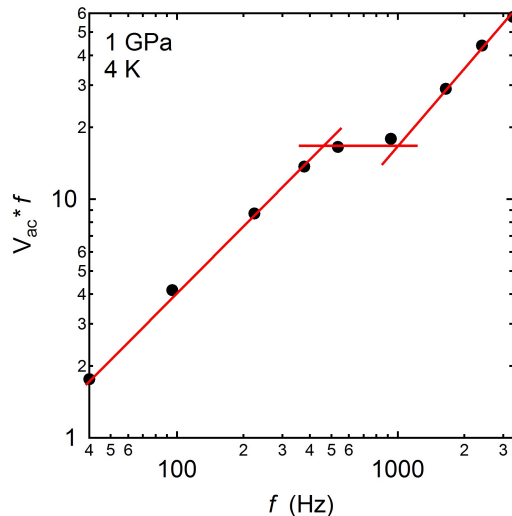


Figure 2.20: *Typical frequency dependence of the signal of the thermocouple multiplied by the frequency in a log-log plot. This example corresponds to the frequency test performed in the ac-calorimetry study in  $\text{YbCu}_2\text{Si}_2$  at 1 GPa and 4 K.*

#### Ac-susceptibility measurement

The technique we use has been adapted from a technique firstly developed in Cambridge [Alireza 2003]. The main problem they encountered was the small sample volume that is available in a DAC which gave a very poor signal-to-noise ratio. This obstacle was solved by placing the detection coil, made of 10 turns with a 12  $\mu\text{m}$  Cu wire, inside the sample chamber as shown in Fig. 2.21. In this way, the filling factor was strongly increased, the background was reduced and so the sensitivity was significantly enhanced allowing the detection of magnetic transitions in materials with weak magnetic moments [Alireza 2003].

In this setup there is no need to make contacts on the sample and at first sight seems easier than the other examples. But the pick-up coil is a tricky stage. It is not easy to wind, is very fragile and can be easily broken during the process of inserting it in the sample chamber. Moreover, it has to be insulated electrically from the gasket and thus some mixture of epoxy and alumina will be placed on the contour of the hole of the gasket. Finally, two grooves are made in the gasket and they are also insulated in order to pass the wires of the coil to avoid that the top diamond breaks them. This coil has to be made each time we load a new sample. On the contrary, the primary coil which has about 300 turns with a 30  $\mu\text{m}$  Cu wire is safely placed around the bottom diamond, under the gasket.

We apply with the Lock-in amplifier an ac-current to the primary coil about 1 mA and with a frequency  $f = 720$  Hz. A magnetic field of about 0.1 mT is generated and it induces a voltage in the pick-up coil that we measured and it is amplified by a factor of  $10^5$ . To simplify the setup, we do not have a compensating coil and thus there is a background contribution which is not well determined. Nevertheless the sensitivity is rather good, for example a superconducting transition represents about 7% of the total signal.

The susceptibility  $\chi$  of the sample is related to the measured voltage,  $e$ , as follows

$$e = \left(\frac{1}{\alpha}\right) V_s 2\pi f H \chi, \quad (2.2)$$

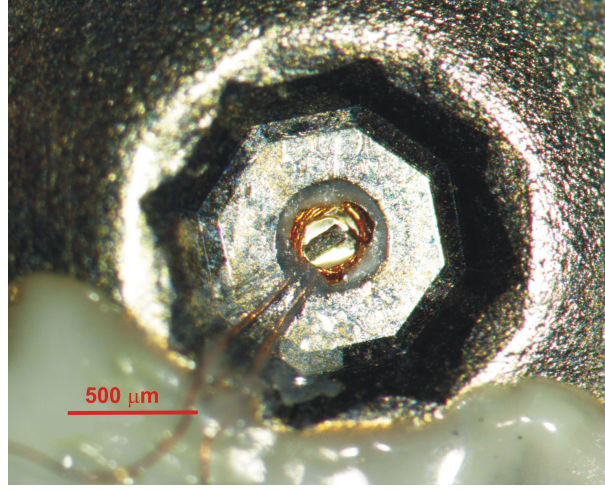


Figure 2.21: *Ac-susceptibility setup: the pick-up coil (10 turns, 12 μm Cu wire) and the sample are inside the pressure chamber.*

where  $\alpha$  is the system calibration coefficient which depends on the characteristics of the pick-up coil as follows

$$\alpha = \frac{\left[\left(\frac{L}{2}\right)^2 + a^2\right]^{1/2}}{(N\pi\mu_0)}, \quad (2.3)$$

$V_s$  is the sample volume,  $H$  the magnetic field,  $f$  the frequency,  $L$  the height of the pick-up coil,  $N$  the number of turns and  $a$  its radius.

As the excitation signal has a frequency  $\omega$ , it can be expressed in a complex notation and also the response signals ( $e$ ,  $\chi$ ):

$$\begin{aligned} \bar{h}(t) &= \bar{h}_0 \exp i\omega t \\ e &= e' + ie'' \propto i\omega \bar{h}(t)(\chi' + i\chi'') \\ e' &\propto \chi'' \\ e'' &\propto \chi', \end{aligned}$$

The signal  $e$  that we measure has two components a real part  $e'$ , the in-phase, and an imaginary part  $e''$ , the out-of-phase contribution, which corresponds to the imaginary and real parts of the susceptibility of the sample respectively. In practice, we use to work and analyze only the imaginary part of the measured signal  $e'' \propto \chi'$ . The detailed principles of this technique are presented in [Guillaume 1999].

### 2.3.4 Magnetization

The Magnetic Property Measurement System (MPMS) from Quantum Design is one of the most currently used Superconducting Quantum Interference Device (SQUID) magnetometers. The MPMS can measure magnetic moments as small as  $10^{-8}$  emu and can measure over a wide range of temperatures (1.9-400K) and magnetic fields (up to  $\pm 7$  T). One of the main constrains for pressure measurements is the reduced sample space which is limited to 9 mm, demanding a big effort on the miniaturization of the pressure cell. Nowadays the use of several piston-cylinder cells up to few GPa is quite extended [Uwatoko 2005, Kamenev 2006]. But our interest was to measure the magnetization of  $\text{YbCu}_2\text{Si}_2$ , whose critical pressure is about 8 GPa, requiring the use of a DAC.

### 2.3. High pressure measurements

Even though its development for commercial SQUID magnetometers is more scarce, there are at least two DAC which achieve pressures above 100 kbars [Easylab , Alireza 2009].

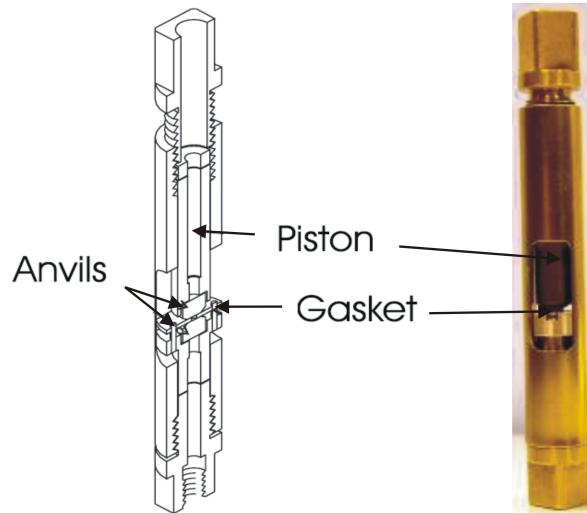


Figure 2.22: (Left) Schematic view of the miniature cell designed for the MPMS [Alireza 2009]. (Right) Actual view of the cell where the piston, the anvils and the gasket are indicated [L-A ].

Magnetization measurements under pressure of  $\text{YbCu}_2\text{Si}_2$  were carried out using a miniature DAC (L-A cell) [Alireza 2009] in a MPMS in collaboration with P.L. Alireza (Cavendish Laboratory, Cambridge). The cell is 8.4 mm in diameter and 64 mm in length. The anvils are made of Moissanite ( $\text{SiC}$ ) which is less hard than diamond and thus easier to break but less expensive, with 0.8 mm culet and they can stand pressures up to 12 GPa. The body of the cell is made of a CuTi alloy instead of the standard BeCu to avoid its ferromagnetic component which requires a demagnetization process. The main advantage of this pressure cell is the low background which allows to detect transitions in the  $10^{-6}$  emu range, one order of magnitude lower than the other model [Easylab ]. For samples with a bigger magnetic moment this difference it is not significant but it turned out to be crucial in our study as the sample signal was lower than  $10^{-5}$  emu as shown in Fig. 2.23 (see details on Chapter 5). The gasket is made of BeCu due to its higher strength. It is pre-indented to  $100 \mu\text{m}$  and the diameter of the pressure chamber is  $350 \mu\text{m}$ . The sample size was  $170 \times 180 \times 60 \mu\text{m}$ . We measured the temperature dependence of the magnetization at different pressures (above and below the critical pressure) at 50 Oe in order to keep the background contribution as low as possible. The pressure was determined via the ruby fluorescence.

These measurements turned out to be more complex than firstly expected because we had to work at the limiting conditions of the MPMS system and the DAC: the transition temperatures are rather low, a few K, and the MPMS can only reach 1.9 K so we could not measure the whole saturation curve. The signal of the sample was very small and the background removal process was not easy. Measuring the magnetization as a function of the magnetic field would have been very desirable but as the background of the DAC is field dependent and the signal of the sample was so weak the results we got were not conclusive because even after extracting as carefully as possible the background we observed hysteresis curves above and below the magnetic temperature transition, indicating that there was still a background contribution mainly due to the CuBe gasket.

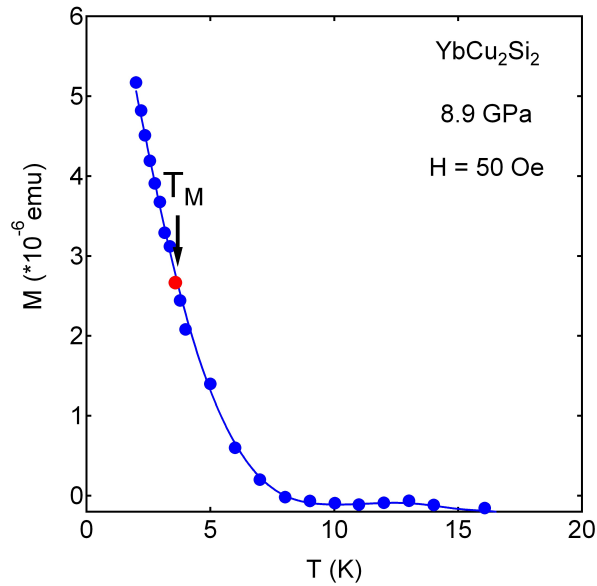


Figure 2.23: Magnetization at 8.9 GPa of  $\text{YbCu}_2\text{Si}_2$  measured at 50 Oe. The red point corresponds to the magnetic temperature transition at this pressure taken from [Fernandez-Pañella 2011].

## 2.4 X-ray spectroscopic measurements

### X-rays

X-rays are a powerful tool to study the structural and electronic properties of a wide variety of materials in condensed matter physics as their wavelengths are the same order of magnitude as the typical interatomic distances in solids, a few ångströms. “Soft X-rays” are usually considered in the range of 0.1-2 keV whereas “hard x-rays” would start above 4-5 keV. The region in between is sometimes called “tender x-ray”.

When a solid sample is illuminated by a X-ray beam of intensity  $I_0$  several processes take place. In general, one observes that the transmitted intensity  $I$  has been attenuated after the beam has crossed the sample. Some of the processes that contributes to this attenuation are summarized in figure 2.24:

The transmitted intensity can be related with the initial  $I_0$  via the Beer-Lambert law:

$$I = I_0 \exp(-\mu x \rho),$$

where  $x$  is the thickness of the sample,  $\rho$  is its density and  $\mu$  is the absorption cross section which depends on the energy and polarization of the incident beam.

### 2.4.1 Valence measurement under extreme conditions

The development of third-generation synchrotron radiation sources with extremely high-brilliance light have permitted the development of spectroscopic techniques like resonant inelastic x-ray spectroscopy (RIXS)<sup>11</sup>.

<sup>11</sup>The intensity of inelastic scattering processes is much weaker than for elastic (Rayleigh) scattering.

## 2.4. X-ray spectroscopic measurements

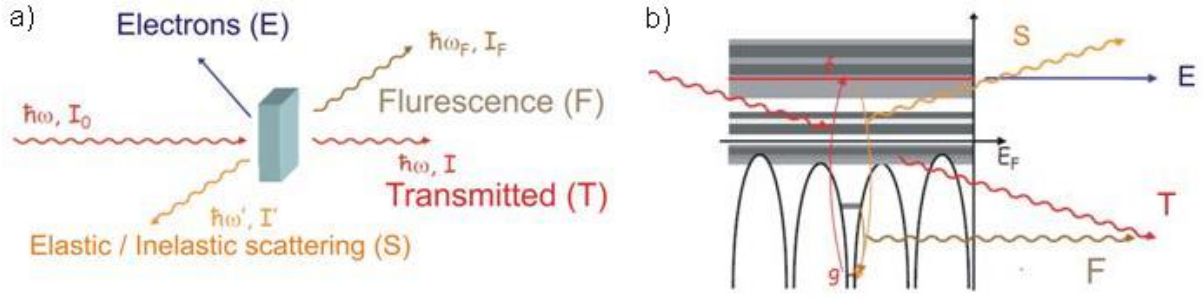


Figure 2.24: a) Some of the processes that take place when a solid is illuminated by a X-ray beam. b) A microscopic view: when a photon with energy  $h\nu$  is absorbed, a core electron is excited from an initial state  $g$  to an empty final state  $f$  above or at the valence band. The different detection modes: measuring the secondary electrons, transmission, elastic/inelastic scattering and fluorescence are related to the transition probability between  $f$  and  $g$ . If we take into account multielectronic processes this scheme becomes more complex (From [Joly 2011]).

RIXS is a photon-in/photon-out, bulk sensitive <sup>12</sup> technique where a core electron is excited by an incident photon with energy  $h\nu_{in}$  and then this excited state decays radiatively by emitting a photon to fill the core hole. RIXS is element and orbital specific. Figure 2.25 shows the energy level scheme for the case of a mixed-valent Yb ion where the relevant transitions in x-ray absorption spectroscopy (XAS) and RIXS are indicated with arrows. The final states in XAS correspond to the intermediate state in RIXS [Dallera 2002, Rueff 2007]. The degeneracy of the initial mixed-valent state  $|g\rangle = c_0 |f^{13}\rangle + c_1 |f^{14}\rangle$  is lifted in the RIXS intermediate states. By tuning the incident energy to a particular intermediate state (in our case, in presence of a  $2p$  core hole), one of the multiple  $f$ -states can be specifically enhanced through resonance [Rueff 2007].

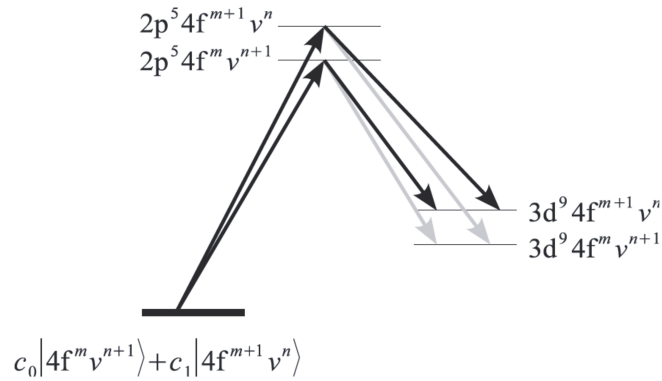


Figure 2.25: Total energy level scheme for an Yb ion in  $YbCu_2Si_2$  in XAS and RIXS. Those in light grey indicate less probable transitions (from [Rueff 2007]). Here the chosen resonance is at the  $L_3$ -edge ( $2p \rightarrow 5d$ ) of the Yb ion and the emission line is the  $L_{\alpha_1}$  ( $3d \rightarrow 2p$ ).

The spectroscopic measurements under extreme conditions (high pressure and low temperature), were performed in collaboration with J. P. Rueff (Synchrotron SOLEIL and CNRS, Paris) and V. Balédent (Synchrotron SOLEIL, Paris) at the ID 16 beam line of the European Synchrotron

<sup>12</sup>The penetration depth is about several  $\mu\text{m}$ .

Radiation Facility (ESRF, Grenoble). The undulator beam was monochromatized with a pair of Si(111) crystals and focused to a size of  $40 \mu\text{m}$  (vertical) and  $100 \mu\text{m}$  (horizontal) at the sample position. The scattered x-rays were analyzed by a Rowland circle spectrometer equipped with a spherically bent Si (620) crystal. The energy resolution was about 1.5 eV. A sample about  $20 \mu\text{m}$  thick was loaded in a membrane-driven diamond anvil cell (DAC) with silicon oil as a pressure transmitting medium. The DAC was mounted in a helium circulation cryostat for low-temperature measurements. The lowest temperature achieved was 7 K. Pressure was estimated from the fluorescence of a ruby chip placed in the sample chamber.

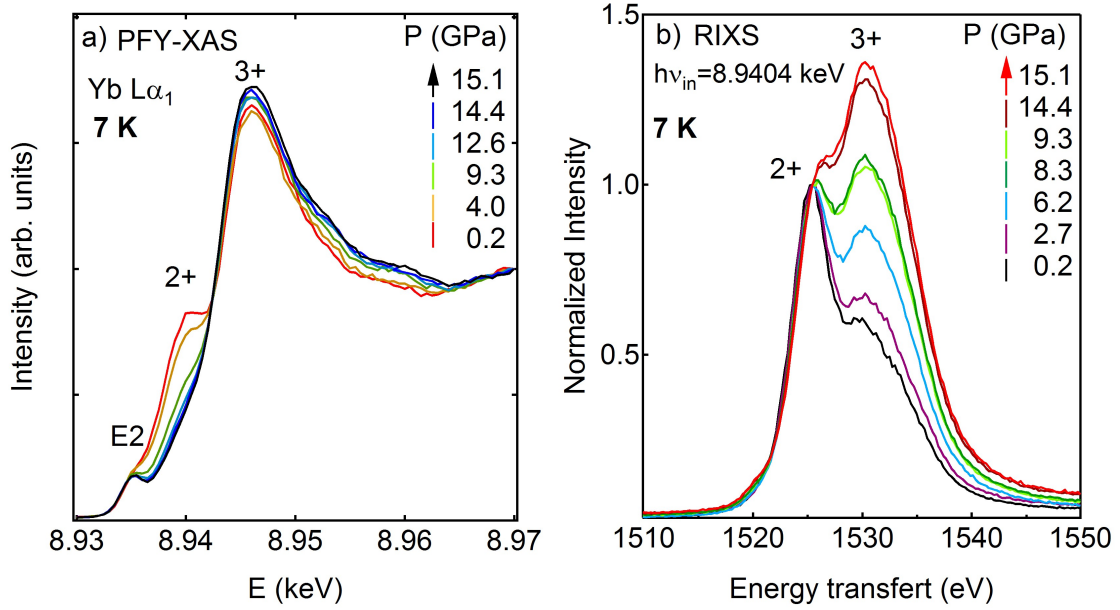


Figure 2.26: a) PFY spectra at 7 K and for selected pressures recorded at the Yb  $L\alpha_1$  line. b) RIXS spectra at 7 K at the resonance of the  $\text{Yb}^{2+}$  component ( $h\nu_{in} = 8.9404 \text{ keV}$ ) and normalized at the maximum of the  $\text{Yb}^{2+}$  intensity.

In figure 2.26 the x-ray absorption (XAS) spectra at 7 K and for several pressures measured at the Yb  $L_3$  edge and recorded in the partial fluorescence yield (PFY) mode<sup>13</sup> at the Yb  $L\alpha_1$ <sup>14</sup> are shown. In figure 2.26 b) there are summarized the RIXS spectra measured at the  $\text{Yb}^{2+}$  resonance ( $h\nu_{in} = 8.9404 \text{ keV}$ ) at selected pressures and also at 7 K. They were normalized at the intensity of the  $\text{Yb}^{2+}$  intensity to enhance spectral changes. The two main features peaking at an energy transfer,  $E_t = h\nu_{in} - h\nu_{out}$  of 1525.5 and 1530.5 eV respectively, correspond to transitions from the  $\text{Yb}^{2+}$  and  $\text{Yb}^{3+}$  component. The advantage of selectively enhance either the  $\text{Yb}^{2+}$  or  $\text{Yb}^{3+}$  component is that the measured spectra have simpler line shapes compared to the XAS spectra. Thus, they provide a higher accuracy in the estimation of the valence [Fernandez-Pañella 2012].

#### 2.4.2 Valence measurement under magnetic field

In order to better understand the origin of the magnetic field effects in the physical properties of heavy fermions compounds like metamagnetism in  $\text{YbCo}_2\text{Zn}_{20}$  or the field-induced QCP in

<sup>13</sup>In the total fluorescence yield (TFY) mode it is recorded the integrated scattered intensity in function of  $h\nu_{in}$ , which is varied across an absorption edge. When only one radiative decay channel is observed as in PFY all the spectra features are better resolved. (See more details in [Dallera 2002, Rueff 2007]).

<sup>14</sup>In order to reduce lifetime broadening effects and to sharpen spectroscopic features.

## 2.4. X-ray spectroscopic measurements

$\text{YbRh}_2\text{Si}_2$  and especially, if they are related to the valent degrees of freedom, we performed X-ray absorption spectroscopic measurements as a function of temperature and magnetic field at 10 T in ID 20 at the ESRF (Grenoble, France) in collaboration with J. P. Rueff, V. Balédent and L. Paolasini. The energy of the x-rays in ID20 was between 3.5 to 12 keV. Thus, the  $K$  and  $L$  edges of transition metals, rare earth elements and also uranium are accessible. The resolution in energy was about  $10^{-4}$  eV.

We measured the  $L_3$  edge XAS spectra in the fluorescence mode for 8 different heavy fermion single crystals:  $\text{YbCu}_2\text{Si}_2$  ( $H \parallel c$ ),  $\text{YbRh}_2\text{Si}_2$  ( $H \parallel a$ ),  $\text{YbCo}_2\text{Zn}_{20}$ ,  $\text{YbIr}_2\text{Zn}_{20}$ , SmS (gold), SmS (black),  $\text{CeCu}_2\text{Si}_2$ ,  $\text{CeCoIn}_5$  and  $\text{CeRhIn}_5$ . The  $L_3$  edge for the Yb ion is located at an energy  $E = 8.943$  keV, for Ce at  $E = 5.723$  keV and for Sm at  $E = 6.716$ .

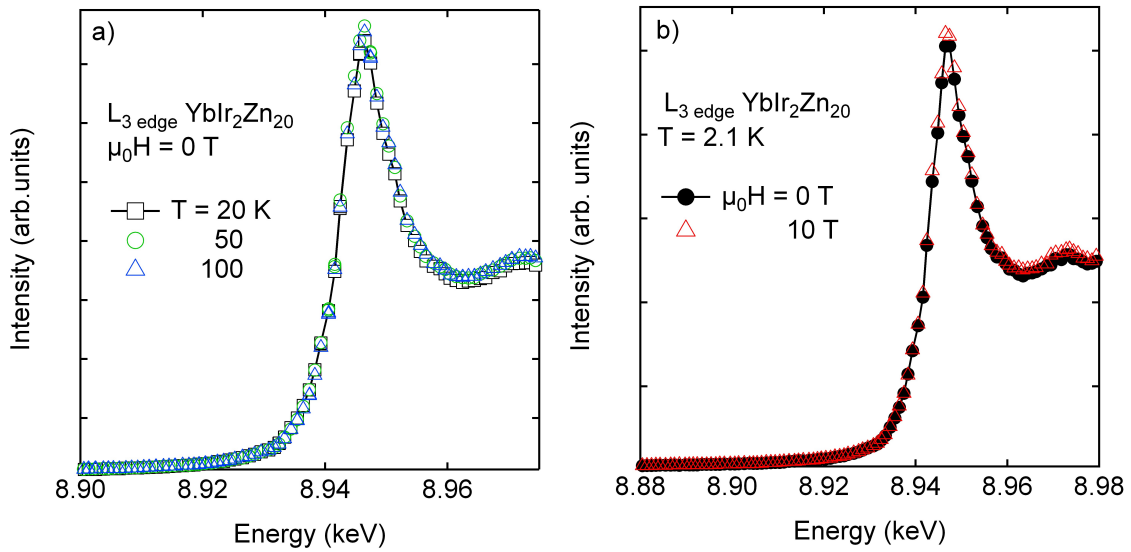


Figure 2.27: XAS spectra a) at different temperatures and zero field b) at zero field and 10 T at 2.1 K at the  $L_3$  edge in  $\text{YbIr}_2\text{Zn}_{20}$ .

In figure 2.27 the XAS spectra at different temperatures (a), and at zero field and 10 T at 2.1 K (b) in  $\text{YbIr}_2\text{Zn}_{20}$  are shown. The main peak centered at  $E = 8.9448$  keV corresponds to  $\text{Yb}^{3+}$  and the weak feature at around  $E = 8.939$  keV corresponds to  $\text{Yb}^{2+}$ . There are no perceptible changes in the line shapes when the temperature is decreased or when the magnetic field is applied. Similar results were obtained for SmS,  $\text{CeCu}_2\text{Si}_2$ ,  $\text{CeCoIn}_5$  and  $\text{CeRhIn}_5$  (not shown here). The spectra of  $\text{YbCu}_2\text{Si}_2$ ,  $\text{YbRh}_2\text{Si}_2$  and  $\text{YbCo}_2\text{Zn}_{20}$  will be shown in the respective chapters but we can anticipate that the magnetic field has no significant effects on the valence in any of these compounds.

# CHAPTER 3

## YbCu<sub>2</sub>Si<sub>2</sub>

### Contents

<b>3.1</b>	<b>Introduction</b>	<b>61</b>
<b>3.2</b>	<b><math>P - T</math> Phase diagram - comparison with previously reported data</b>	<b>64</b>
<b>3.3</b>	<b>Nature of the pressure-induced magnetic order</b>	<b>69</b>
<b>3.4</b>	<b>Metamagnetism</b>	<b>75</b>
<b>3.5</b>	<b>Fermi-Liquid studies throughout the P-T-H phase diagram</b>	<b>80</b>
<b>3.6</b>	<b>Interplay of magnetism and valence change</b>	<b>83</b>
<b>3.7</b>	<b>Conclusions</b>	<b>88</b>

### 3.1 Introduction

YbCu<sub>2</sub>Si<sub>2</sub> is a well known intermediate-valence compound and a moderate heavy fermion,  $\gamma \approx 150 \text{ mJ}/(\text{K}^2\text{mol})$ <sup>1</sup> (figure 4.4 a)) [Dung 2009], with the ThCr<sub>2</sub>Si<sub>2</sub>-type tetragonal crystal structure as shown in figure 4.1. The lattice parameters are  $a = 3.9237(3) \text{ \AA}$  and  $c = 9.9908(13) \text{ \AA}$ . Its valence at low temperature is about 2.8 and increases near 2.9 at room temperature [Lawrence 1994, Moreschini 2007].

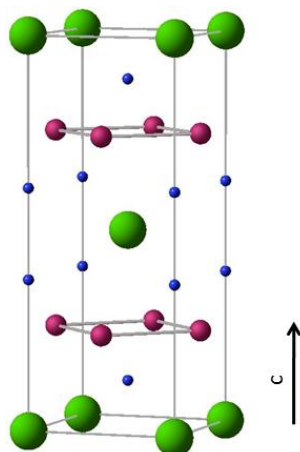


Figure 3.1: *Crystal structure of YbCu<sub>2</sub>Si<sub>2</sub>. The green, fuchsia and blue spheres correspond to Yb, Cu and Si ions respectively.*

The magnetic entropy,  $S_{mag}$ , is shown in figure 3.2 b).  $S_{mag}$  gradually increases with temperature and it reaches the value of  $R \ln 2$  corresponding to the doublet ground state with  $S =$

<sup>1</sup>This value was reported recently in [Dung 2009]. A value slightly weaker  $\gamma \approx 135 \text{ mJ}/(\text{K}^2\text{mol})$  was obtained in other studies [Sales 1976, Colombier 2008].

### 3.1. Introduction

$1/2$ ,  $N = 2$  around 40 K, which is consistent with a Kondo temperature of 50-60 K estimated from the neutron quasi-elastic line width which is about 4-5 meV [Holland-Moritz 1982].

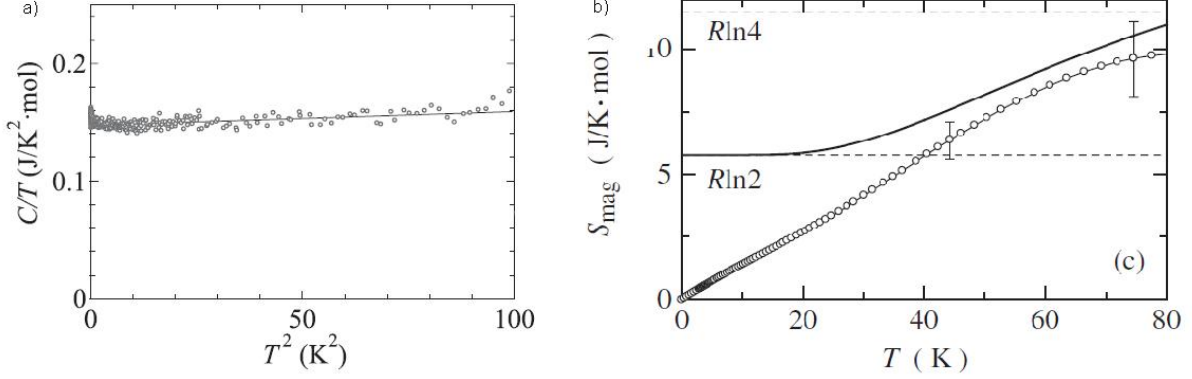


Figure 3.2: a)  $T^2$ -dependence of the specific heat expressed in the form  $C/T$  for  $\text{YbCu}_2\text{Si}_2$  [Dung 2009]. b) Temperature dependence of the magnetic entropy  $S_{\text{mag}}$  [Takeda 2008].

The susceptibility (figure 3.3) is quite anisotropic, reflecting the tetragonal structure. At high temperatures, it follows a Curie-Weiss law above 200 K with an effective magnetic moment  $\mu_{\text{eff}} = 4.47\mu_B/\text{Yb}$  very close to the free moment of  $\text{Yb}^{3+}$ ,  $\mu_{\text{eff}} = 4.54\mu_B$  [Dung 2009]. The susceptibility shows a maximum around 40 K for  $H \parallel [100]$  and it becomes almost temperature independent below 10 K for  $H \parallel [100]$  and  $H \parallel [001]$ . This is consistent with the onset of the Kondo effect at low temperatures where  $f$ -electrons become itinerant and heavy quasiparticles are developed below  $T_{\chi_{\text{Max}}} \approx 40$  K which approximately corresponds to  $T_K$ .

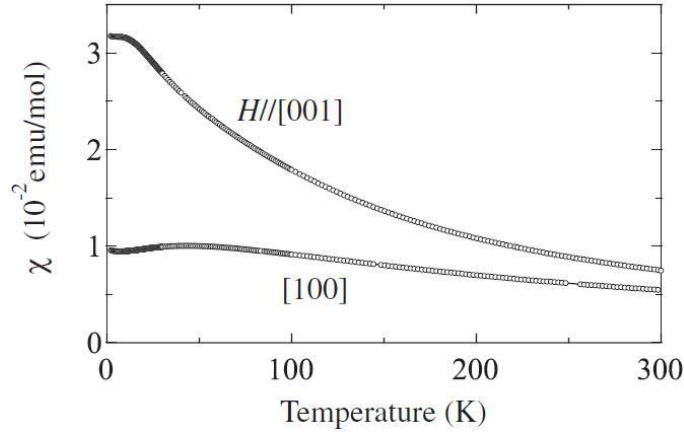


Figure 3.3: Temperature dependence of the magnetic susceptibility in  $\text{YbCu}_2\text{Si}_2$  for  $H \langle 100 \rangle$  and  $H \langle 001 \rangle$  [Dung 2009].

Figure 3.4 a) shows the temperature dependence of the electrical resistivity  $\rho$  for the current  $J$  along the  $[100]$  direction measured at the PPMS in two samples.  $\rho(T)$  shows a shoulder at  $T_{\text{Max}} \approx 140$  K and decreases monotonically with decreasing temperature. The resistivity is also anisotropic. The position of  $T_{\text{Max}}$  is significantly higher for the  $[001]$  direction,  $T_{\text{Max}} \approx 200$  K [Colombier 2008]. As previously mentioned,  $T_{\text{Max}}$  is in general considered proportional to  $T_K$ . However, we note that for this system  $T_{\text{Max}}$  also depends on CEF effects. At low temperatures,  $T < 1.8$  K,  $\rho$  follows the FL relation as shown in figure 3.4 b),  $\rho = \rho_0 + AT^2$  with  $\rho_0 = 0.26 \mu\Omega.\text{cm}$

and  $A = 0.054 \mu\Omega.cm/K^2$ . The high quality of the samples is reflected with the residual resistivity ratio:  $RRR = \rho_{300K}/\rho_0$ ,  $RRR = 307$  and  $270$  for sample A112 and A114 respectively.

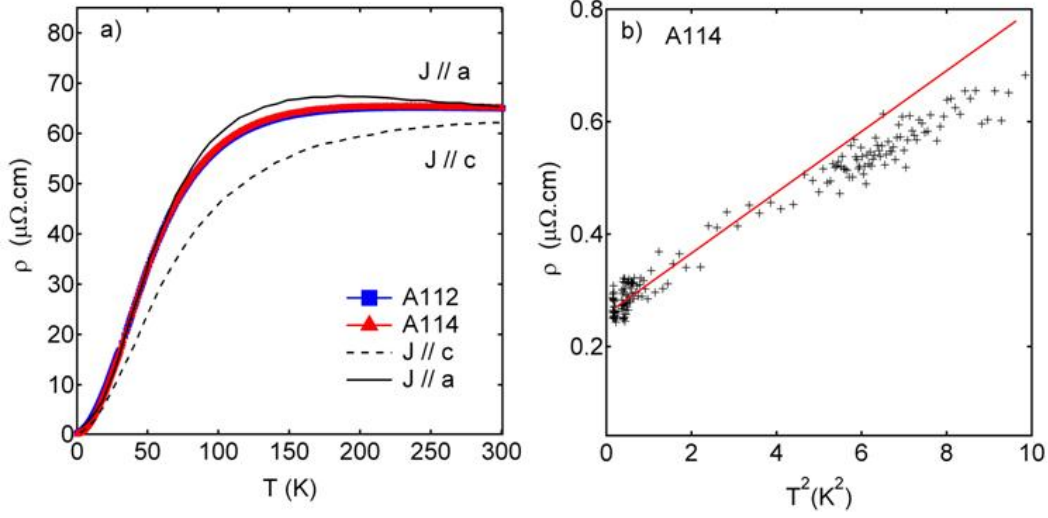


Figure 3.4: a) Temperature dependence of the electrical resistivity in YbCu<sub>2</sub>Si<sub>2</sub> for two different samples A112 (blue curve) and A114 (red curve) used in this work normalized at 65  $\mu\Omega.cm$  at 300 K and with the current  $J$  along the  $[100]$  direction. The solid and the broken black lines correspond to  $\rho(T)$  measured for  $J$  along  $[100]$  and along  $[001]$  respectively as reported in [Colombier 2008]. b)  $T^2$ -dependence at low temperatures for sample A114. The Fermi-liquid relation is verified for  $T < 1.8$  K with  $\rho_0 = 0.26\mu\Omega.cm$  and  $A = 0.054 \mu\Omega.cm/K^2$ .

### Crystal electric field

In the tetragonal crystal field the  $J = 7/2$  Hund's rule ground state splits into four doublets. Five independent parameters are needed to determine the crystal field

$$\mathcal{H}_{CEF}^{tetra} = B_2^0 O_2^0 + B_4^0 O_4^0 + B_6^0 O_6^0 + B_4^4 O_4^4 + B_6^6 O_6^6 \quad (3.1)$$

where  $O_l^m$  are the equivalent Stevens operator and  $B_l^m$  is the set of crystal-field parameters to be determined which can be found via inelastic-neutron scattering experiments.

In figure 5.2 a) and b) are shown the CEF scheme levels deduced by Muzychka [Muzychka 1998] and by Walter *et al.* [Holland-Moritz 1982]. There are slight differences between the energies of the CEF levels, especially in the first excited level which corresponds to a temperature of  $T_{CEF}^1 \approx 130$  K and  $T_{CEF}^1 \approx 190$  K<sup>2</sup> for each scheme respectively. These values are close to the value of  $T_{Max}$ . The overall CEF splitting,  $\Delta_{CEF} \approx 31 - 32$  meV ( $\approx 350$  K), is almost the same in both cases and it is much larger than the CEF splitting (about 100 K) in other RCu<sub>2</sub>Si<sub>2</sub> (R= rare earth) systems with a stable  $4f$ -shell<sup>3</sup>. In general there are three main sources that significantly contribute to the observed crystal splitting: the  $4f$  electron hybridization with conduction electrons, exchange and coulomb interactions with conduction electrons, and the electrical fields due to ionic point charges [Walter 1992]. Thus, the presence of hybridization leads to big differences between the crystal field of a rare-earth ion with a stable or a fluctuating  $4f$  shell ion. This is reflected in the crystal-field parameters of YbCu<sub>2</sub>Si<sub>2</sub>. For example, the fourth-order parameter shows a large anomaly that has

<sup>2</sup>The error in the CEF levels in b) is about 10% [Holland-Moritz 1982].

<sup>3</sup>The IV compound CeCu<sub>2</sub>Si<sub>2</sub> has also an "anomalous" large CEF splitting, about 31 meV [Dung 2009].

### 3.2. $P - T$ Phase diagram - comparison with previously reported data

been related to the hybridization contribution to the CEF potential: in contrast to  $\text{CeCu}_2\text{Si}_2$  where a strong hybridization takes place between the  $4f$  and the Si  $p$  conduction electrons, in  $\text{YbCu}_2\text{Si}_2$  the hybridization takes place between the  $4f$  and the Cu electrons [Muzychka 1998].

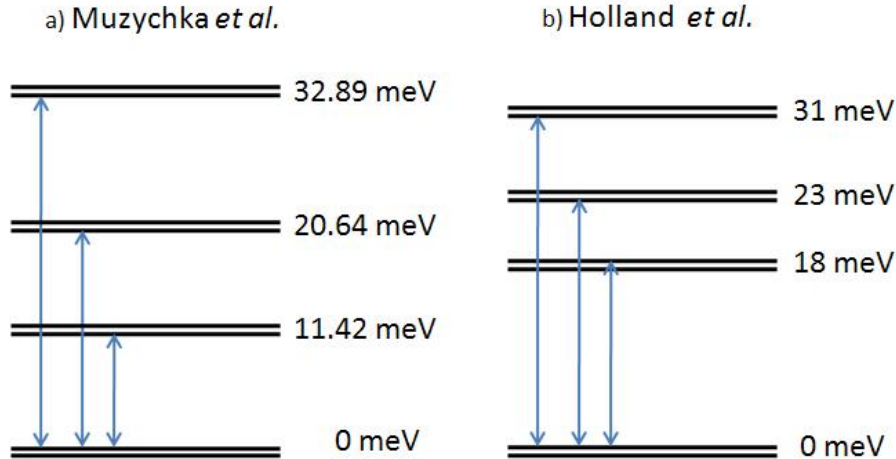


Figure 3.5: Two crystal field schemes for  $\text{YbCu}_2\text{Si}_2$  from inelastic-neutron scattering measurements a) by Muzychka [Muzychka 1998] and b) by Holland-Moritz *et al.* [Holland-Moritz 1982].

### 3.2 $P - T$ Phase diagram - comparison with previously reported data

$\text{YbCu}_2\text{Si}_2$  is a clear example where magnetic order can be induced with pressure. In 1996, Alami Yadri *et al.* observed that a distinctive anomaly appeared in the resistivity curves above 8 GPa which was attributed to the onset of a magnetic order [Yadri 1996, Alami Yadri 1998]. Further studies using Mössbauer spectroscopy [Winkelmann 1999] and micro-calorimetry [Colombier 2009] have all confirmed the presence of long range magnetic order at high pressures.

The work of Alami Yadri *et al.* was performed on polycrystals with a residual resistivity of several  $\mu\Omega.cm$  and in quasi-hydrostatic conditions [Alami Yadri 1998, Winkelmann 1999] up to 25 GPa and down to 300 mK. A few years ago, the first high-purity single crystals were grown in the laboratory, with a  $RRR \approx 120$  and a weak residual resistivity,  $\rho_0 < 0.5 \mu\Omega.cm$ . Colombier *et al.* determined the  $(P - T)$  phase diagram using these high purity single crystals by ac-calorimetry measurements in a DAC up to 11 GPa and down to 1.5 K using the  $^4\text{He}$  pressure *in-situ* device [Colombier 2009].

In this work, we have performed a new set of measurements with a new generation of higher quality single crystals ( $RRR \approx 300$ ,  $\rho_0 = 0.26 \mu\Omega.cm$ ) via ac-calorimetry and ac-susceptibility measurements up to 13 GPa and down to 1.5 K using the  $^4\text{He}$  pressure *in-situ* device, and by resistivity measurements up to 9 GPa and down to 0.04 mK using the *in-situ* pressure tuning device at dilution fridge temperatures.

Several aims motivated these experiments:

- Ac-susceptibility measurements were performed to verify the  $(P - T)$  phase diagram and they were expected to shed some light on the nature of the pressure-induced magnetic order which will be discussed in the next section.

- To measure at very low temperatures in the pressure window  $\Delta P \approx 6 - 8$  GPa, close to the critical pressure  $P_c \approx 8$  GPa, to look for the onset of the magnetic transition because so far magnetism seems to appear suddenly at  $P_c$  and it has not been yet detected below 1 K.
- To look for superconductivity through the whole  $(P - T)$  phase diagram using high-purity single crystals (so far all attempts to find superconductivity have been in vain).
- To study the effect of the magnetic field at very low temperature close to  $P_c$ .

### Ac-calorimetry under pressure

Figure 3.6 a) shows the low-temperature dependence of the ac-calorimetry curves expressed as  $C/T$  at selected pressures. All curves were measured at 730 Hz. Above 7.6 GPa we detect an increase of the signal for  $T < 3$  K. A clear bump appears in the  $C/T$  curves above 8 GPa which we associate to the magnetic transition. Above 10 GPa the peak gets broaden probably because of homogeneity effects inside the sample chamber. Figure 3.6 b) shows the criterion we used to determine the magnetic ordering temperature,  $T_M$ .

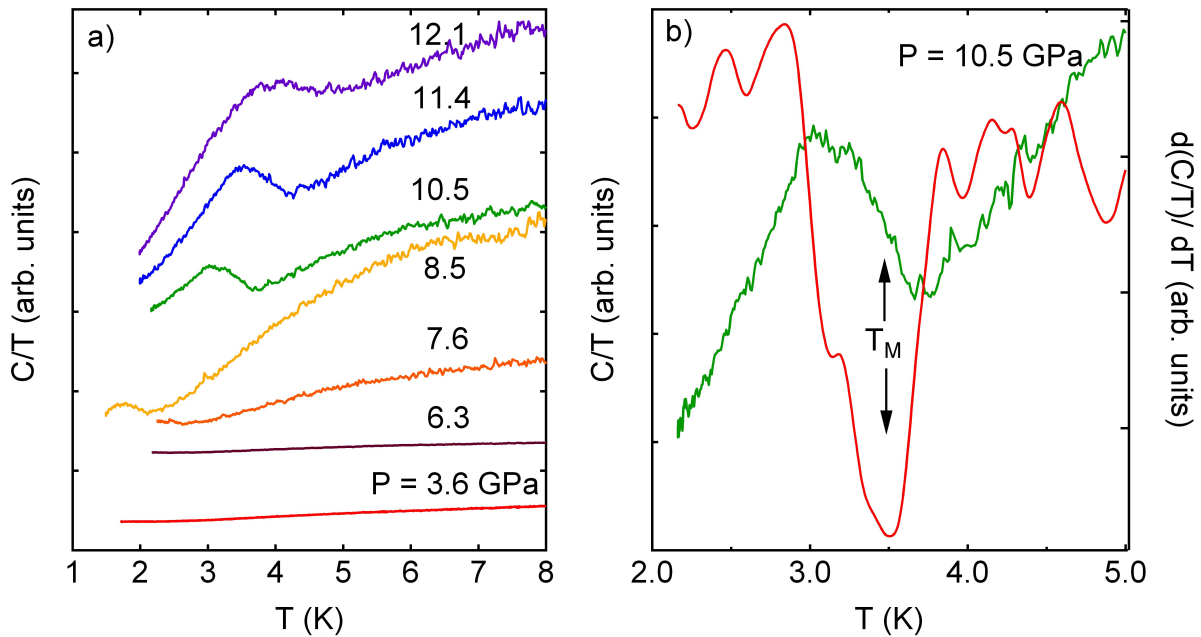


Figure 3.6: a) Low-temperature dependence of ac-calorimetry at selected pressures. b) The criterion used to determine  $T_M$ .

### Ac-susceptibility under pressure

Ac-susceptibility was measured with an ac-field of 0.1 mT generated by the primary coil outside the pressure chamber at a frequency of 721 Hz. The magnetic field was applied parallel to the easy  $c$  axis of magnetization. Figure 3.7 a) shows the low-temperature dependence of the ac-susceptibility,  $\chi'$ , at selected pressures. For pressures above 6.5 GPa we find the onset of an increase of  $\chi'$  for  $T < 4$  K, which again becomes a clear peak for  $P > 8$  GPa corresponding to the magnetic transition which we followed up to nearly 13 GPa. The broadening of the peak and the decreasing intensity of the

### 3.2. $P - T$ Phase diagram - comparison with previously reported data

signal with increasing pressures, especially above 9 GPa, are probably due to a loss of homogeneity as also observed in the ac-calorimetry curves above.

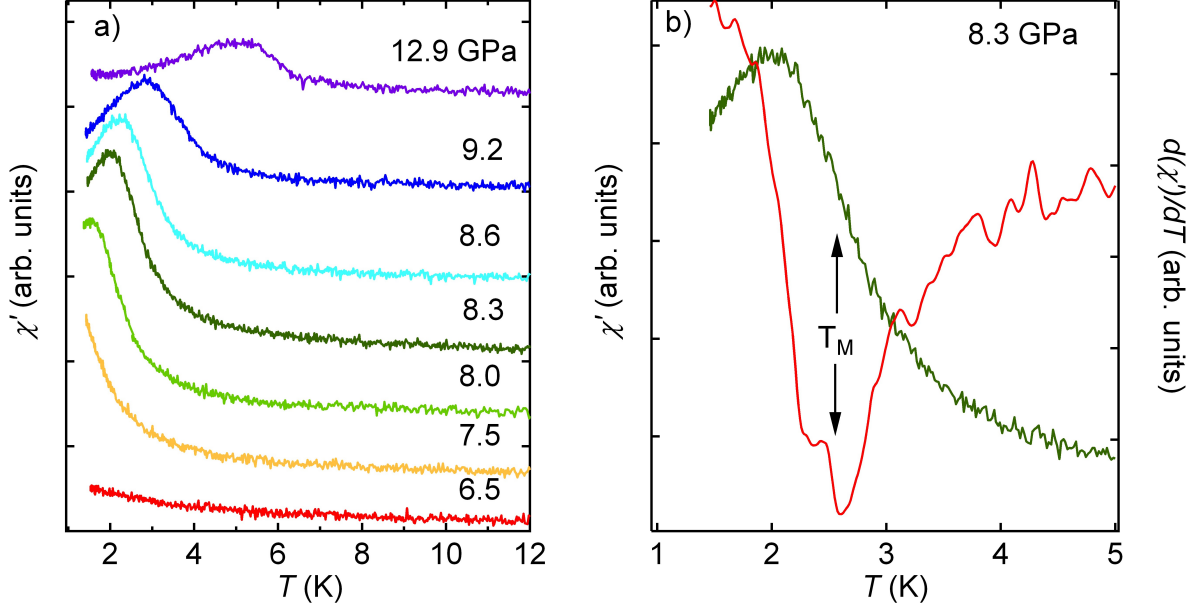


Figure 3.7: a) *Ac-susceptibility versus temperature for different  $P$  below and above the critical pressure,  $P_c \approx 8$  GPa.* b) *The criterion used to determine  $T_M$ .*

### Resistivity under pressure

The electrical resistivity,  $\rho$ , was measured at a frequency of 17 Hz. Figure 3.8 shows the  $\rho$  curves at low temperatures for several pressures up to 9 GPa. A clear kink arises for  $P > 8$  GPa which corresponds to the signature of the magnetic transition.

We have performed a detailed study of the Fermi-liquid behavior under pressure. At low temperatures, in the paramagnetic state, for  $P < P_c$ , a Fermi-Liquid behavior,  $\rho(T) = \rho_0 + AT^2$ , is always found at low temperatures. If the upper interval boundary is extended to higher temperatures, a power law with a smaller exponent ( $n < 2$ ) can be plotted to the data. To determine the Fermi-Liquid temperatures,  $T_{FL}$ , shown in figure 3.9 a), we have plotted  $\rho(T)$  as a function of  $T^2$  and we have fitted the low temperature data with a linear fit.  $T_{FL}$  was taken as the highest temperature of the linear fit before it starts to diverge as indicated in figure 3.9 b).

The Fermi-Liquid region is reduced with increasing pressure when approaching the QCP. In the magnetic ordered phase, the FL behavior is also found at low temperatures. The values of  $T_{FL}$  obtained in this study are in good agreement with those reported in [Alami Yadri 1998] as shown in figure 3.9, except for the value at ambient pressure.

In figure 3.10 the pressure dependence of the  $A$  coefficient and the residual resistivity  $\rho_0$  are shown. They were obtained by fitting the resistivity curves with the  $T^2$  power law using different temperature ranges,  $\Delta T$ . The choice of  $\Delta T$  becomes relevant for  $P > 5$  GPa. Below 5 GPa, we fitted systematically between 40 mK and 500 mK. But above 5 GPa, we reduced the temperature range from 500 mK to 300 mK to not underestimate the  $A$  coefficient. The values of  $\rho_0$  are less sensitive to  $\Delta T$ , so we use the same  $\Delta T$  as for the  $A$  coefficient in each pressure range.

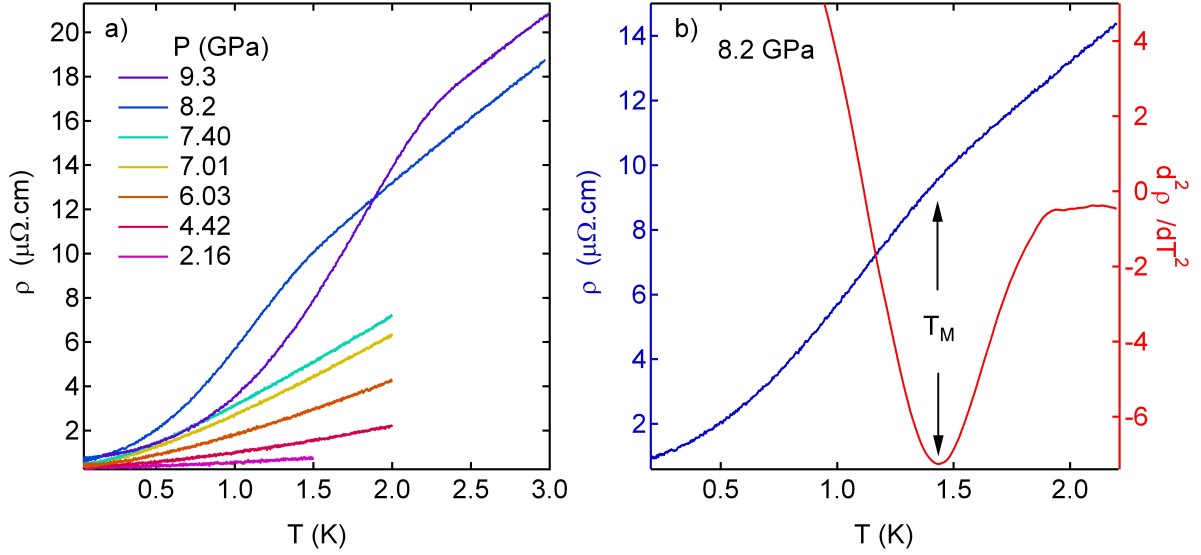


Figure 3.8: a) Temperature dependence of the electrical resistivity,  $\rho$ , at selected pressures below and above  $P_c$ . b) The criterion used to determine  $T_M$ . The blue-left axis corresponds to  $\rho$  and the red-right axis to the  $d^2\rho/dT^2$ . The arrows indicate  $T_M$  for both curves.

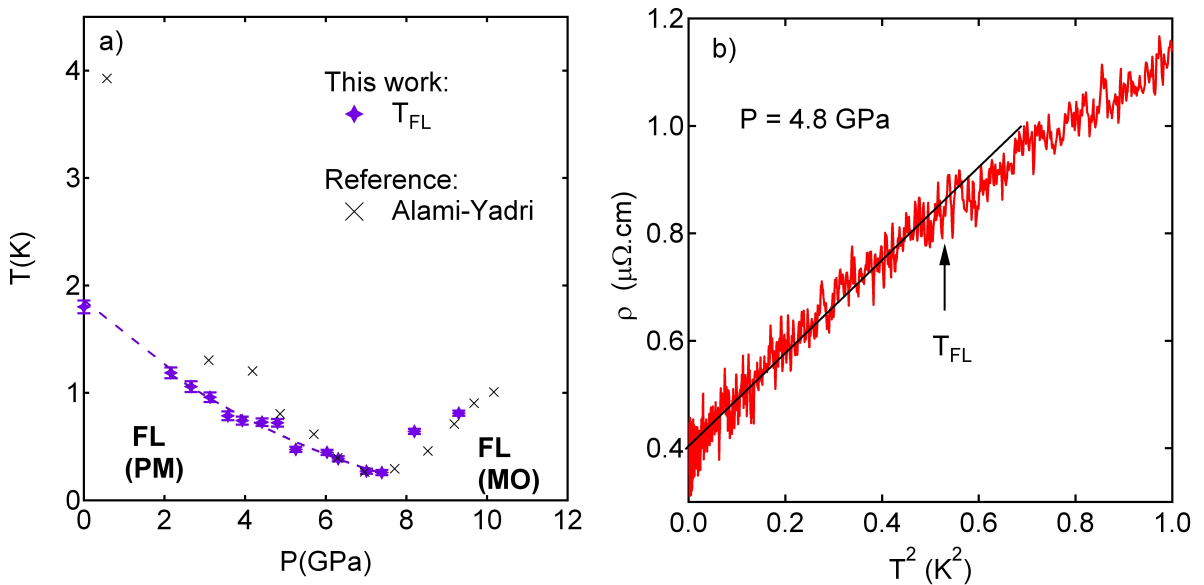


Figure 3.9: a) Pressure dependence of the Fermi-Liquid temperature obtained from the resistivity curves in this work and by [Alami Yadri 1998]. b) For each pressure, here we give an example at 4.8 GPa, we plotted the  $\rho$  as a function of  $T^2$  and we did a linear fit to determine  $T_{FL}$  (indicated by an arrow).

### 3.2. $P - T$ Phase diagram - comparison with previously reported data

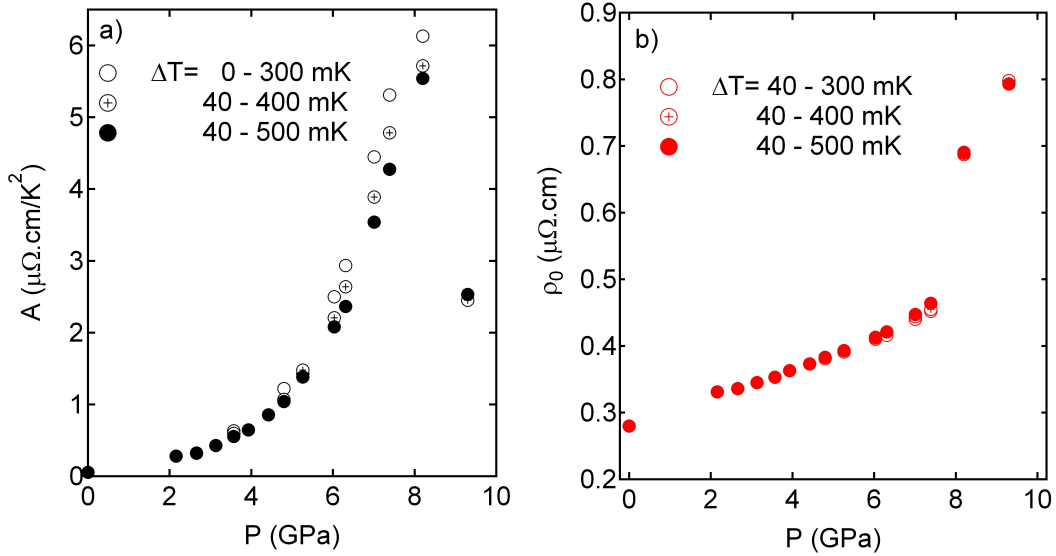


Figure 3.10: Pressure dependence of a) the coefficient  $A$  and b) the residual resistivity  $\rho_0$ . See details in text.

The pressure dependence of the coefficient  $A$  shows a maximum near  $P_c$ .  $A$  strongly increases with pressure: about two orders of magnitude from  $A = 0.054 \mu\Omega.cm/K^2$  (ambient pressure) to  $A = 5.8 \mu\Omega.cm/K^2$  ( $P_c \approx 8$  GPa). Above  $P_c$ , we found that  $A$  decreases in the magnetic ordered state but at 9.3 GPa the value is still rather large,  $A = 2.5 \mu\Omega.cm/K^2$ . This strong increase of  $A$  is often observed in heavy fermions near a magnetic instability due to the presence of strong spin fluctuations.

This enhancement of the coefficient  $A$  by a factor of 100 should correspond to a decrease in  $T_{Max}$  ( $T_K$ ) by a factor of 10 using the relation

$$T_{max} \propto T_K = 1/\sqrt{A} \quad (3.2)$$

which is valid in the FL picture. This value is in good agreement with that from [Alami Yadri 1998]. However, in the cited study  $A$  still increases above  $P_c$  while in the present work it decreases.

The residual resistivity increases smoothly with pressure but above  $P_c$  it is strongly enhanced and in contrast to the coefficient  $A$ , it does not decrease in the magnetic ordered phase but keeps on increasing.

### P-T Phase diagram

The ( $P - T$ ) phase diagram of  $YbCu_2Si_2$  is shown in figure 3.11. Red squares, blues circles and green triangles correspond to  $T_M$  values obtained in this work by ac-susceptibility, ac-calorimetry and resistivity measurements respectively. Black crosses and stars correspond to  $T_M$  values obtained by [Colombier 2009] and [Winkelmann 1999] respectively.

The values of  $T_M$  from the three different techniques (ac-calorimetry, ac-susceptibility and resistivity) are quite similar and in good agreement between them. Curiously, the values obtained via ac-calorimetry in this work are higher than those obtained by [Colombier 2009] measured in similar conditions (i.e., in a DAC with argon as pressure transmitting media in the  $^4He$  pressure *in-situ* device). Maybe the difference is due to sample quality ( $RRR_{this\ work} \approx 300$ ,  $RRR_{Colombier} \approx$

120). However, up to 9 GPa, the values differ about 350 mK, but at higher pressures the discrepancy increases, reaching 800 mK at 11 GPa. This suggests that hydrostatic effects could be related to this discrepancy. Even though we did not measure above 13 GPa, if we extrapolate our values of  $T_M$  to higher pressures, they could agree with those from [Winkelmann 1999] (black stars).

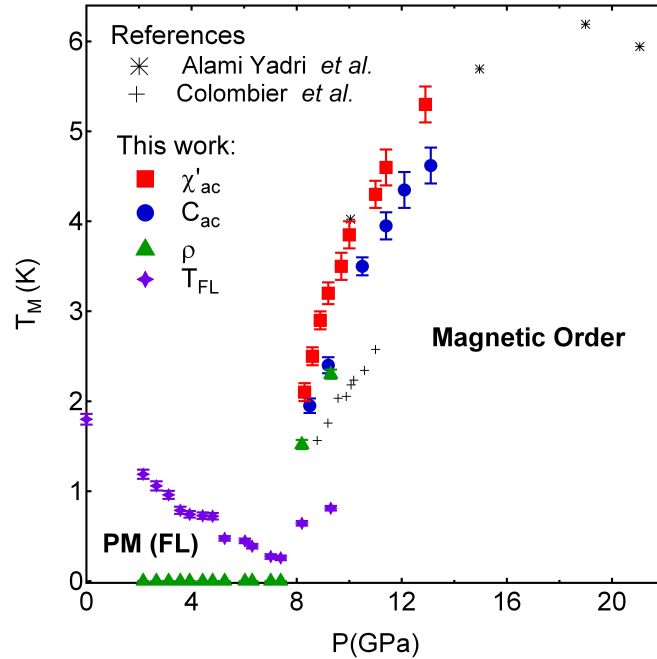


Figure 3.11: Pressure-temperature phase diagram of  $\text{YbCu}_2\text{Si}_2$ . Red squares, blue circles and green triangles correspond to  $T_M$  values obtained in this work by ac-susceptibility, ac-calorimetry and resistivity measurements. Note that the green triangles below  $P_c$  indicate the pressures where we measured  $\rho$  down to 40 mK but no magnetic transition was found.  $T_{FL}$  is also shown (purple symbol). Black stars and crosses correspond to the values of  $T_M$  from [Winkelmann 1999] and [Colombier 2009] respectively.

At first sight, the ( $P-T$ ) phase diagram of  $\text{YbCu}_2\text{Si}_2$  follows the “mirror” image of a Ce system phase diagram, as derived from the Doniach phase diagram discussed in chapter 1. However, there are some significant differences with the phase diagram of its Ce-counterpart,  $\text{CeCu}_2\text{Si}_2$ . First of all, despite the considerable experimental efforts to measure very close to the critical pressure and at low temperatures, we have not detected the transition below 1 K. Magnetic order occurs suddenly, at a pressure of  $P_c \approx 7.5\text{-}8$  GPa and a temperature of about 1.5 K. In fact, the possibility of a first-order transition, in contrast to the second-order transition of the AFM phase in the Doniach phase diagram, was already proposed from Mössbauer results where the coexistence of a magnetic and non-magnetic component was found over a pressure range of several GPa above  $P_c$  [Winkelmann 1999]. This inhomogeneous state could be the cause of the strong increase of  $\rho_0$  at  $P_c$ . Another relevant difference with the phase diagram of  $\text{CeCu}_2\text{Si}_2$  is the absence of superconductivity in  $\text{YbCu}_2\text{Si}_2$  in the whole  $P-T$  phase diagram. At least, down to 40 mK.

### 3.3 Nature of the pressure-induced magnetic order

At the beginning of this thesis, the nature of the pressure-induced magnetic order in  $\text{YbCu}_2\text{Si}_2$  was still an unsolved question because resistivity, calorimetry and Mössbauer studies can not distinguish between antiferromagnetic (AFM) and ferromagnetic (FM) order. Moreover, the critical pressure is

### 3.3. Nature of the pressure-induced magnetic order

too high for neutron scattering measurements, and hence, no direct determination of the magnetic structure is possible. Finally, the ac-susceptibility technique adapted for DACs, firstly developed in Cambridge and afterwards adapted in the laboratory, has succeeded in solving this long lasting question.

As shown previously in figure 3.7, the magnetic transition appears as a peak in the ac-susceptibility. Unlike with a dc-magnetization measurement, distinguishing between a FM and an AFM transition with ac-susceptibility is not as trivial due to irreversibility effects in the FM state as  $\chi'$  can decrease with decreasing temperature below the Curie temperature ( $T_C$ ) and frequently shows a peak as observed in figure 3.12. Indeed a similar effect was seen in  $\text{YbInCu}_4$  [Mito 2007].

In order to determine the nature of the magnetic order we have made an estimation of the absolute value of the susceptibility. This has been done using two methods. First, we calculated the value using estimations of the sample and pick-up coil geometries using equation 2.2 and 2.3 (see chapter 2) with the following parameters:  $f = 721$  Hz,  $V_s = 26.25 \times 10^5 \mu\text{m}^3$ ,  $L \approx 144 \mu\text{m}$ ,  $a \approx 175 \mu\text{m}$ ,  $N = 12$ ,  $H = 86.9$  A/m.

Second, we compared the signal from the sample with the superconducting transition of a Pb sample with the same dimensions in the same set-up. The two methods gave similar results with less than 20% difference.

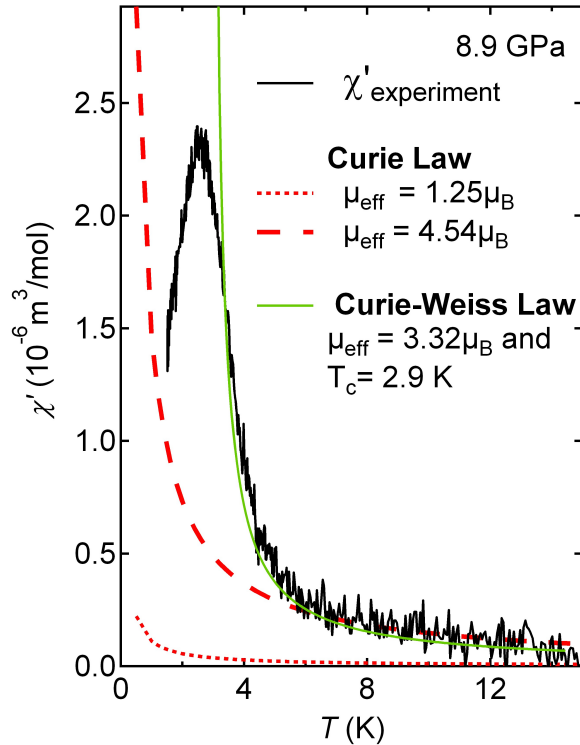


Figure 3.12: Susceptibility at 8.9 GPa compared with expected Curie dependences for:  $\mu_{eff} = 4.54\mu_B$  (dashed line) and  $\mu_{eff} = 1.25\mu_B$  (dotted line).

In figure 3.12 the susceptibility at 8.9 GPa is compared with two Curie laws (red lines) and a Curie-Weiss law (green line). The experimental  $\chi'$  contains an unknown but roughly constant background, so the zero has been taken at the highest temperature measured (15 K). First we compare the experimental curve with the Curie law corresponding to the effective moment of  $\mu_{eff} = 1.25\mu_B$  which was determined experimentally by Mössbauer spectroscopy at a similar

pressure [Winkelmann 1999]. This value is similar to that found in other Yb systems with the tetragonal (ThCr<sub>2</sub>Si<sub>2</sub>) structure showing magnetic order and compatible with the moment expected for Yb<sup>3+</sup> taking into account the effects of the crystalline electric field (CEF) and Kondo screening [Hodges 1987, Bonville 1991, Bonville 1994]. The experimental data show clearly a much larger magnetic signal. In fact, with the present resolution, an AFM system with a moment of  $1\mu_B$  would be lost in the noise, as is probably the case for YbCo<sub>2</sub>Zn<sub>20</sub> (see chapter 4).

We also show the Curie law for an effective magnetic moment corresponding to the theoretical value for the Yb<sup>3+</sup> free ion,  $\mu_{eff} = 4.54\mu_B$ . Even in this case the experimental data still diverges much more quickly than the theoretical curve below 5 K. The agreement of the experimental data above 5 K is probably coincidental and it can also be compatible with a smaller moment and a positive Curie-Weiss temperature. Finally, the green line shows the best fit for this data with a Curie-Weiss law (with  $T_C = 2.9K$  and  $\mu_{eff} = 3.52\mu_B$ ). This value for  $\mu_{eff}$  is surprisingly large. This could be due to a combination of pressure and sample inhomogeneity, and the very strong slope of  $dT_M/dP$ , causing a spread of ordering temperatures within the sample. Nevertheless, all these points strongly lead toward ferromagnetism. Of course from these results we can not exclude a more complex magnetic structure like canted antiferromagnetism as recently suggested in YbInNi<sub>4</sub> [Willers 2011] but we need at least a significant FM component.

### 3.3.1 Ac-susceptibility measurements under magnetic field

Further proof of ferromagnetism is found in the behavior when a small constant magnetic field is superimposed along the *c*-axis. Ac-calorimetry and ac-susceptibility curves for selected pressure around 8.5 GPa are shown in figure 3.13 a) and b) respectively. In both cases, the amplitude of the transition decreases with the application of low magnetic fields but at the same time,  $T_M$  is clearly shifted towards higher values for increasing fields. This trend can be better observed in the phase diagram ( $T_M, H$ ) of figure 3.13 d) where we have plotted the transition temperatures versus the applied magnetic fields. This response, where  $T_C$  increases with field, is consistent with the usual behavior observed in a ferromagnetic system under magnetic field [Willers 2011], in contrast to the usual behavior of an antiferromagnet where  $T_{N\acute{e}el}$  decreases when a magnetic field is applied. Surprisingly, as shown in figure 3.13 c), at 7.5 GPa where no transition is visible down to 1.5 K at zero field we found we could induce a metamagnetic transition by the application of dc fields above 0.2 T. The rapid decrease of the intensity in  $\chi'$  is similar to the effect seen in YbInCu<sub>4</sub> [Mito 2003] and probably mainly reflects the loss of any ac response in the FM state once a single domain has been created with the dc field, as well as the fact that under dc field the transition becomes a crossover as the magnetic field also breaks time-reversal symmetry from a partially to fully polarized state.

### 3.3.2 P-T-H phase diagram

A complete ( $P, H, T$ ) phase diagram of  $T_M$  is shown in figure 3.14. The red points correspond to the values of  $T_M$  at zero field (the values of the ac-susceptibility from the ( $P - T$ ) phase diagram of figure 3.11). The  $T_M$  values under field correspond to the green circles and the values of  $T_M$  for the magnetic-field induced transition at 7.5 GPa are signaled with orange dots. We can observe that the trend of the increase of  $T_M$  under magnetic field at 8.5 GPa is valid for all pressures we measured and simultaneously the transition is rapidly suppressed under field. Interestingly, we find that  $T_M$  does not significantly change for any pressure at very low magnetic fields (up to 0.1 T). We suspect that it could be the field necessary to obtain a single domain and that below this value

### 3.3. Nature of the pressure-induced magnetic order

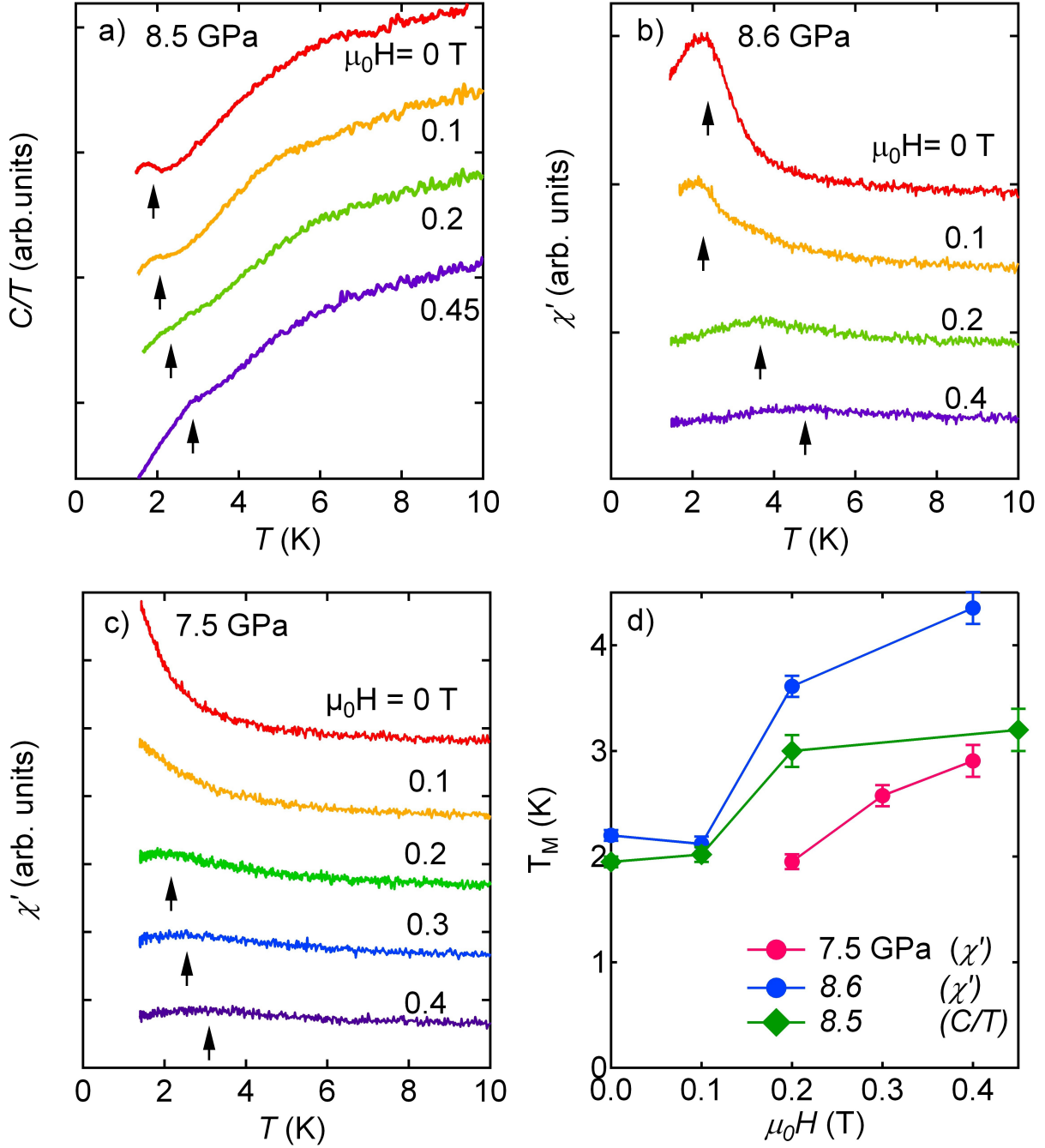


Figure 3.13: Effect of magnetic field a) ac-calorimetry curves at 8.5 GPa and magnetic fields up to 0.45 T. b) Ac-susceptibility as a function of temperature at 8.6 GPa and selected magnetic fields. c) Susceptibility curves at 7.5 GPa under magnetic field. The transition is induced for fields greater than 0.2 T. d) Magnetic field dependence of  $T_M$  near 8.5 GPa (blue and green curves) and 7.5 GPa (fuchsia curve) obtained from specific heat (diamonds) and susceptibility (circles) measurements.

the internal field depends weakly on the applied field. These trends are experimentally consistent with the behavior of a FM system under magnetic field.

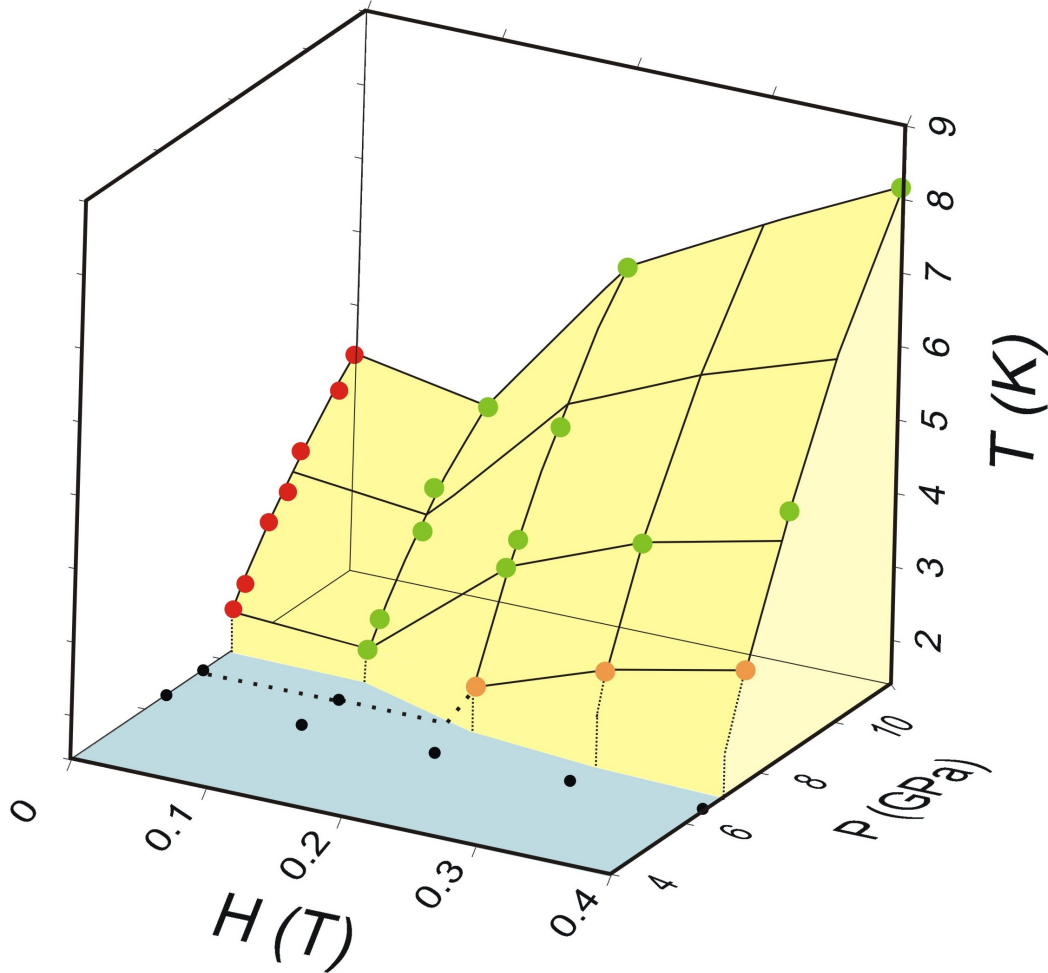


Figure 3.14: Complete phase diagram ( $P, H, T_M$ ) at low-magnetic fields and high pressures. Red and green circles correspond to the values of  $T_M$  at zero field (from 3.11) and under field above the critical pressure respectively. Orange dots are the values of  $T_M$  at 7.5 GPa (from figure 3.13), close to the critical pressure, and the black points indicate where ac-susceptibility curves detected no transition down to 1.5 K.

### 3.3.3 Magnetization measurements under pressure

Magnetization measurements are currently used as a probe for magnetic properties. Nevertheless, performing such measurements under high pressure is still quite challenging from an experimental point of view. In figure 5.11 a) the low-temperature dependence of the magnetization for three different pressures in YbCu<sub>2</sub>Si<sub>2</sub> are shown. We measured at 50 Oe. As it was expected, at ambient pressure, when the system is paramagnetic  $M$  is almost zero. At 7 GPa, close to  $P_c$ , a clear increase in  $M$  is detected for  $T < 6$  K. At 8.9 GPa, above  $P_c$ , the signal starts to increase earlier, for  $T < 7$  K. The relevant point is that below the magnetic ordering temperature at this pressure<sup>4</sup>, the magnetization keeps on increasing. We performed two temperature cycles at each pressure and the values in both measurements (blue squares and circles) are consistent with each other. This is the

<sup>4</sup>The position is marked with an arrow and its value has been taken from the ( $P-T$ ) phase diagram of YbCu<sub>2</sub>Si<sub>2</sub>.

### 3.3. Nature of the pressure-induced magnetic order

behavior expected for a ferromagnetic material in contrast to an antiferromagnetic system, where the magnetization would decrease below  $T_{N\acute{e}el}$ . Unfortunately, we could not measure the whole saturation curve as the magnetic ordering temperatures are very close to the limiting temperature range of the SQUID magnetometer ( $T_{base} \approx 1.8$  K).

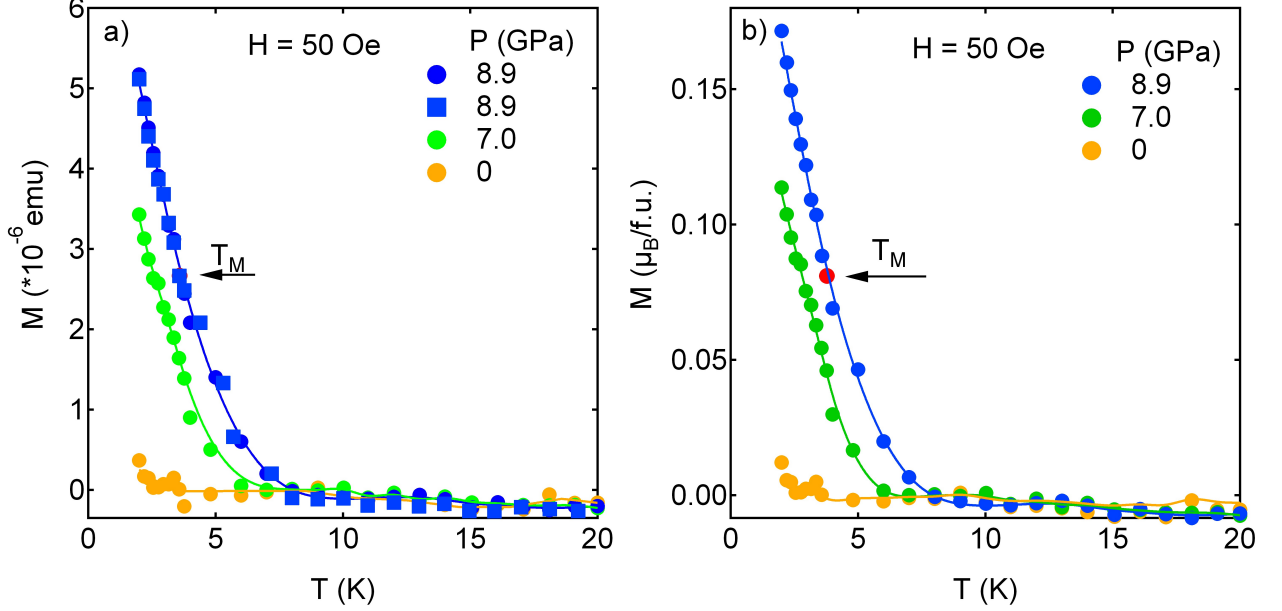


Figure 3.15: *a) Temperature dependence of the magnetization curves for three different pressures: ambient pressure, 7 GPa and 8.9 GPa. b) Here the magnetization is expressed in  $\mu_B$  per formula unit instead of  $emu$ .*

From Mössbauer measurements, Winkelmann *et al.* deduced the magnetic moment of the Yb ion at a similar pressure:  $\mu \approx 1.25\mu_B$  at 8.9 GPa. Assuming that this would be the value that we should obtain in our curve at the same pressure once the magnetization achieves its saturated value, if we express  $M$  in  $\mu_B$  per formula unit instead of  $emu$  we could estimate how far we are from the saturation.

To express  $M$  in  $\mu_B$  we use the following expression:

$$M[\mu_B/f.u.] = M[emu] \times \frac{\bar{M}}{m_{sample} N_{Av} \mu_B} \quad (3.3)$$

where  $\bar{M}$  is the molar mass and  $N_{Av}$  is the Avogadro's Number. As we do not know the  $m_{sample}$  but its dimension, thus its volume,  $V \approx 100 \times 95 \times 50 \mu^3$ , we can make an estimation of  $m_{sample}$  as

$$\begin{aligned} m_{sample} &= \delta \times V, \\ \delta &= \frac{Z\bar{M}}{V_{unit\ cell} N_{Av}}, \end{aligned} \quad (3.4)$$

where  $Z$  is the number of Yb atoms per formula unit and  $V_{unit}$  the unit cell volume.  $YbCu_2Si_2$  has a tetragonal symmetry,  $Z = 2$  and  $V_{unit} = a^2 \times c = 153.8 \times 10^{-24} cm^3$ .

Substituting the  $m_{sample}$  value obtained in eq. 3.4 in eq.3.5 we obtain

$$M[\mu_B/f.u] = M[emu] \times \frac{V_{unit\ cell}}{ZV\mu_B} \quad (3.5)$$

$$M[\mu_B/f.u] \approx 16584 \times M[emu]$$

Figure 5.11 b) shows the magnetization in  $\mu_B$ . Even though the values obtained are an estimation rather than an exact value, we can conclude that we are still far from the estimated saturated magnetization value of  $1.25\mu_B$ . Unfortunately, very few SQUID magnetometers are equipped to measure below the Kelvin range. Finally, we also measured the field dependence of the magnetization at 9.7 GPa at two different temperatures, 1.8 K and 7K, below and above the magnetic ordering temperature, to see any hysteresis behavior. But these measurements were not conclusive because in both curves there was an hysteresis loop. This is due to the difficulty on removing the background contribution which is field dependent to the weak measured signal.

### 3.4 Metamagnetism

In principle, the magnetic field is also a suitable external parameter like pressure to tune the competition between Kondo and RKKY interaction, i.e., to tune the strength of the  $4f$ -conduction electron hybridization. When the Zeeman energy  $g\mu_B H$  becomes comparable to the thermal energy  $k_B T_K$ , the heavy fermion behavior is suppressed and local moment behavior is recovered. Similarly, long-range (AFM) ordering is suppressed when the Zeeman energy is larger than the inter-site coupling strength. Furthermore, applying a magnetic field will introduce a ferromagnetic component to the spin fluctuations. Historically, metamagnetic-like behavior was firstly ascribed to AFM systems but nowadays we talk about metamagnetism when an abrupt non linear increase of the magnetization is observed at a magnetic field  $H_m$ .

Many heavy fermion systems show a metamagnetic-like behavior at a magnetic field  $H_m$  for temperatures  $T < T_{\chi_{max}} \approx T_K$  [Ohya 2010]. For example, YbIr<sub>2</sub>Zn<sub>20</sub>, with a  $T < T_{\chi_{max}} = 7.4$  K metamagnetism is observed at a  $H_m \simeq 100$  kOe [Takeuchi 2010]. In CeRu<sub>2</sub>Si<sub>2</sub>,  $H_m = 80$  kOe ( $T_{\chi_{max}} = 10$  K) [Haen 1987] while in UPt<sub>3</sub>,  $H_m = 200$  kOe and  $T_{\chi_{max}} \approx 20$  K [Sugiyama 1999]. As a general rule, the higher  $T_{\chi_{max}}$  the greater magnetic field is required to observe metamagnetism. Moreover, the ac-susceptibility curves at 7.5 GPa showed that we could induce the magnetic transition by applying weak magnetic fields. This finding motivated us to look for metamagnetism in YbCu<sub>2</sub>Si<sub>2</sub> at ambient pressure and for pressures below  $P_c$ . However, in YbCu<sub>2</sub>Si<sub>2</sub>,  $T_{\chi_{max}} \approx 40$  K (for  $H \parallel [100]$ , see figure 3.3). From the former examples we expect that metamagnetism, if it takes place, will require magnetic fields above  $H > 200$  kOe  $\approx 20$  T.

In the literature there are no reported studies in such high magnetic fields in YbCu<sub>2</sub>Si<sub>2</sub> so far. In the next paragraphs we show the results of two experiments. The first one was carried out at the LNCMI (Toulouse, France) in the high magnetic pulsed facility where we measured the magnetization at ambient pressure up to 53 T and the second was carried out at the LNCMI (Grenoble, France) where we measured the resistivity under pressure (for  $P < P_c$ ) at constant fields up to 28 T.

#### 3.4.1 Magnetization at high magnetic fields

Figure 3.16 shows the field dependence of the magnetization of YbCu<sub>2</sub>Si<sub>2</sub> for  $H \parallel c$  up to 53 T, at ambient pressure and at low temperatures, for  $T < T_{\chi_{max}}$ .

### 3.4. Metamagnetism

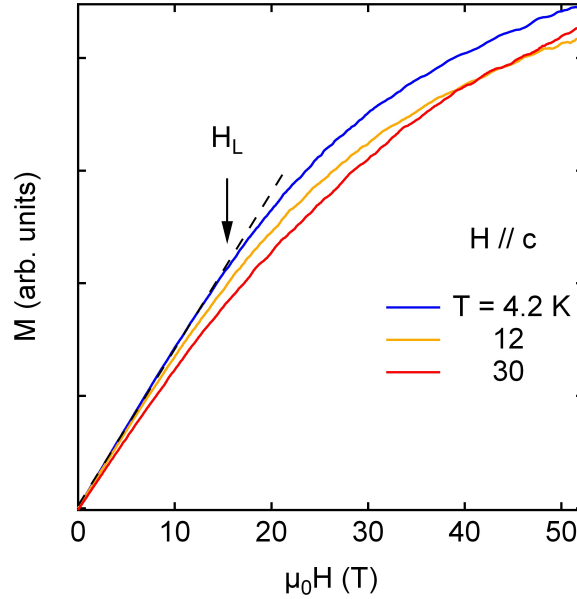


Figure 3.16: *Field dependence of the magnetization of  $\text{YbCu}_2\text{Si}_2$  up to 53 T for three different temperatures: 4, 12 and 30 K for  $H \parallel c$ .*

Initially the magnetization increases linearly up to  $H_L \approx 15$  T at 4 K (indicated by a dashed black curve). With increasing temperature the linear dependence is slightly reduced to  $H_L \approx 11$  T at 30 K. Above  $H_L$ ,  $M(H)$  keeps on increasing continuously with the applied magnetic field without any anomaly or sudden increase for all temperatures. Thus, no metamagnetic-like behavior is detected at least up to 53 T for  $H \parallel c$  at ambient pressure. However, we can not exclude the possibility that metamagnetism could appear at even higher magnetic fields or when the magnetic field would be applied along [100] which is the direction where  $T_{\chi_{max}} \approx 40$  K is observed in the susceptibility curve (figure 3.3). If we apply the experimental relation in  $\text{YbCu}_2\text{Si}_2$  between  $H_m$ , the metamagnetic field, and  $T_{\chi_{max}}$  proposed by Takeuchi *et al.* for heavy fermion compounds [Takeuchi 2011a]

$$H_m(kOe) = 15T_{\chi_{max}}(K) \quad (3.6)$$

we obtained a value of  $H_m \approx 600 kOe = 60 T$ . This value should be taken only as an estimation, not an exact value, but it suggests that 50 T is indeed not enough to detect metamagnetism in  $\text{YbCu}_2\text{Si}_2$ . Only a few facilities, LNCMI (Toulouse), Los Alamos National Laboratory and Dresden High Magnetic Field laboratory can reach, in the present, higher non-destructive pulsed fields, up to 82 (pulse duration,  $t_p = 300$  ms), 100 T ( $t_p = 20$  ms) and 90 T ( $t_s = 10$  ms) respectively. So the door to detect metamagnetic-like behavior in  $\text{YbCu}_2\text{Si}_2$  is not definitively closed.

#### 3.4.2 Magneto-resistivity under pressure

##### Pressures below $P_c$

We have not detected metamagnetism at ambient pressure at least up to 52 T. However, in the ac-susceptibility measurements a metamagnetic-like transition was induced at 7.5 GPa (very close but slightly below  $P_c$ ) by applying a weak magnetic field of 0.2 T (see figure 3.13). So we did not

give up and we looked again for metamagnetic signatures but this time in the resistivity under pressure (for  $P < P_c$ ) and under high magnetic fields up to 28 T.

Figure 3.17 a)-e) shows the magnetoresistivity curves normalized at the value at zero field,  $\rho(H)/\rho(0)$ , for different temperatures and for several pressures. In order to examine a single ion scaling relation, as it is the case for several heavy fermions such YbNi<sub>2</sub>Ge<sub>2</sub> ([Knebel 2001] and YbCo<sub>2</sub>Zn<sub>20</sub> [Saiga 2009], we have plotted  $\rho(H)/\rho(0)$  as a function of  $H/(T + T^*)$ . We did not find a value of the characteristic temperature  $T^*$  that could scale on a single curve all the  $\rho(H)/\rho(0)$  curves for any of the pressures. Figure 3.17 f) shows the best fit we found among all the pressures which corresponds to  $T^* = 1$  K at 6.1 GPa. Even in this case, the scaling is still not unique. The failure of the Kondo scaling is somehow not surprising if we bring to mind that YbCu<sub>2</sub>Si<sub>2</sub> is at low pressures in an intermediate valence regime ( $n_h < 1$ ) whereas YbCo<sub>2</sub>Zn<sub>20</sub> is already trivalent (see chapter 4) with  $n_h \approx 1$ . As pressure increases  $n_h$  also increases, the Yb ion tends to the Yb<sup>3+</sup> state and the Kondo regime will be reached at some point. From these results, we might infer that YbCu<sub>2</sub>Si<sub>2</sub> is still in an intermediate-valence regime up to at least 6 GPa.

At low pressures, 1.2 and 2.0 GPa, decreasing the temperature tends to smear out the large bump observed for  $T > 4$  K in  $\rho(H)/\rho(0)$  centered at 12 T and 7 T for 1.2 and 2.0 GPa, respectively. So, at low pressures, lowering the temperature favors a positive magnetoresistance.

At intermediate pressures, 3.0 and 3.9 GPa, the pressure dependence of the magnetoresistivity gets more complex. The bump observed at low pressures now is very pronounced and it has shifted to lower magnetic fields, at  $H_b \approx 4.4$  T (3.0 GPa) and 2 T (3.9 GPa). The position of the maximum of this bump is weakly temperature dependent. Only above 6 K it shifts to higher field values, up to 5.7 T (3.0 GPa). We can differentiate three different field-dependent regions in  $\rho(H)/\rho(0)$ : at low fields,  $H < H_b$  the magnetoresistivity is positive. Above  $H_b$  it becomes negative and again positive at higher magnetic fields (12-15 T). Pressure tends to shift the bump to lower magnetic fields, hence, reducing the region of positive magnetoresistivity and at 6.1 GPa, we observe a negative magnetoresistivity up to 7-15 T depending on the temperature. The positive magnetoresistivity at high magnetic fields is recovered for all pressures we measured and independently of the temperature.

In figure 3.18 we have plotted the magnetoresistivity,  $\rho(H)$ , as a function of pressure for three selected temperatures: 2 K, 4 K and 6 K.

Now the effect of pressure in  $\rho(H)$  is highlighted. For example, at 2 K, we clearly see how pressure increases  $\rho(0)$  and how the bump arises and shifts to lower fields until only the negative magnetoresistivity is observed at 6.1 GPa ( $H < 10$  T). Above 10 T, we recover the positive magnetoresistivity for all the pressures. As previously discussed, the temperature has no big effects on the magnetoresistivity except that it becomes slightly less sensitive to the magnetic field (the bump smears out). Moreover,  $\rho(0)$  also increases with increasing temperature, as expected from the phonon contribution.

The emergence of the negative magnetoresistivity might be related to the suppression of spin fluctuations as the magnetic field polarize the spins. It is then quite natural to see that as the pressure increases and we approach the critical pressure, the spins will align for lower field values and at 6.1 GPa, the magnetoresistivity is negative also for small magnetic fields. The positive magnetoresistance observed at high fields for all pressures and temperatures may correspond to the usual behavior based on the cyclotron motion of charge carriers due to our experimental configuration as the current  $J \perp c$  and  $H \parallel c$ . Even though we did not detect clear signs of a metamagnetic-like behavior in YbCu<sub>2</sub>Si<sub>2</sub>, more information can be gathered about the effect of magnetic field close to  $P_c$  by studying the low temperature behavior of the resistivity.

### 3.4. Metamagnetism

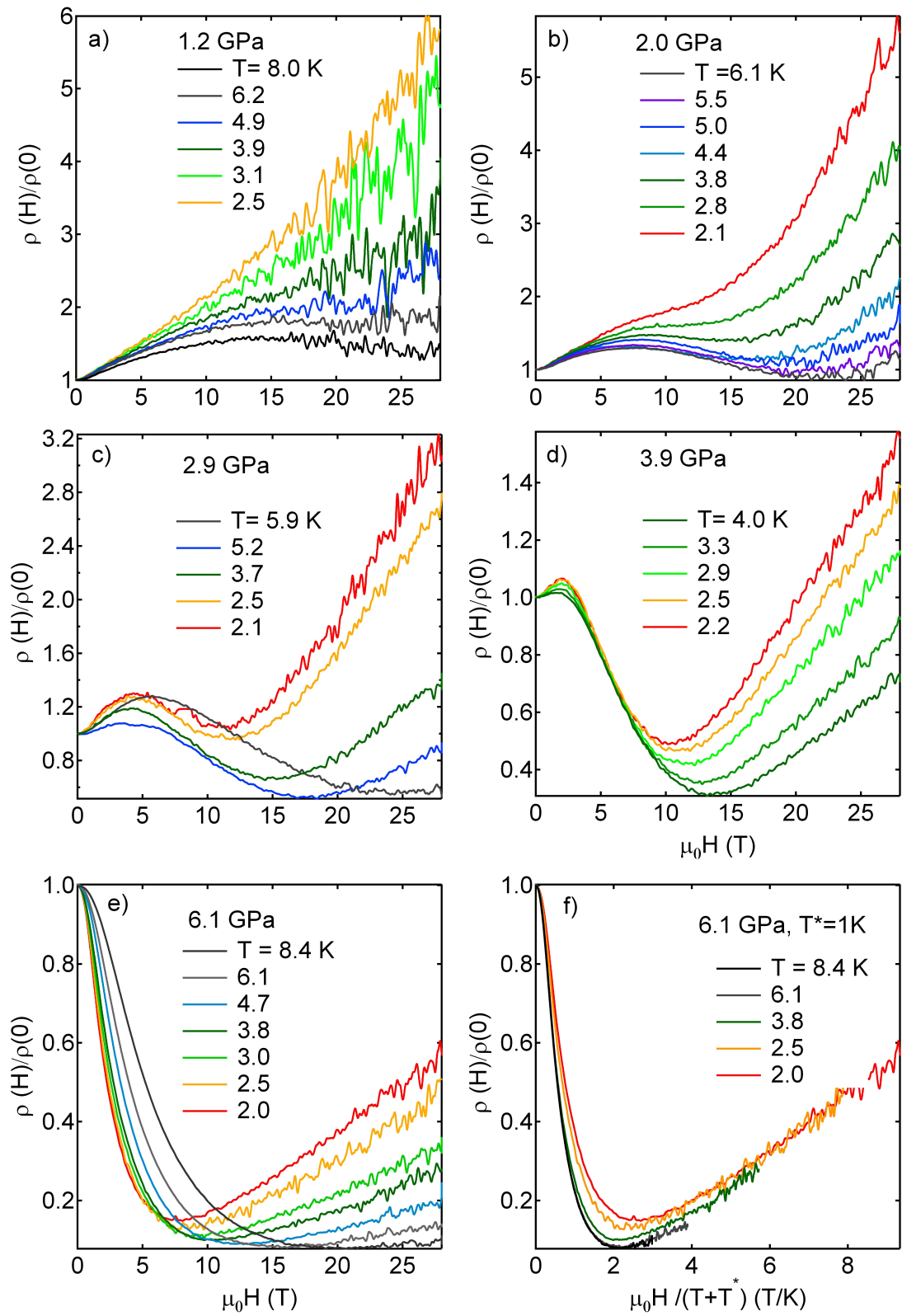


Figure 3.17: a)-e) Temperature dependence of the magnetoresistance,  $\rho(H)/\rho(0)$ , for several pressures below  $P_c$  above  $P_c$ . f) Single ion scaling of the magnetoresistivity (see details in text).

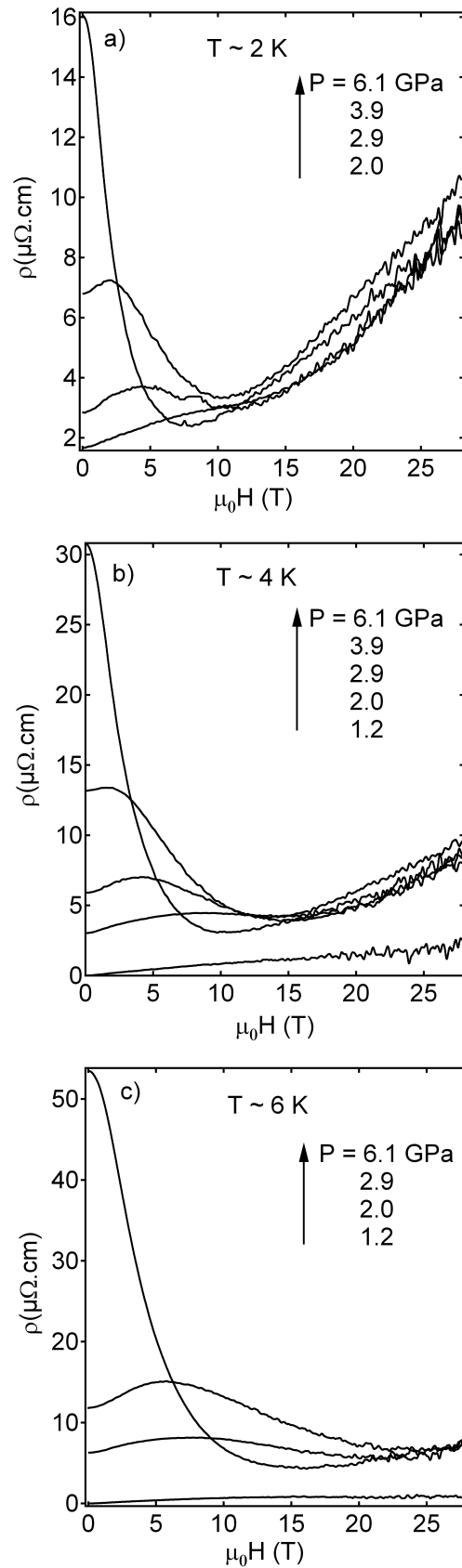


Figure 3.18: Pressure dependence of the magnetoresistivity in  $\text{YbCu}_2\text{Si}_2$  for three different temperatures a)  $T = 2\text{ K}$  b)  $T = 4\text{ K}$  and c)  $T = 6\text{ K}$ .

### 3.5. Fermi-Liquid studies throughout the P-T-H phase diagram

## 3.5 Fermi-Liquid studies throughout the P-T-H phase diagram

In section 3.2 we have reported the pressure dependence of the  $A$  coefficient, the residual resistivity ( $\rho_0$ ) and the Fermi-Liquid region ( $T_{FL}$ ) at zero field. We observed a strong enhancement of  $A$ , which showed a maximum near  $P_c$  as well as  $\rho_0$  whereas the FL region decreased when approaching the QCP.

To fulfill the study of the phase diagram in  $\text{YbCu}_2\text{Si}_2$ , we have followed the field dependence of  $A$ ,  $\rho_0$  and the FL behavior by applying magnetic fields up to 7 T in the resistivity measurements performed throughout the whole ( $P - T$ ) phase diagram (figure 3.11). An example at 8.3 GPa is given in figure 3.19, where the temperature dependence of the resistivity at selected magnetic fields is shown. Contrary to the calorimetry and susceptibility measurements, the anomaly corresponding to magnetic order in  $\rho$  disappears quickly even at very low fields.

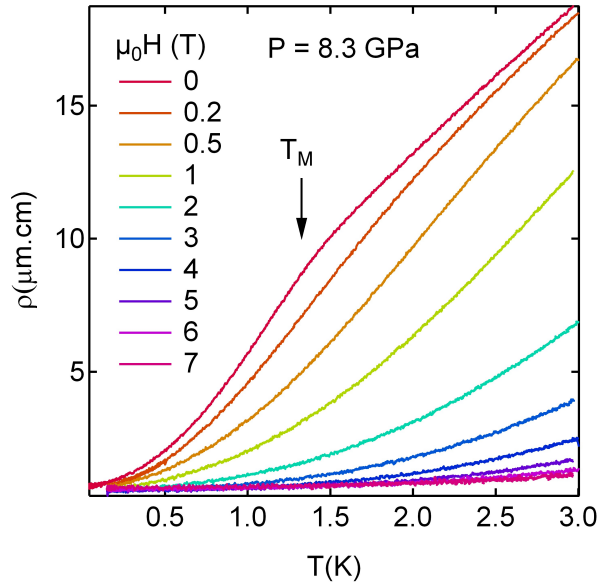


Figure 3.19: The temperature dependence of  $\rho$  at 8.3 GPa at several magnetic fields. The arrow indicates the position of the magnetic ordering temperature,  $T_M$ , at zero field.

The magnetic field dependence of the  $A$  coefficient under pressure is shown in figure 3.20. The red points correspond to the locii in the ( $P - H$ ) phase diagram where we measured the resistivity. First of all, we can clearly see that  $A$  shows a maximum versus pressure not only at zero field but also for  $\mu_0 H \neq 0$  T. Secondly,  $A$  is strongly reduced with increasing magnetic fields. For example, at 7 T, the  $A$  coefficient at 8 GPa is about  $0.25 \mu\text{cm}/\text{K}^2$  whereas at zero field is about  $6.2 \mu\text{cm}/\text{K}^2$ . This reflects a strong reduction of the scattering cross-section among the quasiparticles. In addition, the position of the maximum,  $A_{Max}$ , is field-dependent. The evolution of the maximum of  $A$  is easily distinguished in figure 3.21 a) where the coefficient  $A$  is plotted in a color scale contour plot in the ( $P - H$ ) plane. The red dashed line is a guide to the eyes which follows  $A_{Max}$ . In figure 3.21 b) the precise position of the maximum of  $A$  versus ( $P, H$ ) is plotted.  $A_{Max}$  shifts to lower pressures with increasing fields. At zero field,  $A_{Max}$  is located at  $P_c \approx 8$  GPa while at 7 T it is located about 3.5 GPa. The behavior of  $A$  under field clearly reflects the loss of magnetic spin fluctuations when applying high magnetic fields and how a field-induced polarized magnetic state is favored for low pressures.

The field dependence of  $\rho_0(P)$  is shown in figure 3.22 a). The general tendency is that  $\rho_0$

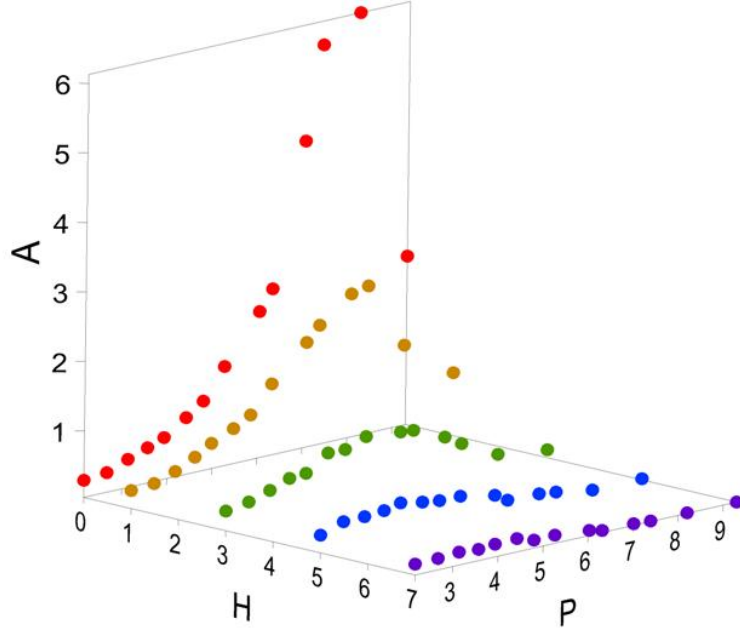


Figure 3.20: *The magnetic field dependence of the A coefficient under pressure for several magnetic fields up to 7 T.*

increases with field but, remarkably, the strong enhancement of  $\rho_0$  observed at zero field for  $P \approx P_c$  is significantly reduced in the high pressure range with magnetic field. For  $\mu_0 H > 2$  T,  $\rho_0$  also shows a maximum which shifts to lower pressures for increasing fields as shown in figure 3.22 b).

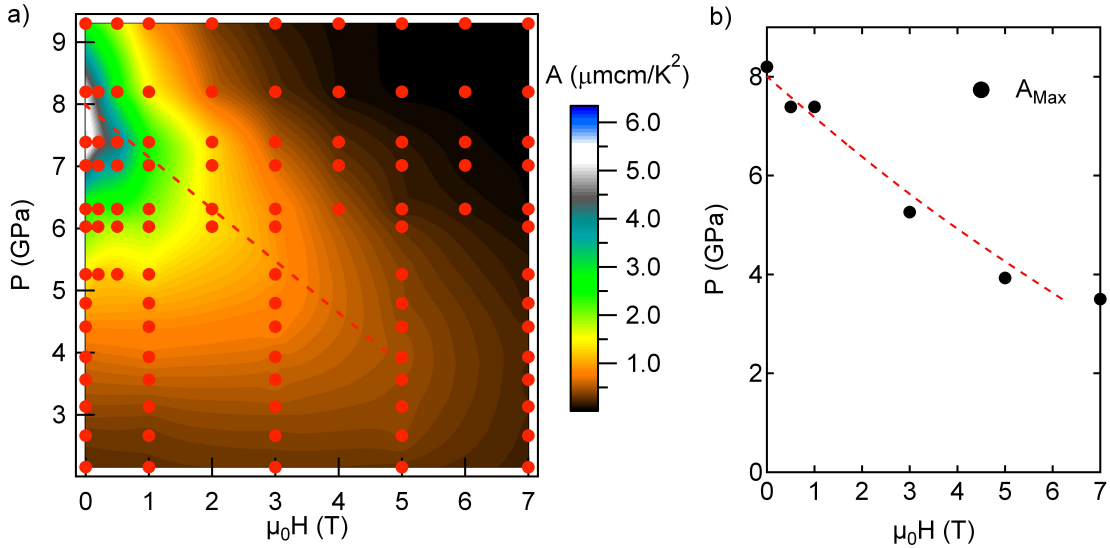


Figure 3.21: *a) Field dependence of the coefficient A versus pressure in a color scale plot. b) Evolution of the maximum of A (filled black circles) in the (P – H) plane. The red dashed lines are a guide to the eyes.*

The position of the maximum of  $A_{Max}$  and  $\rho_0^{Max}$  differ significantly. At 3 T,  $P(A_{Max}) \approx 5$  GPa while  $P(\rho_0^{Max}) \approx 7.5$  GPa. This is likely to be related to differences in the field dependence of the different scattering mechanisms of A and  $\rho_0$ . Nevertheless, both terms are significantly enhanced

### 3.5. Fermi-Liquid studies throughout the P-T-H phase diagram

in the presence of strong spin fluctuations.

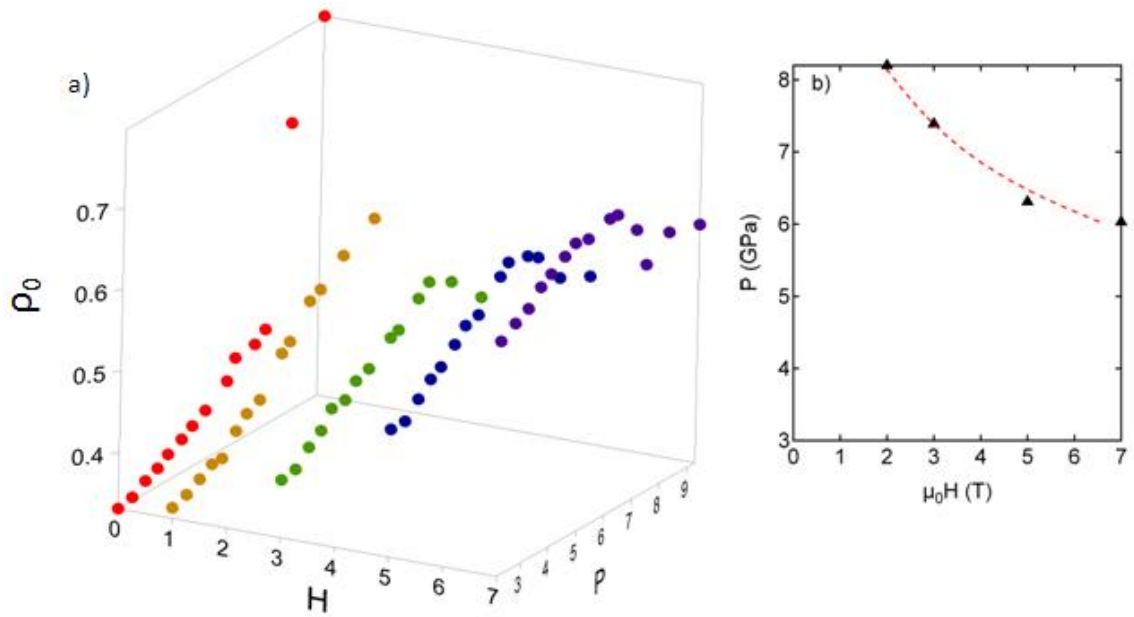


Figure 3.22: a) Field dependence of  $\rho_0$  under pressure for several fields up to 7 T. b) Evolution of the maximum of  $\rho_0$  within the  $(P-H)$  plane.

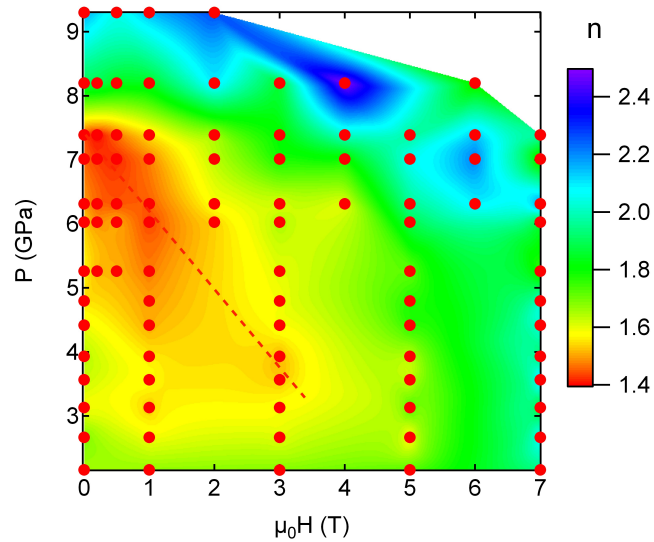


Figure 3.23: Evolution of  $n$ , the exponent in  $\rho(T) = \rho_0 + AT^n$  within the  $(P-H)$  phase diagram of  $YbCu_2Si_2$ . The red dashed line is a guide to the eyes. The white zone corresponds to the high pressure/high field region where the temperature of  $\rho$  became too weak to extract a value of  $n$ .

To conclude, we show in figure 3.23 the evolution of  $n$ , the exponent in

$$\rho(T) = \rho_0 + AT^n, \quad (3.7)$$

within the  $(P-H)$  phase diagram to detect FL and non-Fermi-Liquid (NFL) states. To calculate  $n$  we have performed a fit using equation 3.7 to our resistivity data from the lowest temperature to

1 K. Even at the lowest pressure (2.2 GPa) the fit over the temperature range 0.04– 1 K gives an exponent  $n < 2$  (about 1.8) at  $\mu_0 H = 0$  T. Indeed, in section 3.2 we found that the temperature where a significant deviation from FL behavior at 2.2 GPa was about  $T_{FL} \approx 1$  K.

On increasing pressure  $n$  shows a small but significant minimum at  $P \approx 7.5$  GPa for  $\mu_0 H = 0$  T, coinciding approximately with the critical pressure. Above  $P_c$ , FL behavior is quickly recovered. With an applied field the minimum of  $n$  persists, but again it shifts to lower pressures, at 3 T the minimum is located at  $P \approx 4$  GPa. In the high pressure/high field region the temperature dependence of  $\rho$  becomes too weak to extract a value of  $n$  (white region).

## 3.6 Interplay of magnetism and valence change

From all these results it became clear that the next step to better understand the phase diagram of YbCu<sub>2</sub>Si<sub>2</sub> was the study of the Yb valence throughout the ( $P - T$ ) phase diagram, in order to clarify the interplay between magnetism and valence change and also Kondo related effects.

### 3.6.1 Valence measurements under extreme conditions

As the energy scales and the magnetic ordering temperatures are low, it was important to combine both conditions of high pressure and low temperature. Early measurements in YbCu<sub>2</sub>Si<sub>2</sub> [Lawrence 1994, Moreschini 2007] and in the sibling compounds YbNi<sub>2</sub>Ge<sub>2</sub> and YbPd<sub>2</sub>Si<sub>2</sub> [Yamaoka 2010] at ambient pressure already pointed out a continuous valence decrease with temperature, while under pressure, Yb is shown to approach a trivalent configuration in both YbNi<sub>2</sub>Ge<sub>2</sub> and YbPd<sub>2</sub>Si<sub>2</sub> (at 300 K). But all these measurements were taken far from the critical region, in either pressure or temperature parameter space, to provide an accurate description of the low-energy interactions and of their interplay.

Therefore, we have performed such experiment combining extreme conditions at the ESRF (Grenoble, France) using resonant inelastic x-ray scattering spectroscopy (see Chapter 2), a truly bulk technique that has significantly improved the accuracy of RE valence estimation. As shown in figure 3.24 a), we measured the Yb valence throughout the phase diagram, from deep inside the paramagnetic state to well above the critical pressure, up to 22 GPa and, importantly, at low temperatures, the lowest being 7 K<sup>5</sup>, almost down to the ordering temperature.

Figure 3.24 b) shows the absorption spectra at the Yb  $L_3$  edge at selected pressures and the first sign of the mixed-valent state can be observed. The spectra were recorded in the partial fluorescence (PFY) mode at the Yb  $L\alpha_1$  line in order to reduce lifetime broadening effects and sharpen the spectroscopic features [Rueff 2010]. The spectral line shape presents a double-edge structure reminiscent of an admixture of  $Yb^{2+}$  and  $Yb^{3+}$  ions. A weak feature on the low-energy side of the  $Yb^{2+}$  peak denoted  $E_2$  is related to a quadrupolar transition  $2p^6 4f^{13} \rightarrow 2p^5 4f^{14}$  towards empty  $Yb^{3+}$  state. We notice a strong variation of the  $Yb^{2+}$  to  $Yb^{3+}$  intensity ratio with increasing pressure, signaling the progressive conversion towards the  $Yb^{3+}$  state. Although the valence can, in principle, be extracted from the PFY x-ray absorption spectroscopy (XAS) spectra, the method is somewhat complicated by the uncertainty about the position of the edge step. A better way is to use the resonant emission spectra instead. The main advantage of the resonant regime (RIXS) is the possibility to selectively enhance either the  $Yb^{2+}$  ( $2p^6 4f^{14} 5d^0$ ) or the  $Yb^{3+}$  ( $2p^6 4f^{13} 5d^1$ ) component by an appropriate choice of the incident photon energy  $h_{in}$  which provides a higher accuracy in the estimation of the valence.

<sup>5</sup>Even though we sought to measure the valence inside the magnetic ordering phase, due to technical reasons,

### 3.6. Interplay of magnetism and valence change

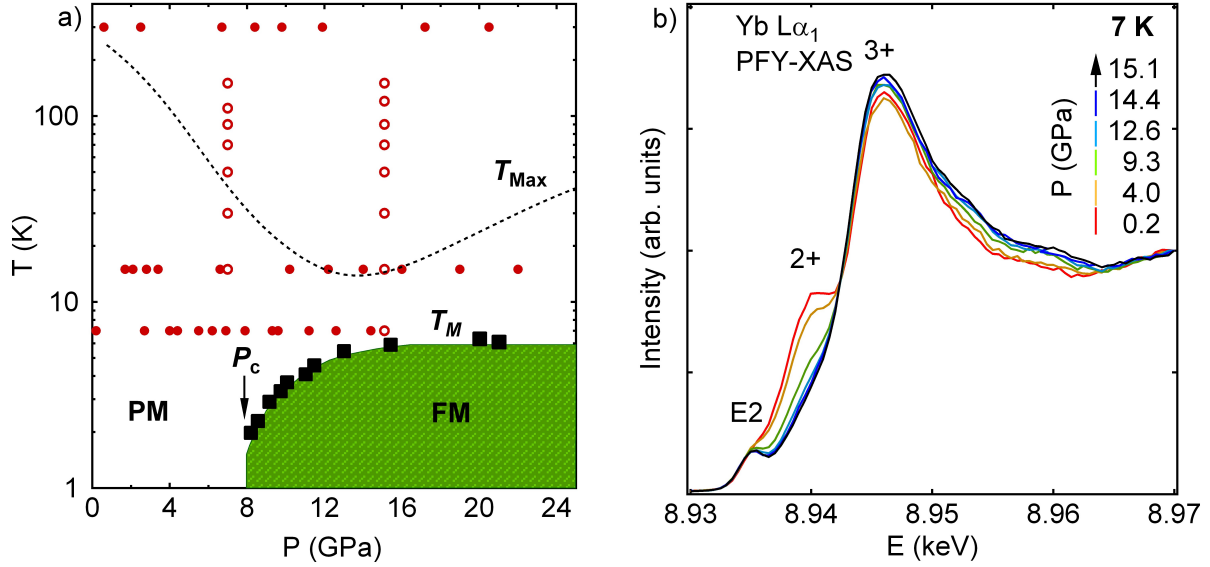


Figure 3.24: a)  $(P-T)$  phase diagram of  $YbCu_2Si_2$  (from figure 3.11 for  $P < 13$  GPa and for  $P > 13$  GPa from Ref. [Winkelmann 1999]).  $T_M$  (squares) and  $P_c$  are the ferromagnetic ordering temperature and the critical pressure respectively. Solid circles indicate the  $(P, T)$  locii where valence was measured at constant temperature (300, 15 and 7 K) while open circles are the locii where valence was measured at constant pressure (7 and 15 GPa).  $T_{Max}$  [Alami Yadri 1998] is related to the Kondo temperature. b) PFY-XAS spectra measured at 7 K at selected pressures. The position of  $Yb^{2+}$  and  $Yb^{3+}$  components are indicated along with the assumed quadrupolar peak E2.

The  $Yb L\alpha_1$  RIXS spectra measured at the  $Yb^{2+}$  resonance ( $h_{in} = 8.9404$  keV) are summarized in figure 3.25 for different pressure and temperature conditions. The two main features peaking at an energy transfer,  $E_t = h_{in} - h_{out}$ , of 1525.5 and 1530.5 eV correspond to transitions from the  $Yb^{2+}$  and  $Yb^{3+}$  components of the initial mixed-valent ground state  $|g\rangle = a|f^{13}\rangle + |f^{14}\rangle$  while the vertical arrow around  $E_t = 1520$  eV indicates the position of the E2 transition which in RIXS spectra is less pronounced than in PFY.

To enhance spectral changes, all the spectra were normalized to the  $Yb^{2+}$  intensity and plotted as a function of  $E_t$ . We observe a clear increase of the  $Yb^{3+}$  intensity under pressure with respect to  $Yb^{2+}$  at all measured temperatures (7, 15 and 300 K (not shown in figure 3.25)), while the weak E2 feature stays mostly unchanged. This transfer of spectral weight is consistent with the expected delocalization of  $4f$  electrons under pressure and the increase of Yb valence. In contrast, the Yb valence is found to decrease upon cooling at 7 and 15 GPa tending towards a divalent state. This behavior agrees with the one reported at ambient pressure [Moreschini 2007].

To extract the Yb valence from the RIXS spectra we used the expression

$$v = 2 + \frac{I^{3+}}{I^{2+} + I^{3+}} \quad (3.8)$$

where  $I^{2+}$  and  $I^{3+}$  are the integrated intensity of the pure-valent spectral components. The spectra were evaluated by fitting the data with two Gaussian line shapes centered on the 2+ and 3+ peaks. The background contribution was taken into account by an arctangent function and the E2 feature was disregarded in the analysis because of its negligible contribution. These calculations were

the cooling power of the cryostat, we could not measure below 7 K.

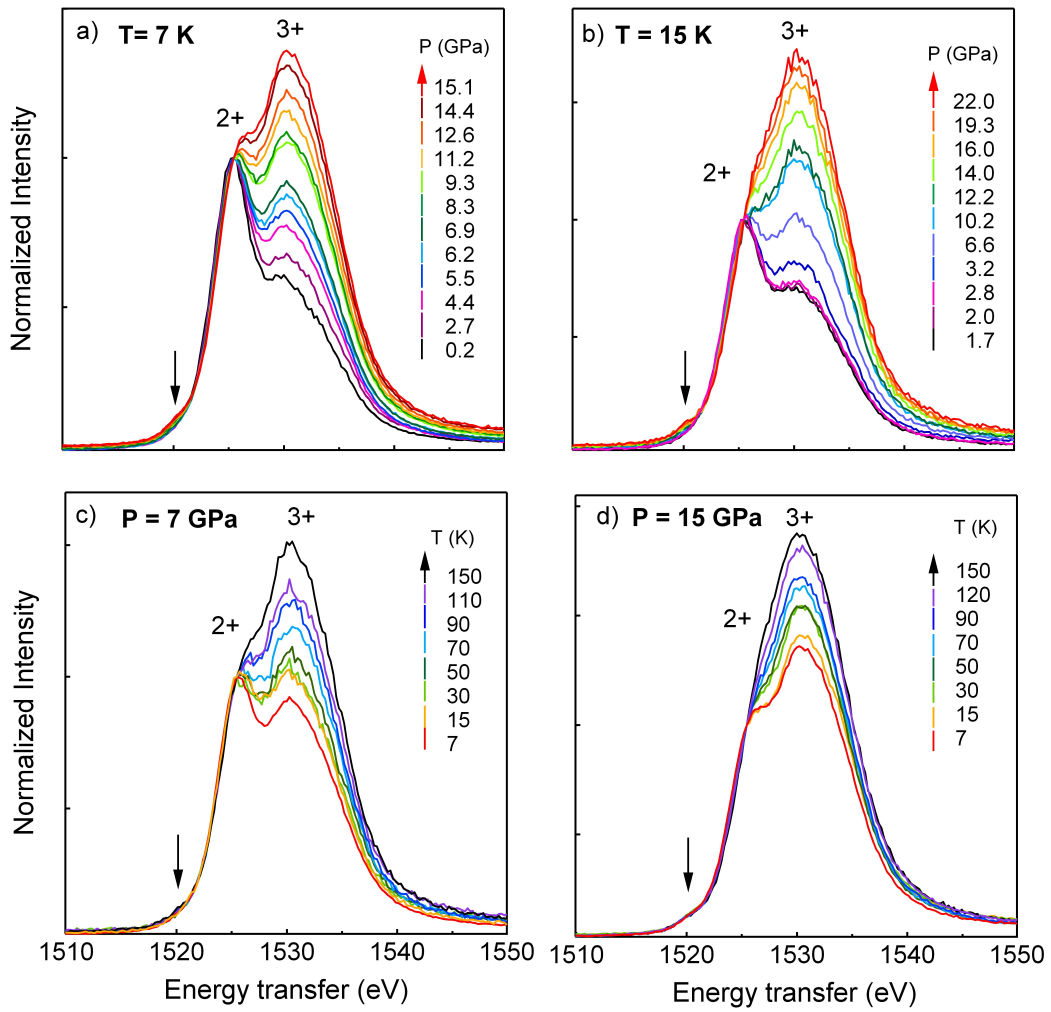


Figure 3.25: Pressure and temperature dependence of the  $\text{Yb } L\alpha_1$  RIXS spectra in  $\text{YbCu}_2\text{Si}_2$ . The four panels summarize the results obtained at constant temperature (a) 7 K, (b) 15 K and constant pressure (c) and (d) at 7 GPa and 15 GPa respectively. The arrow indicates the quadrupolar peak  $E_2$ .

### 3.6. Interplay of magnetism and valence change

carried out by V. Balédent and J. P. Rueff. The results of the pressure and temperature dependence of the valence of  $\text{YbCu}_2\text{Si}_2$  will be discussed in the following sections.

#### 3.6.1.1 Pressure-induced valence crossover

Figure 3.26 shows the pressure dependence of the valence in  $\text{YbCu}_2\text{Si}_2$  at three different temperatures: 300 K, 15 K and 7 K. All three curves show a monotonous increase of the valence under pressure towards trivalency, independently of the temperature, as we previously inferred from the spectra inspection. At all temperatures, the  $v(P)$  dependence shows a strong and close-to-linear increase at low pressures, followed by a much weaker increase at high pressures. This change of slope occurs in a relatively small pressure window (9-11 GPa) for all the temperatures we measured. It is particularly visible at 15 K, where the kink (denoted as  $P_k$  in the following) is found at  $P_k \approx 10$  GPa, a pressure comparable to  $P_c \approx 8$  GPa. Above  $P_k$  the valence keeps increasing, but more slowly. In the vicinity of the magnetic ordered phase, the valence reaches 2.95 (at 15 K) and 2.93 (at 7 K).

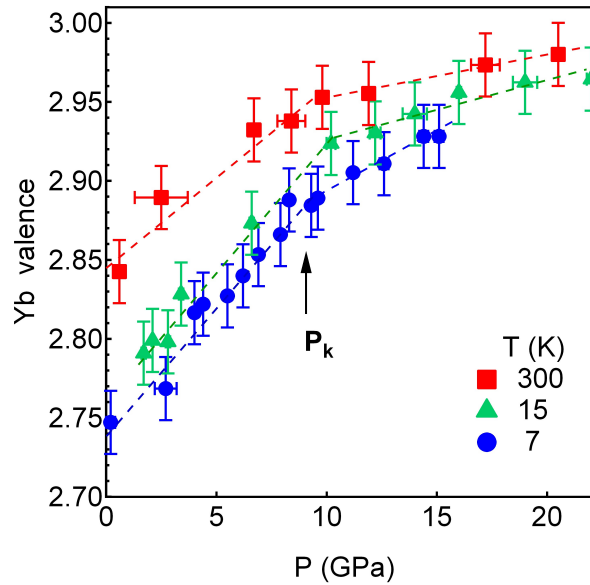


Figure 3.26: Valence-pressure dependence of  $\text{YbCu}_2\text{Si}_2$  at 7, 15 and 300 K. The arrow points the pressure where a kink is observed ( $P_k$ ).

Thus, in the high-pressure region of the phase diagram, magnetism probably sets in for a non-integer valence ( $v < 3$ ). Even though a FOVT at the magnetic ordering temperature  $T_m$  can not be completely discarded, it seems however very unlikely to occur.

#### 3.6.1.2 Valence-temperature dependence

In figure 3.27, the temperature dependence of the valence at constant pressure further highlights the interplay of the significant energy scales. For all pressures the valence decreases with decreasing temperature. The previous reported measurement at ambient pressure [Moreschini 2007] found that this decrease occurs mainly in the temperature range  $T < 150$  K. In this study we focused more specifically on the low-temperature side below 150 K. We do, however, find under pressure

a decrease of the valence in the temperature range 7-150 K, at least as strong as that found at ambient pressure, and virtually no temperature change of the valence between 150 and 300 K.

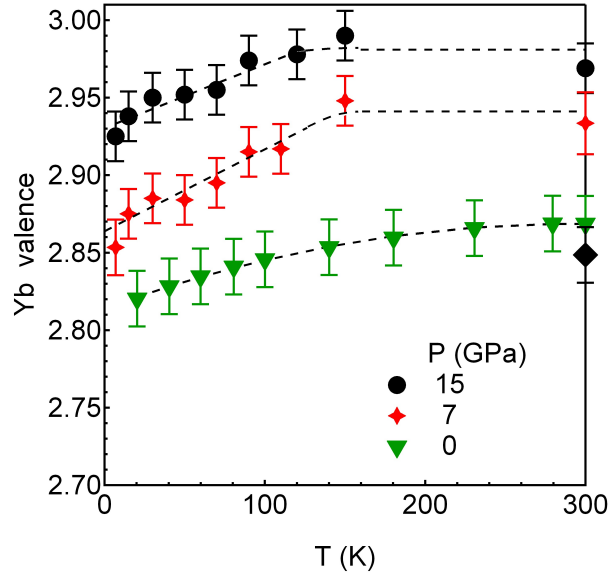


Figure 3.27: *b)* Valence-temperature dependence at 15 GPa, 7 GPa and at ambient pressure (green triangles [Moreschini 2007]. The black diamond is the value we obtained in this work). Dashed lines are guides to the eyes.

This implies that the temperature where the valence starts to decrease is relatively insensitive to pressure and so is probably not directly related to the Kondo temperature, which strongly decreases with pressure (see figure 3.24). These features are likely related to CEF effects and to the localized behavior of the 4f electrons at high temperature which leads the system to favor an integer valence. In fact, neutron measurements [Holland-Moritz 1982, Muzychka 1998] have revealed that the first excited doublet in  $\text{YbCu}_2\text{Si}_2$  is located around 140 K, and the second one is above 300 K. Finally, the initial increase of slope  $|\partial v/\partial T|$  between 0 and 7 GPa may be understood as being due to an increase of magnetic spin fluctuations while approaching  $P_c$ .

### 3.6.1.3 $\text{CeCu}_2\text{Si}_2$ versus $\text{YbCu}_2\text{Si}_2$ valence change

Recent valence measurements carried out in  $\text{CeCu}_2\text{Si}_2$  in similar extreme conditions [Rueff 2011] offer the valuable opportunity to draw a direct comparison between 4f electron (Ce) and hole (Yb) occupancy,  $n_f$ . As  $\text{YbCu}_2\text{Si}_2$  (bulk modulus,  $B_0=168$  GPa) [Sanchez 2000] is harder than  $\text{CeCu}_2\text{Si}_2$  ( $B_0=112$  GPa) [Tsuduki 2005], it is more appropriate to compare their  $n_f$  with respect to their relative critical volume change rather than the applied external pressure as shown in figure 3.28. The critical molar volume,  $V_c$ , for  $\text{YbCu}_2\text{Si}_2$  is taken as  $145.97 \text{ \AA}^3$  (the cell volume at 8 GPa) whereas for  $\text{CeCu}_2\text{Si}_2$  we take the volume at ambient pressure ( $165.324 \text{ \AA}^3$ ) assuming the critical pressure is close to  $P_c=0$ . The upper axis has been shifted in order to align the critical molar volume for both compounds. The blue and red arrows indicate the increasing direction for pressure for  $\text{YbCu}_2\text{Si}_2$  and  $\text{CeCu}_2\text{Si}_2$  respectively. Our results show that the volume effect on the valence for both systems is actually quite similar. However, in  $\text{YbCu}_2\text{Si}_2$  the change of  $n_f$  versus the relative volume change in the region  $V > V_c$  is about 50% larger than in  $\text{CeCu}_2\text{Si}_2$ , and at  $V_c$ ,  $n_f$  is much closer to one in  $\text{CeCu}_2\text{Si}_2$  (0.96) than in  $\text{YbCu}_2\text{Si}_2$  (0.90).

### 3.7. Conclusions

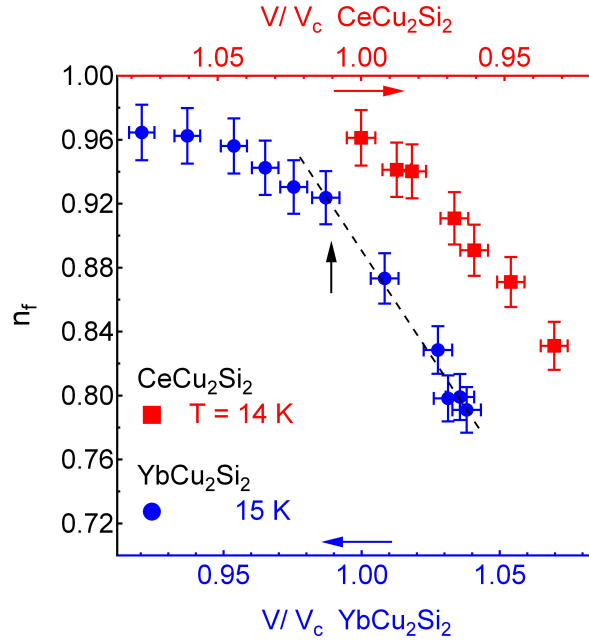


Figure 3.28:  $f$  electron and hole occupancy of  $CeCu_2Si_2$  (upper axis) and  $YbCu_2Si_2$  (low axis) respectively versus their molar volume normalized to their critical molar volume,  $V_c$  (see details in text) at  $T \approx 15$  K. The blue and red arrows indicate the direction of increasing applied external pressure for  $YbCu_2Si_2$  and  $CeCu_2Si_2$  respectively, while the vertical black arrow indicates the volume which corresponds to  $P_k \approx 10$  GPa. The dashed black line is a linear fit for  $V > V_c$ .

As we have already emphasized in  $YbCu_2Si_2$  magnetic order is likely to appear before the trivalent state is reached. For  $YbCu_2Si_2$  the slope change of  $v(P)$  seen in figure 3.26 is also apparent in the  $n_f(V/V_c)$  dependence as the deviation from the linear behavior (dashed black line) at a  $V/V_c \approx 0.99$  which corresponds to  $P_k$  (indicated by the black arrow in figure 3.28). Further studies in other compounds would be of great interest in order to clarify if this is a general tendency in Ce and Yb systems or a particular trend of the 122 family. The most striking result is the different position of the critical volume in relation to the valence change. From these results, it is tempting to conclude that valence fluctuations in  $YbCu_2Si_2$  could seed unconventional superconductivity at high pressure as theoretically predicted in the 122 family [Holmes 2007, Watanabe 2011] and experimentally confirmed in  $CeCu_2Si_2$  [Rueff 2011]. But, as previously reported in [Colombier 2009] and also shown in this work, there is a lack of any evidence of superconductivity in  $YbCu_2Si_2$ . This implies that valence fluctuations does not suffice and other phenomena notably the predominance of ferromagnetic correlations may in fact prevent superconductivity.

#### 3.6.2 Valence measurements under magnetic field

Figure 3.29 shows the XAS spectra at the  $L_3$ -edge of  $YbCu_2Si_2$  measured at 2.1 K at zero field and at 10 T. The spectra are found to be insensitive to the application of the magnetic field.

### 3.7 Conclusions

In this chapter we present a detailed study of the transport, magnetic and electronic properties of the moderate heavy fermion and intermediate-valence compound  $YbCu_2Si_2$  by means of resistivity,

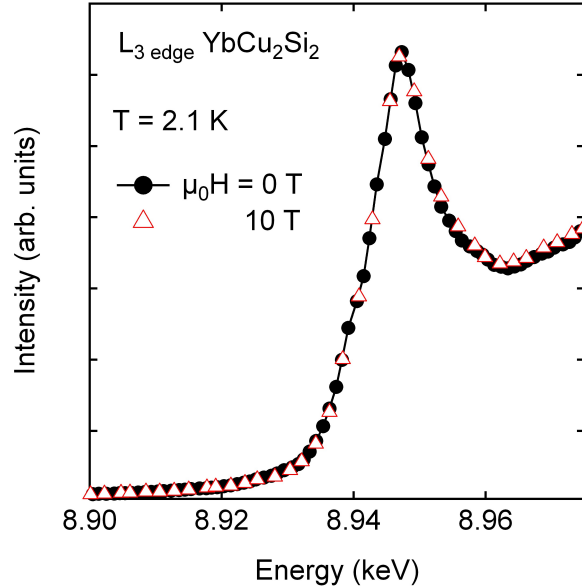


Figure 3.29:  $L_3$ -edge absorption spectra of YbCu<sub>2</sub>Si<sub>2</sub> single-crystal sample taken at 0 and 10 T at 2 K.

ac-calorimetry, ac-susceptibility, magnetization and valence measurements under pressure and high magnetic fields.

The  $(P - T)$  phase diagram of YbCu<sub>2</sub>Si<sub>2</sub> can be interpreted as a first approximation as the “mirror” image of a Ce-based HF phase diagram within the Doniach picture and it is at least qualitatively in agreement with the spin-wave fluctuation scenario: the FL region in the paramagnetic state decreases with increasing pressure and above the critical pressure  $P_c \approx 8$  GPa a magnetic order appears. This is accompanied with a large enhancement of the coefficient  $A$  of the resistivity, about two orders of magnitude, but  $T_K \propto T_{Max} \propto 1/\sqrt{A}$  stays finite across the QCP.

However, there are some relevant differences with the phase diagram of its Ce-counterpart, CeCu<sub>2</sub>Si<sub>2</sub>. First of all, the ac-susceptibility and magnetization measurements show that the nature of the magnetic order is ferromagnetic. The finding of ferromagnetic order could be at first sight quite surprising. Actually, YbCu<sub>2</sub>Si<sub>2</sub> is not the sole example among Yb-based heavy fermion compounds. YbInNi<sub>4</sub> orders ferromagnetically at ambient pressure [Sarrazo 1998] or at least with a strong FM component [Willers 2011]. There is also indirect evidence for ferromagnetism under pressure in at least 2 other systems, YbNi<sub>2</sub>Ge<sub>2</sub> [Knebel 2001] and YbIr<sub>2</sub>Si<sub>2</sub> [Yuan 2006]. It seems that the presence of strong FM correlations might be a general trend in Yb systems, on the contrary to cerium, which orders antiferromagnetically.

Secondly, despite the considerable experimental efforts to measure very close to  $P_c$  and at low temperatures, we have not detected the transition below 1 K. Magnetic order occurs suddenly at a pressure of  $P_c \approx 7.5$ -8 GPa and a temperature of about 1.5 K. The possibility of a first-order transition, in contrast to the second-order transition of the AFM phase in the Doniach phase diagram, was already suggested from Mössbauer results where the coexistence of a magnetic and non-magnetic component was found over a pressure range of several GPa above  $P_c$  [Winkelmann 1999]. Another relevant difference with the phase diagram of CeCu<sub>2</sub>Si<sub>2</sub> is the absence of superconductivity in YbCu<sub>2</sub>Si<sub>2</sub> in the whole  $(P - T)$  phase diagram.

We have performed a detailed search for signatures of metamagnetism in YbCu<sub>2</sub>Si<sub>2</sub>. The magnetization along the  $c$  axis shows no signs of metamagnetic behavior at ambient pressure when

### 3.7. Conclusions

a magnetic field up to 52 T is applied. Under pressure, a clear bump in the magnetoresistivity measurements arises. The position of the maximum shifts to lower magnetic fields with increasing pressure (as summarized in figure 3.10 b) ) and at 6.1 GPa the magnetoresistivity is negative even at low fields. In fact, the magnetoresistivity curves of  $\text{YbCo}_2\text{Zn}_{20}$  at ambient pressure, where metamagnetism is observed, are very similar of those at 6.1 GPa in  $\text{YbCu}_2\text{Si}_2$ . In [Ohya 2010] the field where a bump is observed in the magnetoresistance curves is associated to the metamagnetic field,  $H_m$ . But in  $\text{YbCo}_2\text{Zn}_{20}$  a clear anomaly in the magnetization,  $M(H)$ , is observed. In  $\text{YbCu}_2\text{Si}_2$ , the bump we observe can be ascribed to a cross-over between a paramagnetic state at low fields to a field-induced polarized state at high magnetic fields.

To complete the study of the magnetic field effects in the phase diagram of  $\text{YbCu}_2\text{Si}_2$  we have followed the evolution of the exponent  $n$  ( $\rho(T) = \rho_0 + AT^n$ ), and the  $A$  coefficient and the residual resistivity  $\rho_0$  of the Fermi-liquid regime ( $n = 2$ ).

The evolution of the exponent  $n$  under magnetic field reveals that a large region of the ( $P - H$ ) phase diagram is located in a cross-over regime with  $1.4 < n < 2$  with a minimum close to the critical pressure. At zero field, the value of the exponent  $n$  near the QCP is about  $1.4 - 1.5$ . This value is slightly lower than the one proposed for a 3D ferromagnetic system within the spin fluctuation model which predicts a power law dependence of the resistivity near the QCP of  $\rho \propto T^{5/3}$ . Whereas  $n$  decreases under pressure, the magnetic field tends to increase it and the FL state is found for  $H > 6$  T.

At zero field the maximum of  $A$  and  $\rho_0$  and the minimum of  $n$  correspond to the critical pressure where magnetic order occurs. Under field we quickly lose the signature of a clear phase transition. Nevertheless, the results show a persistence of the critical fluctuations which occur at lower pressures. This could be the signature of the metamagnetic behavior we searched for, however the transition quickly becomes a crossover to the polarized state. Interestingly, the maximum observed in the magnetoresistivity curves at 2 K and the position of  $A_{max}$  have a similar response under field as shown in figure 3.31.

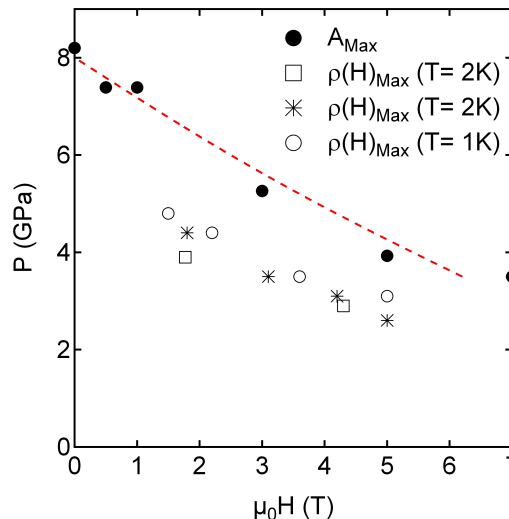


Figure 3.30: (filled black circles) Evolution of  $A_{Max}$ , (Open squares) the maximum observed in the magnetoresistance curves at  $T = 2$  K in figure 3.18 a) and from resistivity measurements in 3.5 (stars) at  $T = 2$  K and (open circles)  $T = 1$  K within the ( $P - H$ ) plane.

All these results drove us to the study of how the Yb valence changes throughout the ( $P - T$ )

phase diagram to better understand the interplay between magnetism and valence change to know how the different regimes, i.e., intermediate-valence, Kondo and RKKY compete.

The knowledge of the pressure dependence of the RE valence is key to quantify the hybridization between the  $4f$  electron and the conduction band. Figure 3.31 shows the most complete ( $P - T$ ) phase diagram of YbCu<sub>2</sub>Si<sub>2</sub> so far. The pressure dependence of the main energy scales are shown: the magnetic ordering temperature  $T_M$ ,  $T_{Max} \propto T_K$  and the Fermi-liquid temperature,  $T_{FL}$ . The pressure dependence of the crystal field, which is another relevant energy scale as deduced from our results, is not known. The kink we observed in the pressure dependence of the valence,  $P_k$ , is also shown.

As discussed in the theoretical introduction (chapter 1), in several heavy fermion compounds the boundary between the intermediate-valence regime ( $n_h < 1$ ) and the Kondo regime ( $n_h \approx 1$ ) is not sharp, i.e instead of a FOVT marked with a discontinuity in  $n_f$ , there is a crossover between both regimes. The kink we observe at  $P_k$  in YbCu<sub>2</sub>Si<sub>2</sub> it might be identify as the pressure where the system passes trough one regime to another.

We can now interpret the ( $P - T$ ) phase diagram of YbCu<sub>2</sub>Si<sub>2</sub> as follows:

At high temperatures (for  $T > T_{Max}$  and  $T_{CEF} \approx 140$  K) and ambient pressure the system is already in an intermediate-valence regime where the  $f$  electrons act as a set of free quasi-localized spins ( $v(0 \text{ GPa}) \approx 2.85$ ). Upon increasing pressure the trivalent state is almost achieved ( $v(22 \text{ GPa}) \approx 2.98$ ).

When cooling and below  $T_{CEF}$ , which is similar to  $T_{Max}$  at ambient pressure, the valence decreases significantly (at 7 K,  $v(0 \text{ GPa}) \approx 2.75$ ). At lower temperatures,  $T < 1$  K, the heavy fermion state develops within the IV regime. As we pointed it out in chapter 1, this is probably one of the major differences with Ce-based HF compounds: in Yb-based HF systems the heavy fermion state can be developed for a wider valence range.

When pressure is applied, the system moves towards the trivalent state and above  $P_k$  the valence is above 2.9, so theoretically it can be described within the Kondo regime ( $n_h \approx 1$ ) approximation in the Anderson model. For  $P > 8$  GPa, the ground state is ferromagnetic with a valence value above 2.9, slightly less than 3, at least up to 25 GPa. In figure 3.32 all these regimes are summarized.

Finally, although YbCu<sub>2</sub>Si<sub>2</sub> seems an ideal candidate to find superconductivity in an Yb-based HF system, we have now performed a rather extensive search down to 40 mK over the whole phase diagram below and slightly above  $P_c$  on a high quality sample. Still no signs of superconductivity have been found.

### 3.7. Conclusions

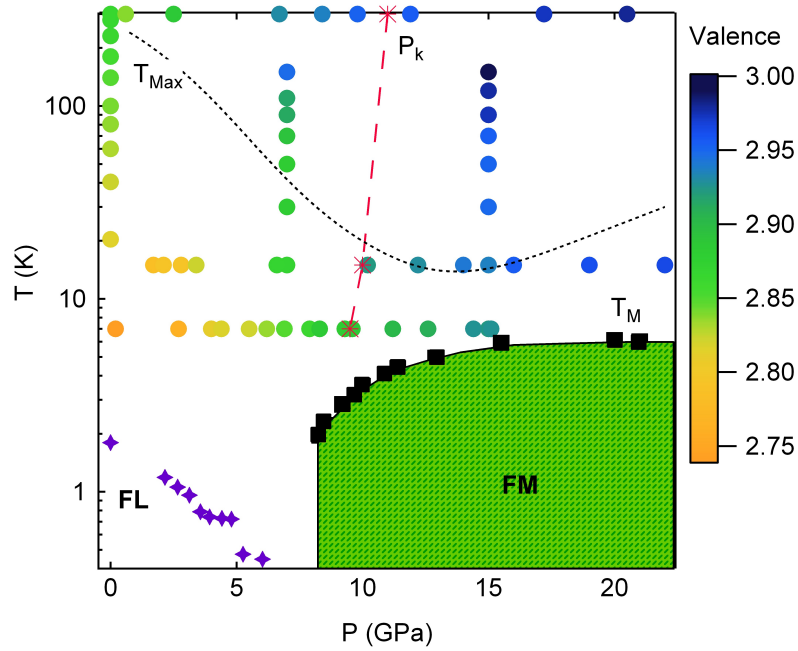


Figure 3.31:  $(P - T)$  phase diagram of  $YbCu_2Si_2$  with all the main energy scales,  $T_M$ ,  $T_{Max} \propto T_K$  and  $T_{FL}$  and in a color scale, the valence of the Yb ion in  $YbCu_2Si_2$ .

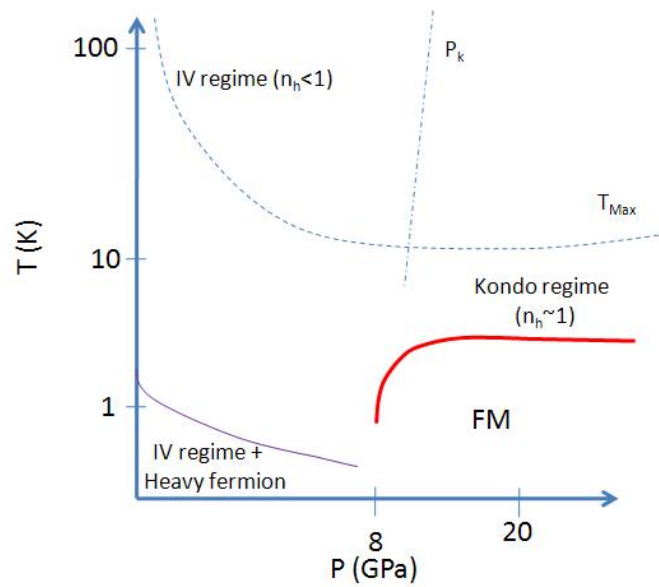


Figure 3.32: Schematic diagram of the different regimes: intermediate-valence regime and Kondo regime as a function of  $P$  and  $T$  in  $YbCu_2Si_2$ .

# CHAPTER 4

## YbCo<sub>2</sub>Zn<sub>20</sub>

---

### Contents

---

<b>4.1</b>	<b>The YbT<sub>2</sub>Zn<sub>20</sub> family</b>	<b>93</b>
<b>4.2</b>	<b>Introduction of YbCo<sub>2</sub>Zn<sub>20</sub></b>	<b>96</b>
<b>4.3</b>	<b>High pressure phase diagram</b>	<b>105</b>
<b>4.4</b>	<b>Conclusions</b>	<b>111</b>

---

The discovery of the new Yb-based heavy fermion family, YbT<sub>2</sub>Zn<sub>20</sub> (T= Fe, Co, Ru, Rh, Os, Ir) by Torikachvili *et al.*, has attracted much attention and at the present moment, it is a very intense and prolific research field [Torikachvili 2007, Matsubayashi 2010] with more than 20 publications since 2008.

This novel family has significantly increased the number of Yb-based HFC known so far and it offers the opportunity to study six new closely related (structurally) compounds of a different family to the YbM<sub>2</sub>X<sub>2</sub> (M= transition metal, X= Si, Ge) with the tetragonal *ThCr<sub>2</sub>Si<sub>2</sub>* structure.

The thermodynamic and transport properties of the YbT<sub>2</sub>Zn<sub>20</sub> family are presented in the following paragraph. Next, I present a detailed review of the physical properties of YbCo<sub>2</sub>Zn<sub>20</sub>, one of the heaviest heavy fermions ever found. Then, the main experimental results on YbCo<sub>2</sub>Zn<sub>20</sub> will be discussed:

- The ( $P - T$ ) phase diagram up to 14 GPa determined through calorimetry measurements.
- The ac-susceptibility measurements and the ( $T - H$ ) phase diagram which shed some light on the nature of the pressure-induced magnetic order.

### 4.1 The YbT<sub>2</sub>Zn<sub>20</sub> family

The YbT<sub>2</sub>Zn<sub>20</sub> family crystallizes in the cubic CeCr<sub>2</sub>Al<sub>20</sub> structure ( $f\bar{d}3m$  space group) as shown in figure 4.1. The lattice constant and the distance between Yb-Yb atoms are rather large,  $a \approx 14 \text{ \AA}$  (see table 4.1) and  $d_{Yb-Yb} \approx 6 \text{ \AA}$  respectively, which probably leads to weaker interactions compared with other compounds with smaller lattice constants [Torikachvili 2007].

The characteristic crystal structure is the following: the transition metallic atoms (T) have an icosahedral zinc coordination which forms a caged structure while each Yb ion is coordinated by a 16 Zn atom Frank-Kasper polyhedron with a cubic point symmetry. It is expected that due to this near spherical distribution of Zn atoms the crystalline electric field splitting will be relatively low and thus, these six compounds are interesting models to investigate the heavy fermion state with a large degeneracy of the Yb ion [Matsubayashi 2010, Torikachvili 2007, Nakanishi 2009] as inferred from figure 4.2: the Kadowaki-Woods (KW) type plot shows that the YbT<sub>2</sub>Zn<sub>20</sub> compounds have a degeneracy  $N$  of  $4 \leq N \leq 8$ .

#### 4.1. The $\text{YbT}_2\text{Zn}_{20}$ family

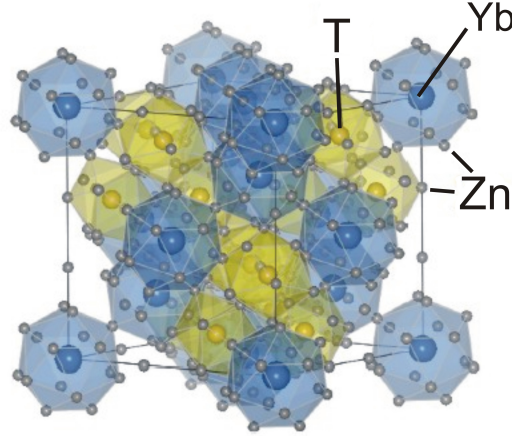


Figure 4.1: Cubic structure of  $\text{YbT}_2\text{Zn}_{20}$  family adapted from Takeuchi et al. [Takeuchi 2010]. Blue spheres correspond to Yb atoms, the yellow to transition (T) atoms and the gray to Zn atoms.

The main thermodynamic and transport properties of the  $\text{YbT}_2\text{Zn}_{20}$  family are summarized in figure 4.3 and table 4.1. First we will focus on  $T = \text{Fe, Ru, Rh, Os}$  and Ir as they have qualitatively similar properties. They all exhibit the heavy fermion behavior at low temperatures: the susceptibility curves follow a Curie-Weiss behavior down to 100 K with an effective magnetic moment close to the value of the free  $\text{Yb}^{+3}$  ion and then they show a loss of the local moment behavior below  $T_{\chi_{max}}$  (figure 4.3 a)). The linear coefficient of the specific heat (figure 4.3 c)) has a value which varies from  $\gamma \approx 500 - 800 \text{ mJ/molK}^2$ <sup>1</sup>. The electrical resistivity follows the characteristic  $T^2$  dependence of a Fermi liquid for  $T < 1 - 10 \text{ K}$  depending on the compound (inset of figure 4.3b)).

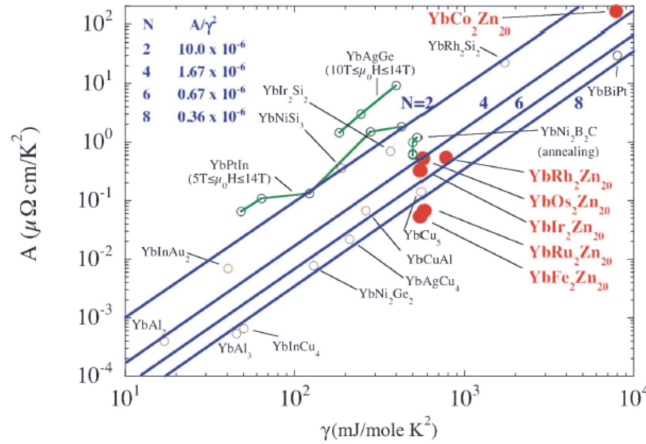


Figure 4.2: Log-log plot of  $A$  versus  $\gamma$  (Kadowaki-Woods plot) of the  $\text{YbT}_2\text{Zn}_{20}$  family. The solid lines correspond to degeneracies  $N=2, 4, 6$  and  $8$  [Torikachvili 2007].

At a first glance, the properties of  $\text{YbCo}_2\text{Zn}_{20}$  differ somehow from the other five compounds: the magnetic susceptibility shows a Curie-Weiss behavior down to 1.8 K (inset of figure 4.3 a)). The Sommerfeld coefficient is extremely large  $\gamma = 7900 \text{ mJ/molK}^2$ , making  $\text{YbCo}_2\text{Zn}_{20}$  one of the heaviest fermion compound so far (figure 4.3 d)) with an estimated Kondo temperature  $\approx 1 \text{ K}$ . But

<sup>1</sup>According to the authors, the rise of the  $C(T)/T$  at low temperatures is probably due to a nuclear Schottky anomaly. For more details see [Torikachvili 2007].

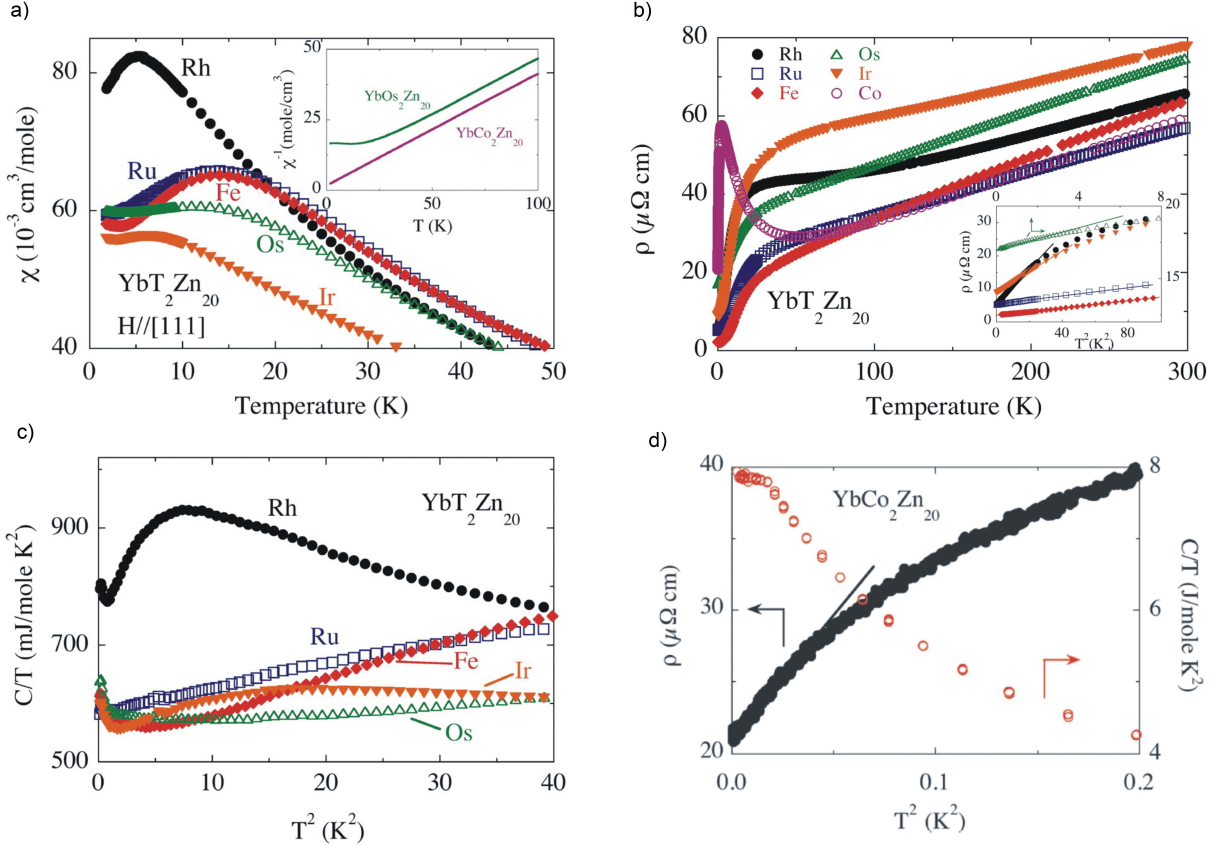


Figure 4.3: Thermodynamic and transport properties of  $\text{YbT}_2\text{Zn}_{20}$  from [Torikachvili 2007]. a) Magnetic susceptibility ( $H=0.1\text{T}$ ). (Inset) Temperature-dependent inverse susceptibility for  $\text{YbCo}_2\text{Zn}_{20}$  and  $\text{YbOs}_2\text{Zn}_{20}$ . b) Electrical resistivity. (Inset) Low temperature resistivity as a function of  $T^2$  for  $T=\text{Fe}, \text{Rh}, \text{Ru}, \text{Os}, \text{Ir}$ ; note separate axes for  $T=\text{Os}$  on top and right. c) Low temperature-specific heat  $C$ , divided by temperature, as a function of  $T^2$  ( $T=\text{Co}$  not shown here). d) Low temperature electrical resistivity (left axis) and  $C/T$  (right axis) of  $\text{YbCo}_2\text{Zn}_{20}$  as a function of  $T^2$ .

T	$a$ , Å	$\Theta$ , K	$\mu_{\text{eff}}$ , $\mu_B$	$\chi_0$ , $10^{-3} \text{ cm}^3/\text{mole}$	$\chi_{\text{max}}$ , $10^{-3} \text{ cm}^3/\text{mole}$	$T_{\chi_{\text{max}}}$ , K	$\rho_0$ , $\mu\Omega \text{ cm}$	$A$ , $\frac{\mu\Omega \text{ cm}}{\text{K}^2}$	RRR	$\gamma$ , $\frac{\text{mJ}}{\text{mol K}^2}$	WR	KWR, $\frac{\mu\Omega \text{ cm mole}^2 \text{ K}^2}{\text{mJ}^2}$	$N$	$T_K$ , K
Fe	14.062	-22.6	4.5	58.0	65.1	14.0	2.1	$5.4 \times 10^{-2}$	31.2	520	1.2	$2.0 \times 10^{-7}$	8	33
Co	14.005	-4.3	4.3	415.1			21	165	2.8	7,900		$27 \times 10^{-7}$	4	1.5
Ru	14.193	-15.5	4.5	58.9	65.4	13.5	5.3	$6.8 \times 10^{-2}$	10.9	580	1.1	$2.0 \times 10^{-7}$	8	30
Rh	14.150	-15.9	4.4	77.7	82.4	5.3	5.6	$54 \times 10^{-2}$	11.8	740	1.3	$10.1 \times 10^{-7}$	4	16
Os	14.205	-19.18	4.5	60.0	60.7	11.5	17	$53 \times 10^{-2}$	4.4	580	1.1	$15 \times 10^{-7}$	4	20
Ir	14.165	-23.8	4.4	55.9	56.3	6.5	8.8	$33 \times 10^{-2}$	8.9	540	1.2	$11 \times 10^{-7}$	4	21

Table 4.1: From [Torikachvili 2007] are shown the cubic parameter lattice,  $a$ ; paramagnetic Curie–Weiss temperature,  $\Theta$ ; the effective moment,  $\mu_{\text{eff}}$ ; low temperature magnetic susceptibility,  $\chi_0$  taken at 1.8 K; magnetic susceptibility maximum,  $\chi_{\text{max}}$ ; residual resistivity,  $\rho_0$ , taken at 20 mK;  $A$  coefficient from the  $T^2$  resistivity (with range of fit below); RRR; Sommerfeld coefficient,  $\gamma$ ; Wilson ratio, WR, Kadowaki–Woods ratio, KWR; degeneracy,  $N$  and estimated Kondo temperature,  $T_K$ .

## 4.2. Introduction of YbCo<sub>2</sub>Zn<sub>20</sub>

at very low temperatures,  $T < 0.2$  K, its ground state corresponds also to a Fermi liquid as shown in figure 4.3 d) with a large coefficient of the  $T^2$  resistivity  $A \approx 165 \mu\Omega \text{ cm}/\text{K}^2$ .

No indications of magnetic order nor superconductivity down to 20 mK are found in any member of the YbT<sub>2</sub>Zn<sub>20</sub> family. Nevertheless, YbCo<sub>2</sub>Zn<sub>20</sub> is considered to be close to a QCP due to its rather low  $T_K \approx 1$  K. In fact, Saiga *et al.* revealed that pressure induces a magnetically ordered state above a critical pressure of only  $\approx 1$  GPa [Saiga 2008]. This finding has opened the study of quantum criticality in a new Yb-based heavy fermion family.

In summary, the fundamental properties of the YbT<sub>2</sub>Zn<sub>20</sub> systems are:

- A strong hybridization between 4*f* and conduction electrons is expected because of the high coordination Zn ions surrounding the Yb ion.
- The Yb site has a high symmetry (cubic) with a nearly spherical cage structure. The CEF splitting is expected to be small and therefore, the degeneracy  $N$  of the Yb ion may play a relevant role in the formation of the heavy fermion state.
- The magnetic interactions are expected to be weak due to the large Yb-Yb distance ( $d_{Yb-Yb} \approx 6 \text{ \AA}$ ). This favors the formation of the heavy fermion state and maybe other exotic ordered states could also arise.

## 4.2 Introduction of YbCo<sub>2</sub>Zn<sub>20</sub>

In the past few years, YbCo<sub>2</sub>Zn<sub>20</sub> has attracted much attention due to its “striking” physical properties related to its large Sommerfeld coefficient. Interesting phenomena arise when a magnetic field or pressure are applied which makes YbCo<sub>2</sub>Zn<sub>20</sub> a good candidate for quantum criticality studies.

### 4.2.1 Heavy fermion state

Takeuchi *et al.* measured the temperature dependence of the specific heat of YbCo<sub>2</sub>Zn<sub>20</sub> and the non-4*f* reference compound LuCo<sub>2</sub>Zn<sub>20</sub> (figure 4.4 a)) [Takeuchi 2011b]. Above 30 K the specific heat data are almost identical in both compounds, suggesting that the total CEF splitting is small, about 30 K. YbCo<sub>2</sub>Zn<sub>20</sub> shows a shoulder-like anomaly at 3 K and then the specific heat  $C$  decreases rapidly with decreasing temperature (see the inset). A second anomaly appears at 1 K. These features are better distinguished when the magnetic specific heat of YbCo<sub>2</sub>Zn<sub>20</sub>  $C_{mag} = C(\text{YbCo}_2\text{Zn}_{20}) - C(\text{LuCo}_2\text{Zn}_{20})$  is plotted as  $C_{mag}/T$  vs  $T$  (figure 4.4 b)). With decreasing temperature, a bump around 2 K arises, then  $C_{mag}/T$  increases logarithmically below 1 K and it saturates around 0.2 K with a large value about  $7.9 \text{ J}/(\text{molK}^2)$  which indicates the formation of the heavy fermion state with large quasi-particle masses, as  $\gamma \propto m^*$ , and a rather low Kondo temperature is estimated,  $T_K \leq 1\text{K}$ .

From de Haas-van Alphen (dHvA) measurements Ohya *et al.* have determined the cyclotron effective mass  $m_c^*$  in YbCo<sub>2</sub>Zn<sub>20</sub> [Ohya 2010]. In figure 4.5 the field dependence of the  $A$  coefficient of the  $T^2$  electrical resistivity and the  $m_c^*$  are shown. At zero field,  $A$  is rather large,  $A \approx 165 \mu\Omega \text{ cm}/\text{K}^2$ . But when a magnetic field is applied both  $m_c^*$  and  $\sqrt{A}$  strongly decreases. From this kind of plot is possible to estimate the  $m_c^*$  at zero field which at  $F = 3.56 \times 10^7 \text{ Oe}$  is large, about  $200 m_0$ .

The origin of the heavy fermion properties of YbCo<sub>2</sub>Zn<sub>20</sub> is still unclear. The occurrence of such an extremely large  $\gamma$  has led to systematic investigations of its magnetic and structural properties

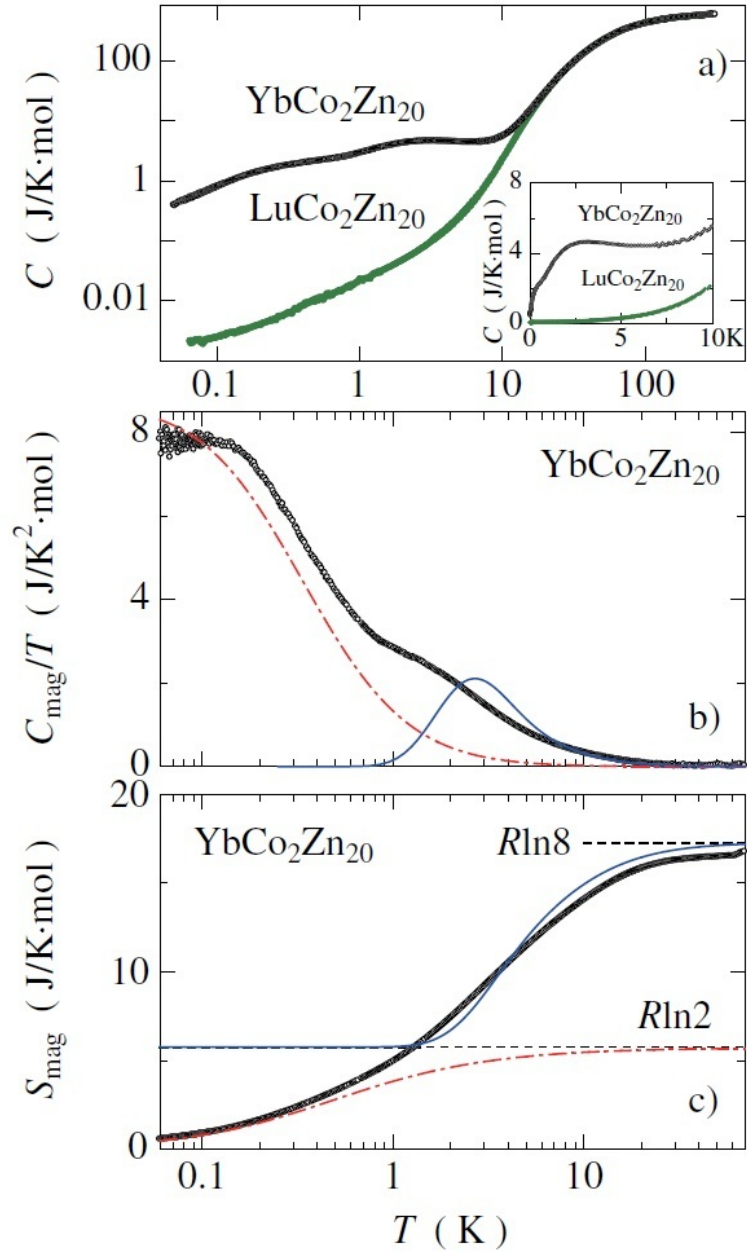


Figure 4.4: a) Temperature dependence of the specific heat  $C$  of  $\text{YbCo}_2\text{Zn}_{20}$  and the reference compound  $\text{LuCo}_2\text{Zn}_{20}$  plotted on log-log scale. The inset shows the data for  $T < 10$  K plotted on linear scales. b) and c) show the temperature dependence of the magnetic specific heat in the form of  $C_{\text{mag}}/T$  and the magnetic entropy  $S_{\text{mag}}$  of  $\text{YbCo}_2\text{Zn}_{20}$  on a logarithmic  $T$  scale, respectively. The red dot-dashed lines show theoretical curves and the blue solid lines are calculated on the basis of the CEF model [Takeuchi 2010].

## 4.2. Introduction of $\text{YbCo}_2\text{Zn}_{20}$

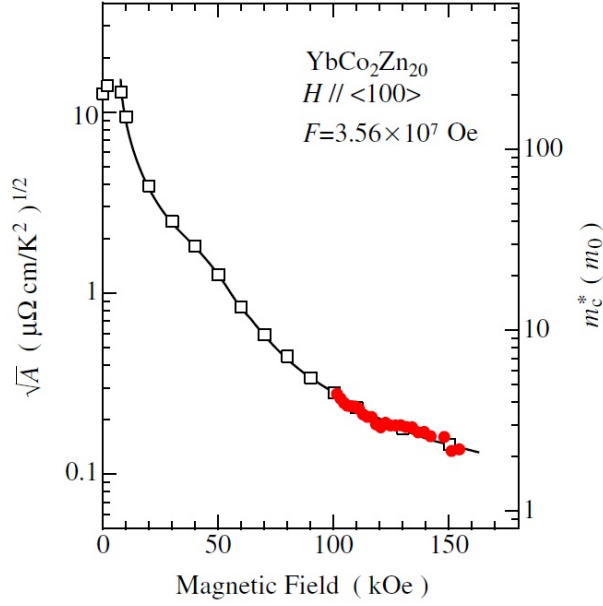


Figure 4.5: The magnetic field dependence of the  $\sqrt{A}$  coefficient for  $J\parallel H\parallel\langle 100\rangle$  shown by squares (left vertical axis). On the right, the field dependence of  $m_c^*$  for  $F = 3.56 \times 10^7$  Oe, shown by closed circles for  $H\parallel\langle 100\rangle$  (on the right) [Ohya 2010].

[Nakanishi 2009, Takeuchi 2011b, Kaneko 2012]. A key point to understand the low-temperature properties is to determine the CEF splitting levels.

By analyzing the magnetic entropy  $S_{mag}$  from figure 4.4 (c), some relevant information of the electronic state of  $\text{YbCo}_2\text{Zn}_{20}$  can be inferred.  $S_{mag}$  crosses  $R\ln 2$  just above 1 K, which corresponds to a degeneracy of the  $\text{Yb}^{3+}$  ion of  $N = 2$  and a spin  $S = 1/2$ .  $S_{mag}$  increases monotonically with increasing temperature up to 30 K, when it reaches  $S_{mag} \approx 17 \text{ J}/(\text{Kmol})$ , a value very close to  $R\ln 8 = 17.3 \text{ J}/(\text{Kmol})$ , which corresponds the total entropy expected for the  $J = 7/2$  multiplet of  $\text{Yb}^{3+}$  [Takeuchi 2011b]. Then, it is possible to deduce that the total CEF splitting in  $\text{YbCo}_2\text{Zn}_{20}$  is rather small, about 30 K. In  $\text{YbIr}_2\text{Zn}_{20}$ , for example, the CEF splitting is significantly larger, about 106 K [Takeuchi 2010].

Takeuchi *et al.* have proposed a CEF schema based on the results of susceptibility, heat capacity and magnetization measurements. The cubic CEF splits the  $J = 7/2$  multiplet of the  $\text{Yb}^{3+}$  ion into a  $\Gamma_6$  doublet, a  $\Gamma_7$  doublet and a  $\Gamma_8$  quartet. The CEF Hamiltonian for the cubic site symmetry is given in terms of the Stevens operators by

$$\mathcal{H}_{CEF}^{cubic} = B_4(O_4^0 + 5O_4^4) + B_6(O_6^0 - 21O_6^4) \quad (4.1)$$

$$= W \left[ x \left( \frac{O_4^0 + 5O_4^4}{F(4)} \right) + (1 - |x|) \left( \frac{O_6^0 - 21O_6^4}{F(6)} \right) \right], \quad (4.2)$$

where  $B_l$  are the CEF parameters,  $O_l^m$  are the Stevens operators, and  $F(4) = 60$  and  $F(6) = 1260$  for the  $\text{Yb}^{3+}$  ion with  $J = 7/2$ . Takeuchi *et al.* propose a set of parameters of  $x = 0.95$  and  $W = -0.95$ , which leads to the following CEF schema:  $\Gamma_6(0 \text{ K}) - \Gamma_8(9.1 \text{ K}) - \Gamma_7(28.5 \text{ K})$  (see figure 4.6 a)) and [Takeuchi 2011b] for more details).

The anomaly in  $C_{mag}/T$  around 2 K can be qualitatively explained as a Schottky excitation among the  $4f$  CEF levels of the  $\text{Yb}^{3+}$  ion. The red dot-dashed line in figure 4.4b) corresponds

to the theoretical specific heat based on the resonant level model using  $S = 1/2$  and a Kondo temperature  $T_K = 1\text{K}$ .

From all of this, it can be deduced that the extremely large value of  $C_{mag}/T$  at low temperatures is due to the Kondo effect below  $T_K \approx 0.2-1\text{K}$  originate from the doublet ground state and it does not come from a degenerated crystal-field ground state, as the energy of the first excited CEF level is much larger than the energy scale of the Kondo temperature [Takeuchi 2011b, Kaneko 2012].

Recent neutron scattering measurements on poly crystalline  $\text{YbCo}_2\text{Zn}_{20}$  samples [Kaneko 2012] corroborates the CEF scheme proposed by Takeuchi *et al.* even though there is a small discrepancy in the energy of the first excited level as shown in figure 4.6. But the overall splitting energy is consistent with the suggested model.

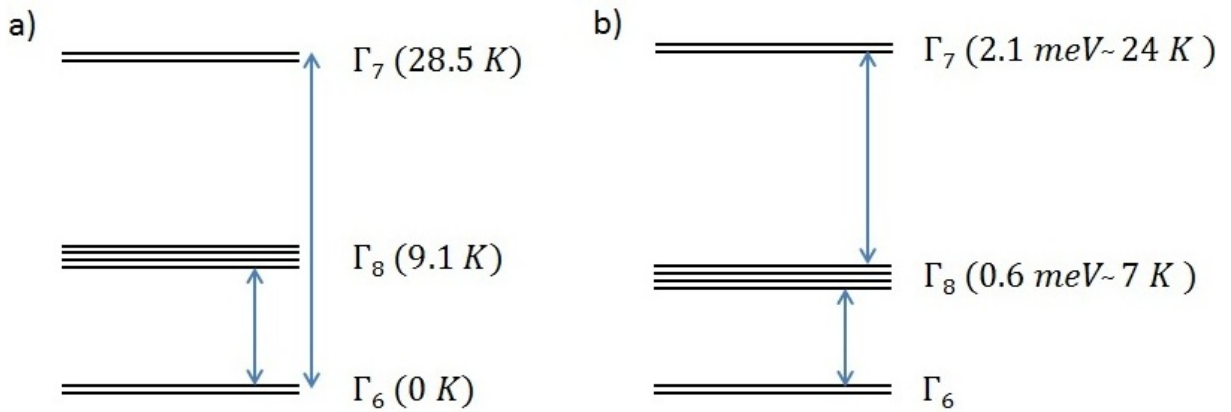


Figure 4.6: Scheme of the CEF levels a) from the model proposed by Takeuchi *et al.* from ac-susceptibility, magnetization and specific heat measurements [Takeuchi 2011b] and b) from neutron scattering measurements on poly-crystalline  $\text{YbCo}_2\text{Zn}_{20}$  samples [Kaneko 2012]. See details in text.

## 4.2.2 Physical properties under magnetic field

### 4.2.2.1 Metamagnetism

Down to 1.8 K the susceptibility of  $\text{YbCo}_2\text{Zn}_{20}$  follows a Curie-Weiss law with a paramagnetic Curie temperature  $\Theta = -4.3\text{K}$  and an effective magnetic moment  $\mu_{eff} = 4.3\mu_B/\text{Yb}$  as shown in figure 4.3. But at lower temperatures, the  $\chi_{ac}(T)$  in figure 4.7 shows a broad maximum at  $T_{\chi_{max}} = 0.32\text{K}$  associated to the formation of the heavy fermion state.

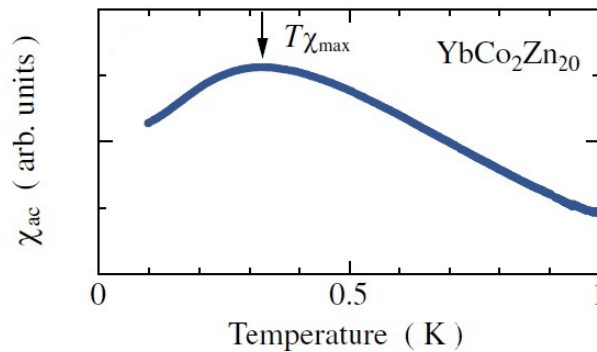


Figure 4.7: Temperature dependence of ac-susceptibility in  $\text{YbCo}_2\text{Zn}_{20}$  [Ohya 2010].

## 4.2. Introduction of YbCo<sub>2</sub>Zn<sub>20</sub>

Figure 4.8 a)-c) shows the field dependence of the ac-susceptibility, heat capacity and magnetoresistance of YbCo<sub>2</sub>Zn<sub>20</sub> for  $H \parallel \langle 100 \rangle$ . A peak in  $\chi_{ac}$  is clearly observed at  $H_m = 5.7$  kOe, which is most likely due to a non linear increase of magnetization. A step-like jump is also observed in the longitudinal magnetoresistance for  $J \parallel H \parallel \langle 100 \rangle$  at  $H_m \approx 5$  kOe for  $T < T_{\chi_{max}}$ . The field dependence of the specific heat  $C(H)$  is more complex. At 95 mK it shows two peaks which are located at 4.0 and 7.5 kOe respectively. This two-peak structure is not seen anymore above  $T \approx 0.3$  K. The likely metamagnetic behavior seen at  $H_m = 5.7$  kOe in the  $\chi_{ac}$  and magnetoresistance plots, it is now located in the  $C(H)/T$  roughly between the two peaks [Ohya 2010].

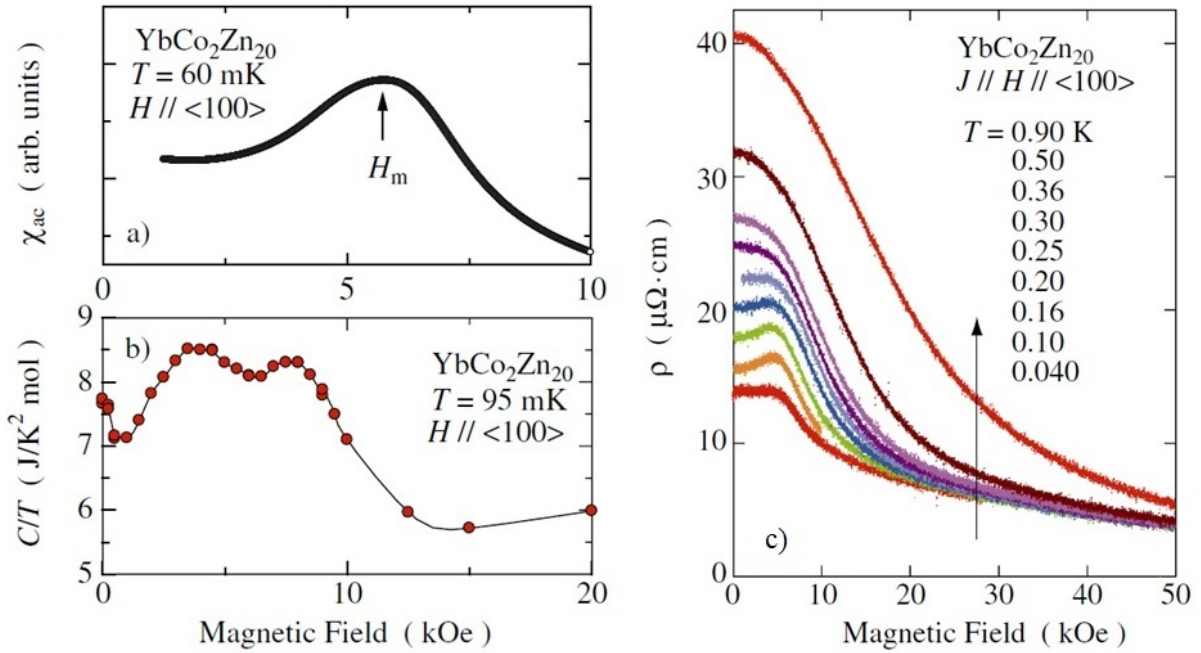


Figure 4.8: *Magnetic field dependences of a) ac-susceptibility at 60 mK for  $H \parallel \langle 100 \rangle$  b) specific heat in form  $C/T$  at 95 mK for  $H \parallel \langle 100 \rangle$  and c) longitudinal magnetoresistance for  $J \parallel H \parallel \langle 100 \rangle$  [Ohya 2010].*

In figure 4.9 the  $(H, T)$  phase diagram of YbCo<sub>2</sub>Zn<sub>20</sub> is shown. The circles correspond to  $H_m$  from the magnetoresistance, the triangles are the two-peak structure from heat capacity measurements  $C(H)$  and the square is the value of  $T_{\chi_{max}}$  [Ohya 2010].

Ohya *et al.* have also measured the temperature dependence of  $\rho(T)$  under several magnetic fields (see figure 4.10). At 0 kOe,  $\rho(T)$  follows a Fermi liquid relation  $\rho = \rho_0 + AT^2$  for  $T < 0.140$  mK. At  $H = 4$  kOe,  $\rho(T)$  shows a T-linear dependence for  $T < 0.2$  K, revealing a non-Fermi liquid behavior. For  $H > 8$  kOe, the Fermi liquid behavior appears again and it expands to higher temperature range. The magnetic field dependence of the A coefficient was already shown in figure 4.5 but not yet analyzed. Firstly, for  $H < H_m$  A increases with increasing magnetic field up to  $H \approx H_m = 5.7$  kOe. At  $H_m$  the authors could not determine its value as  $\rho(T)$  shows NFL behavior. Above  $H_m$ , A is strongly reduced with increasing field, from  $\sqrt{A} = 12.6(\mu\Omega \text{cm}/K^2)^{1/2}$  at 0 kOe to  $\sqrt{A} = 0.145(\mu\Omega \text{cm}/K^2)^{1/2}$  at 150 kOe. It is reduced about a factor of  $10^2$  at high fields [Ohya 2010].

The metamagnetic behavior is definitively proved by recent magnetization measurements below  $T_{\chi_{max}}$  [Shimura 2011] as shown in figure 4.11. A metamagnetic crossover is indeed observed at  $H_m = 0.6$  T which is consistent with the anomalies observed in the ac-susceptibility, resistivity and heat capacity at  $H_m = 0.57$  T previously reported. It is much clear in the inset of figure 4.11 where

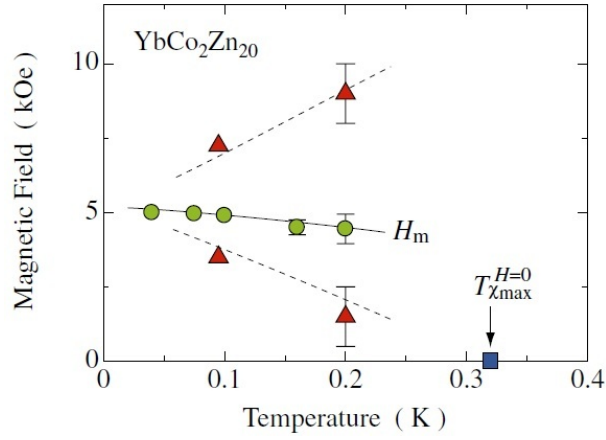


Figure 4.9: Phase diagram obtained by the magnetoresistance (circles) and specific heat (triangles) for  $H \parallel \langle 100 \rangle$  and ac-susceptibility (squares) measurements. The solid line indicates the temperature dependence of the magnetic field showing the metamagnetic like behavior  $H_m$  and broken lines show the magnetic field where the  $C/T$  shows the two peak structure at constant temperature. These lines do not correspond to real transitions but rather crossover lines [Ohya 2010].

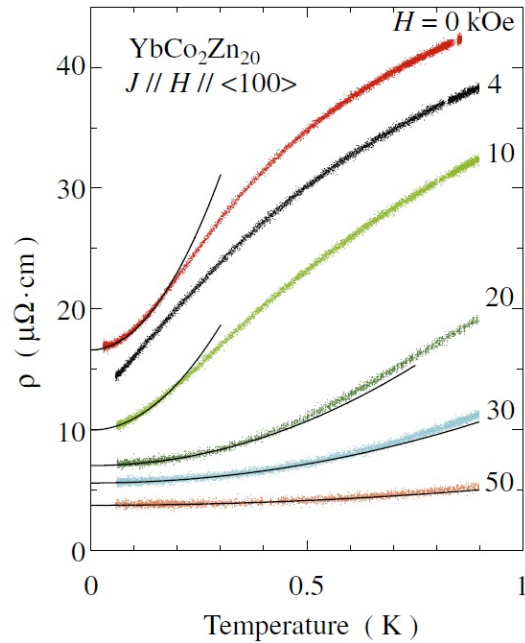


Figure 4.10: Temperature dependence of  $\rho$  under several magnetic fields in  $\text{YbCo}_2\text{Zn}_{20}$ . The data at 0 kOe are shifted upward by  $3 \mu\Omega \cdot \text{cm}$  for clarity. Solid lines indicate the  $T^2$ -dependence of the electrical resistivity [Ohya 2010].

## 4.2. Introduction of $\text{YbCo}_2\text{Zn}_{20}$

$dM/dH$  is plotted for fields below 1 T at 0.07 K.

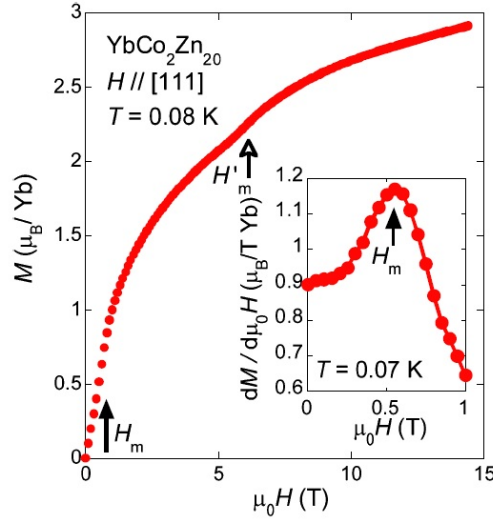


Figure 4.11: Field dependence of  $M(T)$  at 0.08 K for  $H \parallel \langle 111 \rangle$ . The inset shows the field dependence of the differential susceptibility at 0.07 K below 1 T. The solid and open arrow indicate the metamagnetic behavior at  $\mu_0 H_m = 0.6$  T and  $\mu_0 H'_m = 6$  T, respectively [Shimura 2011].

### 4.2.2.2 Field-Induced Quadrupolar Ordered Phase

The high field region of the magnetization in  $\text{YbCo}_2\text{Zn}_{20}$  in figure 4.11 shows a second anomaly at  $\mu_0 H'_m = 6$  T [Shimura 2011]. This anomaly has also been detected by Takeuchi *et al.* via resistivity measurements as shown in figure 4.12 [Takeuchi 2011b] and it has been associated to a field-induced ordered phase (FIOP) (for detailed information see the cited references)<sup>2</sup>.

Figure 4.12 a) shows the  $\rho(H)$  for  $J \parallel \langle 110 \rangle$  direction for several field angles  $\theta$  at 0.08 K. The magnetic field was rotated within the  $\langle 110 \rangle$  plane and  $\theta$  was defined as the angle between the direction of the magnetic field and the  $\langle 110 \rangle$  direction [Takeuchi 2011b].

The metamagnetic transition at  $\mu_0 H_m = 5.7$  kOe for  $H \parallel \langle 100 \rangle$  direction ( $\theta = 0^\circ$ ) shows almost no anisotropy when the magnetic field is tilted. On the contrary, the FIOP transition,  $H_Q$ , is only detected for a reduced angular range  $\Theta$  around the  $\langle 111 \rangle$  direction. For  $\theta > 40^\circ$ , a bump arises around 60 kOe. It becomes a clear peak for  $\theta = 54.7^\circ$  which corresponds to  $H \parallel \langle 111 \rangle$ . For higher field angle  $\theta$ , the peak at  $H_Q \approx 60$  kOe shifts to higher fields and disappears at  $\theta \approx 80^\circ$ .

The temperature dependences below 1.2 K of  $H_m$  and  $H_Q$  are shown in figure 4.12 b). With increasing temperature  $H_m$  rapidly smears out for  $T > 0.3$  K whereas the peak  $H_Q$  slightly shifts to higher fields and it becomes broader but it is still detected up to  $T > 0.6$  K. For higher temperatures it becomes a weak shoulder-like anomaly. This temperature dependence of  $H_Q$  was also observed in magnetization measurements [Shimura 2011].

### 4.2.2.3 H-T phase diagram of the FIOP

Figure 4.13 shows the  $(H - T)$  phase diagram of  $\text{YbCo}_2\text{Zn}_{20}$  [Shimura 2011]. For  $H > 3$  T another (broad) peak arises in the  $M(T)$  curves (not shown here). The temperature at which this peak

<sup>2</sup>Shimura and Takeuchi use two different nomenclatures and units for the FIOP. While Shimura uses the expression  $H'_m$ , Takeuchi uses  $H_Q$ . The former expresses the magnetic field in Tesla while Takeuchi in kOe. I will respect each nomenclature and units for each author.

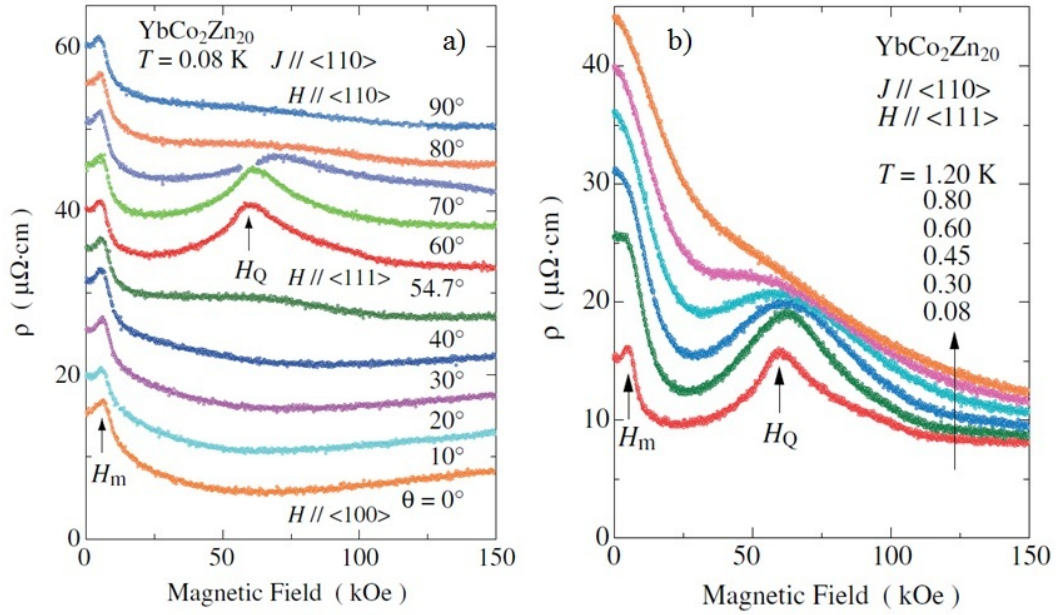


Figure 4.12: a) Field dependence of the electrical resistivity at  $0.08\text{ K}$  for  $H$  and  $J \parallel \langle 111 \rangle$  for different field angles  $\theta$  [Takeuchi 2011b]. b) Temperature dependence of  $H_m$  and  $H_Q$  [Shimura 2011].

arises is defined as  $T_{Max}$ . At even higher fields,  $H > 6\text{ T}$ , a kink in the  $M(T)$  curves is observed and its position corresponds to  $T_o$ . The  $T_o(H)$  line smoothly connects with the  $H'_m(T)$  line. This  $(H - T)$  phase diagram has been corroborated via heat capacity and resistivity measurements by Takeuchi *et al.* It is remarkably that  $\text{YbCo}_2\text{Zn}_{20}$  is likely to be the first Yb-based heavy fermion compound where a FIOP has been observed.

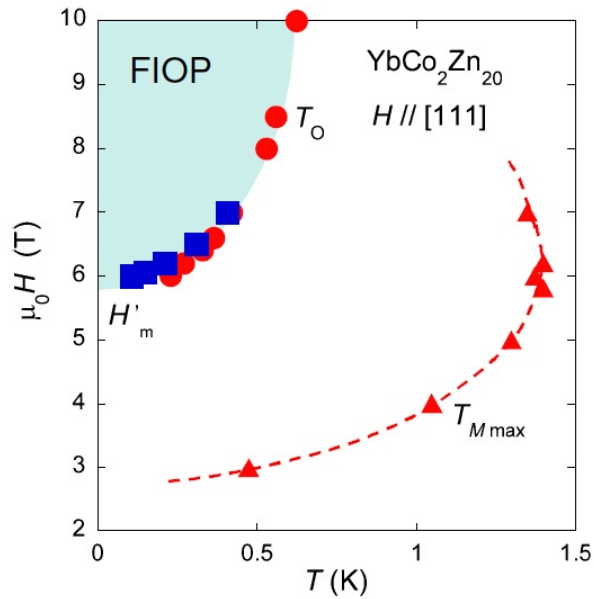


Figure 4.13:  $(H - T)$  phase diagram for  $H \parallel \langle 111 \rangle$  direction for  $\text{YbCo}_2\text{Zn}_{20}$ . Closed circles and squares indicate  $T_o$  and  $H'_m$ , respectively. Filled triangles show  $T_{Max}$ . See [Shimura 2011] for more details.

## 4.2. Introduction of $\text{YbCo}_2\text{Zn}_{20}$

### 4.2.2.4 Order parameter of the FIOP

Several efforts have been done to study this FIOP in  $\text{YbCo}_2\text{Zn}_{20}$  and to determine the order parameter of this phase. Shimura et Takeuchi highlight in their work the similarities between the  $(H - T)$  phase diagram of  $\text{YbCo}_2\text{Zn}_{20}$  and those observed in some cubic Pr-based skutterudites like  $\text{PrOs}_4\text{Sb}_{12}$  [Kohgi 2003] and  $\text{PrFe}_4\text{P}_{12}$  [Tayama 2004] which show a field-induced antiferro-quadrupole (AFQ) ordered phase as shown in figure 4.14.

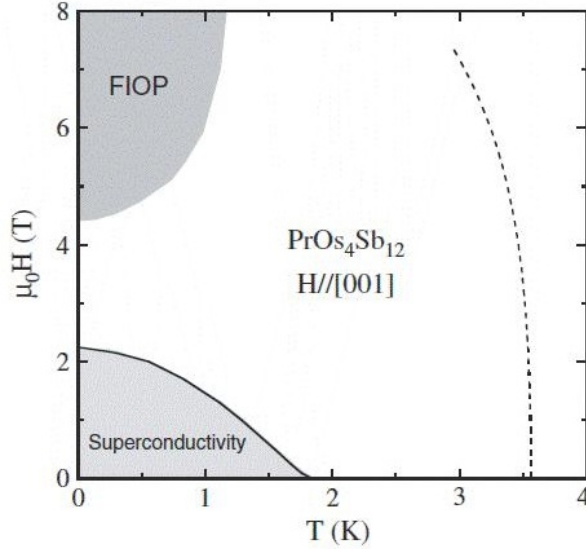


Figure 4.14: Phase diagram of the skutterudite  $\text{PrOs}_4\text{Sb}_{12}$  [Kohgi 2003].

The FIOP in  $\text{PrOs}_4\text{Sb}_{12}$  was observed in a limited angular range around the  $\langle 010 \rangle$  when  $H \parallel \langle 001 \rangle$  [Kohgi 2003]. This behavior (the limited angular range on the FIOP) is also observed in  $\text{YbCo}_2\text{Zn}_{20}$ . Kohgi *et al.* explain the phase diagram of  $\text{PrOs}_4\text{Sb}_{12}$  using a two-sublattice mean-field model with quadrupole interactions for  $O_2^0$  and  $O_2^2$ .

The results of Takeuchi *et al.* show that on the basis of the quadrupole moment  $O_2^0$  the characteristic features on the magnetization in  $\text{YbCo}_2\text{Zn}_{20}$  are well explained and the experimental  $(H - T)$  phase diagram is qualitatively reproduced [Takeuchi 2011b]. Even though there are not yet sufficient experimental data to settle the order parameter of the FIOP in  $\text{YbCo}_2\text{Zn}_{20}$ , this study strongly points out that the FIOP corresponds to a quadrupole ordered phase with a quadrupole moment of  $\Gamma_3$ -type symmetry ( $O_2^0$  or  $O_2^2$ ).

### 4.2.2.5 Valence measurement under magnetic field

In order to better understand the origin of the significant magnetic field effects in the physical properties of  $\text{YbCo}_2\text{Zn}_{20}$  (e.g.: metamagnetism, FIOP, strong decrease of the HF mass,  $m_c^*$ ), and especially if they are related to the valent degrees of freedom we performed X-ray absorption spectroscopic measurements on a single crystal ( $500 \times 400 \times 50 \mu\text{m}^3$ ) as a function of temperature and magnetic fields up to 10 T in ID 20 at the ESRF(Grenoble) in collaboration with J. P. Rueff, V. Balédent and L. Paolasini.

The XAS spectra at the Yb  $L_3$ -edge at 200, 50 and 2 K at zero field are shown in figure 4.15 a). The main peak located at 8.947 keV corresponds to the trivalent component whereas the signal of the  $\text{Yb}^{2+}$ , which should appear around 8.939 keV, is very weak and not clearly distinguished.

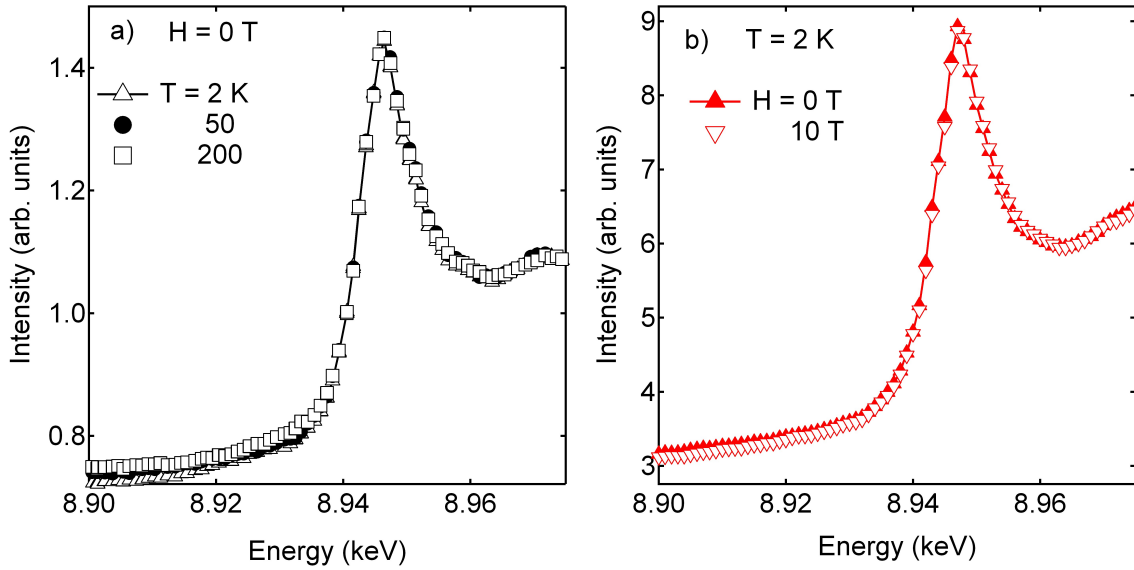


Figure 4.15:  $L_3$ -edge absorption spectra of  $\text{YbCo}_2\text{Zn}_{20}$  single-crystal sample taken a) at 200, 50 and 2 K in zero field b) at 0 and 10 T at 2 K.

There are no differences in the line shape within the experimental error down to 2 K. From this features, it can be inferred that the Yb valence will be very close to the trivalent state for the whole temperature range. This is consistent with the behavior of the susceptibility measurements which follow the Curie-Weiss law down to 1.8 K.

The absorption spectra from figure 4.15 b) are found to be insensitive to the application of a magnetic field of 10 T. No perceptible changes in the Yb valence from the nearly  $3+$  state are observed. These results are equivalent with those reported by Mito *et al.* which were measured on a powdered sample instead of a single crystal [Mito 2010].

### 4.3 High pressure phase diagram

The main contribution of this work in the study of  $\text{YbCo}_2\text{Zn}_{20}$  is to extend the known ( $P - T$ ) phase diagram to higher pressures, up to 14 GPa, and bring some information to the nature of the magnetic order through ac-susceptibility measurements and ac-calorimetry measurements under magnetic field.

#### 4.3.1 Pressure-induced magnetic order

Saiga *et al.* were the first to report the pressure-induced magnetic transition in  $\text{YbCo}_2\text{Zn}_{20}$  [Saiga 2008]. The resistivity measurements on a single crystal up to 2.37 GPa are shown in figure 4.16. They found an anomaly at  $T_M \approx 0.15$  K at about 1 GPa that shifts to higher temperatures with increasing pressure.

Pressure-induced magnetic transitions have already been observed in other Yb-based heavy fermion compounds as  $\text{YbCu}_2\text{Si}_2$  [Alami Yadri 1998],  $\text{YbIr}_2\text{Si}_2$  [Yuan 2006] and  $\text{YbNi}_2\text{Ge}_2$  [Knebel 2001]. In these compounds, the critical pressure is about  $P_c \approx 5 - 8$  GPa in contrast to the low  $P_c \approx 1$  GPa in  $\text{YbCo}_2\text{Zn}_{20}$  which is an advantage for the study of quantum critical phenomena in high-pressure experiments.

### 4.3. High pressure phase diagram

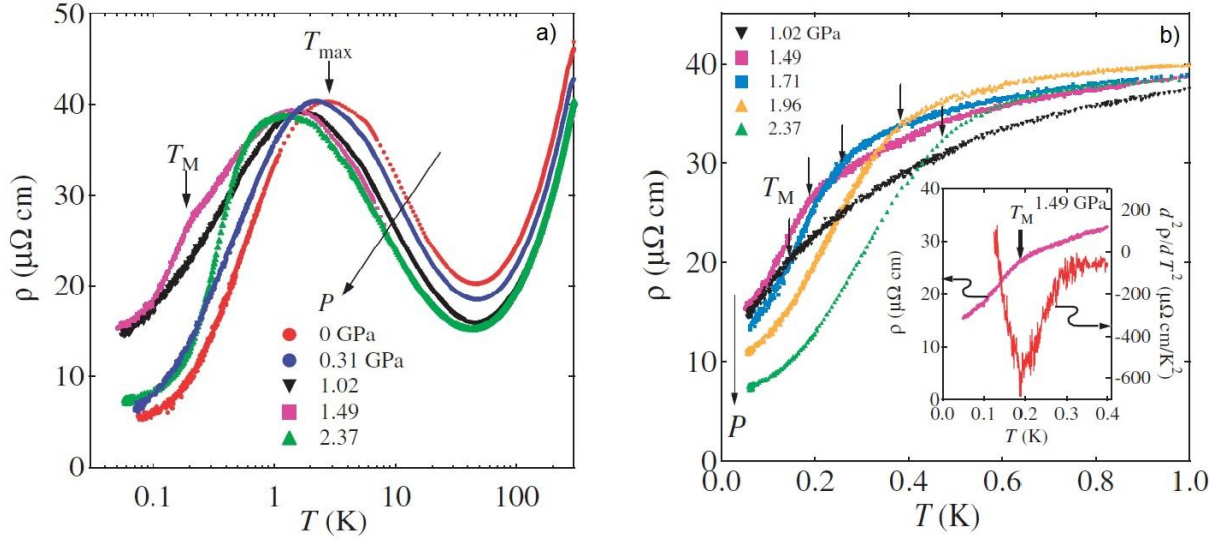


Figure 4.16: *Electrical resistivity of  $\text{YbCo}_2\text{Zn}_{20}$  as a function of the temperature a) from 300 - 0.1 K b) at low temperatures for selected pressures.  $T_{Max}$  and  $T_M$  correspond to the temperature of the maximum in the  $\rho(T)$  and the magnetically ordered temperature respectively [Matsubayashi 2010].*

At ambient pressure  $\rho(T)$  exhibits a minimum around 50 K (which does not significantly move under pressure) and below this temperature,  $\rho(T)$  follows a  $-\ln T$  dependence down to  $\approx 2.5$  K, where a broad maximum arises. Below  $T_{max}$ ,  $\rho(T)$  decreases with decreasing temperature. Applying pressure shifts  $T_{max}$  to lower temperatures. If we assume that  $T_{max}$  scales with  $T_K$ , then  $T_K$  would also decrease with increasing pressure as it is expected in Yb-based heavy fermion compounds when the system is driven near the magnetic QCP.

### Fermi Liquid properties under pressure

Figure 4.17 shows  $\rho(T)$  as a function of  $T^2$  at several pressures in order to study the effect of pressure on the Fermi liquid behavior described by  $\rho(T) = \rho_0 + AT^2$ . At ambient pressure,  $\rho(T)$  shows FL behavior at  $T < T_{FL} \approx 0.2$  K. For  $P < 0.7$  GPa, the slope of the solid line increases because the A coefficient is strongly enhanced in that pressure range (see figure 4.17) but the  $T_{FL}$  gradually decreases. NFL behavior is observed for the pressure range  $0.7 < P < 1.49$  GPa where  $\rho(T)$  deviates from the  $T^2$  dependence and it shows a  $T^n$  dependence with  $1 \leq n \leq 2$ . Finally, the FL behavior is recovered at higher pressures but in a reduced temperature range (at 1.96 GPa  $T_{FL} \approx 0.12$  K) and for lower values of the A coefficient.

The pressure dependence of A and  $\rho$  are represented in figure 4.17. As pressure increases and approaches  $P_c$ , A is strongly enhanced and achieves a value of about  $400 \mu\Omega\text{cm}/\text{K}^2$ . In the pressure range where non-Fermi liquid behavior is observed the A coefficient is not determined. The residual resistivity  $\rho_0$  shows a similar behavior. It increases with pressure and shows a broad peak slightly above  $P_c$ . The enhancement of A and  $\rho_0$  is often observed in heavy fermions systems in the vicinity of a magnetic QCP due to large critical fluctuations.

From all these experimental features, Saiga *et al.* associate the anomaly of the resistivity at  $T_M$  to the appearance of a magnetically ordered state above  $P_c$ .

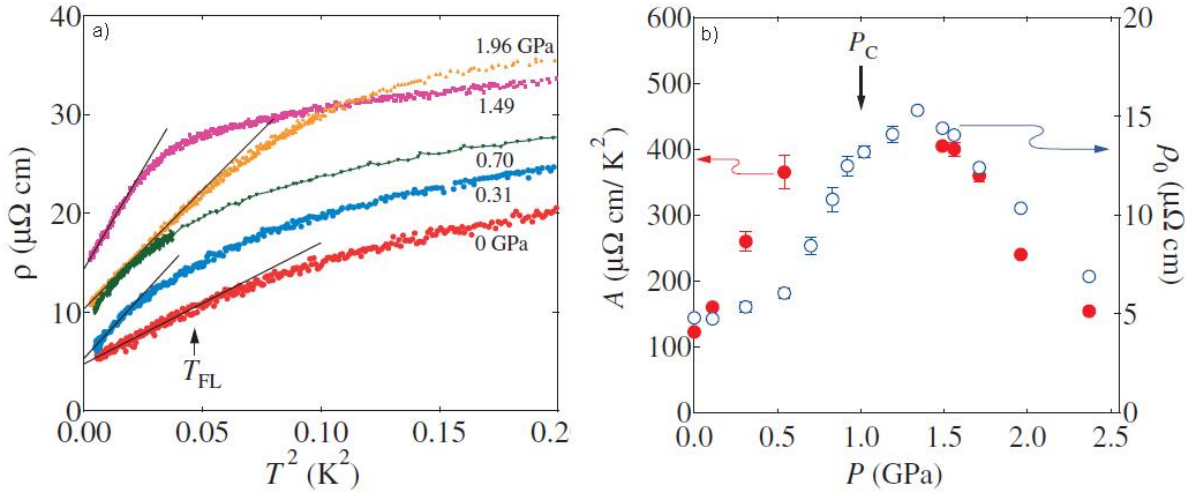


Figure 4.17: a)  $\rho(T)$  as a function of  $T^2$  at selected pressures. Solid lines are fits to  $\rho(T) = \rho_0 + AT^2$ .  $T_{FL}$  corresponds to the upper limit of the  $T^2$  dependence of  $\rho(T)$  (indicated by an arrow) b) Pressure dependence of  $A$  and  $\rho_0$  up to 2.5 GPa in  $\text{YbCo}_2\text{Zn}_{20}$  [Saiga 2008].

### 4.3.2 $P - T$ phase diagram at low pressures

The  $(P - T)$  phase diagram of  $\text{YbCo}_2\text{Zn}_{20}$  obtained by Saiga *et al.* up to 2.5 GPa is shown in figure 4.18 [Saiga 2008]. The crossover temperature  $T_{FL}$  corresponds to the upper limit of the observed  $T^2$  behavior in the  $\rho(T)$ ,  $T_M$  is the magnetic ordering temperature and  $T_{Max}$  is the temperature corresponding to the resistivity maximum. Under pressure  $T_{FL}$  is suppressed near  $P_C$  and  $T_{Max}$  decreases from 2.5 K at ambient pressure to 1 K around 2.4 GPa.  $T_M$  increases monotonically for the pressure range  $P > P_C$ .

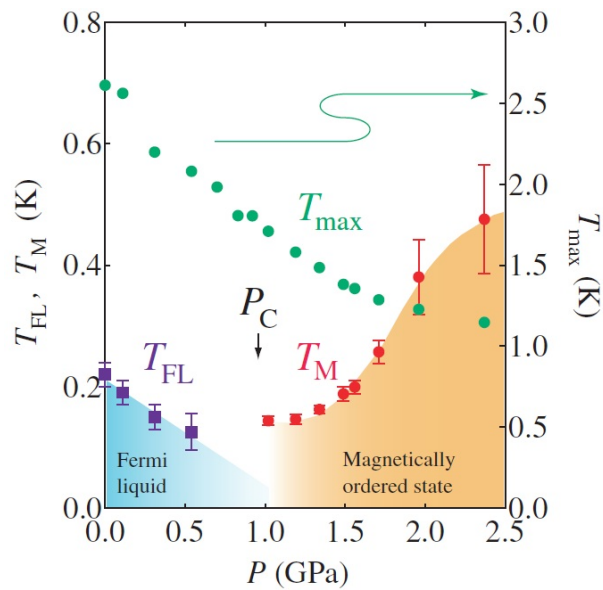


Figure 4.18:  $(P - T)$  phase diagram of  $\text{YbCo}_2\text{Zn}_{20}$  [Saiga 2008].

### 4.3. High pressure phase diagram

#### 4.3.3 $P - T$ phase diagram from ac-calorimetry studies under pressure

The ( $P - T$ ) phase diagram of  $\text{YbCo}_2\text{Zn}_{20}$  from figure 4.18) was obtained by resistivity measurements under pressure up to 2.5 GPa [Saiga 2008]. The magnetic transition manifests itself by a kink on the  $\rho(T)$  curves (figure 4.16) but it is not very marked and it smears out with increasing pressure. In this work we wanted to measure the specific heat of  $\text{YbCo}_2\text{Zn}_{20}$  under pressure and see if the anomaly would be more distinguishable.

We have measured the phase diagram up to 14 GPa via the ac-calorimetry technique of a single  $\text{YbCo}_2\text{Zn}_{20}$  crystal in a DAC with 0.7 mm culet using the dilution fridge with the *in-situ* pressure device. Only one run of measurements was necessary as the thermocouple stood the whole experiment.

In the following paragraphs we will first analyze the phase diagram up to 2.5 GPa and later up to the highest pressures in this study, 14 GPa.

#### Phase diagram up to 2.5 GPa: comparison with previously reported data

We measured the ac-calorimetry at a frequency  $f = 77$  Hz which we chose from the frequency test (see chapter 2 for more details). The curves at different pressures have been measured and compared at the same frequency.

In this paragraph the magnitude  $C/T$  is used rather than  $C$ . In figure 4.19 a) the temperature dependence of  $C(T)/T$  is plotted for all the pressures we measured up to 2.5 GPa. At 0.4 GPa,  $C(T)/T$  increases below  $T < 0.6$  K but no anomaly is detected down to 200 mK, the lowest temperature we reached.

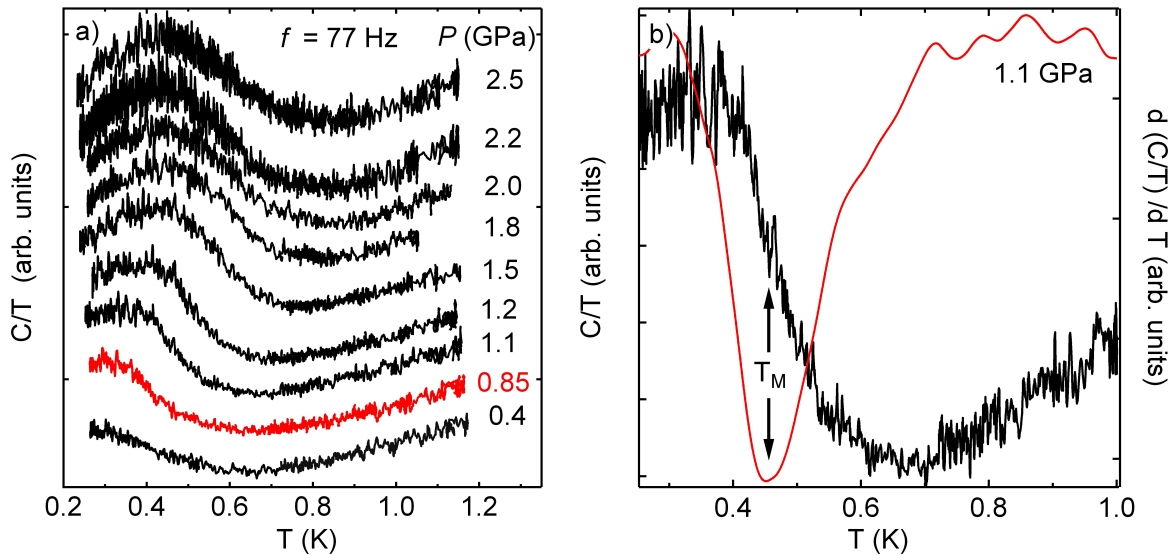


Figure 4.19: a) Temperature dependence of the ac-calorimetry of a single crystal of  $\text{YbCo}_2\text{Zn}_{20}$  plotted as  $C/T$  for all the pressures we measured up to 2.5 GPa. b) The criterion to determine  $T_M$  is shown. We took the inflection point (the minimum in the derivative curve on the right axis).

At 0.85 GPa (red curve), we start to detect a rather large anomaly at  $T \approx 0.4$  mK that we associate to the magnetic transition. The temperature at which the anomaly appears shifts with pressure and even though it gets broader it is more pronounced than the kink on the resistivity curves [Matsubayashi 2010].

Figure 4.20 a) shows the  $(P - T)$  phase diagram we obtained in comparison with the one reported in [Saiga 2008]. The criterion we used to determine the magnetic ordering temperature  $T_M$  is shown in 4.19 b) for 1.1 GPa. We took the inflection point which corresponds to the minimum in the derivative  $C/T$  versus  $T$  curve. The inflection point corresponds to the faster  $C/T$  change and the point where there is a majority volume sample change as well. As the raw data are quite noisy, before the derivative we smoothed them.

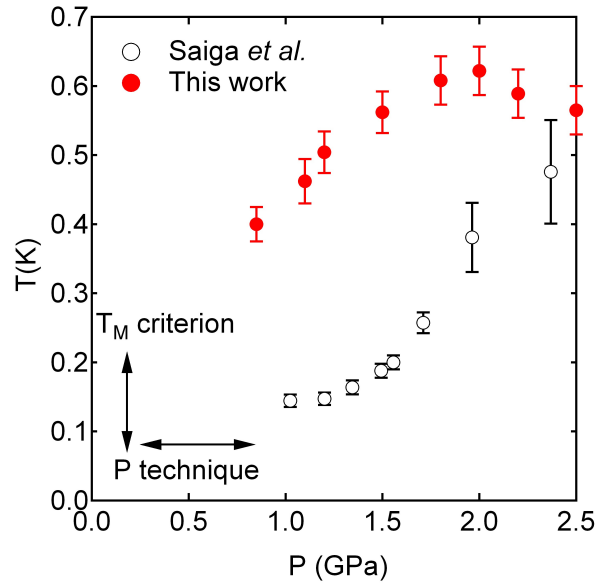


Figure 4.20:  $(P - T)$  phase diagram of  $\text{YbCo}_2\text{Zn}_{20}$  up to 2.5 GPa. Open circles correspond to  $T_M$  values from [Saiga 2008] and red points to  $T_M$  values obtained in this work by ac-calorimetry measurements.

The disagreement between our results with those from [Saiga 2008] are not negligible, especially at low pressures for  $P < 2$  GPa where we find higher values for  $T_M$  and a linear pressure dependence up to 1.5 GPa, but they become comparable for  $P \geq 1.8$  GPa. In addition, they do not detect the transition for  $P < 1$  GPa in the resistivity curves but we do in our ac-calorimetry curves at 0.85 GPa. This discrepancy in the value of  $P_c$  is not very large and could be explained by a difference in the sample quality. The difference in the values of  $T_M$  are likely to be related on the technique criterion ( $\rho$ ,  $C/T$ ) while the shift in pressure where the initial increase occurs could be due to the difference in the high pressure technique: Saiga *et al.* used a hybrid-piston-cylinder-type pressure cell with Daphne oil 7373 as pressure transmitting medium whereas we used a DAC cell with argon as pressure transmitting media which in general has better quasi-hydrostatic conditions.

### Extended $P - T$ phase diagram

The ac-calorimetry curves  $C/T$  for  $P > 3$  GPa and the  $(P - T)$  phase diagram of  $\text{YbCo}_2\text{Zn}_{20}$  up to 14 GPa are shown in figure 4.21 a) and b) respectively.

As mentioned in the previous paragraph  $T_M$  increases linearly up to 1.5 GPa. From 1.5 to 3.0 GPa it decreases slightly and above  $P > 3.0$  GPa it increases monotonically from  $T_M \approx 0.5$  K to nearly 1 K at 14 GPa. The characteristic pressure dependence of  $T_M$  will be discussed in terms of the competition of the principal energy scales of the system ( $T_K$ ,  $T_{CEF}$ ,  $T_{RKKY}$ ) in section 4.4.

### 4.3. High pressure phase diagram

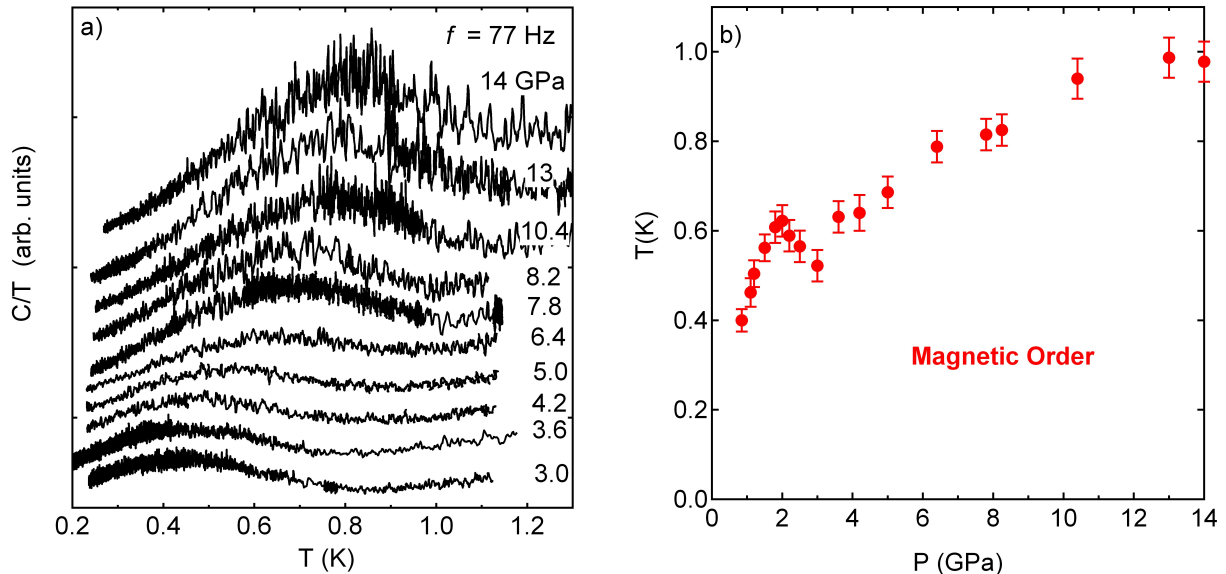


Figure 4.21: a) Temperature dependence of  $C/T$  curves of  $YbCo_2Zn_{20}$  for  $P > 3$  GPa and up to 14 GPa. Curves have been shifted for clarity. b)  $(P-T)$  phase diagram of  $YbCo_2Zn_{20}$  up to 14 GPa by ac-calorimetry measurements in this work (red points).

#### 4.3.4 Nature of the magnetic order

In chapter 3 we have shown how the existence of ferromagnetic order in  $YbCu_2Si_2$  has been determined by ac-susceptibility measurements under pressure and under magnetic field. These results motivated us to apply this technique to other compounds like  $YbCo_2Zn_{20}$  where the metamagnetic behavior found at ambient pressure might suggest a tendency towards ferromagnetism.

Here we present the ac-susceptibility measured at  $f = 723$  Hz of  $YbCo_2Zn_{20}$  in the dilution refrigerator before the pressure *in-situ* device was set in. Unfortunately the contacts of the pick-up coil short circuited after 5 pressure changes and the highest pressure we achieved was 2 GPa. But as  $P_c$  in  $YbCo_2Zn_{20}$  is only about 1 GPa, this setback did not prevent us to measure in the relevant pressure range.

In figure 4.22 the temperature dependence of the imaginary or out-of-phase contribution ( $e'' \propto \chi''$ ) of the measured signal (Lock-In output) is plotted for two selected pressures: at 0.4 GPa and 2 GPa, below and above  $P_c$  respectively. There are no differences between both curves, we do not detect any anomaly in the susceptibility curve at 2 GPa down to 0.1 K in contrast with the ac-calorimetry measurements, where  $T_M$  at 2 GPa was estimated  $T_M \approx 0.5$  mK. We also measured at 1.2, 1.35 and 1.6 GPa (not shown here) and the experimental curves are as flat as for 0.4 and 2 GPa. Notice that in figure 4.7,  $T_{\chi_{Max}}$  in the  $\chi_{ac}$  curve at ambient pressure is detected whereas we have a flat curve. The reason is that they have a larger sensitivity because they used a piston-cylinder cell where the volume of the sample is much larger than in a DAC. In a recent study, also with a piston-cylinder type cell Ohya [Taga 2012] have detected the magnetic transition under pressure with ac-susceptibility.

The arrow in figure 4.22 indicates the amplitude of the anomaly in the ac-susceptibility curves of  $YbCu_2Si_2$  above  $P_c \approx 8$  GPa. The magnetic order in  $YbCu_2Si_2$  has been identified as ferromagnetic (or at least with a ferromagnetic component).

All these elements suggest that the magnetic order is likely to be antiferromagnetic with a

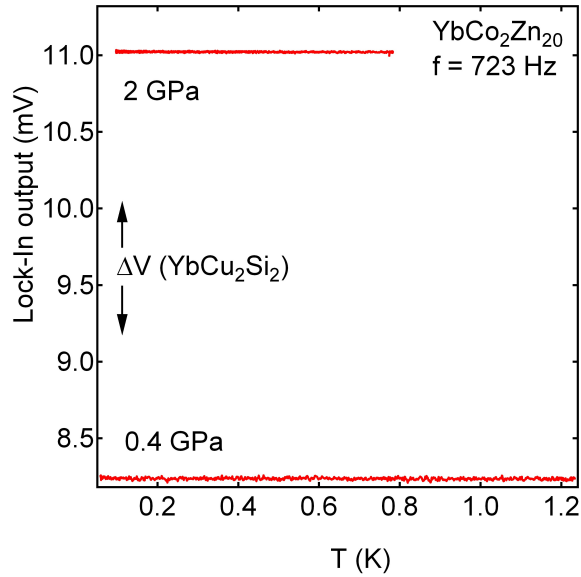


Figure 4.22: The temperature dependence of the measured signal, Lock-In output, is plotted for two selected pressures: at 0.4 GPa and 2 GPa below and above  $P_c \approx 1$  GPa respectively. The arrows indicate the amplitude of the Lock-in output measured in  $\text{YbCu}_2\text{Si}_2$  above  $P_c \approx 8$  GPa (see details in text).

magnetic ordering moment too weak to be detected by measuring the ac-susceptibility using a DAC.

Another element that supports antiferromagnetic order comes from the behavior of  $T_M$  when a magnetic field is applied as shown in figure 4.23. We applied 2, 4 and 6 T at 14 GPa in the ac-calorimetry curve and  $T_M$  slightly decreases with increasing field as shown in the  $(H - T)$  phase diagram in figure 4.23 b).

In general, in a ferromagnetic compound  $T_M$  increases with field as in  $\text{YbCu}_2\text{Si}_2$  whereas it decreases for an antiferromagnetic system. Note that the criterion to determine  $T_M$  is not the same as the criterion used for the  $(P - T)$  phase diagram as we did not measure above 1.2 K and thus we can not determine precisely the inflection point. The criterion used in this plot is shown in the curve at zero field which corresponds to the position of the maximum, using this criterion  $T_M$  is 200 mK lower than the value obtained in the  $(P - T)$  phase diagram at zero field.

Direct proof of the magnetic order has been recently reported in [Takeuchi 2011b]. Recent neutron scattering measurements<sup>3</sup> clarify that the nature of the magnetic order in  $\text{YbCo}_2\text{Zn}_{20}$  is antiferromagnetic as inferred from our results.

## 4.4 Conclusions

I present here ac-calorimetry measurements under pressure in  $\text{YbCo}_2\text{Zn}_{20}$  which extends the  $(P - T)$  phase diagram up to 14 GPa. The critical pressure in this study is  $P_c \approx 0.85$  GPa. At low pressures the  $T_M$  values are significantly higher than in previously reported data [Saiga 2008].

The whole phase diagram is now shown in figure 4.24 a) with the Fermi-liquid region (values of  $T_{FL}$  were taken from [Saiga 2008]). In 4.24 b) the pressure dependence of  $T_{Max} \propto T_K$ , which corresponds to the maximum of the resistivity is shown. The phase diagram can be interpreted in

<sup>3</sup>Cited as a private communication.

#### 4.4. Conclusions

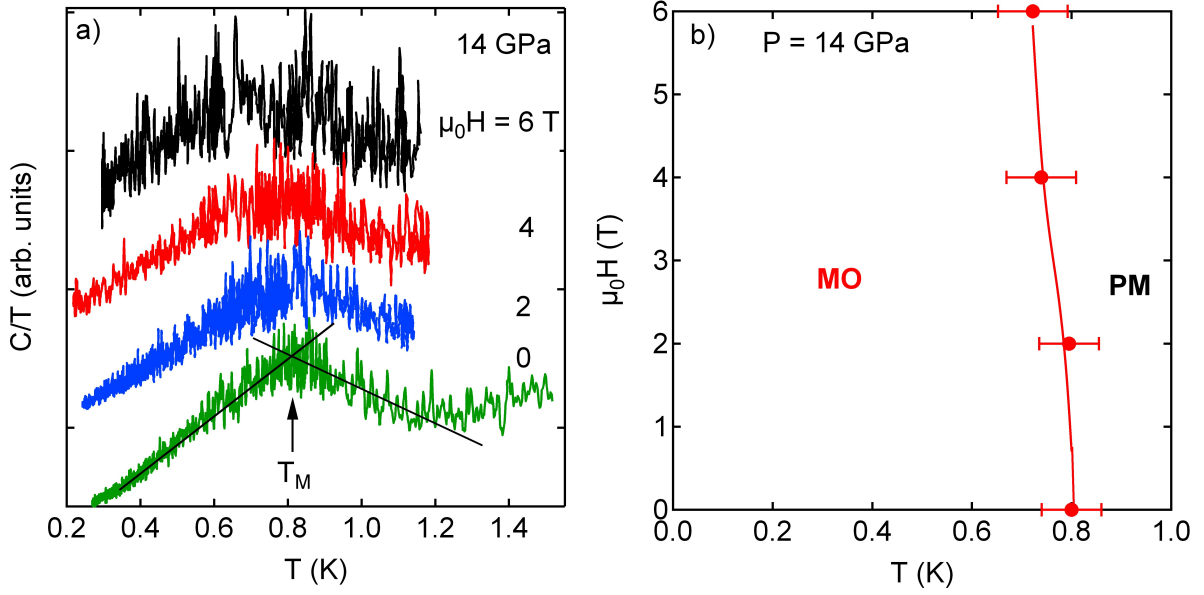


Figure 4.23: a) Temperature dependence of the ac-calorimetry curves at 14 GPa for several magnetic fields. b)  $(H - T)$  phase diagram of  $\text{YbCo}_2\text{Zn}_{20}$  at 14 GPa. The criterion used to determine  $T_M$  is shown in a) for the curve at zero field.

terms of the competition between the Kondo and RKKY interactions as in the Doniach picture.

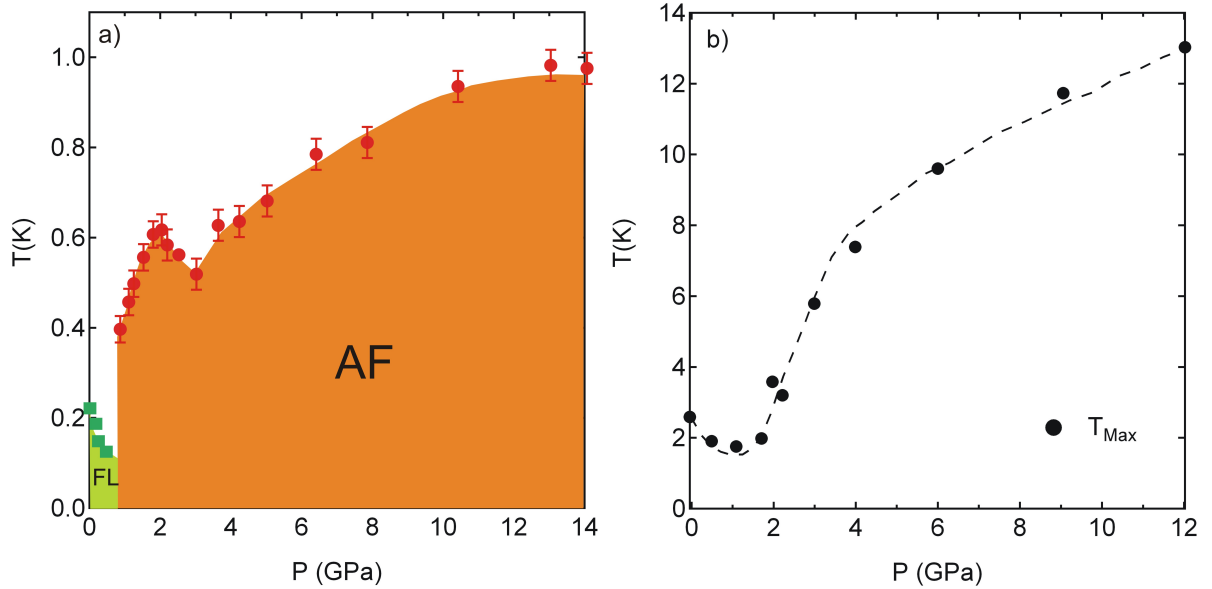


Figure 4.24: a)  $(P - T)$  phase diagram of  $\text{YbCo}_2\text{Zn}_{20}$ . Red circles correspond to the values of  $T_M$  from this work and green squares are the values of the Fermi-liquid temperature,  $T_{FL}$  from [Saiga 2008]. b) Pressure dependence of  $T_{Max}$ , the temperature where the maximum in the resistivity is observed, for  $\text{YbCo}_2\text{Zn}_{20}$  [Matsubayashi 2010] (broken lines are guides to the eyes).

For  $P < P_c$ , a heavy fermion ground state dominates but when pressure is increased  $T_{FL}$  and

$T_{Max}$  decreases as expected for Yb-based heavy-fermion compounds. Near  $P_c$  NFL behavior is observed. For  $P_c \approx 0.85$  GPa the RKKY interaction becomes dominant and a magnetic ordering state occurs at  $T_M \approx 0.4$  K.

However, the pressure dependence of  $T_M$  shows a non-monotonic behavior and it decreases from 2 to 4 GPa. Interestingly,  $T_{Max}$  exhibits a minimum near  $P \approx 1.5$  GPa, a value close to  $P_c$  and the pressure where  $T_M$  starts to decrease. Upon further increasing pressure,  $T_{Max}$  increases reaching 13 K at 12 GPa [Matsubayashi 2010]. Even though it is tempting to associate the increase of  $T_{Max}$  to the increase of  $T_K$  which might explain the non conventional behavior of  $T_M$ , we can not discard CEF effects in the pressure dependence of  $T_{Max}$  even though the overall CEF splitting in YbCo<sub>2</sub>Zn<sub>20</sub> is small. This is another hallmark of this compound, the energy scales involved in this system are low:  $T_K \leq 1$  K,  $\Delta_{CEF} \approx 9$  K (of the first excited level) and  $T_M \approx 0.4 - 1$  K.

We have also measured the ac-susceptibility and the field dependence of the ac-calorimetry curve at 14 GPa to shed some light in the nature of the magnetic order. In contrast to YbCu<sub>2</sub>Si<sub>2</sub> where a clear jump in the signal was observed when measuring in a DAC, here no anomaly was detected above  $P_c$ . This suggests that the magnetic order is probably antiferromagnetic. Also the field dependence of  $T_M$ , which decreases under field, corresponds to the behavior generally observed in antiferromagnetic compounds. Direct proof of antiferromagnetism has been recently reported by neutron scattering measurements. The non-monotonic behavior of  $T_M$  could also indicate a change of the magnetic structure under pressure. It will be interesting to repeat the ac-susceptibility measurements, but this time at  $P > 4$  GPa.

Finally, the valence of a single crystal of YbCo<sub>2</sub>Zn<sub>20</sub> has been measured using XAS under magnetic field and at different temperatures down to 2 K. The results show that there is no perceptible change from the almost trivalent state from room temperature to 2 K and neither between zero field and 10 T. This behavior contrasts with the strong field dependences observed in the physical properties under magnetic field like metamagnetism, FIOP and the strong decrease of the HF mass,  $m_c^*$ . Hence, the origin of the field effects in YbCo<sub>2</sub>Zn<sub>20</sub> close to the magnetic-nonmagnetic transition are probably related to the interaction between the magnetic field and the magnetic moments (spin) of the 4*f* electrons and not from the valence (charge degree) of the Yb ions.



# CHAPTER 5

## YbRh<sub>2</sub>Si<sub>2</sub>

---

### 5.1 Introduction

YbRh<sub>2</sub>Si<sub>2</sub> is another ternary compound with the ThCr<sub>2</sub>Si<sub>2</sub>-type tetragonal crystal structure as YbCu<sub>2</sub>Si<sub>2</sub> (see figure 4.1), but now the fuchsia spheres correspond to the *Rh* atoms instead of Cu. The lattice parameters are  $a = 4.010 \text{ \AA}$  and  $c = 9.841 \text{ \AA}$ . YbRh<sub>2</sub>Si<sub>2</sub> is a heavy fermion with  $T_K \approx 25 \text{ K}$  [Gegenwart 2006] and a Sommerfeld coefficient of  $\gamma \approx 1.2 \text{ J/molK}^2$  (from the extrapolation of the specific heat curve,  $C/T \rightarrow 0$ ). YbRh<sub>2</sub>Si<sub>2</sub> at ambient pressure is also at an intermediate-valence state and its valency is about 2.92 at room temperature. It orders antiferromagnetically at ambient pressure for  $T_N \approx 70 \text{ mK}$  [Trovarelli 2000] with a tiny magnetic moment about  $\mu_{eff} \approx 10^{-2} - 10^{-3} \mu_B$  [Gegenwart 2002, Knebel 2005].

The susceptibility follows a Curie-Weiss law for  $T > 200 \text{ K}$  along both crystallographic directions ( $a$  and  $c$ ) with  $\mu \approx \mu_{Yb^{3+}} = 4.53 \mu_B$ . As shown in figure 5.1 there is a strong magnetocrystalline anisotropy and at  $T = 2 \text{ K}$ , the magnetic susceptibility measured along the basal  $ab$  plane is about 20 times larger compared to the value measured when the magnetic field is applied along the  $c$  axis. Thus, the  $ab$  plane is the “easy” magnetization plane whereas the  $c$  axis is the “hard” magnetization axis, contrary to YbCu<sub>2</sub>Si<sub>2</sub>.

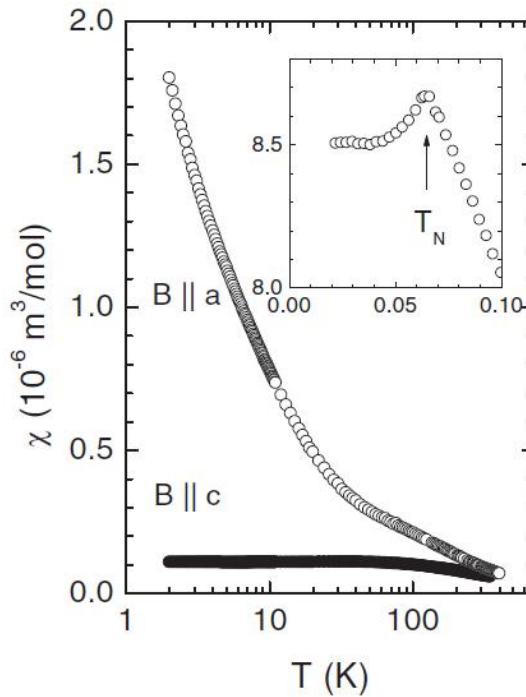


Figure 5.1: *Magnetic susceptibility for both crystallographic directions ( $a$  and  $c$ ) in YbRh<sub>2</sub>Si<sub>2</sub>. The inset shows the sharp AFM transition at 70 mK [Gegenwart 2003].*

## 5.1. Introduction

### 5.1.1 Crystal electric field

From inelastic neutron-scattering measurements on  $\text{YbRh}_2\text{Si}_2$  powder the CEF excitations of the  $\text{Yb}^{3+}$  ion in the tetragonal symmetry have been determined and the scheme is given in figure 5.2 [Stockert 2006].

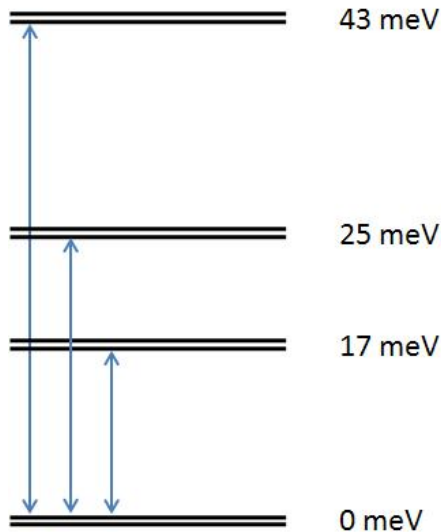


Figure 5.2: CEF scheme obtained by inelastic neutron-scattering measurements using  $\text{YbRh}_2\text{Si}_2$  powder [Stockert 2006].

The doublet ground state is well separated from the first excited CEF level ( $17 \text{ meV} \approx 200 \text{ K}$ ). This CEF level scheme is consistent with the magnetic entropy  $S_m(T)$  of the  $\text{Yb}^{3+}$  where the value corresponding to the  $J = 7/2$  multiplet is recovered above room temperature while the single-ion Kondo temperature of the CEF ground state which corresponds to  $S_m(T_K) = R \ln 2$  is found for  $T_K \approx 25 \text{ K}$  [Gegenwart 2006].

### 5.1.2 Field-induced quantum critical point

On cooling,  $\text{YbRh}_2\text{Si}_2$  shows strong deviations from the standard FL properties already at ambient pressure and zero magnetic field, being the first Yb-based HF compound showing NFL behavior at such conditions. In fact, only a few examples of stoichiometric HF systems does it (e.g.  $\text{UBe}_{13}$ ,  $\text{CeNi}_2\text{Ge}_2$  and  $\text{CeCu}_2\text{Si}_2$ ) [Mederle 2001]. As shown in figure 5.3 a) the temperature dependence of the resistivity is linear ( $\Delta\rho = \rho - \rho_0 \propto T$ ) over a large temperature range and the specific heat increases as  $C/T \propto -\ln T$  between 0.3 and 10 K (figure 5.3 b) ) [Trovarelli 2000]. Very often, NFL effects are observed not just at, but also in the vicinity of a magnetic quantum critical point like in some Ce-based HF compounds by varying the chemical composition [Löhneysen 1994] or in stoichiometric HF systems by applying hydrostatic pressure as a control parameter to reach the QCP like in  $\text{YbCu}_2\text{Si}_2$  and  $\text{YbCo}_2\text{Zn}_{20}$  (see details in Chapter 3 and 4).

In contrast,  $\text{YbRh}_2\text{Si}_2$  is at ambient pressure located very close to an AFM field-induced QCP. The Néel temperature  $T_N$  decreases with increasing field and the weak magnetic order is suppressed in a field of  $H_c \approx 0.06 \text{ T}$  applied in the easy magnetic  $ab$  plane. Due to the large magnetic anisotropy the critical field necessary in the hard  $c$  axis is  $H_c \approx 0.6 \text{ T}$ . In figure 5.4 the  $(T - H)$  phase diagram is shown for  $H \perp c$  [Gegenwart 2007].

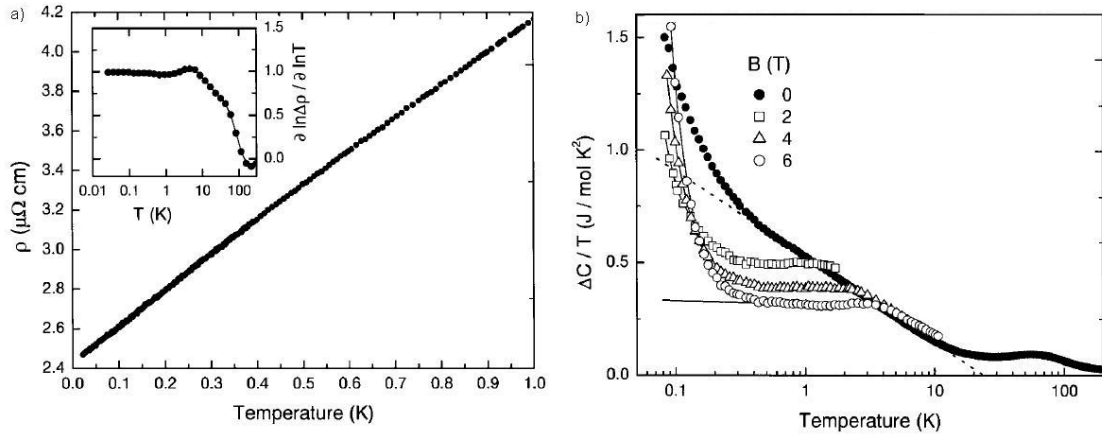


Figure 5.3: a) Low-temperature electrical resistivity of  $\text{YbRh}_2\text{Si}_2$  at ambient pressure along the  $a$  axis obeying  $\rho(T) = \rho_0 + bT^n$ , with  $n \approx 1$ . (Inset) Temperature dependence of the effective exponent  $n$ , defined as the logarithmic derivative of  $\rho - \rho_0$  with respect to  $T$ . b) Yb increment to the specific heat as  $\Delta C/T$  vs  $T$  on a logarithmic scale at different fields applied along the  $a$  axis. The dotted line, representing  $\Delta C/T = \gamma_0 \ln T_0/T$ , is a guide to the eye [Trovarelli 2000].

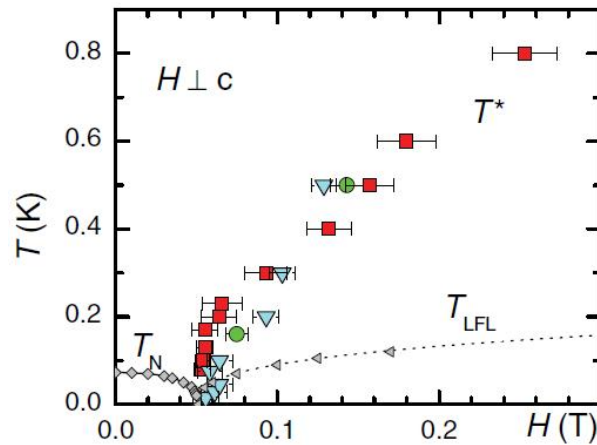


Figure 5.4: The  $(T-H)$  phase diagram of  $\text{YbRh}_2\text{Si}_2$  at ambient pressure for  $H \perp c$ . The gray diamonds and triangles represent, respectively, the Néel ordering temperature ( $T_N$ ) and the crossover temperature ( $T_{LFL}$ ) below which the electrical resistivity has the Fermi liquid behavior. The solid and dotted lines are guides to the eyes [Gegenwart 2007].

## 5.2. $P - T - H$ phase Diagram

As mentioned in the theoretical introduction, the magnetic field is also a suitable control parameter to tune the competition between Kondo effect and RKKY interaction, i.e., to tune the strength of the  $4f$ -conduction electron hybridization. But in literature there are only a few systems that had been tuned by magnetic field through a QCP, e.g.,  $\text{CeCu}_{6-x}\text{Ag}_x$  [Heuser 1998] and  $\text{YbCu}_{5-x}\text{Al}_x$  [Seuring 2000]. Therefore,  $\text{YbRh}_2\text{Si}_2$  has attracted much attention in the past few years because it is a good candidate for quantum criticality studies as it is an stoichiometric HF compound where a field-induced QCP is reached by applying low  $H_c$ . Above the critical field, the dominance of the Kondo effect causes the formation of a heavy Fermi-liquid state at sufficiently low temperatures.

The nature of the QCP in  $\text{YbRh}_2\text{Si}_2$  has been largely discussed. It was reported that just above  $H_c$  the coefficient  $A$  may diverge as  $A \propto (H - H_c)^{-1}$  [Gegenwart 2002]. An unusual temperature dependence of the Grüneisen parameter just above  $T_N$  [Küchler 2003] or a possible drop of the Hall constant at  $H_c$  [Paschen 2004] are features that can not be explained within the conventional spin fluctuation scenario and they were taken as evidences for a local quantum criticality scenario where the hallmark is a strong renormalization at the Fermi surface at the QCP where the heavy quasi-particles decomposed (“Kondo breakdown”).

## 5.2 $P - T - H$ phase Diagram

Pressure tends to favor the trivalent magnetic configuration in the Yb ion<sup>1</sup>. Therefore, as shown in the  $(P - T)$  phase diagram of  $\text{YbRh}_2\text{Si}_2$  in figure 5.5 [Knebel 2006a], applying pressure moves  $\text{YbRh}_2\text{Si}_2$  away from a pressure-induced QCP as the magnetic ordering temperature increases with increasing pressure. It has been argued that for a tiny volume expansion at a negative pressure  $P_c \approx -0.2$  GPa a continuous switch from antiferromagnetism to a paramagnetic state would occur. This is supported, at least qualitatively, by the drop of  $T_N$  from 70 to 20 mK on doping  $\text{YbRh}_2\text{Si}_2$  with nominally 5% of germanium [Küchler 2003].

The  $(P - T)$  phase diagram can be divided in three regions:

1. For  $P < 3$  GPa,  $T_H(P)$  increases with a rate of 0.37 GPa/K and a second anomaly identified as  $T_L$  appears at low temperatures above 1 GPa [Mederle 2001, Gegenwart 2002, Knebel 2006a].
2.  $T_H(P)$  shows a broad maximum around 4-5 GPa and for further increasing pressure, both  $T_H(P)$  and  $T_L(P)$  decrease.
3. Above  $P^* > 9$  GPa, only one anomaly is detected.  $T_N$  increases at a rate of 0.1 GPa/K up to 15 GPa and it is constant,  $T_N \approx 7.5$  K, for higher pressures [Plessel 2003].

The drastic change in  $T_N(P)$  at  $P^*$  seems associated to the first-order magnetic phase transition from a low-moment to a high-moment state ( $\mu_{eff} = 1.9 \mu_B$ )<sup>2</sup> occurring at 10 GPa which was detected in Mössbauer measurements [Plessel 2003]. In figure 5.6 the pressure dependence of the magnetic moment is shown.

Finally, Knebel *et al.* reported a very sharp and large jump in the magnetoresistance for a limited pressure range when the field was applied along the hard axis ( $H \parallel c$ )

In this thesis we have measured the resistivity of  $\text{YbRh}_2\text{Si}_2$  under pressure and under magnetic field to deepen the understanding of two main issues:

<sup>1</sup>As largely discussed in chapter 1 and made it evident with the valence measurements under pressure in  $\text{YbCu}_2\text{Si}_2$  in chapter 3.

<sup>2</sup>In this high-moment phase the valence of the Yb ion might be very close to  $\text{Yb}^{3+}$ . The value of  $\mu_{eff}$  is highly reduced from the one expected from the free Yb ion ( $4.53\mu_B$ ) due to CEF effects.

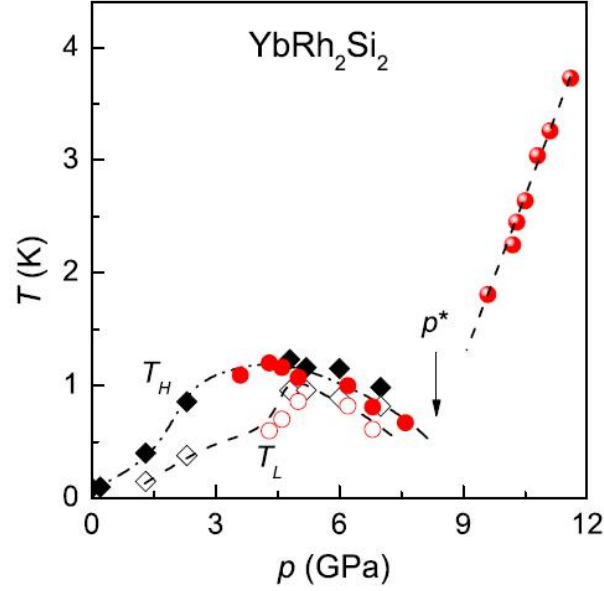


Figure 5.5:  $(P - T)$  phase diagram of  $\text{YbRh}_2\text{Si}_2$  from:  $T_H$  corresponds to the Néel temperature and  $T_L$  to the magnetic ordering temperature of the second low-temperature anomaly.  $P^*$  marks the critical pressure where the valence of the Yb ion might be very close to  $\text{Yb}^{3+}$  (see details in text) [Knebel 2006a].

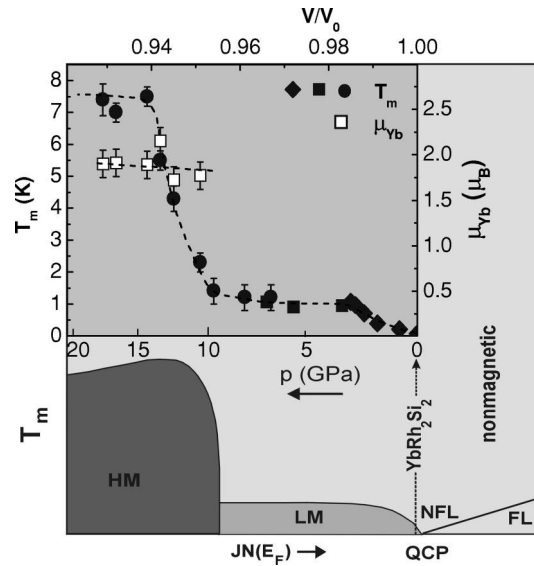


Figure 5.6: The upper part shows the pressure-temperature magnetic phase diagram for  $\text{YbRh}_2\text{Si}_2$ . The lower part shows the pressure dependence of the magnetic moment  $\mu_{\text{Yb}}$  [Plessel 2003].

## 5.2. $P - T - H$ phase Diagram

- To study the  $(P - T)$  phase diagram in greater detail to verify the evolution of  $T_H$ ,  $T_L$  and  $T_N$  versus pressure. Especially in the pressure range between 6-10 GPa, close to  $P^*$ .
- To perform a detailed research of the  $(H - T)$  phase diagram under pressure in  $\text{YbRh}_2\text{Si}_2$  to investigate the evolution of the magnetic ordering temperatures,  $T_H$  and  $T_L$ , as a function of  $H$  and  $P$  to better understand the interplay of these control parameters. One major motivation of this work was to confirm and precise this feature.

### 5.2.1 $P - T$ phase diagram

We have measured the resistivity of  $\text{YbRh}_2\text{Si}_2$  under pressure and under magnetic field in three different runs but in each one we used a high-purity single crystal from the same batch with a  $RRR = 300$ . We measured at low temperatures down to 100 mK using the dilution fridge. However, in the first two runs, we measured up to 5 GPa because the modulation pressure device was not yet working and we changed the pressure at room temperature. For the third run, we could changed the pressure at low temperatures and we measured in the high pressure range from 6 to 9 GPa.

In this section we will present the results we obtained at zero field. In figure 5.7 a) the resistivity curves at zero field (from Run 1) for two selected pressures are shown: at 0.3 GPa one anomaly is detected (signaled by an arrow). At 1.3 GPa,  $T_H$  has shifted to a higher value and a second anomaly is also detected at low temperatures ( $T_L$ ). Figure 5.7 b) shows the derivative  $\partial\rho/\partial T$  that we used as the criterion to determine the values of  $T_L$  and  $T_H$ .

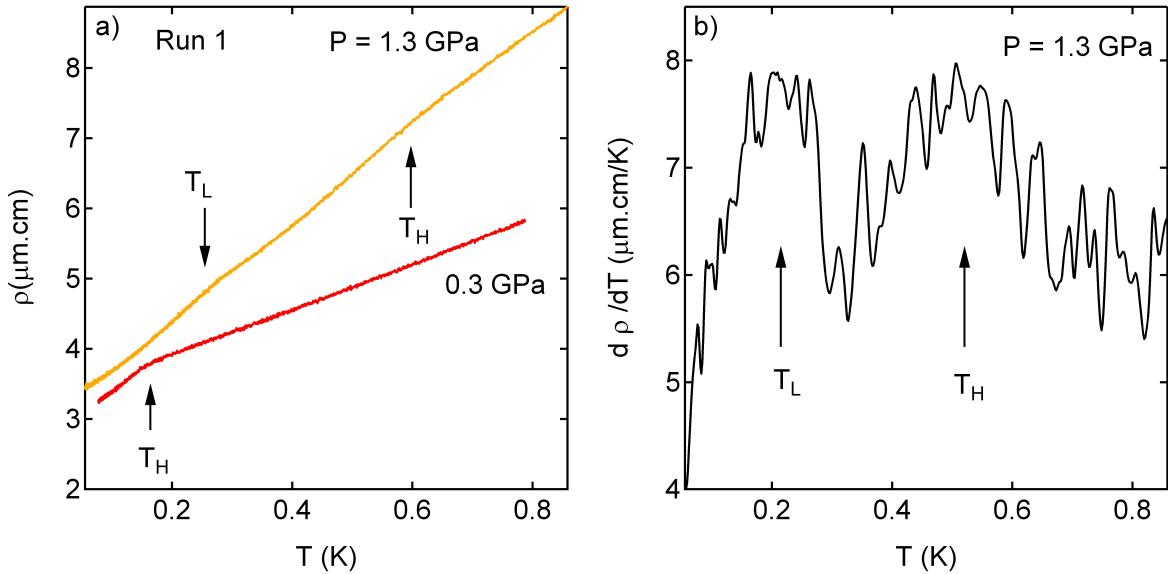


Figure 5.7: a) Low-temperature electrical resistivity of  $\text{YbRh}_2\text{Si}_2$  at 0.3 and 1.3 GPa at zero field (from Run 1). At 0.3 GPa, only one anomaly is detected whereas above 1 GPa, here we show an example at 1.3 GPa, there are two anomalies ( $T_L$  and  $T_H$ ). b) The values of  $T_L$  and  $T_H$  were determined from the derivative  $\partial\rho/\partial T$ .

The  $(P - T)$  phase diagram of  $\text{YbRh}_2\text{Si}_2$  is shown in figure 5.8. Figure 5.8 a) shows the results from the 3 runs. The values obtained in Run 1 (circles) and Run 2 (diamonds) for a similar pressure range agree well so from now on we will use those values from Run1 as we achieved higher pressures.

In figure 5.8 b) our results (Run1 + Run3) are compared with the previously reported ( $P - T$ ) phase diagram from figure 5.5. Between 6 and 8 GPa, in contrast to their results, we did not detect two anomalies in  $\rho$  but one (even though we keep the nomenclature  $T_H$ ). Nevertheless, the results obtained in both studies are almost equivalent.

We could tune the pressure very precisely in the pressure range from 6 to 9 GPa and our results are in good agreement with those from [Plessel 2003].

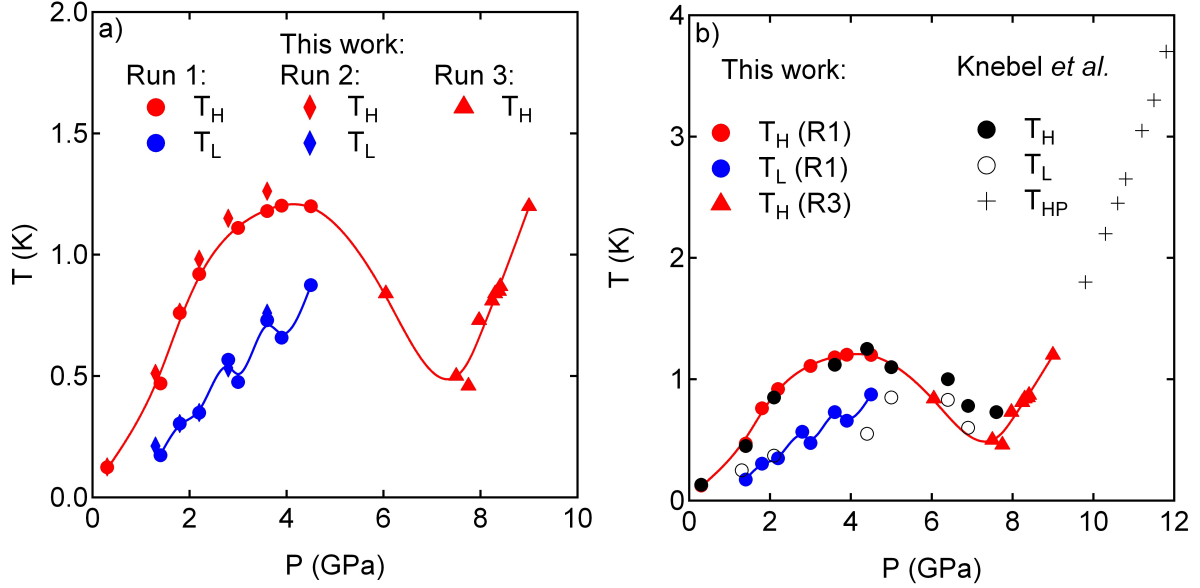


Figure 5.8: a) ( $P - T$ ) phase diagram of  $\text{YbRh}_2\text{Si}_2$  from the resistivity measurements of this work. Circles, diamonds and triangles correspond to the different experiment runs. Red and blue colors correspond to  $T_H$  and  $T_L$  respectively. b) A comparison with a previously reported phase diagram [Knebel 2006b].

### 5.2.2 Magnetic field effect under pressure

The low-temperature resistivity for different magnetic fields is shown in figure 5.9 for two selected pressures,  $P = 1.3$  GPa and  $P = 3.9$  GPa. The magnetic field was applied  $H \parallel c$  and the current along the  $ab$  plane. For  $P = 1.3$  GPa, both anomalies,  $T_L$  and  $T_H$ , are shown whereas for  $P = 3.9$  GPa we have plotted only the low-temperature anomaly,  $T_L$ . For all the pressures we measured the anomalies are quickly suppressed for fields about 1 T or even slightly weaker. Note that the critical field at ambient pressure for  $H \parallel c$  was about 0.6 T. So at first sight, it seems that pressure does not have a big effect in the critical magnetic field.

In the high pressure region, we detect only one anomaly and it is sharper than at lower pressures as shown in figure 5.10. The application of a magnetic field shifts the magnetic transition to lower temperatures and it is suppressed at  $H \approx 3$  T. This behavior is in contrast with the trend found in [Knebel 2006b] where weak magnetic fields shifted to higher values the magnetic transition and it was taken as an indication that ferromagnetic fluctuations could dominated in the high pressure region.

The magnetoresistance of  $\text{YbRh}_2\text{Si}_2$  has been measured at several pressures throughout the ( $P - T$ ) phase diagram. Here we will discuss in detailed the results for  $P = 3.0$  GPa and  $P = 3.9$  GPa. Figure 5.11 a) and b) displays the magnetoresistance  $\rho(H)/\rho(0)$  at 3.0 and 3.9 GPa respectively, as a function of field for different temperatures. For  $P = 3.0$  GPa, the magnetoresistance is positive

## 5.2. $P - T - H$ phase Diagram

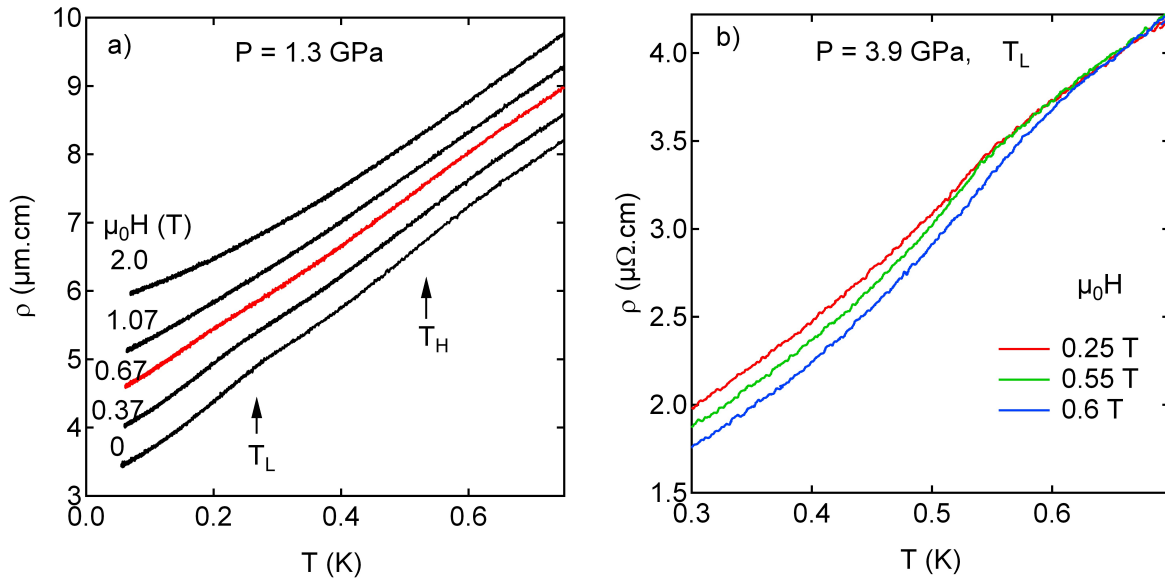


Figure 5.9: Temperature dependence of  $\rho$  for several magnetic fields at a)  $P = 1.3 \text{ GPa}$  and b)  $P = 3.9 \text{ GPa}$ .

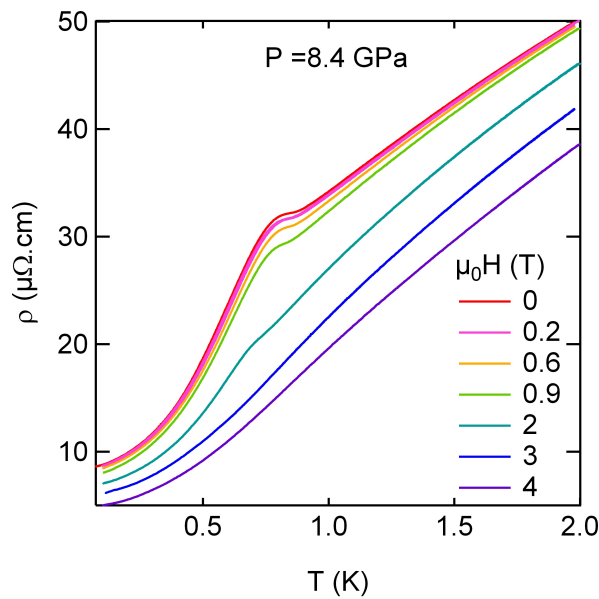


Figure 5.10: Temperature dependence of  $\rho$  for several magnetic fields at  $P = 8.4 \text{ GPa}$ .

at the lowest pressures whereas is almost constant for  $H < 1$  T at  $P = 3.9$  GPa. In both cases, the magnetoresistance shows a sharp anomaly at  $H_x \approx 1.5$  T and  $H_x \approx 0.6$  T respectively. Above  $H_x$  and for low temperatures ( $T < 0.7$  K) it is positive. At higher temperatures, for  $T > T_L$  the anomaly becomes washed out and the magnetoresistance is negative. In the high pressure region, above  $P > 6$  GPa, the magnetoresistivity does not show any sharp signature under field.

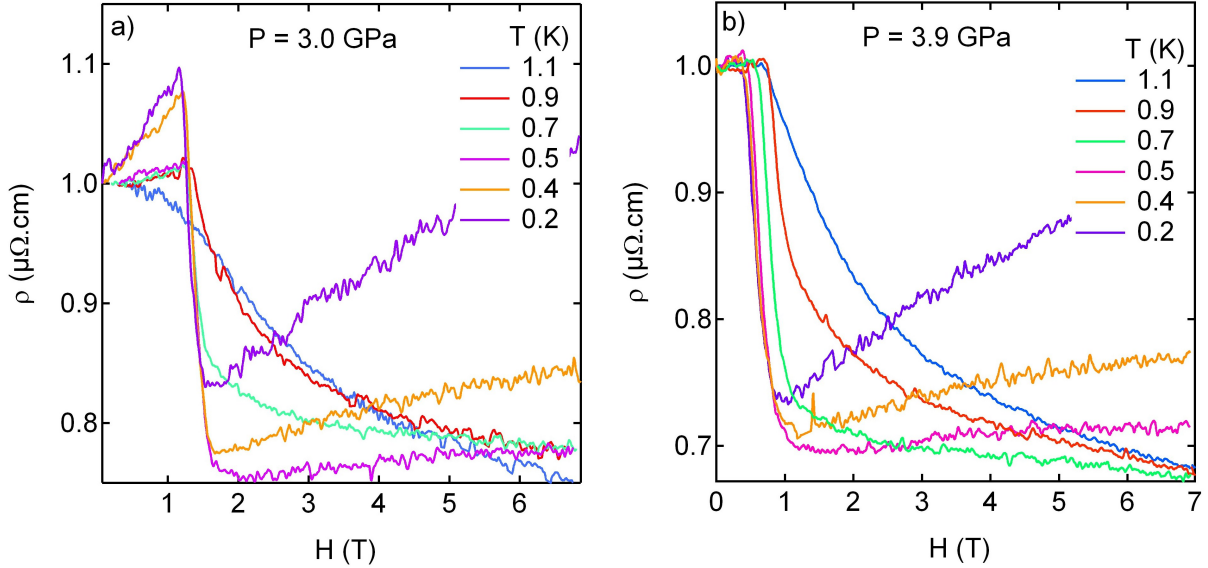


Figure 5.11: Magnetoresistance of YbRh<sub>2</sub>Si<sub>2</sub> for different temperatures at a)  $P = 3.0$  GPa and b)  $P = 3.9$  GPa.

### 5.2.3 H-T phase diagram under pressure

From these measurements the ( $H - T$ ) phase diagram at several pressures could be extracted. They are shown in figure 5.12.  $T_L$  and  $T_H$  have been determined from the temperature dependence of the resistivity as shown in figure 5.9.  $H_x$  corresponds to the sharp anomaly observed in the magnetoresistance curves as shown in figure 5.11.  $T_L$  and  $T_H$  have a smooth field dependence for all the pressures we measured except for  $P = 3.9$  GPa where  $T_H$  decreases with increasing field. As already inferred from the temperature dependence of  $\rho$  in figure 5.9, the critical field where the magnetic order is suppressed does not significantly change with pressure. Only for  $P = 3.9$  GPa, the ( $H - T$ ) phase diagram has shrunk significantly as the critical field has decreased from a value of  $H \approx 1 - 2$  T at lower pressures to  $H \approx 0.6$  T at  $P = 3.9$  GPa.

## 5.3 Conclusions

These results show the power of the *in-situ* pressure tuning device at low temperature to explore the region of the phase diagram around  $P \approx 8.4$  GPa, between the low pressure and high pressure region. Previously, the high pressure region had only been explore down to 1.5 K.

Our resistivity measurements in a high-purity single crystal have confirmed the pressure-temperature phase diagram of YbRh<sub>2</sub>Si<sub>2</sub> which it turns out to be surprisingly rich. Above  $P \approx 1$  GPa, two anomalies are detected in the resistivity curves. This behavior is not very common and it is quite surprising taking into account that up to 10 GPa, YbRh<sub>2</sub>Si<sub>2</sub> has a tiny magnetic moment.

### 5.3. Conclusions

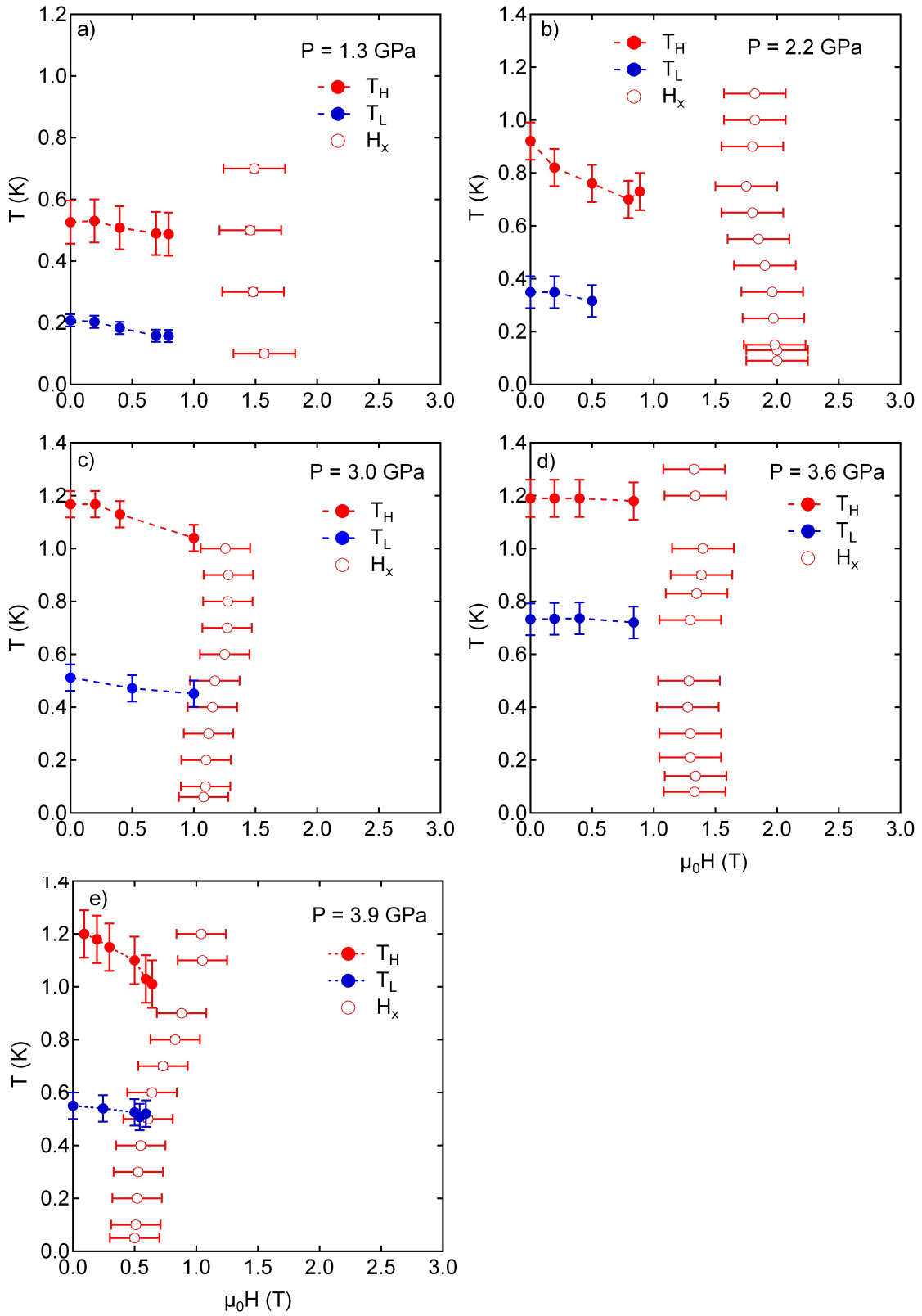


Figure 5.12:  $(H - T)$  phase diagram of  $\text{YbRh}_2\text{Si}_2$  for  $H \parallel c$  at selected pressures: a)  $P = 1.3$  GPa b)  $P = 2.2$  GPa, c)  $P = 3.0$  GPa d)  $P = 3.6$  GPa and e)  $P = 3.9$  GPa. The transition temperature  $T_L$  and  $T_H$  were determined from the temperature dependence of  $\rho$  whereas  $H_x$  was determined from the sharp anomaly detected in the magnetoresistance curves  $\rho(H)$ .

Moreover, the high-pressure region can not be explained in the usual picture of the competition of the Kondo interaction and the RKKY interaction within the Doniach phase diagram. The drastic change in the phase diagram is associated to a switch to another magnetic structure with a high-magnetic moment as indicated from Mössbauer measurements.

Most surprising is the huge anomaly in the magnetoresistance curves. We have confirmed this, and drawn the ( $H - T$ ) phase diagram for several pressures. However, we still have no explanation for this anomaly nor the nature of the different phases.



# CHAPTER 6

## Conclusions

---

An important achievement of this thesis is the setup of a pressure *in-situ* tuning device adapted for the use of diamond anvil cells in a dilution fridge. The advantages of changing the pressure at low temperatures far outweighs all the effort and hard work that has demanded. Nowadays, with just one thermal cycle we can explore in a wide parameter space either in pressure (up to 15 GPa), magnetic field (up to 7 T) or temperature (down to 40 mK), the phase diagram of most heavy fermion compounds, especially Yb-based heavy fermion systems which in general have higher critical pressures than Cerium or Uranium based heavy fermion compounds.

This thesis presents the results on three different Ytterbium based heavy fermion compounds, the intermediate-valence compounds  $\text{YbCu}_2\text{Si}_2$  and  $\text{YbRh}_2\text{Si}_2$ , and the “super heavy”  $\text{YbCo}_2\text{Zn}_{20}$ .

Several measurement techniques under pressure and in high magnetic fields were used to explore the ground state properties of these materials. Resistivity, ac-calorimetry, ac-susceptibility and x-ray spectroscopic measurements were performed in extreme conditions of pressure (up to 22 GPa), temperature (down to 40 mK) and magnetic field (up to 52 T).

The recent development of a new high pressure technique in DAC, ac-susceptibility, has permitted to identify that the magnetic order in  $\text{YbCu}_2\text{Si}_2$  is ferromagnetic<sup>1</sup>. The approach of comparing the electronic and magnetic properties throughout the  $(P - T)$  phase diagram has contributed to the understanding of the interplay between valence change, magnetism and Kondo related effects in this system. Nowadays, the phase diagram of  $\text{YbCu}_2\text{Si}_2$  is well established and rather well understood.

Though, there are still some open questions to solve. Despite the experimental efforts done during this work, we have not detected metamagnetism in  $\text{YbCu}_2\text{Si}_2$ . The experimental challenge is now to detect, if it exists, the metamagnetic transition. Two different approaches would be interesting to try: to measure the magnetization at ambient pressure at higher magnetic fields, above 50 T in both directions,  $H \parallel c$  and  $H \perp c$  and to measure the magnetization under pressure as a function of field and compare the results with our magnetoresistance measurements. Finally, we have recently heard about another spectroscopic technique, x-ray magnetic circular dichroism (XMCD) that could be interesting to use in  $\text{YbCu}_2\text{Si}_2$  as this technique can give information on the magnetic properties of the atom, such as its spin and orbital magnetic moment and apparently it is possible to measure in the sought pressure range and at low temperatures.

The studies in  $\text{YbCo}_2\text{Zn}_{20}$  have been very prolific since its discovery and nowadays there is already a rather good comprehension of the main physical properties of this system, especially at ambient pressure or even at intermediate pressures (up to 5 GPa). Now, what is needed is further studies at high pressures. It would be pertinent to compare our results and the  $(P - T)$  phase diagram we have obtained with other studies. So far, there are no results of the evolution of the complex  $(H - T)$  phase diagram under pressure. These measurements are highly desirable in order to understand which is the interplay between the FIOP and the pressure-induced magnetic ordered phase.

---

<sup>1</sup>Or at least with a ferromagnetic component.

As largely discussed throughout this thesis, a key point to better understand the complex physics that underlies in heavy fermions and especially in intermediate-valence compounds is to quantify the hybridization of the  $4f$  and conduction electrons. Thus, further measurements under extreme conditions of high pressure and low temperatures, as we have performed in  $\text{YbCu}_2\text{Si}_2$ , are highly desirable. A good candidate would be  $\text{YbRh}_2\text{Si}_2$ . Mössbauer studies have already shown that a first-order magnetic transition from a low-magnetic moment (LM) to a high magnetic-moment (HM) occurs at 10 GPa. The knowledge of its valence throughout the  $(P - T)$  phase diagram would probably complete its understanding. In fact, such measurements have already been done by C. Dallera *et al.* [Dallera 2005] and these results have some similarities with those obtained in  $\text{YbCu}_2\text{Si}_2$ .

Another promising path would be to choose a system where a large range of valence change can be explored. If sufficiently high pressures can be applied, it would be possible in principle to explore the whole range from intermediate valence to the Kondo regime and magnetic order.  $\text{YbCu}_2\text{Ge}_2$  could be a good candidate for such a study as it is almost divalent at ambient pressure.

## Résumé

Cette thèse a pour objet l'étude de 3 systèmes de fermions lourds à base d'Ytterbium,  $\text{YbCu}_2\text{Si}_2$ ,  $\text{YbCo}_2\text{Zn}_{20}$  et  $\text{YbRh}_2\text{Si}_2$ , dans des conditions extrêmes de hautes pressions, basses températures et hauts champs magnétiques. Une partie très importante dans ce travail a été le développement d'un dispositif de génération de force à très basses températures permettant une modulation de la pression *in-situ* adapté à des cellules à enclumes diamant.

Pour  $\text{YbCu}_2\text{Si}_2$ , les mesures de ac-susceptibilité sous pression et sous champ magnétiques ainsi que les mesures d'aimantation sous pression montrent que l'ordre magnétique qui apparaît pour  $P > 8$  GPa est ferromagnétique. L'étude du changement de la valence de l'ion Yb par des mesures de diffusion inélastique en conditions résonantes de rayons X ont permis de clarifier son interaction avec le magnétisme. Même si l'état trivalent est clairement favorisé sous pression, la valence reste inférieure à 3 proche de l'ordre magnétique, même dans les plus hautes pressions et plus basses températures. Nous avons également procédé à une recherche détaillée pour les signatures de metamagnétisme avec des mesures à très haut champ.

Dans la deuxième partie de ma thèse, les mesures de ac-calorimétrie et ac-susceptibilité sous pression ont permis d'établir le diagramme de phase ( $P - T$ ) dans  $\text{YbCo}_2\text{Zn}_{20}$  jusqu'à 14 GPa. En plus, nos résultats suggèrent que l'ordre magnétique qui apparaît pour  $P > 1$  GPa est anti-ferromagnétique. Les forts effets du champ magnétique observés dans les propriétés physiques dans  $\text{YbCo}_2\text{Zn}_{20}$  sont probablement liés à l'interaction entre le champ magnétique et les spins des électrons  $4f$  et non à leur charge car la valence de l'Yb s'avère insensible à l'application d'un champ magnétique de 10 T.

La partie finale de cette thèse est consacrée à l'étude du diagramme de phase ( $H - T$ ) sous pression dans  $\text{YbRh}_2\text{Si}_2$  pour déterminer l'évolution de la température de l'ordre magnétique  $T_N$  en fonction de  $H$  et  $P$  et mieux comprendre les effets liés à ce deux paramètres de contrôle.

## Mots-Clés

Systèmes à fermions lourds  
systèmes à valence intermédiaire  
haute pression point critique quantique  
 $\text{YbCu}_2\text{Si}_2$   
 $\text{YbCo}_2\text{Zn}_{20}$   
 $\text{YbRh}_2\text{Si}_2$



# Bibliography

- [Abrikosov 1965] A. A. Abrikosov. *Electron scattering on magnetic impurities in metals and anomalous resistivity effects*. Physics, vol. 2, page 5, 1965.
- [Alami Yadri 1998] K. Alami Yadri, H. Wilhelm and D. Jaccard. *Pressure-induced magnetically ordered Kondo lattice state in  $\text{YbCu}_2\text{Si}_2$* . Eur. Phys. J. B, vol. 6, pages 5–11, 1998.
- [Alireza 2003] P. Alireza and S. R. Julian. *Susceptibility measurements at high pressures using a microcoil system in an anvil cell*. Rev. Sci. Instrum., vol. 74, page 4728, 2003.
- [Alireza 2009] P. Alireza and G. Lonzarich. *Miniature anvil cell for high-pressure measurements in a commercial superconducting quantum interference device magnetometer*. Rev. Sci. Instrum., vol. 80, page 023906, 2009.
- [Anderson 1961] P. W. Anderson. *Localized Magnetic States in Metals*. Phys. Rev., vol. 124, pages 41–53, Oct 1961.
- [Andrei 1983] N. Andrei, K. Furuya and J. H. Lowenstein. *Solution of the Kondo problem*. Rev. Mod. Phys., vol. 55, pages 331–402, Apr 1983.
- [Andres 1975] K. Andres, J. E. Graebner and H. R. Ott. *4f-Virtual-Bound-State Formation in  $\text{CeAl}_3$  at Low Temperatures*. Phys. Rev. Lett., vol. 35, pages 1779–1782, Dec 1975.
- [Aoki 2001] D. Aoki, A. Huxley, E. Ressouche, D. Braithwaite, J. Flouquet, J.-P. Brison, E. Lhotel and C. Paulsen. *Coexistence of superconductivity and ferromagnetism in  $\text{URhGe}$* . Nature, vol. 413, pages 613–616, 2001.
- [Ashcroft 1975] N.W. Ashcroft and N.D. Mermin. Solid state physics. Holt, Rinehart and Winston,, 1975.
- [Béal-Monod 1968] M. T. Béal-Monod, Shang-Keng Ma and D. R. Fredkin. *Temperature Dependence of the Spin Susceptibility of a Nearly Ferromagnetic Fermi Liquid*. Phys. Rev. Lett., vol. 20, pages 929–932, Apr 1968.
- [Bellarbi 1984] B. Bellarbi, A. Benoit, D. Jaccard, J. M. Mignot and H. F. Braun. *High-pressure valence instability and  $T_c$  maximum in superconducting  $\text{CeCu}_2\text{Si}_2$* . Phys. Rev. B, vol. 30, pages 1182–1187, Aug 1984.
- [Bonville 1991] P. Bonville, J.A. Hodges, P. Imbert, G. Jehanno, D. Jaccard and J. Sierro. *Magnetic ordering and paramagnetic relaxation of  $\text{Yb}^{3+}$  in  $\text{YbNi}_2\text{Si}_2$* . J. Magn. Magn. Mater., vol. 97, no. 1-3, pages 178 – 186, 1991.
- [Bonville 1994] P. Bonville, J.A. Hodges, P. Imbert, G. Jahanno and P. Thuary. *A neutron diffraction and  $^{170}\text{Yb}$  Mössbauer study of  $\text{Yb}_3\text{Pd}_4$* . J. Magn. Magn. Mater., vol. 136, no. 3, pages 238 – 244, 1994.
- [Brandt 1984] N.B. Brandt and V.V. Moshchalkov. *Concentrated Kondo systems*. Advances in Physics, vol. 33, no. 5, pages 373–467, 1984.

## BIBLIOGRAPHY

- [Brooks 1996] M.S.S. Brooks. *Conduction electrons in magnetic metals*. Mfm, vol. 45, pages 291–314, 1996.
- [Burdin 2000] S. Burdin, A. Georges and D. R. Grempel. *Coherence Scale of the Kondo Lattice*. Phys. Rev. Lett., vol. 85, pages 1048–1051, Jul 2000.
- [Chaussy 1982] J. Chaussy, P. Gandit, K. Matho and A. Ravex. *Absolute thermoelectric-power of AuFe alloys between 0.01 K and 7 K*. J. Low. Temp. Phys., vol. 49, pages 167–175, 1982.
- [Clogston 1962] A. M. Clogston, B. T. Matthias, M. Peter, H. J. Williams, E. Corenzwit and R. C. Sherwood. *Local Magnetic Moment Associated with an Iron Atom Dissolved in Various Transition Metal Alloys*. Phys. Rev., vol. 125, pages 541–552, Jan 1962.
- [Coleman 2007] P. Coleman. *Heavy Fermions: electrons at the edge of magnetism*. arXiv:condmat, vol. 0612006v3, page 90, 2007.
- [Colombier 2008] E. Colombier. *Développement instrumental pour les mesures de résistivité sous pression hydrostatique. Etude de systèmes à électrons corrélés d'ytterbium et de la famille  $A_{0.33}V_2O_5$* . PhD thesis, Université de Grenoble, 2008.
- [Colombier 2009] E. Colombier, D. Braithwaite, G. Lapertot, B. Salce and G. Knebel. *High-pressure transport and microcalorimetry studies on high quality  $YbCu_2Si_2$  single crystals*. Phys. Rev. B, vol. 79, page 245113, Jun 2009.
- [Coqblin 1969] B. Coqblin and J. R. Schrieffer. *Exchange Interaction in Alloys with Cerium Impurities*. Phys. Rev., vol. 185, pages 847–853, Sep 1969.
- [Cornelius 1995] A. L. Cornelius, J. S. Schilling, D. Mandrus and J. D. Thompson. *Anomalous hydrostatic pressure dependence of the Curie temperature of the Kondo-lattice compound  $YbNiSn$  to 38 GPa*. Phys. Rev. B, vol. 52, pages R15699–R15702, Dec 1995.
- [Custers 2003] J. Custers, P. Gegenwart, H. Wilhelm, K. Neumaier, Y. Tokiwa, O. Trovarelli, C. Geibel, F. Steglich, C. Pepin and P. Coleman. *The break-up of heavy electrons at a quantum critical point*. Nature, vol. 424, no. 6948, pages 524–527, 2003.
- [Dallera 2002] C. Dallera, M. Grioni, A. Shukla, G. Vankó, J. L. Sarrao, J. P. Rueff and D. L. Cox. *New Spectroscopy Solves an Old Puzzle: The Kondo Scale in Heavy Fermions*. Phys. Rev. Lett., vol. 88, page 196403, Apr 2002.
- [Dallera 2004] C. Dallera, M. Grioni, A. Palenzona, M. Taguchi, E. Annese, G. Ghiringhelli, A. Tagliaferri, N. B. Brookes, Th. Neisius and L. Braicovich.  *$\alpha - \gamma$  transition in metallic Ce studied by resonant x-ray spectroscopies*. Phys. Rev. B, vol. 70, page 085112, Aug 2004.
- [Dallera 2005] C. Dallera, E. Anesse, M. Grioni, G. Knebel, A. Barla and M. D'astuto. *First direct study of heavy fermions valence at high pressure and low temperature*. Rapport technique, User Report ESRF, 2005.
- [de Haas 1934] W.J. de Haas, J. de Boer and G.J. van den Berg. *The electrical resistance of gold, copper and lead at low temperatures*. Physica, vol. 1, no. 712, pages 1115 – 1124, 1934.
- [De Muer 2000] A. De Muer. *Etude du point critique magnétique quantique des fermions lourds sous pression hydrostatique*. PhD thesis, Université Joseph Fourier Grenoble, 2000.

## BIBLIOGRAPHY

- [Degiorgi 1999] L. Degiorgi. *The electrodynamic response of heavy-electron compounds*. Rev. Mod. Phys., vol. 71, pages 687–734, Apr 1999.
- [Doniach 1977] S. Doniach. *The Kondo lattice and weak antiferromagnetism*. Physica B+C, vol. 91, no. 0, pages 231 – 234, 1977.
- [Dung 2009] N.D. Dung, Y. Ota, K. Sugiyama, T.D. Matsuda, Y. Haga, K. Kindo, M. Hagiwara, T. Takeuchi, R. Settai and Y. Onuki. *Magnetic Properties of Single Crystalline  $RCu_2Si_2$  ( $R$ : Rare Earth)*. J. Phys. Soc. Jpn, vol. 78, no. 2, page 024712, 2009.
- [Dunstan 1989] D. J. Dunstan and I. L. Spain. *Technology of diamond anvil high-pressure cells: I. Principles, design and construction*. Journal of Physics E: Scientific Instruments, vol. 22, no. 11, page 913, 1989.
- [Easylab ] Easylab. <http://www.easylab.co.uk>, Mcell ultra.
- [Enns 2005] C. Enns and S. Hunklinger. Low temperature physics. Springer Verlag, 2005.
- [Felner 1986] I. Felner and I. Nowik. *First-order valence phase transition in cubic  $Yb_xIn_{1-x}Cu_2$* . Phys. Rev. B, vol. 33, pages 617–619, Jan 1986.
- [Fernandez-Pañella 2011] A. Fernandez-Pañella, D. Braithwaite, B. Salce, G. Lapertot and J. Flouquet. *Ferromagnetism in  $YbCu_2Si_2$  at high pressure*. Phys. Rev. B, vol. 84, page 134416, Oct 2011.
- [Fernandez-Pañella 2012] A. Fernandez-Pañella, V. Balédent, D. Braithwaite, L. Paolasini, R. Verbeni, G. Lapertot and J.-P. Rueff. *Valence instability of  $YbCu_2Si_2$  through its magnetic quantum critical point*. Phys. Rev. B, vol. 86, page 125104, Sep 2012.
- [Fisk 1988] Z. Fisk, D. W. Hess, C. J. Pethick, D. Pines, J. L. Smith, J. D. Thompson and J. O. Willis. *Heavy-Electron Metals: New Highly Correlated States of Matter*. Science, vol. 239, no. 4835, pages 33–42, 1988.
- [Fisk 1995] Z. Fisk, J. L. Sarrao, J. L. Smith and J. D. Thompson. *The physics and chemistry of heavy fermions*. Proceedings of the National Academy of Sciences, vol. 92, no. 15, pages 6663–6667, 1995.
- [Flouquet 2005] J. Flouquet, A. Barla, R. Boursier, J. Derr and G. Knebel. *Kondo Engineering: From Single Kondo Impurity to the Kondo Lattice*. Journal of the Physical Society of Japan, vol. 74, no. 1, pages 178–185, 2005.
- [Flouquet 2009] J. Flouquet and H. Harima. *Heavy fermion material: Ce versus Yb case*. Arxiv preprint arXiv:0910.3110, 2009.
- [Forman 1972] R. A. Forman, G. J. Piermarini, J. D. Barnett and S. Block. *Pressure Measurement Made by the Utilization of Ruby Sharp-Line Luminescence*. Science, vol. 176, no. 4032, pages 284–285, 1972.
- [Gegenwart 2002] P. Gegenwart, J. Custers, C. Geibel, K. Neumaier, T. Tayama, K. Tenya, O. Trovarelli and F. Steglich. *Magnetic-Field Induced Quantum Critical Point in  $YbRh_2Si_2$* . Phys. Rev. Lett., vol. 89, page 056402, Jul 2002.

## BIBLIOGRAPHY

- [Gegenwart 2003] P. Gegenwart, J. Custers, T. Tayama, K. Tenya, C. Geibel, G. Sparn, N. Harrison, P. Kersch, D. Eckert, K.-H. Maller and F. Steglich. *Tuning Heavy Fermion Systems into Quantum Criticality by Magnetic Field*. Journal of Low Temperature Physics, vol. 133, pages 3–15, 2003.
- [Gegenwart 2006] P. Gegenwart, Y. Tokiwa, T. Westerkamp, F. Weickert, J. Custers, J. Ferstl, C. Krellner, C. Geibel, P. Kersch, K. H. Müller and F. Steglich. *High-field phase diagram of the heavy-fermion metal  $\text{YbRh}_2\text{Si}_2$* . New Journal of Physics, vol. 8, page 171, 2006.
- [Gegenwart 2007] P. Gegenwart, T. Westerkamp, C. Krellner, Y. Tokiwa, S. Paschen, C. Geibel, F. Steglich, E. Abrahams and Q. Si. *Multiple energy scales at a quantum critical point*. Science, vol. 315, no. 5814, pages 969–971, 2007.
- [Goltsev 2005] A.V. Goltsev and M. M. Abd-Elmeguid. *Origin of the pressure dependence of the Kondo temperature in Ce- and Yb-based heavy-fermion compounds*. Journal of Physics: Condensed Matter, vol. 17, no. 11, page S813, 2005.
- [Gonzalez 1986] J. Gonzalez, J. M. Besson and G. Weill. *Electrical transport measurements in a gasketed diamond anvil cell up to 18 GPa*. Review of Scientific Instruments, vol. 57, no. 1, pages 106–107, 1986.
- [Guillaume 1999] A. Guillaume. *Transitions de phases dans les fermions lourds sous contrainte uniaxiale*. PhD thesis, Université Joseph Fourier Grenoble 1, 1999.
- [Haen 1987] P. Haen, J. Flouquet, F. Lapierre, P. Lejay and G. Remenyi. *Metamagnetic-like transition in  $\text{CeRu}_2\text{Si}_2$* . Journal of Low Temperature Physics, vol. 67, pages 391–419, 1987.
- [Hertz 1976] J. A. Hertz. *Quantum critical phenomena*. Phys. Rev. B, vol. 14, pages 1165–1184, Aug 1976.
- [Heuser 1998] K. Heuser, E.-W. Scheidt, T. Schreiner and G. R. Stewart. *Disappearance of hyper-scaling at low temperatures in non-Fermi-liquid  $\text{CeCu}_{5.2}\text{Ag}_{0.8}$* . Phys. Rev. B, vol. 58, pages R15959–R15961, Dec 1998.
- [Hewson 1993] A. C. Hewson. *The kondo problem to heavy fermions*. Cambridge, 1993.
- [Hodges 1987] J. A. Hodges. *Magnetic Ordering of Ytterbium in  $\text{YbCo}_2\text{Si}_2$  and  $\text{YbFe}_2\text{Si}_2$* . Europhys. Lett., vol. 4, no. 6, page 749, 1987.
- [Holland-Moritz 1982] E. Holland-Moritz, D. Wohlleben and M. Loewenhaupt. *Anomalous paramagnetic neutron spectra of some intermediate-valence compounds*. Phys. Rev. B, vol. 25, pages 7482–7503, Jun 1982.
- [Holmes 2004] A. T. Holmes, D. Jaccard and K. Miyake. *Signatures of valence fluctuations in  $\text{CeCu}_2\text{Si}_2$  under high pressure*. Phys. Rev. B, vol. 69, page 024508, Jan 2004.
- [Holmes 2007] T. A. Holmes, D. Jaccard and K. Miyake. *Valence Instability and Superconductivity in Heavy Fermion Systems*. Journal of the Physical Society of Japan, vol. 76, no. 5, page 051002, 2007.
- [Itskevich 1978] E. S. Itskevich and V. F. Kraidenov. *Measurement of temperatures in the liquid-helium region under pressure*. Instrum. Exp. Tech., vol. 21, pages 1640–1643, 1978.

## BIBLIOGRAPHY

- [Jayaraman 1983] A. Jayaraman. *Diamond anvil cell and high-pressure physical investigations*. Rev. Mod. Phys., vol. 55, pages 65–108, Jan 1983.
- [Jensen 1991] J. Jensen and A. R. Mackintosh. Rare earth magnetism. Clarendon press, 1991.
- [Joly 2011] Y. Joly. *Les spectroscopies d'absorption X*. review, 2011.
- [Kadowaki 1986] K. Kadowaki and S.B. Woods. *Universal relationship of the resistivity and specific heat in heavy-Fermion compounds*. Solid State Communications, vol. 58, no. 8, pages 507 – 509, 1986.
- [Kamenev 2006] K. V. Kamenev, S. Tancharakorn, N. Robertson and A. Harrison. *Long symmetric high-pressure cell for magnetic measurements in superconducting quantum interference device magnetometer*. Review of Scientific Instruments, vol. 77, no. 7, page 073905, 2006.
- [Kanatzidis 2005] M.G. Kanatzidis, R. Pattgen and W. Jeitschko. *The Metal Flux: A Preparative Tool for the Exploration of Intermetallic Compounds*. Angewandte Chemie International Edition, vol. 44, no. 43, pages 6996–7023, 2005.
- [Kaneko 2012] K. Kaneko, S. Yoshiuchi, T. Takeuchi, F. Honda, R. Settai and Y. Ōnuki. *Effect of magnetic field in heavy-fermion compound  $\text{YbCo}_2\text{Zn}_{20}$* . ArXiv e-prints, April 2012.
- [Kasuya 1996] Tadao Kasuya. *Physical Mechanism in Kondo Insulator*. Journal of the Physical Society of Japan, vol. 65, no. 8, pages 2548–2558, 1996.
- [Knebel 2001] G. Knebel, D. Braithwaite, G. Lapertot, P.C. Canfield and J. Flouquet. *Magnetically ordered Kondo lattice in  $\text{YbNi}_2\text{Ge}_2$  at high pressure*. J. Phys. Condens. Matter, vol. 13, no. 48, page 10935, 2001.
- [Knebel 2005] G. Knebel, V. Glazkov, A. Pourret, P. G. Niklowitz, G. Lapertot, B. Salce and J. Flouquet. *High-pressure phase diagram of  $\text{YbRh}_2\text{Si}_2$* . Physica B-condensed Matter, vol. 359, pages 20–22, 2005.
- [Knebel 2006a] G. Knebel, R. Boursier, E. Hassinger, G. Lapertot, P. G. Niklowitz, A. Pourret, B. Salce, J. P. Sanchez, I. Sheikin, P. Bonville, H. Harima and J. Flouquet. *Localization of  $4f$  state in  $\text{YbRh}_2\text{Si}_2$  under magnetic field and high pressure: Comparison with  $\text{CeRh}_2\text{Si}_2$* . J. Phys. Soc. Jpn., vol. 75, page 114709, 2006.
- [Knebel 2006b] G. Knebel, E. Hassinger, G. Lapertot, P. G. Niklowitz, J. P. Sanchez and J. Flouquet. *On the high-pressure phase diagram of  $\text{YbRh}_2\text{Si}_2$* . Physica B-condensed Matter, vol. 378-80, pages 68–69, 2006.
- [Kohgi 2003] M. Kohgi, K. Iwasa, M. Nakajima, N. Metoki, S. Araki, N. Bernhoeft, J-M. Mignot, A. Gukasov, H. Sato, Y. Aoki and H. Sugawara. *Evidence for Magnetic-Field-Induced Quadrupolar Ordering in the Heavy-Fermion Superconductor  $\text{PrOs}_4\text{Sb}_{12}$* . Journal of the Physical Society of Japan, vol. 72, no. 5, pages 1002–1005, 2003.
- [Kojima 1989] K. Kojima, H. Hayashi, A. Minami, Y. Kasamatsu and T. Hihara. *Crystal phases and Yb valence transition in  $\text{Yb}_x\text{In}_{1-x}\text{Cu}_2$* . Journal of Magnetism and Magnetic Materials, vol. 81, no. 3, pages 267 – 272, 1989.
- [Kondo 1964] J. Kondo. *Resistance Minimum in Dilute Magnetic Alloys*. Progress of Theoretical Physics, vol. 32, no. 1, pages 37–49, 1964.

## BIBLIOGRAPHY

- [Kontani 2004] H. Kontani. *Generalized Kadowaki–Woods Relation in Heavy Fermion Systems with Orbital Degeneracy*. Journal of the Physical Society of Japan, vol. 73, no. 3, pages 515–518, 2004.
- [Koshimaki 1978] D.G. Koshimaki and K.A. Gschneider. Handbook of the physics and chemistry of rare earth. North Holland, 1978.
- [Küchler 2003] R. Küchler, N. Oeschler, P. Gegenwart, T. Cichorek, K. Neumaier, O. Tegus, C. Geibel, J. A. Mydosh, F. Steglich, L. Zhu and Q. Si. *Divergence of the Grüneisen Ratio at Quantum Critical Points in Heavy Fermion Metals*. Phys. Rev. Lett., vol. 91, page 066405, Aug 2003.
- [Kuramoto 1999] Y. Kuramoto and Y. Kitaoka. Dynamics of heavy fermions. Oxford, 1999.
- [L-A ] *L-A cell Manual, Cambridge pressure cells*.
- [Lawrence 1994] J. M. Lawrence, G. H. Kwei, P. C. Canfield, J. G. DeWitt and A. C. Lawson. *L<sub>III</sub> x-ray absorption in Yb compounds: Temperature dependence of the valence*. Phys. Rev. B, vol. 49, pages 1627–1631, Jan 1994.
- [Levallois 2008] J. Levallois. *Oscillations quantiques et magntotransport dans des systmes fortes corrllations lectroniques*. PhD thesis, Univeristé de Toulouse III-Paul Sabater, 2008.
- [Löhneysen 1994] H. v. Löhneysen, T. Pietrus, G. Portisch, H. G. Schlager, A. Schröder, M. Sieck and T. Trappmann. *Non-Fermi-liquid behavior in a heavy-fermion alloy at a magnetic instability*. Phys. Rev. Lett., vol. 72, pages 3262–3265, May 1994.
- [Löhneysen 1996] H.. Löhneysen. *Non-Fermi-liquid behaviour in the heavy-fermion system*. Journal of Physics: Condensed Matter, vol. 8, no. 48, page 9689, 1996.
- [Lounasmaa 1979] O V Lounasmaa. *Dilution refrigeration*. Journal of Physics E: Scientific Instruments, vol. 12, no. 8, page 668, 1979.
- [Macaluso 2007] R. T. Macaluso, S. Nakatsuji, K. Kuga, E. L. Thomas, Y. Machida, Y. Maeno, Z. Fisk and J.Y. Chan. *Crystal Structure and Physical Properties of Polymorphs of LnAlB<sub>4</sub> (Ln = Yb, Lu)*. Chemistry of Materials, vol. 19, no. 8, pages 1918–1922, 2007.
- [Malterre 1996] D. Malterre, M. Grioni and Y. Baer. *Recent developments in high-energy spectroscopies of Kondo systems*. Advances in Physics, vol. 45, pages 299–348, 1996.
- [Maple 1986] M. B. Maple, J. W. Chen, Y. Dalichaouch, T. Kohara, C. Rossel, M. S. Torikachvili, M. W. McElfresh and J. D. Thompson. *Partially gapped Fermi surface in the heavy-electron superconductor URu<sub>2</sub>Si<sub>2</sub>*. Phys. Rev. Lett., vol. 56, pages 185–188, Jan 1986.
- [Matsubayashi 2010] K. Matsubayashi, Y. Saiga, T. Matsumoto and Y. Uwatoko. *Pressure-induced variation of Kondo behavior on the heavy fermion compounds YbT<sub>2</sub>Zn<sub>20</sub> (T = Co, Rh, Ir)*. Journal of Physics: Conference Series, vol. 200, no. 1, page 012112, 2010.
- [Mattens 1980] W.C.M. Mattens, H. Hölscher, G.J.M. Tuin, A.C. Moleman and F.R. de Boer. *Thermal expansion and magneto-volume effects in the mixed-valent compound YbCuAl*. Journal of Magnetism and Magnetic Materials, vol. 1518, Part 2, no. 0, pages 982 – 984, 1980.

- [Measson 2005] M-A. Measson. *La skutterudite  $PrOs_4Sb_{12}$ : supraconductivité et corrélations*. PhD thesis, Université Joseph Fourier Grenoble 1, 2005.
- [Mederle 2001] S. Mederle, R. Borth, C. Geibel, F. M. Grosche, G. Sparn, O. Trovarelli and F. Steglich. *Unconventional metallic state in  $YbRh_2Si_2$  - a high-pressure study*. Journal of Magnetism and Magnetic Materials, vol. 226, pages 254–255, 2001.
- [Millis 1993] A. J. Millis. *Effect of a nonzero temperature on quantum critical points in itinerant fermion systems*. Phys. Rev. B, vol. 48, pages 7183–7196, Sep 1993.
- [Mito 2003] T. Mito, T. Koyama, M. Shimoide, S. Wada, T. Muramatsu, T. C. Kobayashi and J. L. Sarrao. *Magnetic ordering in the pressure-stabilized high-temperature phase of  $YbInCu_4$* . Phys. Rev. B, vol. 67, page 224409, Jun 2003.
- [Mito 2007] T. Mito, M. Nakamura, M. Otani, T. Koyama, S. Wada, M. Ishizuka, M. K. Forthaus, R. Lengsdorf, M. M. Abd-Elmeguid and J. L. Sarrao. *Magnetic properties of the pressure-induced ordering state in  $YbInCu_4$  investigated with NMR, magnetization, and x-ray diffraction measurements*. Phys. Rev. B, vol. 75, page 134401, Apr 2007.
- [Mito 2010] T. et al. Mito. *Magnetic Field Effect on Yb-Based Heavy Fermions near Magnetic-Nonmagnetic Transition*. Acta Physica Polonica A, vol. 118, pages 870–872, 2010.
- [Miyake 2007] K Miyake. *New trend of superconductivity in strongly correlated electron systems*. Journal of Physics: Condensed Matter, vol. 19, no. 12, page 125201, 2007.
- [Monthoux 2001] P. Monthoux and G. G. Lonzarich. *Magnetically mediated superconductivity in quasi-two and three dimensions*. Phys. Rev. B, vol. 63, page 054529, Jan 2001.
- [Moreschini 2007] L. Moreschini, C. Dallera, J. J. Joyce, J. L. Sarrao, E. D. Bauer, V. Fritsch, S. Bobev, E. Carpena, S. Huotari, G. Vankó, G. Monaco, P. Lacovig, G. Panaccione, A. Fondacaro, G. Paolicelli, P. Torelli and M. Grioni. *Comparison of bulk-sensitive spectroscopic probes of Yb valence in Kondo systems*. Phys. Rev. B, vol. 75, page 035113, Jan 2007.
- [Moriya 1995] T. Moriya and T. Takimoto. *Anomalous Properties around Magnetic Instability in Heavy Electron Systems*. Journal of the Physical Society of Japan, vol. 64, no. 3, pages 960–969, 1995.
- [Moriya 2000] T. Moriya and K. Ueda. *Spin fluctuations and high temperature superconductivity*. Adv. Phys, vol. 49, page 555, 2000.
- [Muzychka 1998] A. Muzychka. *Crystal-field effects in the intermediate-valence compound  $YbCu_2Si_2$* . Journal of Experimental and Theoretical Physics, vol. 87, pages 162–174, 1998.
- [Nakanishi 2009] Yoshiki Nakanishi, Takuya Fujino, Kankichi Ito, Mitsuteru Nakamura, Masahito Yoshizawa, Yuta Saiga, Masashi Kosaka and Yoshiya Uwatoko. *Elastic constants of the single crystalline Yb based heavy-fermion compound  $YbCo_2Zn_{20}$* . Phys. Rev. B, vol. 80, page 184418, Nov 2009.
- [Nakatsuji 2008] S Nakatsuji, K. Kuga, Y. Machida, T. Tayama, T. Sakakibara, Y. Karaki, H. Ishimoto, S. Yonezawa, Y. Maeno, E. Pearson, G.G. Lonzarich, L. Balicas, H. Lee and Z Fisk. *Superconductivity and quantum criticality in the heavy-fermion system  $\beta - YbAlB_4$* . Nat. Phys., vol. 4, pages 603–607, 2008.

## BIBLIOGRAPHY

- [Noack 1979] R.A. Noack and W. B. Holzapfel. High pressure science and technology. Plenum, 1979.
- [Nozières 1980] Ph. Nozières and A. Blandin. *Kondo effect in real metals*. J. Phys. France, vol. 41, no. 3, pages 193–211, 1980.
- [Nozières 2005] Ph. Nozières. *Kondo Lattices and the Mott Metal–Insulator Transition*. Journal of the Physical Society of Japan, vol. 74, no. 1, pages 4–7, 2005.
- [Ohya 2010] M. Ohya, M. Matsushita, S. Yoshiuchi, S. Takeuchi, F. Honda, F. Settai, F. Tanaka, Y. Kubo and Y. Ōnuki. *Strong Field Quenching of the Quasiparticle Effective Mass in Heavy Fermion Compound  $\text{YbCo}_2\text{Zn}_{20}$* . Journal of the Physical Society of Japan, vol. 79, no. 8, page 083601, 2010.
- [Paschen 2004] S. Paschen, T. Luhmann, S. Wirth, P. Gegenwart, O. Trovarelli, C. Geibel, F. Steglich, P. Coleman and Q. Si. *Hall-effect evolution across a heavy-fermion quantum critical point*. Nature, vol. 432, pages 881–885, 2004.
- [Pines 1990] D. Pines. *Spin excitations and superconductivity in cuprate oxide and heavy electron superconductors*. Physica B: Condensed Matter, vol. 163, no. 13, pages 78 – 88, 1990.
- [Plessel 2003] J. Plessel, M. M. Abd-Elmeguid, J. P. Sanchez, G. Knebel, C. Geibel, O. Trovarelli and F. Steglich. *Unusual behavior of the low-moment magnetic ground state of  $\text{YbRh}_2\text{Si}_2$  under high pressure*. Phys. Rev. B, vol. 67, page 180403, May 2003.
- [Rasul 1984] J.W. Rasul and A.C. Hewson. *Bethe ansatz and  $1/N$  expansion results for  $N$ -fold degenerate magnetic impurity models*. Journal of Physics C: Solid State Physics, vol. 17, no. 14, page 2555, 1984.
- [Reinhold 1996] E. Reinhold and S. Herbert. *RKKY interaction for strongly correlated electrons*. Czechoslovak Journal of Physics, vol. 46, pages 1909–1910, 1996. 10.1007/BF02570946.
- [Rosch 2000] A. Rosch. *Magnetotransport in nearly antiferromagnetic metals*. Phys. Rev. B, vol. 62, pages 4945–4962, Aug 2000.
- [Ruderman 1954] M. A. Ruderman and C. Kittel. *Indirect Exchange Coupling of Nuclear Magnetic Moments by Conduction Electrons*. Phys. Rev., vol. 96, pages 99–102, Oct 1954.
- [Rueff 2007] J.-P. Rueff. *Strongly Correlated Electrons at High Pressure: An Approach by Inelastic X-ray Scattering*. PhD thesis, Université Pierre et Marie Curie - Paris 6, 2007.
- [Rueff 2010] J.-P. Rueff and A. Shukla. *Inelastic X-ray Scattering by Electronic Excitations under High Pressure*. Rev. Mod. Phys., vol. 82, page 847, 2010.
- [Rueff 2011] J.-P. Rueff, S. Raymond, M. Taguchi, M. Sikora, J.-P. Itié, F. Baudalet, D. Braithwaite, G. Knebel and D. Jaccard. *Pressure-Induced Valence Crossover in Superconducting  $\text{CeCu}_2\text{Si}_2$* . Phys. Rev. Lett., vol. 106, page 186405, May 2011.
- [Sachdev 2011] S. Sachdev. Quantum phase transitions. Cambridge University Press, 2011.
- [Saiga 2008] Y. Saiga, K. Matsubayashi, T. Fujiwara, M. Kosaka, S. Katano, M. Hedo, T. Matsumoto and T. Uwatoko. *Pressure-induced Magnetic Transition in a Single Crystal of  $\text{YbCo}_2\text{Zn}_{20}$* . Journal of the Physical Society of Japan, vol. 77, no. 5, page 053710, 2008.

## BIBLIOGRAPHY

- [Saiga 2009] Y. Saiga, K. Matsubayashi, T. Fujiwara, M. Kosaka, S. Katano and T. Uwatoko. *Magnetoresistivity of  $\text{YbCo}_2\text{Zn}_{20}$  at low temperature*. Journal of Physics: Conference Series, vol. 150, no. 4, page 042168, 2009.
- [Salce 2000] B. Salce, J. Thomasson, A. Demuer, J.J. Blanchard, J.M Martinod, L. Devoille and A. Guillaume. *Versatile device for low temperature in situ generation of forces up to 25 kN: Application to hydrostatic pressure experiments*. Rev. Sci. Instrum., vol. 71, page 2461, 2000.
- [Sales 1976] B.C. Sales and R. Viswanathan. *Demagnetization due to interconfiguration fluctuations in the RE-Cu<sub>2</sub>Si<sub>2</sub> compounds*. Journal of Low Temperature Physics, vol. 23, no. 3-4, pages 449–467, 1976. cited By (since 1996) 44.
- [Sampathkumaran 1986] E. Sampathkumaran. *Intermediate valence in rare earth systems*. Hyperfine Interactions, vol. 27, pages 183–192, 1986.
- [Sanchez 2000] J.P. Sanchez and M.M. Abd-Elmeguid. *Pressure-induced magnetic phase transitions in Yb Kondo lattice systems*. Hyperfine Interactions, vol. 128, pages 137–150, 2000.
- [Sarrao 1998] J. L. Sarrao, R. Modler, R. Movshovich, A. H. Lacerda, D. Hristova, A. L. Cornelius, M. F. Hundley, J. D. Thompson, C. L. Benton, C. D. Immer, M. E. Torelli, G. B. Martins, Z. Fisk and S. B. Oseroff. *Ferromagnetism and crystal fields in  $\text{YbInNi}_4$* . Phys. Rev. B, vol. 57, pages 7785–7790, Apr 1998.
- [Satoh 1989] K. Satoh, T. Fujita, Y. Maeno, Y. Ōnuki and T. Komatsubara. *Low-Temperature Specific Heat of  $\text{Ce}_x\text{La}_{1-x}\text{Cu}_6$* . Journal of the Physical Society of Japan, vol. 58, no. 3, pages 1012–1020, 1989.
- [Schrieffer 1966] J. R. Schrieffer and P. A. Wolff. *Relation between the Anderson and Kondo Hamiltonians*. Phys. Rev., vol. 149, pages 491–492, Sep 1966.
- [Seuring 2000] C. Seuring, K. Heuser, E.-W. Scheidt, T. Schreiner, E. Bauer and G.R. Stewart. *Evidence of field-induced non-Fermi-liquid behavior in  $\text{YbCu}_{5-x}\text{Al}_x$  compounds*. Physica B: Condensed Matter, vol. 281282, no. 0, pages 374 – 376, 2000.
- [Shimura 2011] Y. Shimura, T. Sakakibara, S. Yoshiuchi, F. Honda, R. Settai and Y. Ōnuki. *Evidence of a Field-Induced Ordering in  $\text{YbCo}_2\text{Zn}_{20}$  in a [111] Magnetic Field*. Journal of the Physical Society of Japan, vol. 80, no. 7, page 073707, 2011.
- [Silvera 1985] I.F. Silvera and R.J. Wijngaarden. *Diamond anvil cell and cryostat for low-temperature optical studies*. Review of Scientific Instruments, vol. 56, no. 1, pages 121–124, 1985.
- [Spain 1989] I. L. Spain and D.J. Dunstan. *The technology of diamond anvil high-pressure cells: II. Operation and use*. Journal of Physics E: Scientific Instruments, vol. 22, no. 11, page 923, 1989.
- [Steglich 1979] F. Steglich, J. Aarts, C. D. Bredl, W. Lieke, D. Meschede, W. Franz and H. Schäfer. *Superconductivity in the Presence of Strong Pauli Paramagnetism:  $\text{CeCu}_2\text{Si}_2$* . Phys. Rev. Lett., vol. 43, pages 1892–1896, Dec 1979.

## BIBLIOGRAPHY

- [Steglich 1996] F. Steglich, P. Gegenwart, C. Geibel, R. Helfrich, P. Hellmann, M. Lang, A. Link, R. Modler, G. Sparn, N. Battgen and A. Loidl. *New observations concerning magnetism and superconductivity in heavy-fermion metals*. Physica B: Condensed Matter, vol. 223-224, no. 0, pages 1 – 8, 1996.
- [Stewart 2001] G. R. Stewart. *Non-Fermi-liquid behavior in d- and f-electron metals*. Rev. Mod. Phys., vol. 73, pages 797–855, Oct 2001.
- [Stockert 2006] O. Stockert, M.M. Koza, J. Ferstl, A.P. Murani, C. Geibel and F. Steglich. *Crystalline electric field excitations of the non-Fermi-liquid*. Physica B: Condensed Matter, vol. 378380, no. 0, pages 157 – 158, 2006.
- [Sugiyama 1999] K. Sugiyama, M. Nakashima, D. Aoki, K. Kindo, N. Kimura, H. Aoki, T. Komatsubara, S. Uji, Y. Haga, E. Yamamoto, H. Harima and Y. Ōnuki. *Metamagnetic transition in UPt<sub>3</sub> studied by high-field magnetization and de Haas–van Alphen experiments*. Phys. Rev. B, vol. 60, pages 9248–9251, Oct 1999.
- [Suhl 1965] H. Suhl. *Dispersion Theory of the Kondo Effect*. Phys. Rev., vol. 138, pages A515–A523, Apr 1965.
- [Sullivan 1968] P. F. Sullivan and G. Seidel. *Steady-State, ac-Temperature Calorimetry*. Phys. Rev., vol. 173, pages 679–685, Sep 1968.
- [Sumiyama 1986] A. Sumiyama, Y. Oda, H. Nagano, Y. Ōnuki, K. Shibusaki and T. Komatsubara. *Coherent Kondo State in a Dense Kondo Substance: Ce<sub>x</sub>La<sub>1-x</sub>Cu<sub>6</sub>*. Journal of the Physical Society of Japan, vol. 55, no. 4, pages 1294–1304, 1986.
- [Syassen 1982] K. Syassen, G. Wortmann, J. Feldhaus, K. H. Frank and G. Kaindl. *Mean valence of Yb metal in the pressure range 0 to 340 kbar*. Phys. Rev. B, vol. 26, pages 4745–4748, Oct 1982.
- [Taga 2012] Y. Taga, S. Yoshiuchi, M. Ohya, J. Sakaguchi, Y. Hirose, F. Honda, T. Takeuchi, R. Settai and Y. Onuki. *Quantum Criticality and Heavy Fermion State in YbCo<sub>2</sub>Zn<sub>20</sub> under Pressure and Magnetic Field*. Journal of the Physical Society of Japan, vol. "in press", 2012.
- [Takeda 2008] Y. Takeda, N.D. Dung, Y. Nakano, T. Ishikura, S. Ikeda, T.D. Matsuda, E. Yamamoto, Y. Haga, T. Takeuchi, R. Settai and Y. Ōnuki. *Calorimetric Study in Single Crystalline RCu<sub>2</sub>Si<sub>2</sub> (R: Rare Earth)*. Journal of the Physical Society of Japan, vol. 77, no. 10, page 104710, 2008.
- [Takeuchi 2010] T. Takeuchi, S. Yasui, M. Toda, M. Matsushita, S. Yoshiuchi, M. Ohya, K. Katayama, Y. Hirose, N. Yoshitani, F. Honda, K. Sugiyama, M. Hagiwara, K. Kindo, E. Yamamoto, Y. Haga, T. Tanaka, Y. Kubo, R. Settai and Y. Ōnuki. *Metamagnetic behavior in heavy-fermion compound YbIr<sub>2</sub>Zn<sub>20</sub>*. Journal of the Physical Society of Japan, vol. 79, no. 6, page 064609, 2010.
- [Takeuchi 2011a] T. Takeuchi, M. Ohya, S. Yoshiuchi, M. Matsushita, F. Honda, R. Settai and Y. Onuki. *Metamagnetic behavior in a heavy fermion compound YbCo<sub>2</sub>Zn<sub>20</sub>*. Journal of Physics: Conference Series, vol. 273, no. 1, page 012059, 2011.

## BIBLIOGRAPHY

- [Takeuchi 2011b] T. Takeuchi, S. Yoshiuchi, M. Ohya, Y. Taga, Y. Hirose, K. Sugiyama, M. Hagiwara, K. Kindo, R. Settai and Y. Onuki. *Field-Induced Quadrupolar Ordered Phase for  $H \parallel \langle 111 \rangle$  in Heavy-Fermion Compound  $\text{YbCo}_2\text{Zn}_{20}$* . Journal of the Physical Society of Japan, vol. 80, no. 11, page 114703, 2011.
- [Tayama 2004] T. Tayama, J. Custers, H. Sato, T. Sakakibara, H. Sugawara and H. Sato. *New High-Field Ordered State in  $\text{PrFe}_4\text{P}_{12}$* . Journal of the Physical Society of Japan, vol. 73, no. 12, pages 3258–3261, 2004.
- [Thomasson 1997] J. Thomasson, Y. Dumont, J.-C. Griveau and C. Ayache. *Transport measurements at low temperatures in a diamond anvil cell with helium as pressure medium*. Review of Scientific Instruments, vol. 68, no. 3, pages 1514–1517, 1997.
- [Thompson 1994] J.D. Thompson and J.M. Lawrence. *Chapter 133 High pressure studies, physical properties of anomalous Ce, Yb and U compounds*. In LeRoy Eyring G. H. Lander Karl A. Gschneidner Jr. and G. R. Choppin, editors, Lanthanides/Actinides: Physics - II, volume 19 of *Handbook on the Physics and Chemistry of Rare Earths*, pages 383 – 478. Elsevier, 1994.
- [Tinkham 2004] M. Tinkham. Introduction to superconductivity. Dover publications, 2004.
- [Torikachvili 2007] M. S. Torikachvili, S. Jia, E. D. Mun, S. T. Hannahs, R. C. Black, W. K. Neils, Dinesh Martien, S. L. Bud'ko and P. C. Canfield. *Six closely related  $\text{YbT}_2\text{Zn}_{20}$  ( $T = \text{Fe}, \text{Co}, \text{Ru}, \text{Rh}, \text{Os}, \text{Ir}$ ) heavy fermion compounds with large local moment degeneracy*. Proceedings of the National Academy of Sciences, vol. 104, no. 24, pages 9960–9963, 2007.
- [Trovarelli 2000] O. Trovarelli, C. Geibel, S. Mederle, C. Langhammer, F. M. Grosche, P. Gegenwart, M. Lang, G. Sparn and F. Steglich.  *$\text{YbRh}_2\text{Si}_2$ : Pronounced Non-Fermi-Liquid Effects above a Low-Lying Magnetic Phase Transition*. Phys. Rev. Lett., vol. 85, pages 626–629, Jul 2000.
- [Tsuduki 2005] S. Tsuduki, A. Onodera, K. Ishida, Y. Kitaoka, A. Onuki, N. Ishimatsu and O. Shimomura. *Synchrotron X-ray diffraction and absorption studies of  $\text{CeM}_2\text{X}_2$  ( $M = \text{Cu}, \text{Ni}$  and  $X = \text{Si}, \text{Ge}$ ) at high pressure*. Solid State Communications, vol. 134, no. 11, pages 747 – 751, 2005.
- [Tsuji 2005] N. Tsuji, H. Kontani and K. Yoshimura. *Universality in Heavy Fermion Systems with General Degeneracy*. Phys. Rev. Lett., vol. 94, page 057201, Feb 2005.
- [Tsunetsugu 1997] H. Tsunetsugu, M. Sigrist and K. Ueda. *The ground-state phase diagram of the one-dimensional Kondo lattice model*. Rev. Mod. Phys., vol. 69, pages 809–864, Jul 1997.
- [Uwatoko 2005] Y. Uwatoko, T. Fujiwara, M. Hedo, F. Tomioka and I. Umehara. *The development of a high pressure micro-cell for magnetization and specific heat measurements: the effect of pressure on the magnetism in  $\text{CeAg}$* . Journal of Physics: Condensed Matter, vol. 17, no. 11, page S1011, 2005.
- [Varma 1976] C. M. Varma. *Mixed-valence compounds*. Rev. Mod. Phys., vol. 48, page 219, 1976.
- [Waber 1965] J. T. Waber and Don T. Cromer. *Orbital Radii of Atoms and Ions*. The Journal of Chemical Physics, vol. 42, no. 12, pages 4116–4123, 1965.

## BIBLIOGRAPHY

- [Walter 1992] U. Walter, E. Holland-Moritz and U. Steigenberger. *Pressure-induced valence and crystal field shifts in  $\text{YbCu}_2\text{Si}_2$  and  $\text{TmTe}$  by neutron scattering*. Zeitschrift für Physik B Condensed Matter, vol. 89, pages 169–176, 1992.
- [Watanabe 2008] S. Watanabe, A. Tsuruta, K. Miyake and J. Flouquet. *Magnetic-Field Control of Quantum Critical Points of Valence Transition*. Phys. Rev. Lett., vol. 100, page 236401, Jun 2008.
- [Watanabe 2009] S. Watanabe, A. Tsuruta, K. Miyake and J. Flouquet. *Valence Fluctuations Revealed by Magnetic Field and Pressure Scans: Comparison with Experiments in  $\text{YbXCu}_4$  ( $X = \text{In, Ag, Cd}$ ) and  $\text{CeYIn}_5$  ( $Y = \text{Ir, Rh}$ )*. Journal of the Physical Society of Japan, vol. 78, no. 10, page 104706, 2009.
- [Watanabe 2010a] S. Watanabe and K. Miyake. *Influence of quantum critical point of first-order valence transition on Ce- and Yb-based heavy fermions*. physica status solidi (b), vol. 247, no. 3, pages 490–494, 2010.
- [Watanabe 2010b] S. Watanabe and K. Miyake. *Quantum Valence Criticality as an Origin of Unconventional Critical Phenomena*. Phys. Rev. Lett., vol. 105, page 186403, Oct 2010.
- [Watanabe 2011] S. Watanabe and K. Miyake. *Roles of critical valence fluctuations in Ce- and Yb-based heavy fermion metals*. J. Phys. Condens. Matter., vol. 23, no. 9, page 094217, 2011.
- [Webb 1976] A. W. Webb, D. U. Gubser and L. C. Towle. *Cryostat for generating pressures to 100 kilobar and temperatures to 0.03 K*. Review of Scientific Instruments, vol. 47, no. 1, pages 59–62, 1976.
- [White 1979] G. K. White. Experimental techniques in low-temperature physics. Clarendon press, 1979.
- [Willers 2011] T. Willers, N. Hollmann, S. Wirth, H. Kierspel, A. Bianchi, Z. Fisk and A. Severing. *Nature of magnetic order in  $\text{YbInNi}_4$* . Arxiv preprint arXiv:1101.4770, 2011.
- [Winkelmann 1998] H. Winkelmann, M. M. Abd-Elmeguid, H. Micklitz, J. P. Sanchez, C. Geibel and F. Steglich. *Pressure-Induced Local Moment Magnetism in the Nonmagnetic Heavy Fermion Compound  $\text{Yb}_2\text{Ni}_2\text{Al}$* . Phys. Rev. Lett., vol. 81, pages 4947–4950, Nov 1998.
- [Winkelmann 1999] H. Winkelmann, M. M. Abd-Elmeguid, H. Micklitz, J. P. Sanchez, P. Vulliet, K. Alami-Yadri and D. Jaccard. *Direct observation of a magnetically ordered state in  $\text{YbCu}_2\text{Si}_2$  under high pressure*. Phys. Rev. B, vol. 60, pages 3324–3330, Aug 1999.
- [Yadri 1996] K. Alami Yadri and D. Jaccard. *High pressure electrical resistivity of  $\text{YbCu}_2\text{Si}_2$* . Solid State Communications, vol. 100, no. 6, pages 385 – 387, 1996.
- [Yamaoka 2010] H. Yamaoka, I. Jarrige, N. Tsujii, J-F Lin, N. Hiraoka, H. Ishii and K-D Tsuei. *Temperature and pressure-induced valence transitions in  $\text{YbNi}_2\text{Ge}_2$  and  $\text{YbPd}_2\text{Si}_2$* . Phys. Rev. B, vol. 82, page 035111, Jul 2010.
- [Yuan 2006] H. Q. Yuan, M. Nicklas, Z. Hossain, C. Geibel and F. Steglich. *Quantum phase transition in the heavy-fermion compound  $\text{YbIr}_2\text{Si}_2$* . Phys. Rev. B, vol. 74, page 212403, Dec 2006.